Please do not adjust margins

Dalton Transactions

ARTICLE

Sky-blue emitting bridged diiridium complexes: beneficial effects of intramolecular π–π stacking

Received 00th January 20xx,
Accepted 00th January 20xx

DOI: 10.1039/x0xx00000x

www.rsc.org/

Daniel G. Congrave, Yu-Ting Hsu, Andrei S. Batsanov, Andrew Beeby and Martin R. Bryce*

The potential of intramolecular π–π interactions to influence the photophysical properties of diiridium complexes is an unexplored topic, and provides the motivation for the present study. A series of diarylhydrazide-bridged diiridium complexes functionalised with phenylpyridine (ppy)-based cyclometalating ligands is reported. It is shown by NMR studies in solution and single crystal X-ray analysis that intramolecular π–π interactions between the bridging and cyclometalating ligands rigidify the complexes leading to high luminescence quantum efficiencies in solution and in doped films. Fluorine substituents on the phenyl rings of the bridge promote the intramolecular π–π interactions. Notably, these non-covalent interactions are harnessed in the rational design and synthesis of the first examples of highly emissive sky-blue diiridium complexes featuring conjugated bridging ligands, for which they play a vital role in the structural and photophysical properties. Experimental results are supported by computational studies.

Introduction

Iridium(III) complexes possess rich metal-ligand based photochemistry, typically with high luminescence quantum efficiency (Φ) and short excited state lifetimes (τ_p). They are widely employed in applications[1] such as photocatalysis,[2] biological labelling,[3] sensing[4] and as emissive dopants in phosphorescent organic light-emissive devices (PhOLEDs).[5,6] Their emission colour can be tuned across the entire visible spectrum by systematic variation of the ligands.[7]

Unlike their monometallic analogues, diiridium complexes are rarely studied for luminescence applications due to their generally low photoluminescence quantum yields (PLQYs) and limited colour range.[8–17] However, there are examples where the favourable luminescent properties of monoiridium complexes are retained in diiridium complexes by the careful choice of conjugated bridging ligands.[18–27] Moreover, bridging ligands offer scope for increased structural variation compared to monoiridium analogues, and allow tuning of the electronic communication between the iridium centres which may lead to interesting photophysical properties, such as improved spin-orbit coupling effects,[24,26] or dual emission. Diiridium complexes are known with efficient emission from red to green;[18–26] however, we are not aware of any blue / sky-blue diiridium complexes featuring conjugated bridging ligands.[28]

Department of Chemistry, Durham University, South Road, Durham DH1 3LE, UK. E-mail: m.r.bryce@durham.ac.uk.

Electronic Supplementary Information (ESI) available: synthetic details, NMR spectra, X-ray data, electrochemistry, thermal gravimetric analysis; computations and photophysics. See DOI: 10.1039/x0xx00000x

Recently, we described diarylhydrazide-bridged diiridium complexes functionalised with phenylpyridine (ppy)-based cyclometalating ligands.[22] These complexes are highly emissive in the green region when doped into rigid poly(methylmethacrylate) (PMMA) films, but are practically nonemissive in solution, presumably due to the flexibility of their non-ancillary bridging units which leads to non-radiative decay via intramolecular motion. An interesting structural feature was observed: the pendant aryl rings on the bridge engage in intramolecular face-to-face π–π stacking with the cyclometalating phenyl ligands in the solid state (complex **1**, Figure 1).

Intramolecular π–π stacking between aryl and heteroaryl rings has been reported in a few specific monoiridium complexes (e.g. **2-6**, Figure 1), particularly in charged derivatives.[29–33] For example, in complex **2** intramolecular π–π stacking between a cyclometalating ligand and a pendant pentafluorophenyl group leads to an order of magnitude increase in solution PLQY, due to a reduction in the non-radiative rate constant (k_{nr}).[31] Intramolecular π–π stacking in complex **3** leads to increased operational stability of light-emitting electrochemical cells (LEECs).[29] Nonetheless, the potential of intramolecular π–π interactions to influence the photophysical properties of diiridium complexes remains unexplored, and provides the motivation for the present study.

We now show that intramolecular π–π stacking can be exploited to rigidify diiridium complexes and to obtain high luminescence quantum efficiencies in solution and in doped films. We also present the first examples of highly emissive sky-blue diiridium complexes featuring conjugated bridging

Please do not adjust margins

Please do not adjust margins

ligands, for which the π–π interactions play an important role in the structural and photophysical properties.

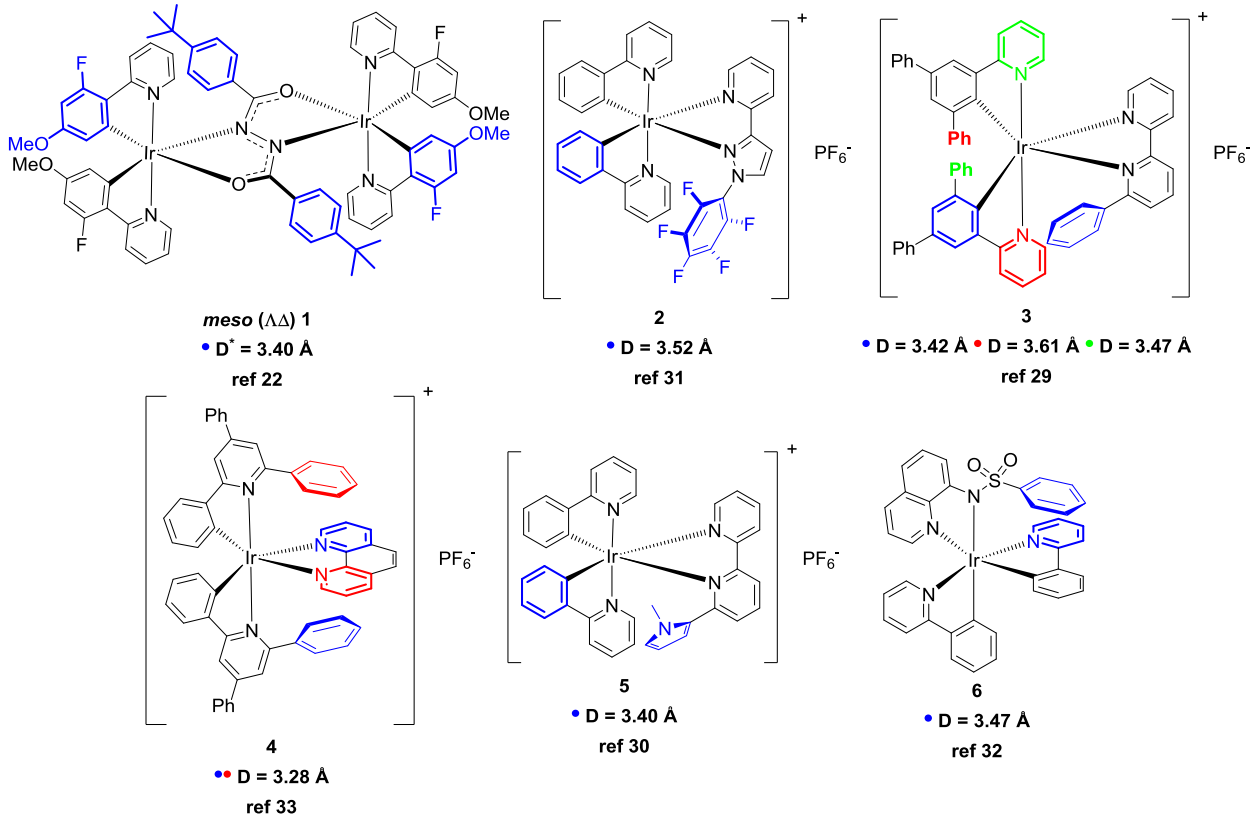

Figure 1. Representative iridium complexes which display intramolecular π–π stacking interactions, highlighted by the coloured rings. D = centroid–centroid distance determined by X-ray diffraction for the same-coloured rings. D* = distance between the centroid of the bridge aryl ring and the plane of the cyclometalating ligand.

Results and discussion

Design, synthesis and characterisation

The structural versatility of **1** and analogues[22] provides an ideal opportunity to explore how intramolecular π–π interactions between the bridging and cyclometalating ligands can influence the photophysical properties of diiridium systems. Benzene is well known to stack with hexafluorobenzene in a slipped face-to-face configuration in the solid state.[34–36] Complexes **7-9** (Figure 2) with an increasing number of fluorine substituents on the phenyl rings of the bridge, were, therefore, designed with the aim of promoting intramolecular π–π interactions. Methoxy derivative **10** was also included based on calculations (discussed below) which predict the bridge of **10** to be non-ancillary despite the highly fluorinated aryl rings (in contrast to **8** and **9**). The analogues **12** and **14**, featuring CF_3 substituents instead of perfluoroaryl rings, were studied as model compounds for which π–π interactions involving the bridge are not possible. For derivatives **11-15**, the substituents on the pyridyl rings serve to enhance solubility. For **13-15** the difluorophenyl rings of the ppy ligands were chosen to blue shift the emission, based on monoiridium precedents.[37,38]

The diarylhydrazide bridges **17a–d** (Figure 2) were synthesised (Scheme S1) by condensation of hydrazine monohydrate with the corresponding benzoyl chlorides, which were either commercially available or prepared from the corresponding benzoic acid (**16a–d**). The bridge units were heated in a 1:1 molar ratio with $[Ir(ppy)_2\mu–Cl]_2$ in either 2-ethoxyethanol (**17a**) or dry diglyme (**17b-d**) in the presence of K_2CO_3, to obtain the complexes **7–10** as diastereomeric mixtures (*meso* ΛΔ and *rac* ΛΛ/ ΔΔ) (Figure 2). In previous investigations, the diastereomers of analogous phenylpyridine-functionalised diiridium systems were separated and minimal differences were observed in the photophysical properties of the two diastereomers.[21,22] Therefore, complexes **7-10** were characterised as diastereomeric mixtures. The complexes were unambiguously identified by ^{1}H, ^{19}F and ^{13}C (where solubility allowed) NMR spectroscopy, MALDI–TOF mass spectrometry and elemental analysis. NMR peak assignments were aided by ^{1}H–^{1}H COSY, ^{1}H–^{1}H NOESY, ^{1}H–^{1}H ROESY, ^{1}H–^{13}C HSQC, ^{1}H–^{13}C HMBC and ^{19}F–^{19}F COSY 2D NMR experiments.

For complexes **7-10** the ^{19}F NMR data are of particular interest. For the bis(difluorophenyl)hydrazide-bridged complex **7**, a single peak is observed in the ^{19}F spectrum of the diastereomeric mixture (Figure S2), analogous to the spectrum of the free bridge (**17a**) (Figure S74). This indicates that the ^{19}F environments are very similar for each diastereomer of **7** and that the bridging phenyl rings are freely rotating in solution on the NMR timescale.

This journal is © The Royal Society of Chemistry 20xx

Please do not adjust margins

Please do not adjust margins

Dalton Transactions

ARTICLE

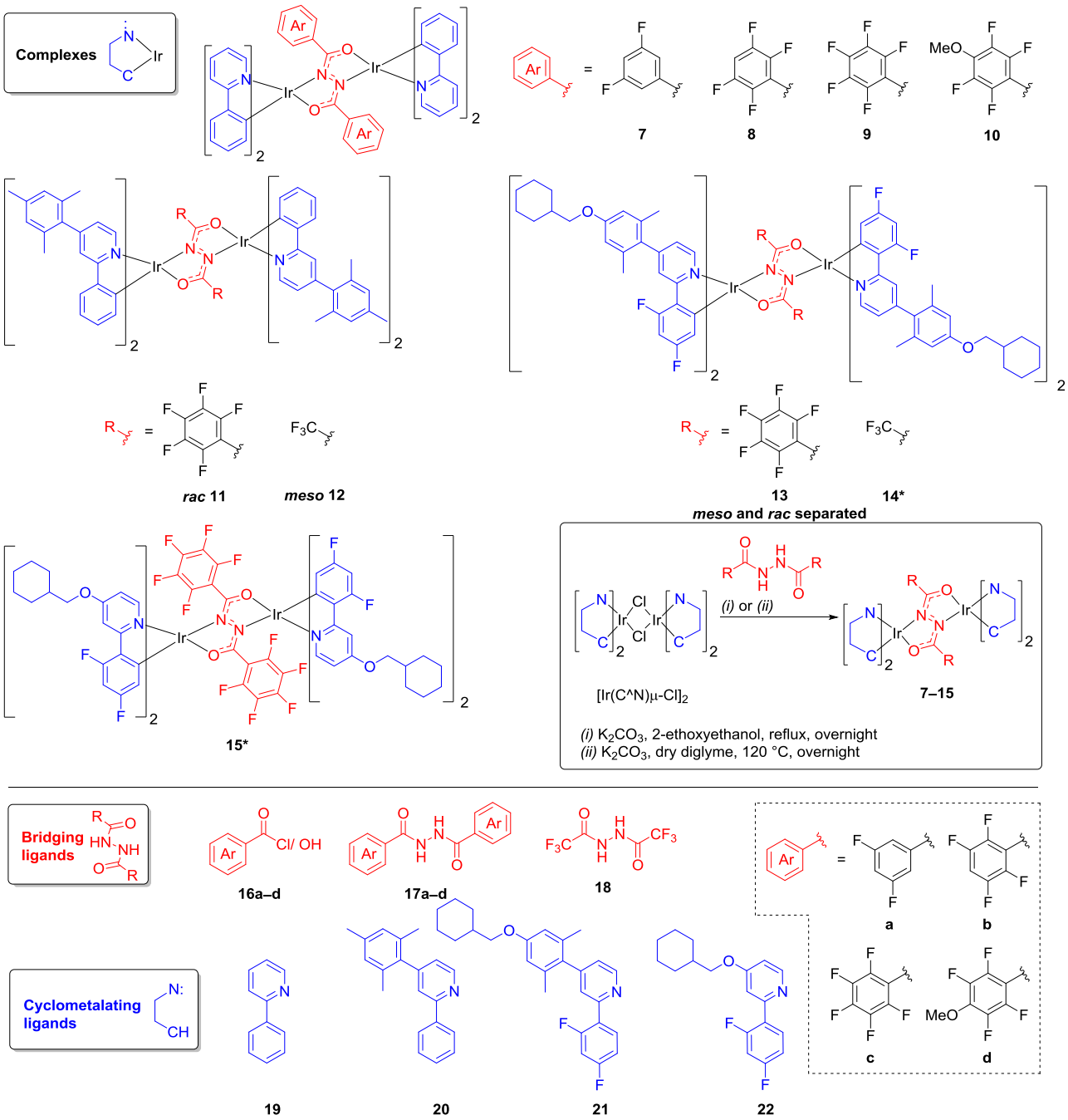

Figure 2. (Top) Structures for the diiridium complexes studied in this work. (Bottom) structures for the bridging and cyclometalating ligands. Complexes were studied as diastereomeric mixtures unless otherwise stated. * Complexes **14** and **15** were isolated as single diastereomers; their absolute configurations are unknown.

Please do not adjust margins

Please do not adjust margins

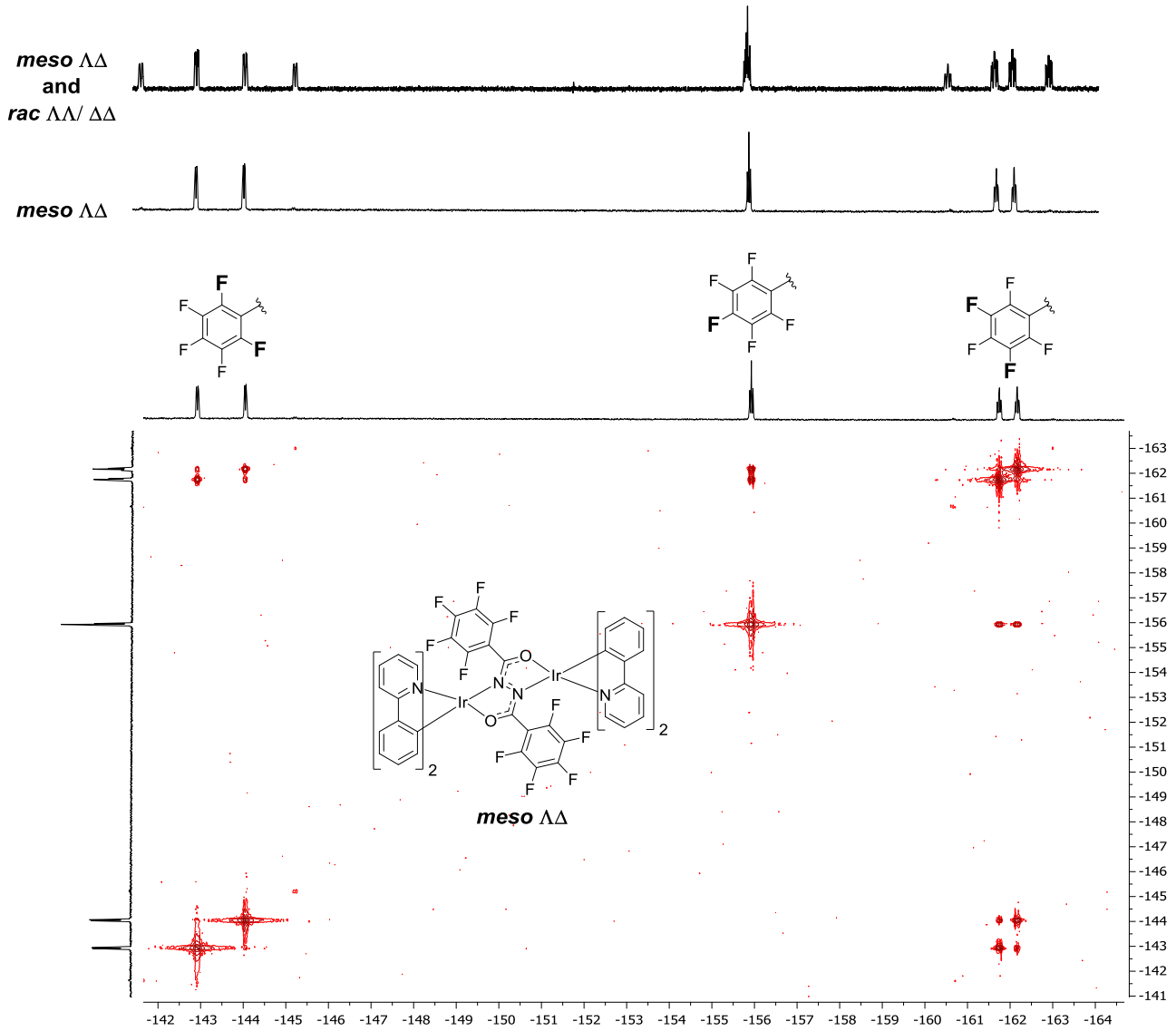

Figure 3. (Top) ^{19}F NMR spectrum of the diastereomeric mixture of **9** (*ca.* 5:4 molar ratio of *meso* (ΛΔ) and *rac* (ΛΛ/ ΔΔ)). (Middle) ^{19}F NMR spectrum of *meso* **9** (Bottom) ^{19}F–^{19}F COSY NMR spectrum of *meso* **9** Chemical shifts are in ppm.

This contrasts with the data for the bis(pentafluorophenyl)hydrazide-bridged complex **9**. The ligand **17c** features 3 distinct environments in its ^{19}F NMR spectrum as expected (Figure S80), whereas the ^{19}F NMR spectrum of *meso* **9** features 5 well-resolved distinct environments (Figure 3, Figure S15) due to an apparent breakdown in symmetry, suggesting that rotation of the bridging pentafluorophenyl rings is restricted at room temperature in solution. This was confirmed when *meso* **9** was further studied by ^{19}F–^{19}F COSY NMR (Figure 3). This is because, although only *ortho* ($^{3}J \approx 23$ Hz) and *para* ($^{5}J \approx 6$ Hz) couplings are observed (in agreement with the multiplicities of the signals in the 1D spectrum), the data indicate that all 5 fluorine environments are on the same ring. *Meta* (^{4}J) ^{19}F–^{19}F coupling constants that are considerably smaller than those for *ortho* and *para* coupling (or even absent) have been commonly reported for heavily fluorinated aryl systems.[39–43] It has been

Please do not adjust margins

Please do not adjust margins

suggested that this is because π-conjugation contributes significantly to $^{19}F–^{19}F$ coupling.[39,43]

We propose that this restriction of rotation is due to intramolecular π–π interactions. Steric restriction alone is unlikely to explain such well-resolved ^{19}F NMR signals, considering that fluorine atoms exert similar steric effects as protons,[44] and that the analogous difluoro complex **7** does not exhibit this effect. The ^{19}F NMR spectra of complexes **8**, **10**, **11**, **13** and **15** also show this feature (Figures S5, S18, S24, S42, S51 and S68). These observations indicate that a bridge tetrafluorophenyl group is sufficient to promote strong intramolecular π–π interactions in solution, and that fluorine atoms on the cyclometalating phenyl rings of ppy ligands (**13** and **15**) do not suppress them.

The bis(trifluoromethyl) bridge **18**[45] (Figure 2) was also investigated, as although it is strongly electron withdrawing like the perfluoroaryl bridge **17c**,[46] it cannot engage in intramolecular π–π stacking. Attempts to isolate a complex analogous to **9** by reacting the bridge **18** with $[Ir(ppy)_2μ–Cl]_2$ were unsuccessful, due to its extremely poor solubility. (Mass spectra suggested the complex had formed). As an alternative, complex **12** was synthesised (Figure 2), which features 4-mesityl-2-phenylpyridine (**20**) cyclometalating ligands. Mesityl groups are known to improve the solubility of cyclometalated iridium complexes while exerting minimal influence on their photophysical properties.[47,48,49] Complex **12** was isolated as a diasteromerically pure *meso* sample (confirmed by X-ray diffraction, Figure S102) in 61% yield. No *rac* diastereomer was detected in the crude reaction mixture. This stereoselectivity is surprising as DFT calculations predict the *rac* diastereomer to be the more thermodynamically stable, as is usually the case for diiridium systems.[21,22,50] Attempts to isomerise **12** thermally or photochemically were unsuccessful, as previously reported for other diiridium diastereomers.[22]

To allow a direct comparison with complex **12**, complex **11** (the mesityl-functionalised analogue of complex **9**) (Figure 2), was also synthesised. Interestingly, the presence of mesityl groups leads to a larger difference in the solubilities of the diastereomers of **11** compared to **9**, making them trivial to separate by column chromatography. However, the extremely poor solubility of *meso* **11** prevented its purification and so only *rac* **11** is studied here (stereochemistry confirmed by X-ray diffraction, Figure S101). It is noteworthy that *meso* **11** is less soluble than complex **9** despite the presence of mesityl groups, in contrast to the expectation based on previous reports.[47,48,50] A tentative explanation is based on the symmetry of the complex.[51]

We have previously shown that colour tuning of the emission of diarylhydrazide-bridged diiridium complexes within the range λ_{max} 520–490 nm can be achieved through functionalisation of either the bridge or cyclometallating phenyl rings with electron withdrawing groups.[21,22] We reasoned, therefore, that simultaneous functionalisation of both moieties with electron withdrawing groups might afford blue / sky-blue diiridium complexes, which to date remain elusive.

Initial attempts to obtain diiridium complexes through a combination of 2-(2,4-difluorophenyl)pyridine (dfppy) or 2-(2,4-difluorophenyl)-4-mesitylpyridine[48] with the bis(pentafluorophenyl)/(trifluoromethyl) bridges **17c** and **18** (Figure 2) were unsuccessful due to the extremely poor solubility of the products.
To enhance solubility the new dfppy derivative **21** (Figure 2) was synthesised (Scheme S1), wherein the mesityl group is replaced by a methylenecyclohexylether-functionalised xylyl group. The methylenecyclohexyl group provides the beneficial solubilising properties of a branched alkyl group while being achiral. Additionally, the xylyl spacer in **21** is a rigid non-conjugated linker to limit the electronic influence of the electron-donating ether group.
The ligand **22** (Figure 2) was also synthesised (Scheme S1) to investigate the effect of directly functionalising the pyridyl moiety with the methylenecyclohexyl group, which is expected to destabilise the lowest unoccupied molecular orbital (LUMO) and further blue shift emission.

As observed for **12**, the bis(trifluoromethyl) bridge **18** resulted in only a single diastereomer for complex **14** (Figure 2). These two examples (**12** and **14**) suggest that bis(alkyl)hydrazide bridges afford diiridium complexes from racemic μ-dichloro dimers without the formation of diastereomeric mixtures. This is complementary to using enantiomerically pure dichloro-bridged dimers, as reported for other systems.[49,52]

Analogous to the mesityl-functionalised complex **11**, the diastereomers *rac* **13** (stereochemistry confirmed by X-ray diffraction, Figure 4) and *meso* **13** were easily separated. The improved solubility imparted by the methylenecyclohexylether groups allowed both diastereomers to be fully characterised. Complex **15** was isolated as a single diastereomer: the absolute configuration is unknown, although it is probably the *meso* structure from inspection of the ^1H NMR spectrum (Figure S66). A second diastereomer was observed by NMR but could not be isolated.

Thermal gravimetric analysis (TGA) shows that all the complexes **7-15** possess good thermal stability (Figures S144–S153).

X-Ray molecular structures

Complexes **7** and **9–13** (Figures 4 and S97–S103) were characterised by single-crystal X-ray crystallography. Relevant parameters are listed in Table S1. All structures except **9** and **10** contained disordered CH_2Cl_2 or CD_2Cl_2 of crystallisation.

In *meso* complexes **7**, **9** and **12**, the molecule possesses a crystallographic inversion centre (located at the midpoint of the N–N bond) relating the Λ and Δ metal centres. The *rac* complexes **10**, **11** and **13** all crystallise in centrosymmetric space groups, thus each molecule is chiral (ΛΛ or ΔΔ) but the crystal is racemic. Two solvent-free polymorphs of **10** formed concomitantly; in α-**10** the molecule lies on a crystallographic twofold axis while in β-**10** (as in **11** and **13**) it has no crystallographic symmetry. Each Ir atom has distorted octahedral coordination, involving one N and one O atom of the bridging hydrazide (OCNNCO) ligand, and two C^N cyclometalating ligands. As usual, the N atoms of the latter occupy axial positions, *trans* to one another.[6,21] As reported

Please do not adjust margins

Please do not adjust margins

earlier,[22] in *meso* complexes the hydrazide moiety is planar, while in *rac* isomers it is variously (by 7 to 24°) folded along the central N–N bond into two planar OCNN chelating fragments. The chelated Ir atoms can be coplanar with, or displaced from, their planes, but this does not affect the bonding pattern significantly. Each aryl substituent (*A*) at the bridging ligand is oriented approximately perpendicular to the hydrazide plane (thus precluding π-conjugation) and is stacked face-to-face (π–π) with a cyclometalating ligand, essentially with its phenyl ring (*B*) (Figures 4, S98–S101 and S103). This will shorten the effective conjugation length of the bridge and is beneficial for shifting emission towards the blue (see below).

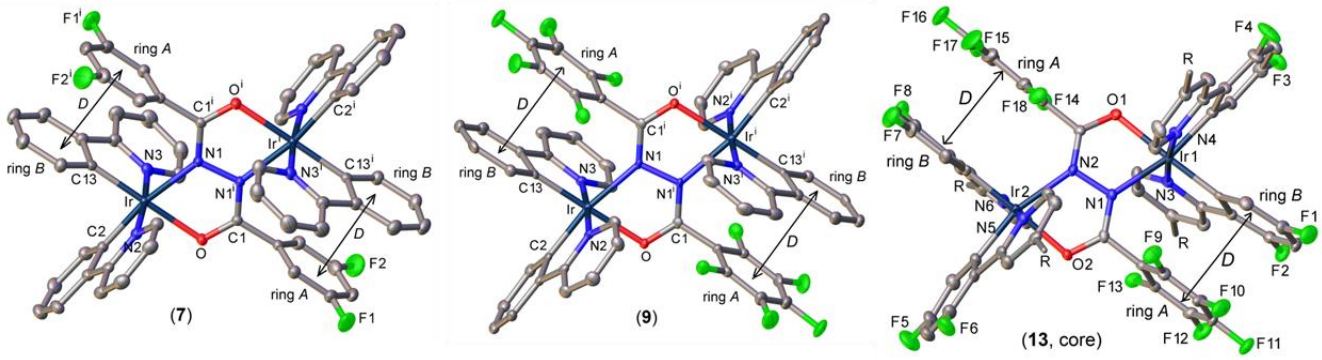

Figure 4. X-ray molecular structures of *meso* **7**, *meso* **9** and the core part of *rac* **13** (ΔΔ) with the xylyl substituents (R) omitted. Thermal ellipsoids are drawn at 50% probability level. H atoms are omitted for clarity. Vector *D* identifies intramolecular π–π interactions, *meso* **7** = 3.32 Å, *meso* **9** =3.24 Å, *rac* **13** = 3.27, 3.19 Å.

Generally, the stacking is closer and more parallel than in previously studied analogues with *t*-Bu and CF_3-substitutuents.[21,22] To the best of our knowledge the systems studied here demonstrate the closest intramolecular π–π stacking reported for cyclometallated iridium complexes.[22,29–33] Comparison of the two polymorphs of **10** shows that different crystal packing has limited effect on the molecular conformation: in α-**10** both rings *A* in a molecule are eclipsed with corresponding rings *B*, in β-**10** one pair is nearly eclipsed and the other shows a quasi-graphitic overlap, ring *A* shifting towards the pyridyl ring of the C^N ligand. Interestingly, molecule **12**, which lacks intramolecular stacking, is much less rigid – note the different conformations of two crystallographically non-equivalent molecules in the crystal (Figure S102).

Computational study

The optimised ground state S_0 geometries for the complexes were calculated at the B3LYP/LANL2DZ:3-21G* level with the LANL2DZ pseudopotential for the iridium atoms and the 3-21G* basis set for other atoms. This model chemistry was selected on the basis of previous computational studies,[50,53] and ensures that these calculations are directly comparable with those reported for other diiridium complexes (such as complex **1**).[21,22] For the complexes **13**–**15** the methylene cyclohexylether groups were substituted for methoxy groups to shorten calculation times. The geometries of the central hydrazide fragments are in good agreement with the XRD results discussed above.

Molecular orbital calculations provided insight into the localisation of the frontier molecular orbitals (FMOs). Reasonable agreement is observed between diastereomers for all complexes. The LUMOs are localised on the cyclometalating ligands, particularly the pyridyl moieties.[21,22] However, the localisation of the highest occupied molecular orbitals (HOMOs) varies more significantly between complexes: in some cases the HOMO contribution from the bridge centre is high (≥ 30%) (complexes **7**, **10**, **13** and **15**) whereas in other cases the bridging ligands display ancillary character (complexes **8**, **9**, **11**, **12** and **14**). In this study, if the average HOMO contribution from the bridge centre for both diastereomers is <15%, the bridge is considered ancillary. This is summarised in Table S2. FMO plots for complexes **7**, **9**, **12** and **13** are given in Figure 5 as representative examples. FMO plots for the other complexes are shown in Figures S126–S143.

This journal is © The Royal Society of Chemistry 20xx

Please do not adjust margins

Please do not adjust margins

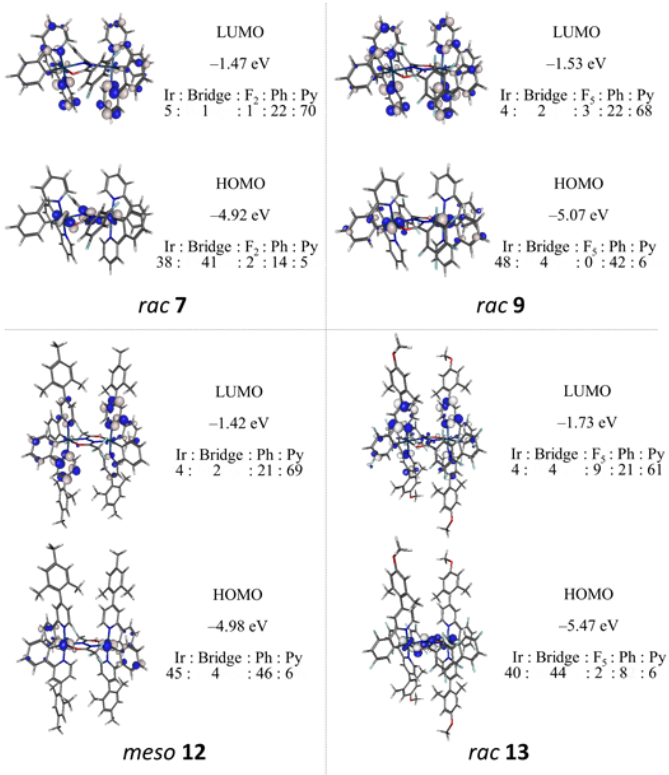

Figure 5. Molecular orbital compositions for complexes *rac* **7**, *rac* **9**, *meso* **12** and *rac* **13**. The stated ratios represent the atom/ group contributions in percentages.

For complex **7** the HOMO has significant contributions from the Ir centres, the central component of the hydrazide bridge and the cyclometalating phenyl moieties, as in complex **1**.[21,22] Further fluorination of the bridging aryl rings decreases the bridge HOMO contributions for complexes **8** (octafluoro) and **9** (decafluoro), so their HOMOs are primarily localised on the Ir centres and the cyclometalating phenyl groups, with their bridges expected to behave as ancillary ligands. As complex **10** also features methoxy groups on the bridging unit, the effect of the electron withdrawing fluorine atoms is somewhat negated and the bridge still features notable HOMO localisation (32% average). Calculations predict very similar HOMO contributions for complexes **9** and **11**, indicating that the mesityl groups have a negligible electronic effect, as expected.[47,48] Lowering the π orbital energy of the cyclometalating ligands of complexes **13** and **15** through fluorination strongly shifts their HOMOs onto the bridging ligands so that the cyclometalating phenyl moieties have very low HOMO contributions (average of both diastereomers < 15% for both complexes). There is negligible frontier orbital (HOMO or LUMO) contribution from the bridge aryl rings for all complexes featuring diarylhydrazide bridges, even upon perfluorination.

Table 1. Oxidation potentials for the Ir^{3+}/ Ir^{4+} couples (E^{ox}/ V) of compounds **7–15** referenced to FcH/ FcH^{+} = 0.00 V.

Complex	Isomer	$E^{ox(1)}$ /V E_{pa}/ E_{pc} [$E_{1/2}$]	$E^{ox(2)}$ /V E_{pa} /E_{pc} [$E_{1/2}$]	$\Delta E_{1/2}$ /V[a]	E^{red}_{onset} /V[b]	HOMO /eV[c]	LUMO /eV[d]
7	*mixture*	0.53/ 0.31 [0.42]	0.77/ 0.58 [0.67]	0.25	−2.38	–5.22	–2.42
8	*mixture*	0.56/ 0.49 [0.52]	0.81/ 0.74 [0.77]	0.25	−2.18	–5.32	–2.62
9	*mixture*	0.61/ 0.52 [0.56]	0.85/ 0.76 [0.81]	0.25	−2.37	–5.36	–2.43
10	*mixture*	0.54/ 0.46 [0.50]	0.80/ 0.72 [0.76]	0.26	−2.29	–5.30	–2.51
11	*rac*	0.66/ 0.49 [0.58]	0.96/ 0.84 [0.90]	0.32	−2.37	–5.38	–2.43
12	*meso*	0.67/ 0.57 [0.62]	0.85/ 0.72 [0.78]	0.16	−2.44	–5.42	–2.36
13	*meso*	0.96/ 0.90 [0.93]	1.36/ 1.21 [1.28]	0.35	−2.16	–5.73	–2.66
	rac	1.00/ 0.93 [0.97]	1.43/ 1.23 [1.33]	0.36	−2.14	–5.77	–2.64
14	*	0.99/ 0.91 [0.95]	1.18/ 1.07 [1.12]	0.17	−2.15	–5.75	–2.65
15	*	0.87/ 0.75 [0.81]	1.24/ 1.12 [1.18]	0.37	−2.19	–5.61	–2.61

[a] Peak splitting between $E^{ox(1)}$ and $E^{ox(2)}$. [b] All reductions are electrochemically irreversible. [c] HOMO levels calculated from CV potentials by HOMO = –4.8 + (–$E_{1/2}^{ox(1)}$), using ferrocene as the standard. [d] LUMO levels calculated from CV potentials by LUMO = –4.8 + (–E^{red}_{onset}), using ferrocene as the standard. * Complexes **14** and **15** were isolated as single diastereomers; their absolute configurations are unknown.

For complexes **12** and **14** the bridging ligands are ancillary with negligible HOMO contributions (average of both diastereomers = 4% for both complexes), regardless of cyclometalating ligand fluorination. This is indicative of the shorter conjugation length of the bis(trifluoromethyl) bridge **18** compared to the diarylhydrazide bridges studied here.

Electrochemistry

Complexes **7–15** (Figure 2) were studied by cyclic voltammetry (CV) to obtain their oxidation and reduction potentials. The data are listed in Table 1 and voltammograms are shown in Figures S104–S125. All complexes display two electrochemically reversible oxidation waves. These represent sequential oxidation of the iridium centres (Ir^{3+}/ Ir^{4+} redox couples), which are electronically coupled via the conjugated bridging units and so are electrochemically inequivalent. For

Please do not adjust margins

Please do not adjust margins

complexes **11** and **15** as representative examples, both oxidation processes were shown to be chemically reversible over 10 cycles (Figures S114 and S115).

Complex **7**, which features 4 fluorine atoms on the bridging unit, displays the lowest first oxidation potential ($E^{ox(1)}$). As expected, increasing to 8 (complex **8**) and 10 fluorine atoms (complex **9**) leads to successively higher oxidation potentials. Due to the addition of electron-rich methoxy groups to the octafluoro bridging unit, the oxidation potential of complex **10** is slightly decreased by 0.02 V compared to complex **9**. A relatively small variation in oxidation potentials (0.04 V) across the series **7**–**10** supports DFT predictions that the bridges in **8** and **9** behave as ancillary ligands. Complexes **7**–**10**, which vary only in the extent of bridge fluorination, all feature very similar peak splittings ($\Delta E_{1/2}$ ca. 0.25 V), indicating similar electronic coupling between the Ir centres for this series.

Functionalising the ppy ligands of complex **11** with mesityl groups does not significantly influence $E^{ox(1)}$ (an increase of only 0.02 V is observed compared to complex **9**), indicating that they have minimal electronic effect.[47,48] However, it is interesting that the second oxidation potential ($E^{ox(2)}$) of **11** is shifted to a significantly higher potential compared to complex **9** (0.90 V vs. 0.81 V) leading to a larger $\Delta E_{1/2}$ value of 0.32 V for **11** compared to 0.25 V for **9**. A tentative explanation is that the mesityl groups, could sterically interact over the bridging unit (Figure S101). This would lower the molecular flexibility and could hinder structural rearrangement to the dication, thereby increasing $E^{ox(2)}$ of **11** compared to the more flexible complex **9**.

The oxidation potential of **12** is higher than that of **11** by 0.04 V, suggesting that the bis(trifluoromethyl)-functionalised bridge (**18**) is more strongly electron withdrawing than the bis(pentafluorophenyl) bridge (**17c**).[46] The $\Delta E_{1/2}$ value obtained for **12** (0.16 V) is also half of that observed for **11**, implying weak communication between the two iridium centres. This is in line with the ancillary nature of the bridge and in agreement with DFT (Table S2). The addition of fluorinated cyclometalating ligands to complexes *meso* **13** and *rac* **13** further shifts their oxidation potentials to more positive values, as expected from DFT, which predicts high HOMO contributions from the cyclometalating phenyl rings of complex **11** (Table S2). The $\Delta E_{1/2}$ values for *meso* **13** and *rac* **13** are also greater than for complex **11** (by 0.03/ 0.04 V) which may be due to the reduced ancillary character of the bis(pentafluorophenyl) bridge in these complexes, also in line with DFT predictions.

Complex **14** has an oxidation potential almost identical to *meso* **13** and *rac* **13**, indicating very similar HOMO energies. Analogous to the relationship between complexes **11** and **12**, complex **14** displays a much lower $\Delta E_{1/2}$ value than either diastereomer of complex **13**, which suggests a higher ancillary character of the bis(trifluoromethyl) bridge (and so weaker Ir---Ir communication), as inferred by DFT.

The first oxidation potential of **15** is cathodically shifted compared to complexes **13** (by *ca.* 0.1 V). This is due to the absence of the xylyl spacer which electronically decouples the electron donating methylenecyclohexylether group from the ppy ligands. Complex **15** also has the largest $\Delta E_{1/2}$ value (0.37 V), in agreement with DFT which predicts the bridging unit to be the least ancillary of the series (Table S2).

The reduction potentials for **7**–**15** were also estimated by CV. The data for the reduction scans are included in Table 1 and the voltammograms are shown in Figure S116–125. All complexes display irreversible reductions. This adds significant error to their accurate determination, complicating the detailed analysis of any trends. A similar situation has been previously encountered in the study of monoiridium complexes by Baranoff and Nazeeruddin et al.[54] Nevertheless, the reduction onsets for the complexes **7**–**15** are in the range of −2.1 – –2.4 V vs. FcH/ FcH^+, which is a reasonable fit with their emission energies (discussed below) and are similar to those reported for ppy-based monoiridium complexes.[55] Generally, functionalisation of the cyclometallating ligands of **13**−**15** with electron-withdrawing fluorine atoms decreases their reduction potentials compared to those of complexes **7**−**12** as expected.[55] The reduction potential for **15** is marginally greater than for **13** and **14** (−2.19 V vs. −2.14/ −2.16 V and −2.15 V), which is expected from the DFT data upon direct functionalisation of the LUMO-bearing pyridyl moieties with electron-donating methylenecyclohexyl ether groups.

Photophysical data

The emission spectra for the complexes are shown in Figures 6–9 and Figures S155–S157 and the key photophysical data are given in Table 2. Absorption data are presented in Figure S154 and Table S3. Complex **7** is nonemissive in DCM solution at room temperature, while being highly emissive (PLQY = 61 ± 10%) when doped into a rigid poly(methyl methacrylate) (PMMA) matrix. This is consistent with the data for complex **1**[22], for which the flexible central bridging unit (that DFT predicts to have significant HOMO character) can provide a pathway for non-radiative quenching of the excited state in solution, which can be inhibited by doping the complex into a rigid host matrix.

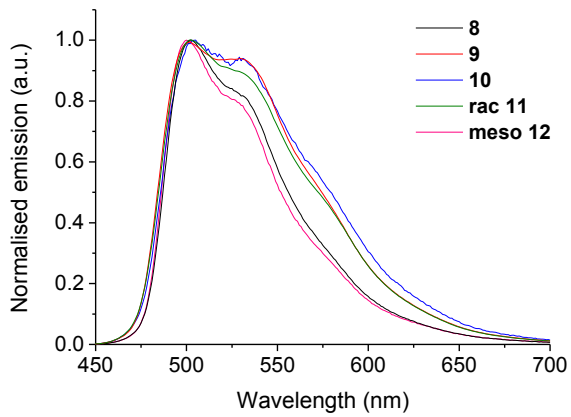

Figure 6. Normalised emission spectra of complexes **8**–**12** in degassed DCM solutions at room temperature (λ_{exc} 355 nm).

This journal is © The Royal Society of Chemistry 20xx

Please do not adjust margins

Please do not adjust margins

Complexes **8**–**10** have significantly different photophysical properties than **7**, in that they are highly emissive in solution and in PMMA, with very similar PLQY values in both media. This is consistent with rigidification of **8**–**10** by intramolecular π–π stacking, which restricts rotation of the bridge aryl rings. This is observed in the solution ^{19}F NMR spectra of **8**–**10** (Figures 3, S5, S9, S15 and S18) and removes the requirement to impede bridge flexibility by using a rigid matrix such as PMMA.

Another possible explanation is that for complexes with an ancillary bridging unit (Table S2) such as **8** and **9**, motion of the bridge does not provide as efficient a non-radiative pathway to the ground state in solution. However, as complex **10** features a non-ancillary bridge with notable HOMO character (Table S2) while still exhibiting a high solution PLQY (78 ± 5%), it is evident that intramolecular π–π stacking is the main reason for high solution PLQYs in highly fluorinated diarylhydrazide-bridged diiridium complexes.

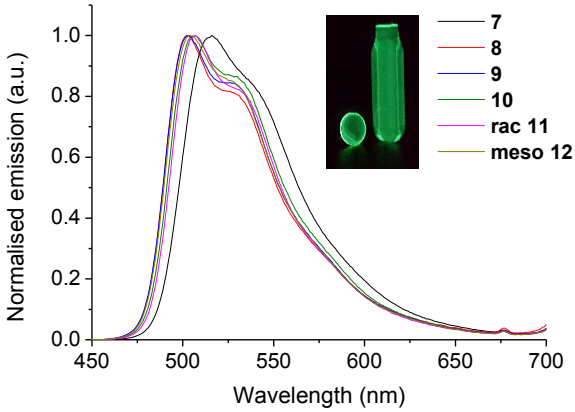

Figure 7. Normalised emission spectra of complexes **7**–**12** doped into PMMA at 1 wt. % at room temperature (λ_{exc} 355 nm). Inset: photograph of emission from a doped PMMA film (left) and degassed DCM solution (right) of *rac* **11** under irradiation from a 365 nm UV lamp.

The emission spectra of **8**–**10** are blue shifted compared to **7** (by *ca.* 10 nm in PMMA) (Figure 7). This is a result of HOMO stabilisation through further fluorination of the bridging units (in agreement with electrochemical data – Table 1). Complexes **8**–**10** exhibit near identical Commission Internationale de L'Éclairage (CIE_{xy}) colour coordinates in PMMA of (0.25, 0.62/0.63) in the green region of the spectrum. The triplet energies (E_T) for **8**–**10** (obtained from emission spectra recorded in 2-MeTHF at 77 K, Figure S156) are also nearly identical (2.56–2.57 eV). These data provide additional experimental support for the DFT prediction that the bridges in **8** and **9** behave as ancillary ligands.

The mesityl groups in *rac* **11** result in a significant increase in the radiative rate constant (k_r) compared to complex **9** in DCM solution (5.30 vs. 3.40 × 10^5 s^{-1}) and in PMMA (5.18 vs. 4.41 × 10^5 s^{-1}). This leads to a small increase in solution PLQY (88 ± 5% for *rac* **11** vs. 76 ± 5% for complex **9**), whereas the PLQYs in PMMA for **9** and *rac* **11** are very similar (71 ± 10% and 72 ± 10%, respectively). The incorporation of mesityl groups is known to increase PLQYs and k_r values in monoiridium systems.[47,48] As mesityl groups have a negligible electronic effect, the CIE_{xy} coordinates (in both DCM an PMMA) and E_T values for **9** and *rac* **11** are nearly identical.[47,48]

Complex *meso* **12** is moderately emissive in DCM solution (PLQY = 22 ± 5%) and is highly emissive in PMMA (PLQY = 66 ± 10%). This is due to an order of magnitude decrease in k_{nr} upon doping the complex into PMMA (Table 2), which can be attributed to higher molecular flexibility inferred from the XRD data (discussed above, Figure S102). Although *meso* **12** is not rigidified by intramolecular π–π interactions, it is still emissive in solution, albeit to a lesser extent than *rac* **11**. This may be related to the ancillary nature of the bridging ligand (predicted by DFT), which may reduce the efficiency of non-radiative quenching through bridge motion, as mentioned above.

Other than their solution PLQY values and the presence/ absence of intramolecular π–π interactions, complexes *rac* **11** and *meso* **12** display similar theoretical (Table S2), electrochemical (Table 1) and photophysical (Table 2) properties. A direct comparison therefore serves as good evidence that intramolecular π–π interactions contribute significantly to the high solution PLQYs of the diarylhydrazide-bridged complexes.

Incorporation of the fluorinated cyclometalating ligand **21** into the diastereomers *meso* **13** and *rac* **13** shifts their emission energies into the sky-blue region (Figures 8 and 9). In DCM both *meso* **13** and *rac* **13** have PLQYs of 47/ 48 ± 5% with CIE_{xy} coordinates (0.18, 0.36) marginally lower than the archetypal sky-blue emitter FIrpic (Figure 8)[38,56] (0.19, 0.37), even though their λ_{max} values are red shifted compared to FIrpic by 2 nm. This is related to their narrower full width at half maximum (FWHM) values because of diminished $v_{0,1}$ vibronic shoulders: FWHM FIrpic = 82 nm, *meso* **13** = 63 nm, *rac* **13** = 69 nm. This is again consistent with higher molecular rigidity, due to the intramolecular π–π interactions (observed in the ^{19}F NMR spectra of *meso* **13** and *rac* **13** – Figure S42 and S51).

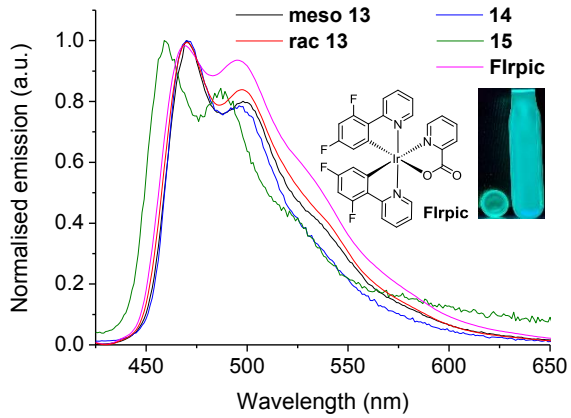

Figure 8. Normalised emission spectra of complexes **13**–**15** and FIrpic in degassed DCM solutions at room temperature (λ_{exc} 355 nm). The emission spectrum of **15** is poorly resolved due to a low solution PLQY. Inset: (left) chemical structure of FIrpic. (Right) photograph of emission from a doped PMMA film and degassed DCM solution of *rac* **13** under irradiation from a 365 nm UV lamp.

Please do not adjust margins

Please do not adjust margins

Molecular rigidity also influences the Huang-Rhys factor (S_M), which is proportional to the degree of structural distortion which occurs in the excited state of a molecule relative to the ground state.[57] S_M values were estimated for FIrpic, *meso* **13** and *rac* **13** from the relative heights of the $v_{0,0}$ and $v_{0,1}$ peaks in their 77 K emission spectra (Figure S157, FIrpic spectrum obtained from ref. [56]).[57,58] The following values were obtained: FIrpic = 0.7, *meso* **13** = 0.4, *rac* **13** = 0.5 (1 s.f.). These values indicate a lower intensity vibronic progression for the rigid diiridium complexes compared to FIrpic, which is vital for obtaining high colour purity.

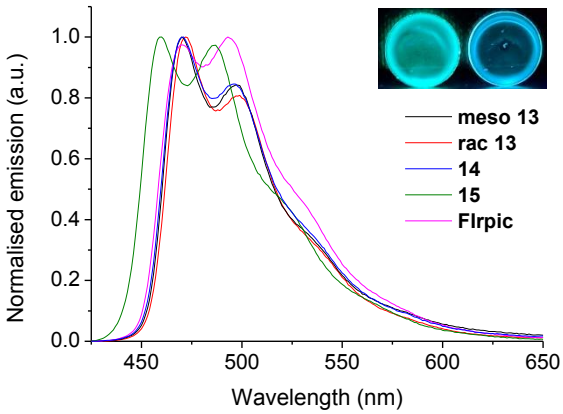

Figure 9. Normalised emission spectra of complexes **13–15** and FIrpic doped into PMMA at 1 wt. % at room temperature (λ_{exc} 355 nm). Inset: photograph of the emission from doped PMMA films of *rac* **13** (left) and **15** (right) under irradiation from a 365 nm UV lamp.

Similarly, favourable photophysical properties are also observed for *meso* **13** and *rac* **13** when doped into PMMA: high PLQYs of 60/ 65 ± 10% (FIrpic 74 ± 10%) and comparatively narrow FWHM values of 55/ 56 nm (FIrpic 67 nm) (Figure 9).

These comparatively narrow emission spectra are significant as the complexes are predicted to feature non-ancillary bridging ligands (see the DFT discussed above), which will likely lead to excited states with noteworthy interligand charge transfer (ILCT) character. ILCT character leads to broader, less structured emission due to more diffusely localised excited states.[58–60] It is expected that the rigidifying effect of the intramolecular π–π interactions counteracts this, promoting sharper emission bands. These data indicate that diiridium complexes show promise as a platform for developing blue phosphors with good colour purity.

This journal is © The Royal Society of Chemistry 20xx

Please do not adjust margins

Please do not adjust margins

Dalton Transactions

ARTICLE

Table 2. Summary of the key photoluminescence data for complexes **7–15** and FIrpic

Complex	Isomer	DCM solution[a]					2-MeTHF glass[b]		Doped into PMMA 1% wt.[c]				
		$\lambda_{max\,em}$ /nm [CIE_{xy}]	PLQY /% (± 5%)	τ_p /μs	k_r/× 10^5 s^{-1}	k_{nr}/× 10^5 s^{-1}	$\lambda_{max\,em}$ /nm ($\lambda_{10\%\,em}$ /nm)[d] [E_T /eV][e]	τ_p /μs	$\lambda_{max\,em}$ /nm [CIE_{xy}]	PLQY /% (± 10%)	τ_p /μs	k_r/× 10^5 s^{-1}	k_{nr}/× 10^5 s^{-1}
7	*mixture*	Non-emissive[f]					500 (490) [2.53]	3.62	516 [0.28, 0.64]	61	1.81	3.37	2.15
8	*mixture*	503 [0.27, 0.61]	66	1.84	3.61	1.83	492 (484) [2.56]	3.41	503 [0.25, 0.62]	59	2.00	2.95	2.05
9	*mixture*	499 [0.30, 0.58]	76	2.24	3.40	1.07	492 (482) [2.57]	3.55	503 [0.25, 0.62]	71	2.08	3.41	1.39
10	*mixture*	505 [0.31, 0.58]	78	2.09	3.73	1.05	493 (485) [2.56]	3.33	507 [0.25, 0.63]	66	2.02	3.27	1.68
11	*rac*	502 [0.30, 0.58]	88	1.66	5.30	0.72	494 (485) [2.56]	2.67	507 [0.25, 0.63]	72	1.39	5.18	2.01
12	*meso*	500 [0.26, 0.60]	22	0.34	6.41	22.7	491 (483) [2.57]	2.30	504 [0.25, 0.63]	66	1.14	5.79	2.98
13	*meso*	470 [0.18, 0.36]	48	0.69	6.93	7.48	461 (455) [2.72]	2.24	470 [0.16, 0.33]	65	1.19	5.46	2.94
	rac	470 [0.18, 0.36]	47	0.73	6.49	7.23	463 (456) [2.72]	1.78	472 [0.15, 0.33]	60	1.18	5.51	3.39
14	*	470 [0.16, 0.33]	4[g]	0.07	5.77	135	462 (454) [2.73]	1.92	471 [0.15, 0.33]	46	1.12	4.11	4.82
15	*	459 [0.20, 0.28]	2[h]	0.11	1.64	89.3	451 (441) [2.81]	2.24	460 [0.15, 0.24]	69	1.62	4.26	1.91
FIrpic[i]	-	468 [0.19, 0.37]	73	1.85	3.95	1.46	463 [2.62][j]	2.24[j]	470sh, 493 [0.15, 0.33]	74	1.69	4.38	1.54

*Single diastereomer of unknown absolute configuration. sh = Shoulder. [a]Solution photoluminescence measurements were recorded in degassed DCM solutions at *ca.* 20 °C with an excitation wavelength of 355 nm with quinine sulfate in 0.5 M H_2SO_4 as standard (Φ = 0.546).[61] [b]Measured at 77 K using an excitation wavelength of 355 nm. [c]Measured in an integrating sphere under air using an excitation wavelength of 355 nm. [d]Wavelength at 10% intensity on the blue edge of the spectrum obtained at 77 K. [e]Estimated using $E_T = hc/\lambda_{10\%\,em}$. [f]Non-emissive is defined as PLQY <0.05%. [g]Error = ± 4%. [h]Error = ± 2%. [i]All FIrpic data were obtained in-house for direct comparison unless otherwise stated. [j]Values taken from ref [62]. $\tau_p = 1/k_{nr} + k_r$.

Please do not adjust margins

Please do not adjust margins

Meso **13** and *rac* **13** feature higher k_r values than FIrpic (by ~20–40%) under directly comparable conditions in both DCM solution and PMMA. This may be related to the strong Ir---Ir coupling observed in the electrochemistry (Table 1), and results in notably shorter τ_p values in PMMA of 1.18/ 1.19 µs (vs. 1.69 µs for FIrpic).

Enhanced radiative rate constants compared to monoiridium analogues have been reported for green to red diiridium complexes, which may be due to augmented spin-orbit coupling.[23,24,26,50,63] Blue phosphors tend to possess excited states with more LC character than green emitting complexes,[64–66] which is an indication of poorer LC/ MLCT state mixing (lower MLCT character) and can lead to inherently lower k_r values and so longer τ_p. The observations presented here indicate that diiridium complexes are promising systems for developing blue phosphors with higher k_r values and therefore shorter τ_p which is a highly sought-after property.[67]

In a similar manner to the relationship between *rac* **11** and *meso* **12**, complex **14** is an analogue of **13** which cannot exhibit intramolecular π–π interactions between the cyclometalating and bridging ligands. As a result, **14** displays a low solution PLQY of 4 ± 4%. In PMMA the PLQY of **14** increases to 46 ± 10%, which is ascribed to a restriction of intramolecular motion, evident from the substantial decrease in k_{nr} (Table 2). The PLQY of **14** in PMMA is, however, significantly lower than those for either diastereomer of **13** (60/ 65 ± 10%). This is due to: 1) a substantially higher k_{nr} value, which crucially indicates that intramolecular π–π interactions are also beneficial for obtaining high solid state PLQY values in diiridium complexes, and 2) a lower k_r value (Table 2), which may be related to the smaller Ir---Ir coupling in **14** observed in the electrochemistry (Table 1).

Despite the lack of rigidifying intramolecular π–π interactions, **14** exhibits sharp emission similar to **13** (FWHM in PMMA = 57 nm) (Figure 9). This is consistent with the ancillary nature of the bis(trifluoromethyl) bridge **18**, which is expected to limit the ILCT character of the excited state. The estimated S_M value for **14** is 0.6 (1 s.f.): larger than for either diastereomer of **13**, but still smaller than for FIrpic. These data indicate that designing diiridium complexes with highly ancillary bridges could be a way to obtain sharp emission from such systems.

The emission from complex **15** is shifted deeper into the blue than for **13** or **14**. This is attributed to the LUMO-destabilising methylenecyclohexylether groups. As well as being tentatively observed in the reduction potentials above (Table 1), this can also be concluded from the more reliable oxidation potential data which indicate that the HOMO of **15** is shallower than for **13** or **14**. When doped into PMMA, **15** displays a high PLQY of 69 ± 10%. This is comparable to the value obtained for FIrpic under the same experimental conditions, while the colour is notably superior: **15** emits at a λ_{max} of 460 nm, pushing the CIE_{xy} coordinates to a total value below 0.4 (0.15, 0.24). Complex **15** also displays a τ_p of 1.62 µs in PMMA, which is short in a doped film for an Ir complex with total CIE_{xy} < 0.4/ $\lambda_{max} \leq 460$ nm and a high PLQY.[47,68–71] This can be attributed to the high k_r, which is likely related to the dinuclear nature of the complex as mentioned above.

Despite the presence of rigidifying intramolecular π–π interactions (observed in the ^{19}F NMR spectrum – Figure S68), the PLQY for **15** in DCM solution is low (2 ± 2%). This fits a trend of decreasing solution PLQY with increasing emission energy in the complexes *rac* **11** (λ_{max} = 502 nm, PLQY = 88 ± 5%), **13** (λ_{max} = 470 nm, PLQY = 47/ 48 ± 5%) and **15** (λ_{max} = 459 nm, PLQY = 2 ± 2%) due to incremental order of magnitude increases in their k_{nr} values (0.72, 7.23/ 7.48 and 89.3 × 10^5 s^{-1}). In contrast, all three complexes exhibit high PLQYs (> 60%) and similar k_{nr} values (1.91–3.39 × 10^5 s^{-1}) when doped into PMMA. Therefore, it appears that as the excited state energy increases, the rigidifying effect of the intramolecular π–π interactions is overcome and their capability to promote emission in solution is reduced.

Emission in the sky-blue region from diiridium complexes with conjugated bridging ligands is unprecedented. It has been accomplished by the synergistic choice of bridging and cyclometalating ligands. The key role of the bridge is clear as there are reports of diiridium complexes bearing dfppy-type peripheral ligands for which sky-blue emission was not achieved.[8,16,72–74] Although diiridium systems have shown promise as high performing phosphors in the lower energy range (from red through to green),[21–24,26,27,50,75] to the best of our knowledge no complex displaying λ_{max} (PL) below *ca.* 490 nm at room temperature has been reported thus far.[22] Mazzanti and co-workers reported a fluorinated diiridium complex with a vibronic sideband at 477 nm, but the λ_{max} is *ca.* 510 nm and the emission extends to 800 nm.[16] The results presented here considerably extend the diiridium complex literature, and indicate that if the complexes are correctly designed, their colour versatility is potentially comparable to monoiridium systems.

Conclusions

We have developed new concepts in the chemistry of diiridium complexes with the synthesis, structural and optoelectronic characterisation of a series of highly fluorinated hydrazide-bridged complexes.

Complexes **7**–**12** represent an ideal platform for investigating intramolecular π–π interactions between aryl and

Please do not adjust margins

Please do not adjust margins

perfluoroaryl rings in organometallic systems, both in the solid state (by XRD) and in solution (by ^{19}F NMR spectroscopy). These interactions are shown to be an innovative way to rigidify diiridium complexes, leading to significant and advantageous effects on their photophysical properties. Electrochemical and computational studies have further extended the understanding of these systems. This knowledge has been applied to the rational design and synthesis of the first reported sky-blue emitting diiridium complexes **13**–**15**. Their favourable photophysical properties are a consequence of both the dinuclear nature of the complexes and the beneficial intramolecular π–π interactions. They possess high PLQYs, λ_{max} as low as 460 nm ($CIE_{x+y} < 0.4$), high k_r, relatively short τ_p, and in some cases, notably sharp emission. The results presented here greatly extend the versatility of luminescent diiridium complexes by shifting phosphorescence into the sky-blue region of the visible spectrum with the aid of tailored non-covalent interactions. It is now a challenge to design and implement further structural modifications that could shift the emission of diiridium complexes deeper in the blue region.

Acknowledgements

Dr Alan Kenwright and Dr Juan Aguilar-Malavia are acknowledged for their help in devising, running and interpreting 2D NMR experiments. Prof. Graham Sandford is acknowledged for helpful ^{19}F NMR discussion. We thank EPSRC grant EP/L02621X/1 for funding.

Notes and references

1 Z. Q. Chen, Z. Q. Bian and C. H. Huang, *Adv. Mater.*, 2010, **22**, 1534–1539.
2 M. S. Lowry and S. Bernhard, *Chem. Eur. J.*, 2006, **12**, 7970–7977.
3 K. K.-W. Lo, K. H.-K. Tsang, K.-S. Sze, C.-K. Chung, T. K.-M. Lee, K. Y. Zhang, W.-K. Hui, C.-K. Li, J. S.-Y. Lau, D. C.-M. Ng and N. Zhu, *Coord. Chem. Rev.*, 2007, **251**, 2292–2310.
4 R. Gao, D. G. Ho, B. Hernandez, M. Selke, D. Murphy, P. I. Djurovich and M. E. Thompson, *J. Am. Chem. Soc.*, 2002, **124**, 14828–14829.
5 X. Yang, G. Zhou and W.-Y. Wong, *Chem. Soc. Rev.*, 2015, **44**, 8484–8575.
6 C. Ulbricht, B. Beyer, C. Friebe, A. Winter and U. S. Schubert, *Adv. Mater.*, 2009, **21**, 4418–4441.
7 Y. Chi and P.-T. Chou, *Chem. Soc. Rev.*, 2010, **39**, 638–655.
8 X. Yuan, S. Zhang and Y. Ding, *Inorg. Chem. Commun.*, 2012, **17**, 26–29.
9 L. Donato, C. E. McCusker, F. N. Castellano and E. Zysman-Colman, *Inorg. Chem.*, 2013, **52**, 8495–504.
10 A. Tsuboyama, T. Takiguchi, S. Okada, M. Osawa, M. Hoshino and K. Ueno, *Dalton Trans.*, 2004, 1115–1116.
11 E. A. Plummer, W. Hofstraat and L. De Cola, *Dalton Trans.*, 2003, 2080–2084.
12 A. Auffrant, A. Barbieri, F. Barigelletti, J. Lacour, P. Mobian, J.-P. Collin, J.-P. Sauvage and B. Ventura, *Inorg. Chem.*, 2007, **46**, 6911–6919.
13 V. L. Whittle and J. A. G. Williams, *Inorg. Chem.*, 2008, **47**, 6596–6607.
14 W.-J. Xu, S.-J. Liu, X. Zhao, N. Zhao, Z.-Q. Liu, H. Xu, H. Liang, Q. Zhao, X.-Q. Yu and W. Huang, *Chem. Eur. J.*, 2013, **19**, 621–629.
15 V. Chandrasekhar, B. Mahanti, P. Bandipalli and K. Bhanuprakash, *Inorg. Chem.*, 2012, **51**, 10536–10547.
16 E. S. Andreiadis, D. Imbert, J. Pécaut, A. Calborean, I. Ciofini, C. Adamo, R. Demadrille and M. Mazzanti, *Inorg. Chem.*, 2011, **50**, 8197–8206.
17 A. G. Tennyson, E. L. Rosen, M. S. Collins, V. M. Lynch and C. W. Bielawski, *Inorg. Chem.*, 2009, **48**, 6924–6933.
18 T. Hajra, A. J. K. Bera and V. Chandrasekhar, *Aust. J. Chem.*, 2011, **64**, 561–566.
19 A. M. Prokhorov, A. Santoro, J. A. G. Williams and D. W. Bruce, *Angew. Chemie Int. Ed.*, 2012, **51**, 95–98.
20 M. Graf, R. Czerwieniec and K. Sünkel, *Z. Anorg. Allg. Chem.*, 2013, **639**, 1090–1094.
21 Y. Zheng, A. S. Batsanov, M. A. Fox, H. A. Al-Attar, K. Abdullah, V. Jankus, M. R. Bryce and A. P. Monkman, *Angew. Chem. Int. Ed.*, 2014, **53**, 11616–11619.
22 D. G. Congrave, Y.-t. Hsu, A. S. Batsanov, A. Beeby and M. R. Bryce, *Organometallics*, 2017, **36**, 981–993.
23 G. Li, Y. Wu, G. Shan, W. Che, D. Zhu, B. Song, L. Yan, Z. Su and M. R. Bryce, *Chem. Commun.*, 2014, **50**, 6977–6980.
24 P.-H. Lanoë, C. M. Tong, R. W. Harrington, M. R. Probert, W. Clegg, J. A. G. Williams and V. N. Kozhevnikov, *Chem. Commun.*, 2014, **50**, 6831–6834.
25 V. Chandrasekhar, T. Hajra, J. K. Bera, S. M. W. Rahaman, N. Satumtira, O. Elbjeirami and M. A. Omary, *Inorg. Chem.*, 2012, **51**, 1319–1329.
26 R. E. Daniels, S. Culham, M. Hunter, M. C. Durrant, M. R. Probert, W. Clegg, J. A. G. Williams and V. N. Kozhevnikov, *Dalton Trans.*, 2016, **45**, 6949–6962.
27 X. Yang, Z. Feng, J. Zhao, J.-S. Dang, B. Liu, K. Zhang and G. Zhou, *ACS Appl. Mater. Interfaces*, 2016, **8**, 33874–33887.
28 Z. Hao, H. Jiang, Y. Liu, Y. Zhang, J. Yu, Y. Wang, H. Tan, S. Su and W. Zhu, *Tetrahedron*, 2016, **72**, 8542–8549. Although emission of a similar colour to FIrpic is reported, the two Ir centres are non-conjugated.
29 A. M. Bünzli, E. C. Constable, C. E. Housecroft, A. Prescimone, J. A. Zampese, G. Longo, L. Gil-Escrig, A. Pertegás, E. Ortí and H. J. Bolink, *Chem. Sci.*, 2015, **6**, 2843–2852.
30 E. C. Constable, C. E. Housecroft, P. Kopecky, C. J. Martin, I. A. Wright, J. A. Zampese, H. J. Bolink and A. Pertegas, *Dalton Trans.*, 2013, **42**, 8086–8103.
31 L. He, D. Ma, L. Duan, Y. Wei, J. Qiao, D. Zhang, G. Dong, L. Wang and Y. Qiu, *Inorg. Chem.*, 2012, **51**, 4502–4510.
32 S. Kumar, Y. Hisamatsu, Y. Tamaki, O. Ishitani and S. Aoki, *Inorg. Chem.*, 2016, **55**, 3829–3843.
33 P. Li, G. G. Shan, H. T. Cao, D. X. Zhu, Z. M. Su, R. Jitchati and M. R. Bryce, *Eur. J. Inorg. Chem.*, 2014, 2376–2382.
34 C. R. Patrick and G. S. Prosser, *Nature*, 1960, 187, 1021.
35 V. J. H. Williams, J. K. Cockcroft and N. Fitch, *Angew. Chem.*, 1992, **104**, 1666–1669.
36 J. H. Williams, *Acc. Chem. Res.*, 1993, **26**, 593–598.

Please do not adjust margins

Please do not adjust margins

37 A. B. Tamayo, B. D. Alleyne, P. I. Djurovich, S. Lamansky, I. Tsyba, N. N. Ho, R. Bau and M. E. Thompson, *J. Am. Chem. Soc.*, 2003, **125**, 7377–7387.

38 A. F. Rausch, M. E. Thompson and H. Yersin, *J. Phys. Chem. A*, 2009, **113**, 5927–5932.

39 S. Berger, S. Braun and H.-O. Kalinowski, *NMR Spectroscopy of the Non-Metallic Elements*, Wiley, 1st edition, 1997.

40 R. E. Banks and R. N. Haszeldine, *J. Chem. Soc*, 1967, 1822–1826.

41 E. Klauke, L. Oehlmann and B. Baasner, *J. Fluor. Chem.*, 1982, **21**, 495–513.

42 J. Zhou, M. W. Kuntze-Fechner, R. Bertermann, U. S. D. Paul, J. H. J. Berthel, A. Friedrich, Z. Du, T. B. Marder and U. Radius, *J. Am. Chem. Soc.*, 2016, **138**, 5250–5253.

43 R. J. Abraham, D. B. Macdonald and E. S. Pepper, *J. Am. Chem. Soc.*, 1968, **90**, 147–153.

44 J. Wang, J. Luis, C. Pozo, A. E. Sorochinsky, S. Fustero, V. A. Soloshonok and H. Liu, *Chem. Rev.*, 2014, **114**, 2432–2506.

45 R. Jana, B. Sarkar, D. Bubrin, J. Fiedler and W. Kaim, *Inorg. Chem. Commun.*, 2010, **13**, 1160–1162.

46 C. Hansch, A. Leo and R. W. Taft, *Chem. Rev.*, 1991, **91**, 165–195. The σ_{meta}, σ_{para} and inductive/ field factor (F) values for C_6F_5 and CF_3 are 0.26, 0.27, 0.27 and 0.43, 0.54, 0.38, respectively. Therefore, CF_3 is expected to be the stronger electron-withdrawing group.

47 A. F. Henwood, A. K. Bansal, D. B. Cordes, A. M. Z. Slawin, I. D. W. Samuel and E. Zysman-Colman, *J. Mater. Chem. C*, 2016, **4**, 3726–3737.

48 V. N. Kozhevnikov, Y. Zheng, M. Clough, H. A. Al-Attar, G. C. Griffiths, K. Abdullah, S. Raisys, V. Jankus, M. R. Bryce and A. P. Monkman, *Chem. Mater.*, 2013, **25**, 2352–2358.

49 D. R. Martir, C. Momblona, A. Pertegás, D. B. Cordes, A. M. Z. Slawin, H. J. Bolink and E. Zysman-Colman, *ACS Appl. Mater. Interfaces*, 2016, **8**, 33907–33915.

50 A. M'hamedi, M. A. Fox, A. S. Batsanov, H. A. Al-Attar, A. P. Monkman and M. R. Bryce, *J. Mater. Chem. C*, 2017, **5**, 6777–6789.

51 Calculations predict the structure of *meso* **11** (Figure S124) to be much less folded than *rac* **11** (Figure S125) and 'rod-like'. This increased aspect ratio may facilitate solid state packing more strongly than for complex **9**. DFT gas phase optimised structures in both this study and for previous analogues have been in good agreement with XRD data.[21,22]

52 S.-Y. Yao, Y.-L. Ou and B.-H. Ye, *Inorg. Chem.*, 2016, **55**, 6018–6026.

53 A. M'hamedi, A. S. Batsanov, M. A. Fox, M. R. Bryce, K. Abdullah, H. A. Al-Attar and A. P. Monkman, *J. Mater. Chem.*, 2012, **22**, 13529–13540.

54 E. Baranoff, S. Fantacci, F. De Angelis, X. Zhang, R. Scopelliti, M. Grätzel and M. K. Nazeeruddin, *Inorg. Chem.*, 2011, **50**, 451–462.

55 J. Frey, B. F. E. Curchod, R. Scopelliti, I. Tavernelli, U. Rothlisberger, M. K. Nazeeruddin and E. Baranoff, *Dalton Trans.*, 2014, **43**, 5667–5679.

56 E. Baranoff and B. F. E. Curchod, *Dalton Trans.*, 2015, **44**, 8318–8329.

57 J. Li, P. I. Djurovich, B. D. Alleyne, M. Yousufuddin, N. N. Ho, J. C. Thomas, J. C. Peters, R. Bau and M. E. Thompson, *Inorg. Chem.*, 2005, **44**, 1713–1727.

58 G. Li, T. Fleetham, E. Turner, X. C. Hang and J. Li, *Adv. Opt. Mater.*, 2015, **3**, 390–397.

59 K. Dedeian, J. Shi, N. Shepherd, E. Forsythe and D. C. Morton, *Inorg. Chem.*, 2005, **44**, 4445–4447.

60 T. Fleetham, G. Li, Z. Q. Zhu and J. Li, *SID Symp. Dig. Tech. Pap.*, 2015, **46**, 411–414.

61 H. Benjamin, Y. Zheng, A. S. Batsanov, M. A. Fox, H. A. Al-Attar, A. P. Monkman and M. R. Bryce, *Inorg. Chem.*, 2016, **55**, 8612–8627.

62 E. Baranoff, B. F. E. Curchod, F. Monti, F. Steimer, G. Accorsi, I. Tavernelli, U. Rothlisberger, R. Scopelliti, M. Grätzel and M. K. Nazeeruddin, *Inorg. Chem.*, 2012, **51**, 799–811.

63 The k_r values reported here, although comparatively high for sky blue phosphors, are not as high as those of lower energy diiridium emitters.[24,26] This is not surprising due to the lower MLCT/ higher LC character excited states commonly exhibited by blue complexes, evident from their more highly structured emission spectra.[65,66]

64 M. A. Baldo, S. R. Forrest and M. E. Thompson, in *Organic Electroluminescence*, ed. Z. H. Kafafi, CRC and SPIE Press, 2005.

65 L. Yang, F. Okuda, K. Kobayashi, K. Nozaki, Y. Tanabe, Y. Ishii and M.-A. Haga, *Inorg. Chem.*, 2008, **47**, 7154–7165.

66 G. Li, A. Wolfe, J. Brooks, Z. Zhu and J. Li, *Inorg. Chem.*, 2017, **56**, 8244–8256.

67 S. Haneder, E. Da Como, J. Feldmann, J. M. Lupton, C. Lennartz, P. Erk, E. Fuchs, O. Molt, I. Münster, C. Schildknecht and G. Wagenblast, *Adv. Mater.*, 2008, **20**, 3325–3330.

68 C.-H. Yang, M. Mauro, F. Polo, S. Watanabe, I. Muenster, R. Frohlich and L. De Cola, *Chem. Mater.*, 2012, **24**, 3684–3695.

69 T. Duan, T.-K. Chang, Y. Chi, J.-Y. Wang, Z.-N. Chen, W.-Y. Hung, C.-H. Chen and G.-H. Lee, *Dalton Trans.*, 2015, **44**, 14613–14624.

70 H. J. Park, J. N. Kim, H. Yoo, K. Wee, S. O. Kang and D. W. Cho, *J. Org. Chem.*, 2013, **78**, 8054–8064.

71 T. B. Fleetham, L. Huang, K. Klimes, J. Brooks and J. Li, *Chem. Mater.*, 2016, **28**, 3276–3282.

72 G. Nasr, A. Guerlin, F. Dumur, L. Beouch, E. Dumas, G. Clavier, F. Miomandre, F. Goubard, D. Gigmes, D. Bertin, G. Wantz and C. R. Mayer, *Chem. Commun.*, 2011, **47**, 10698–10700.

73 F. Lafolet, S. Welter, Z. Popović and L. De Cola, *J. Mater. Chem.*, 2005, **15**, 2820–2828.

74 R. D. Costa, G. Fernandez, L. Sanchez, N. Martín, E. Ortí and H. J. Bolink, *Chem. Eur. J.*, 2010, **16**, 9855–9863.

75 X. Yang, X. Xu, J. Dang, G. Zhou, C.-L. Ho and W.-Y. Wong, *Inorg. Chem.*, 2016, **55**, 1720–1727.

This journal is © The Royal Society of Chemistry 20xx

Please do not adjust margins

Supporting Information

Sky-blue emitting bridged diiridium complexes: beneficial effects of intramolecular π–π stacking

Daniel G. Congrave, Yu–Ting Hsu, Andrei S. Batsanov, Andrew Beeby, and Martin R. Bryce*

Department of Chemistry, Durham University, Durham DH1 3LE, U.K.

Email: m.r.bryce@durham.ac.uk

Contents **Page**

Experimental Section	S2
Copies of NMR Spectra	S23
X–ray Crystallography	S119
Electrochemistry	S125
Computations	S132
Thermal analysis	S151
Photophysics	S161
References	S163

Experimental Section

General

^{1}H, ^{13}C and ^{19}F NMR spectra were recorded on Bruker Avance 400 MHz, Varian Mercury 200, and 400 MHz, Varian Inova 500 MHz or Varian VNMRS 600 and 700 MHz spectrometers. All spectra were either referenced against the residual solvent signal or tetramethylsilane (TMS) and peak shifts are reported in ppm. Where assigned, cyclohexyl protons are labelled 'e' or 'a' to denote equatorial or axial positions, respectively. The labels 'ap. t' and 'bs' denote an apparent triplet and a broad singlet, respectively. For ^{13}C NMR assignment the labels * and # denote 2 and 3 overlapping signals, respectively. Electrospray ionisation (ESI) mass spectra were recorded on a Waters Ltd. TQD spectrometer. Atmospheric solids analysis probe (ASAP) mass spectra were recorded on a LCT premier XE spectrometer. Matrix-assisted laser desorption time-of-flight (MALDI–TOF) mass spectra were recorded on a Bruker Daltonik Autoflex II spectrometer running in positive ion reflectron mode. MALDI–TOF samples were prepared in CH_2Cl_2 (DCM) with *trans*-2-[3-(4-*tert*-butylphenyl)-2-methyl-2-propenylidene]malononitrile (DCTB) as the matrix. Elemental analyses were obtained on an Exeter Analytical Inc. CE-440 elemental analyser. Thermal analysis was run under a helium atmosphere at a rate of 10 °C min^{-1} using a Perkin-Elmer Pyris 1 instrument. Reactions requiring an inert atmosphere were carried out under argon which was first passed through a phosphorus pentoxide column. Thin layer chromatography (TLC) was carried out on silica gel (Merck, silica gel 60, F254) or alumina (Merck, neutral alumina 60 type E, F254) plates and visualized using UV light (254, 315, 365 nm). Flash chromatography was carried out using either glass columns or a Biotage® Isolera OneTM automated flash chromatography machine on 60 micron silica gel purchased from Fluorochem Ltd.

Chemicals

All commercial chemicals were of ≥95% purity and were used as received without further purification. $[Ir(ppy)_2\mu–Cl]_2$[1] and 4-(2,4,6-trimethylphenyl)-2-chloropyridine[2] were synthesised according to literature procedures. All solvents used were of analytical reagent grade or higher. Anhydrous solvents were dried through a HPLC column on an Innovative Technology Inc. solvent purification system or purchased from Acros (dry diglyme).

Calculations

All calculations were carried out with the Gaussian 09 package.[3] All optimized S_0 geometries of the diiridium complexes were carried out using B3LYP[4,5] with the pseudopotential (LANL2DZ)[6–8] for iridium and 3–21G* basis set for all other atoms.[9,10]All S_0 geometries were true minima based on no imaginary frequencies found. Electronic structure calculations were also carried out on the optimised geometries at B3LYP/LANL2DZ:3–21G*. The MO diagrams and orbital contributions were generated with the aid of Gabedit[11] and GaussSum[12] packages, respectively.

X-ray Crystallography

X-ray diffraction experiments were carried out at 120 K on a Bruker 3-circle diffractometer D8 Venture with a PHOTON 100 CMOS area detector, using Mo-*K*α radiation from a IμS microsource with focussing mirrors and a Cryostream (Oxford Cryosystems) open-flow N_2 gas cryostat. The absorption correction was carried out by numerical integration based on crystal face indexing, using SADABS program.[13] The structures were solved by Patterson (**7**, **11**, **12**) or direct methods using SHELXS 2013/1 software[14] and refined in anisotropic approximation by full matrix least squares against F^2 off all data, using OLEX2[15] and SHELXL 2016/6 software.[16]

Electrochemistry

Cyclic voltammetry experiments were recorded using either BAS CV50W electrochemical analyzer or a a PalmSens EmStat^2 potentiostat with PSTrace software. A three-electrode system consisting of a Pt disk (Ø = 1.8 mm) as the working electrode, a Pt wire as an auxiliary electrode and an Pt wire as a quasireference electrode was used. Cyclic voltammetry experiments were conducted at a scan rate of 100 mV/s. Experiments were conducted in dry, degassed DCM with *n*-Bu_4NPF_6 (0.1 M) as the supporting electrolyte and were referenced internally to ferrocene. Oxidation processes are assigned as being electrochemically reversible based on the equal magnitudes of corresponding oxidation and reduction peaks.

Photophysics

General The absorption spectra were measured on either a Unicam UV2-100 spectrometer operated with the Unicam Vision software or a Thermo Scientific Evolution 220 spectrometer with the Thermo Scientific Insight software in quartz cuvettes with a path length of 20 mm. The pure solvent was used for the baseline correction. The extinction coefficients were calculated using the Beer-Lambert Law, $A = \varepsilon cl$. The photoluminescence spectra were recorded on a Horiba Jobin Yvon SPEX Fluorolog 3-22 spectrofluorometer in quartz cuvettes with a path length of 10 mm. All Ir complexes were measured in degassed DCM (repeated freeze-pump-thaw cycles using a turbomolecular pump). The quantum yields of all samples were determined by the comparative method relative to. quinine sulphate in 0.5 M H_2SO_4 (Φ = 0.546[17]) following the literature procedure.[18] The quantum yields of complexes doped into poly(methyl methacrylate) (PMMA) thin films were recorded on a Horiba Jobin Yvon SPEX Fluorolog 3 using a calibrated Quanta-Φ integrating sphere and were calculated according to the literature method.[19] Solid state PLQY data were obtained in triplicate from three samples that were prepared in parallel: the calculated standard error values were ≤10%. Lifetime measurements were recorded using an N_2 laser (337 nm, 10 μJ, 10 Hz) as an excitation source in a custom spectrometer which produced a 1 kHz train of pulses of 20 ns duration. The luminescence was collected at 90° and focused onto the entrance slit of a monochromator (Bethan TM 300V). The emission was detected by a photon counting PMT and the arrival times of photons at the detector determined using a multichannel scaler. The data were transferred to a PC and analysed using non-linear regression. The decay data were fitted to exponential functions. Low temperature emission spectra and lifetime data were measured in a DN1704 optical cryostat (Oxford Instruments) with a ITC601 temperature controller (Oxford Instruments).

PMMA film preparation An adaptation of our previously reported method was used.[20] This adaptation was possible due to the improved solubility of the complexes studied here in chlorobenzene (CB) and is experimentally simpler. 100 μL of a 1 mg mL^{-1} solution of the diiridium complex in DCM was added to 1 mL of a 10 mg mL^{-1} solution of PMMA in CB and the resulting solution was stirred open to air at room temperature (*ca.* 2 h). The solution was then drop-cast using a Gilson precision pipette onto a 10 × 1 mm circular quartz disk (UQG Optics Ltd., UK) in a single. 150 μL portion. The substrate was heated to *ca.* 40 ºC overnight on a hot plate under air. Photophysical analysis was then immediately carried out. The PLQY values obtained using films prepared in this manner were the same (within experimental error) as those obtained using our previously reported method.

Synthesis

The synthesis of **21** (Scheme S1) started with etherification of the xylenol **23** with bromomethylcyclohexane to obtain the aryl ether **24** in 98% yield. Subsequent trapping of the lithiated derivative of **24** with $SnBu_3Cl$ afforded the stannane **25**. This was coupled with 4-iodo-2-chloropyridine in a Stille reaction to chemoselectively obtain the 2-chloropyridine derivative **26**. Finally, Suzuki-Miyaura coupling of **26** with 2,4-difluorophenylboronic acid afforded **21** in 90% yield. **22** was synthesised from **27** via a sequential etherification and cross coupling strategy analogous to ligand **21**

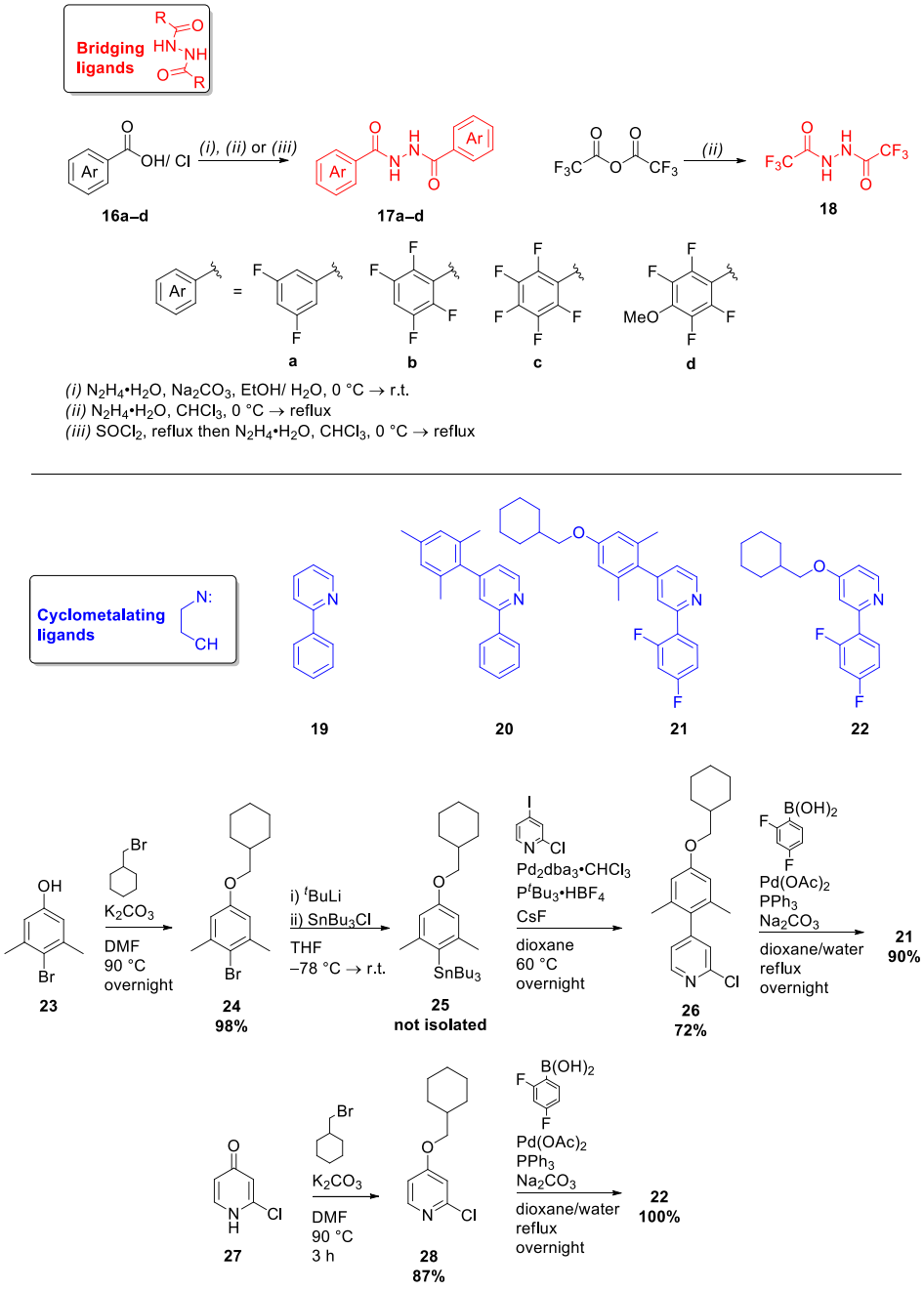

Scheme S1. Structures and synthetic schemes for the bridging and cyclometalating ligands studied in this work.

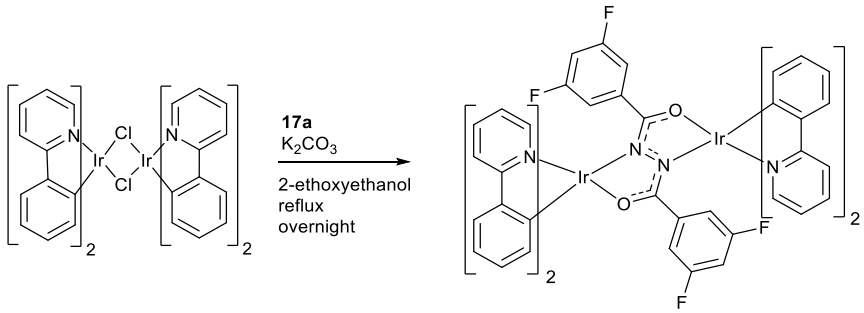

[Ir(ppy)$_2$μ–Cl]$_2$ **7 75%**

Complex 7. *N*,*N′*-Bis(3,5-difluorobenzoyl)hydrazide (**17a**) (87 mg, 0.28 mmol, 1.00 eq.), [Ir(ppy)$_2$μ-Cl]$_2$ (300 mg, 0.28 mmol, 1.00 eq.) and K_2CO_3 (116 mg, 0.84 mmol, 3.00 eq.) were added to 2-ethoxyethanol (15 mL) under and argon atmosphere and heated to reflux overnight. The reaction mixture was then cooled to room temperature and the solvent was removed under reduced pressure. The residue was then dissolved in DCM and suspended onto celite (*c.a.* 2 g) under reduced pressure, before being subjected to flash chromatography on silica gel (eluent: gradient *n*-hexane/ DCM sat. K_2CO_3 3:7 – 0:1). The yellow band was collected and after removing the solvent under reduced pressure, the residue was dissolved in a minimal amount of DCM (*ca*. 20 mL). Addition of methanol (*ca*. 20 mL) followed by reducing the volume of the mixture to 20 mL afforded complex **7** (275 mg, 0.21 mmol, 75%) as a yellow precipitate which was isolated via filtration and washed sequentially with methanol followed by pentane. The isolated product was a mixture of diastereomers in a *ca.* 9:1 ratio. MS (MALDI–TOF): *m/z* 1312.2 [M^+]. Calcd. for $C_{58}H_{38}F_4Ir_2N_6O_2^+$: 1312.2; Anal. Calcd. for $C_{58}H_{38}F_4Ir_2N_6O_2$: C, 53.12; H, 2.92; N, 6.41, Calcd. for $C_{58}H_{38}F_4Ir_2N_6O_2{\cdot}0.2CH_2Cl_2$: C, 52.62; H, 2.91; N, 6.33. Found: C, 52.62; H, 2.95; N, 6.27.;

Major diastereomer: ^{1}H NMR (600 MHz, CD_2Cl_2, TMS) δ (ppm) = 9.00 (ddd, *J* = 5.7, 1.6, 0.8 Hz, 2H$_A$), 8.70 (dt, *J* = 5.6, 1.2 Hz, 2H$_B$), 8.02 – 7.89 (m, 4H$_{2A}$), 7.85 – 7.76 (m, 4H$_{2B}$), 7.54 – 7.45 (m, 4H$_{A,D}$), 7.36 (dd, *J* = 7.8, 1.4 Hz, 2H$_C$), 7.10 (ddd, *J* = 6.7, 5.7, 2.2 Hz, 2H$_B$), 6.80 (td, *J* = 7.5, 1.3 Hz, 2H$_D$), 6.68 – 6.58 (m, 4H$_{C,D}$), 6.41 (td, *J* = 7.5, 1.4 Hz, 2H$_C$), 6.17 (tt, *J* = 9.1, 2.4 Hz, 2H$_{E2}$), 6.07 – 6.00 (m, 2H$_D$), 5.91 (dd, *J* = 7.8, 1.2 Hz, 2H$_C$), 5.88 (s, 4H$_{E4}$); ^{19}F {^{1}H} NMR (376 MHz, CD_2Cl_2) δ (ppm) = -110.65 (s, 2F).

Due to poor solubility in organic solvents, a solution sufficiently concentrated to obtain a ^{13}C NMR spectrum of the diastereomeric mixture could not be obtained. The ^{1}H NMR spectrum of the minor diastereomer could not be completely deconvoluted due to its low concentration and the presence of overlapping signals. The ^{1}H NMR spectrum of the mixture is shown as Figure S1. Single crystals of the *meso* diastereomer suitable for X-ray diffraction were grown by vapour diffusion of methanol into a DCM solution of the complex.

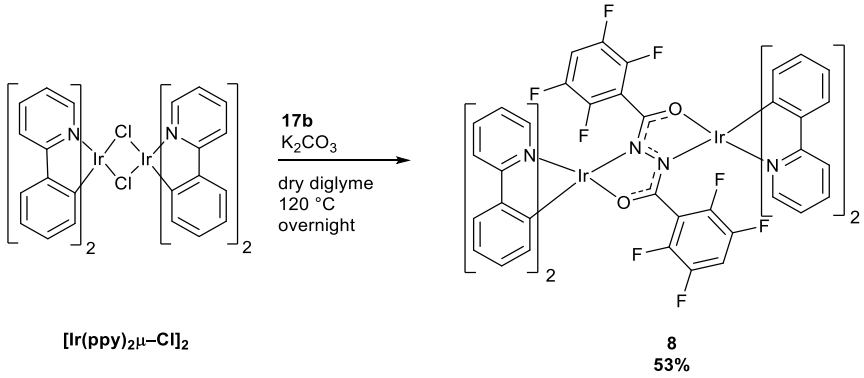

Complex 8. *N,N'*-Bis(2,3,5,6-tetrafluorobenzoyl)hydrazide (**17b**) (108 mg, 0.28 mmol, 1.00 eq.) was added to dry diglyme (10 mL) with K_2CO_3 (200 mg, 1.45 mmol, 5.18 eq.) and heated to 50 °C under an argon atmosphere for 30 min to obtain a pale yellow suspension. $[Ir(ppy)_2\mu\text{-}Cl]_2$ (300 mg, 0.28 mmol, 1.00 eq.) was then added and the mixture was heated to 120 °C overnight. The reaction mixture was then cooled to room temperature and the solvent was removed under reduced pressure. The residue was dissolved in DCM and suspended onto celite (*c.a.* 2 g) under reduced pressure, before being subjected to flash chromatography on silica gel (eluent: DCM sat. K_2CO_3). The glowing yellow band was collected and after removing the solvent under reduced pressure, the residue was dissolved in a minimal amount of DCM (*ca*. 10 mL). Addition of hexane (*ca*. 20 mL) followed by reducing the volume of the mixture to 25 mL afforded complex **8** (207 mg, 0.15 mmol, 53%) as a yellow precipitate which was isolated via filtration and washed with pentane. The product was isolated as a mixture of diastereomers in a *ca.* 9:1 ratio. MS (MALDI–TOF): *m/z* 1384.2 [M^+]. Calcd. for $C_{58}H_{34}F_8Ir_2N_6O_2^+$: 1384.2; Anal. Calcd. for $C_{58}H_{34}F_8Ir_2N_6O_2$: C, 50.36; H, 2.48; N, 6.08. Found: C, 50.06; H, 2.47; N, 6.00;

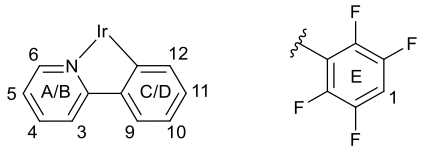

Major diastereomer: ^{1}H NMR (600 MHz, CD_2Cl_2, TMS) δ (ppm) = 9.18 (d, *J* = 5.6 Hz, $2H_{A6}$), 8.31 (d, *J* = 5.6 Hz, $2H_{B6}$), 7.97 – 7.94 (m, $2H_{A4}$), 7.93 – 7.87 (m, $6H_{A3, B4, B3}$), 7.50 (d, *J* = 7.1 Hz, $2H_{C9}$), 7.46 (ddd, *J* = 7.5, 5.6, 1.5 Hz, $2H_{A5}$), 7.37 (d, *J* = 7.2 Hz, $2H_{D9}$), 7.14 (ddd, *J* = 7.2, 5.6, 1.6 Hz, $2H_{B5}$), 6.79 (td, *J* = 7.4, 1.2 Hz, $2H_{C10}$), 6.63 – 6.59 (m, $4H_{C11, D10}$), 6.47 (td, *J* = 7.5, 1.0 Hz, $2H_{D11}$), 6.38 – 6.32 (m, $2H_{E1}$), 6.12 (d, *J* = 7.7 Hz, $2H_{D12}$), 5.91 (d, *J* = 7.4 Hz, $2H_{C12}$); ^{19}F {^{1}H} NMR (376 MHz, CD_2Cl_2) δ (ppm) =-138.37 (dd, *J* = 24.5, 12.0 Hz, 2F), -140.73 (dd, *J* = 23.0, 12.4 Hz, 2F), -141.90 (dd, *J* = 24.5, 12.4 Hz, 2F), -145.59 (dd, *J* = 23.0, 12.0 Hz, 2F).

Minor diastereomer: ^{19}F NMR (376 MHz, CD_2Cl_2) δ (ppm) =-139.55 (dd, *J* = 24.2, 11.7 Hz), -139.80 (dd, *J* = 23.4, 12.4 Hz), -143.09 (dd, *J* = 24.2, 11.7 Hz), -144.38 (dd, *J* = 23.4, 12.4 Hz).

Due to poor solubility in organic solvents, a solution sufficiently concentrated to obtain a ^{13}C NMR spectrum of the diastereomeric mixture could not be obtained. The ^{1}H NMR spectrum of the minor diastereomer could not be completely deconvoluted due to its low concentration and the presence of overlapping signals. The ^{1}H NMR spectrum of the mixture is shown as Figure S4.

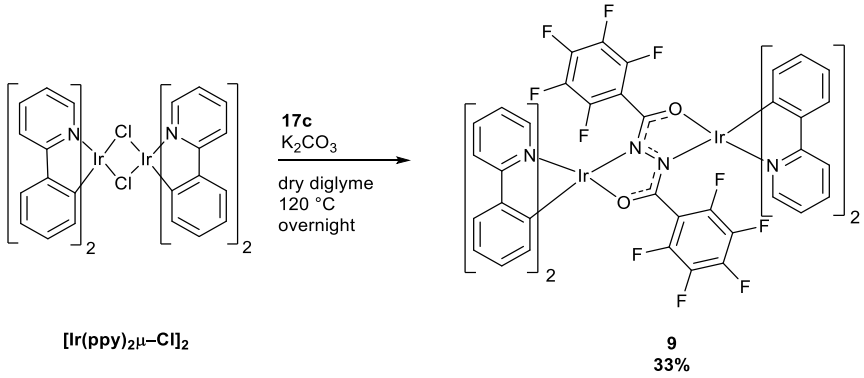

Complex 9. [Ir(ppy)$_2$μ-Cl]$_2$ (160 mg, 0.15 mmol, 1.00 eq.) and *N,N′*-bis(pentafluorobenzoyl)hydrazide (**17c**) (63 mg, 0.15 mmol, 1.00 eq.) were added to dry diglyme (20 mL) and heated to 120 °C under an argon atmosphere for 24 h. The reaction mixture was then cooled to room temperature and the solvent was removed under reduced pressure. The residue was then dissolved in DCM and suspended onto celite (*c.a.* 2 g) under reduced pressure, before being subjected to flash chromatography on silica gel (eluent: *n*-hexane/ DCM sat. K_2CO_3 1:1 v/v). The glowing yellow band was collected and after removing the solvent under reduced pressure, the residue was dissolved in a minimal amount of DCM (*ca*. 10 mL). Addition of hexane (*ca*. 20 mL) followed by reducing the volume of the mixture to 25 mL afforded complex **9** (70 mg, 0.05 mmol, 33%) as a yellow precipitate which was isolated via filtration and washed with pentane. The product was isolated as a mixture of diastereomers in a *ca.* 5:4 ratio (*meso:rac*). MS (MALDI–TOF): *m/z* 1420.1 [M$^+$]. Calcd. for $C_{58}H_{32}F_{10}Ir_2N_6O_2^+$: 1420.2; Anal. Calcd. for $C_{58}H_{32}F_{10}Ir_2N_6O_2$: C, 49.08; H, 2.27; N, 5.92. Found: C, 49.16; H, 2.31; N, 5.89.

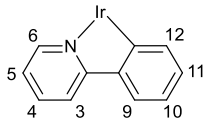

A/B

<u>^{1}H and ^{19}F NMR</u>

Meso diastereomer: ^{1}H NMR (700 MHz, CD_2Cl_2, TMS) δ (ppm) = 8.94 (d, *J* = 5.4 Hz, 2H$_{B6}$), 8.69 (d, *J* = 5.6 Hz, 2H$_{A6}$), 7.98 – 7.88 (m, 4H$_{B4,B3}$), 7.81 – 7.75 (m, 4H$_{A4,A3}$), 7.51 – 7.48 (m, 2H$_{B5}$), 7.47 – 7.44 (m, 2H$_{A9}$), 7.42 – 7.38 (m, 2H$_{B9}$), 7.02 (ddd, *J* = 7.3, 5.6, 2.0 Hz, 2H$_{A5}$), 6.81 – 6.77 (m, 2H$_{A10}$), 6.71 – 6.67 (m, 2H$_{B10}$), 6.64 – 6.59 (m, 2H$_{A11}$), 6.54 – 6.48 (m, 2H$_{B11}$), 6.07 (d, *J* = 7.7 Hz, 2H$_{B12}$), 5.96 (dd, *J* = 7.9, 1.2 Hz, 2H$_{A12}$); ^{19}F {^{1}H} NMR (376 MHz, CD_2Cl_2) δ (ppm) = -142.9 (dd, *J* = 24.2, 7.8 Hz, 2F), -144.0 (dd, *J* = 24.4, 7.8 Hz, 2F), -155.8 – -155.9 (m, 2F), -161.7 (td, *J* = 22.8, 7.8 Hz, 2F), -162.1 (td, *J* = 22.7, 7.7 Hz, 2F).

Rac diastereomer: ^{1}H NMR (700 MHz, CD_2Cl_2, TMS) δ (ppm) = 9.13 (d, *J* = 5.6 Hz, 2H$_{B6}$), 8.27 (d, *J* = 5.4 Hz, 2H$_{A6}$), 7.98 – 7.88 (m, 8H$_{B4,B3,A4,A3}$), 7.51 – 7.48 (m, 2H$_{A9}$), 7.47 – 7.44 (m, 2H$_{B5}$), 7.42 – 7.38 (m, 2H$_{B9}$), 7.14 (ddd, *J* = 7.2, 5.6, 1.5 Hz, 2H$_{A5}$), 6.81 – 6.77 (m, 2H$_{A10}$), 6.71 – 6.67 (m, 2H$_{B10}$), 6.64 – 6.59 (m, 2H$_{A11}$), 6.54 – 6.48 (m, 2H$_{B11}$), 6.12 (d, *J* = 7.8 Hz, 2H$_{B12}$), 5.90 (dd, *J* = 7.6, 1.1 Hz, 2H$_{A12}$); ^{19}F {^{1}H} NMR (376 MHz, CD_2Cl_2) δ (ppm) = -141.6 (d, *J* = 22.6 Hz, 2F), -145.2 (d, *J* = 23.7 Hz, 2F), -155.8 – -155.9 (m, 2F), -160.5 – -160.7 (m, 2F), -162.9 – -163.1 (m, 2F).

<u>^{13}C NMR</u>

Meso diastereomer: ^{13}C NMR (176 MHz, CD_2Cl_2, TMS) δ (ppm) = 149.2 (C$_{A6}$), 147.93 (C$_{B6}$), 131.8 (C$_{B12}$), 131.5 (C$_{A12}$), 129.2 (C$_{A11}$), 128.9 (C$_{B11}$), 123.8 (C$_{A9}$), 123.8 (C$_{B9}$), 121.6 (C$_{A10}$), 121.6 (C$_{B5}$), 121.5 (C$_{A5}$), 119.6 (C$_{B10}$).

Rac diastereomer: ^{13}C NMR (176 MHz, CD_2Cl_2, TMS) δ (ppm) = 149.8 (C$_{B6}$), 148.4 (C$_{A6}$), 131.8 (C$_{A12}$), 131.5 (C$_{B12}$), 129.1 (C$_{A11}$), 128.8 (C$_{B11}$), 123.5 (C$_{B9}$), 121.9 (C$_{A5}$), 121.7 (C$_{A10}$), 121.7 (C$_{A9}$), 121.5 (C$_{B5}$), 120.0 (C$_{B10}$). Due to low solubility in organic solvents, extensive coupling to ^{19}F nuclei and overlapping signals due to the presence of two diastereomers, some of the ^{13}C NMR signals could not be unambiguously assigned. All signals that could be clearly identified in the ^{13}C, ^{1}H–^{13}C

HSQC and ^{1}H–^{13}C HMBC NMR spectra are reported. The spectra are included as Figures S8, S11 and S12. To obtain a sample of the *meso* (ΛΔ) isomer, which was used to grow crystals suitable for X-ray diffraction, the diastereomeric mixture was suspended in toluene at a concentration of 1 mg/ mL. The suspension was refluxed for 20 minutes and then hot filtered to obtain a sample of the *meso* (ΛΔ) isomer as the filtrand. Crystals were grown by layering a near-saturated DCM solution of the complex with hexane.

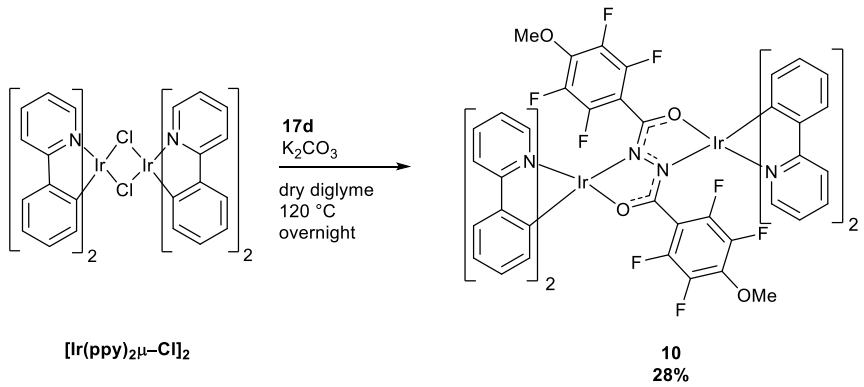

Complex 10. *N,N'*-Bis(2,3,5,6-tetrafluoro-4-methoxybenzoyl)hydrazide (**17d**) (62 mg, 0.14 mmol, 1.00 eq.) was added to dry diglyme (5 mL) with K_2CO_3 (96 mg, 0.70 mmol, 5.00 eq.) and heated to 50 °C under an argon atmosphere for 30 min to obtain a pale yellow suspension. $[Ir(ppy)_2\mu\text{-}Cl]_2$ (150 mg, 0.14 mmol, 1.00 eq.) was then added and the mixture was heated to 120 °C overnight. The reaction mixture was then cooled to room temperature and the solvent was removed under reduced pressure. The residue was then dissolved in DCM and suspended onto celite (*c.a.* 2 g) under reduced pressure, before being subjected to flash chromatography on silica gel (eluent: DCM sat. K_2CO_3). The glowing yellow band was collected and after removing the solvent under reduced pressure, the residue was dissolved in a minimal amount of DCM (*ca*. 5 mL). Addition of methanol (*ca*. 20 mL) followed by reducing the volume of the mixture to *ca*. 20 mL afforded complex **10** (57 mg, 0.04 mmol, 28%) as a yellow precipitate which was isolated via filtration and washed with pentane. The product was obtained as a mixture of diastereomers in a *ca.* 5:4 ratio. MS (MALDI–TOF): *m/z* 1444.2 [M^+]. Calcd. for $C_{60}H_{38}F_8Ir_2N_6O_4^+$: 1444.2; Anal. Calcd. for $C_{60}H_{38}F_8Ir_2N_6O_4$: C, 49.93; H, 2.65; N, 5.82, Calcd. for $C_{60}H_{38}F_8Ir_2N_6O_4 \cdot 0.2CH_2Cl_2$: C, 49.51; H, 2.65; N, 5.75. Found: C, 49.50; H, 2.76; N, 5.70.

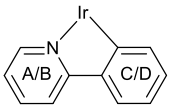

<u>^{1}H and ^{19}F NMR</u>

Major diastereomer: ^{1}H NMR (600 MHz, CD_2Cl_2, TMS) δ (ppm) = 9.16 (d, *J* = 5.6 Hz, $2H_A$), 8.27 (dt, *J* = 5.5, 1.2 Hz, $2H_B$), 7.96 – 7.86 (m, $8H_{2A,\,2B}$), 7.50 – 7.41 (m, $4H_{A,C}$), 7.40 – 7.36 (m, $2H_D$), 7.11 (ddd, *J* = 7.3, 5.7, 1.7 Hz, $2H_B$), 6.80 – 6.75 (m, $2H_C$), 6.65 – 6.57 (m, $4H_{C,D}$), 6.50 – 6.43 (m, $2H_D$), 6.11 (d, *J* = 7.7 Hz, $2H_D$), 5.91 (dd, *J* = 7.8, 1.2 Hz, $2H_C$), 3.86 (s, $6H_{MeO}$); ^{19}F {^{1}H} NMR (376 MHz, CD_2Cl_2) δ (ppm) = -143.2 – -143.5 (m, 2F), -146.6 – -146.8 (m, 2F), -157.7 – -157.9 (m, 2F), -159.4 – -159.7 (m, 2F).

Minor diastereomer: ^{1}H NMR (600 MHz, CD_2Cl_2, TMS) δ (ppm) = 8.95 (dd, *J* = 5.4, 1.3 Hz, $2H_A$), 8.72 (d, *J* = 5.7 Hz, $2H_B$), 7.96 – 7.86 (m, H_{2A}), 7.79 – 7.73 (m, $4H_{2B}$), 7.50 – 7.41 (m, $H_{A,C}$), 7.40 – 7.36 (m, $2H_D$), 7.01 (ddd, *J* = 7.2, 5.7, 2.0 Hz, $2H_B$), 6.80 – 6.75 (m, $2H_C$), 6.65 – 6.57 (m, $4H_{C,D}$), 6.50 – 6.43 (m, $2H_D$), 6.06 (d, *J* = 7.7 Hz, $2H_D$), 5.96 (dd, *J* = 7.8, 1.1 Hz, $2H_C$), 3.86 (s, $6H_{MeO}$); ^{19}F {^{1}H} NMR (376 MHz, CD_2Cl_2) δ (ppm) = -144.4 – -144.7 (m, 2F), -145.5 – -145.8 (m, 2F), -158.5 – -158.9 (m, 4F).

<u>^{13}C NMR</u>

Diasteromeric mixture: ^{13}C NMR (151 MHz, CD_2Cl_2, TMS) δ (ppm) = 169.3, 168.8, 168.6, 168.5, 165.2, 151.5 –148.5 (C_{ArF}), 145.0, 144.9, 143.6, 143.5, 138.1, 137.8, 137.6, 132.5, 132.3, 132.1, 132.1, 129.6, 129.6, 129.3, 129.2, 124.3, 124.3, 124.0, 124.0, 122.4, 122.3, 122.1, 122.0, 122.0, 120.2, 120.1, 119.7, 119.3, 119.3, 118.9, 62.0. Due to low solubility in organic

solvents, extensive coupling to ^{19}F nuclei and overlapping signals due to the presence of two diastereomers, some of the ^{13}C NMR signals could not be unambiguously assigned. All signals that could be clearly identified in the ^{13}C, ^{1}H–^{13}C HSQC and ^{1}H–^{13}C HMBC NMR spectra are reported. The spectra are included as Figures S17, S20 and S21. Single crystals of the *rac* diastereomer suitable for X-ray diffraction were grown by layering a near-saturated DCM solution of the complex with hexane.

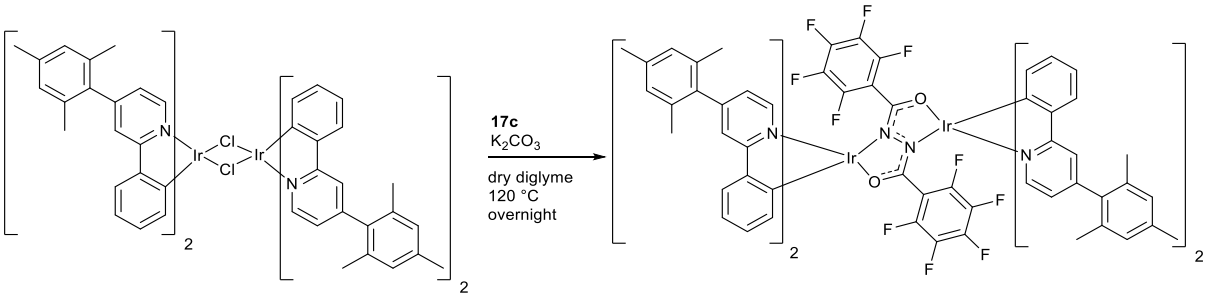

[Ir(mesppy)$_2$μ–Cl]$_2$ **rac 11 31%**

Complex *rac* **11.** *N*,*N'*-Bis(pentafluorobenzoyl)hydrazide (**17c**) (82 mg, 0.19 mmol, 1.00 eq.) was added to dry diglyme (15 mL) with K_2CO_3 (80 mg, 0.70 mmol, 2.98 eq.) and heated to 50 °C under an argon atmosphere for 30 min to obtain a pale yellow suspension. [Ir(mesppy)$_2$μ-Cl]$_2$ (300 mg, 0.19 mmol, 1.00 eq.) was then added and the mixture was heated to 120 °C overnight. The reaction mixture was then cooled to room temperature and the solvent was removed under reduced pressure. The residue was then dissolved in DCM and suspended onto celite (*c.a.* 2 g) under reduced pressure, before being subjected to flash chromatography on silica gel (eluent: gradient *n*-hexane/ DCM sat. K_2CO_3 9:1–1:1 v/v). First to elute was the *rac* (ΛΛ/ ΔΔ) diastereomer, which after removal of the solvent was dissolved in a minimal amount of DCM (*ca*. 5 mL). Addition of hexane (*ca*. 20 mL) followed by reducing the volume of the mixture to *ca*. 20 mL afforded complex *rac* **11** as a yellow precipitate which was isolated via filtration and washed with pentane (115 mg, 0.6 mmol, 31%).

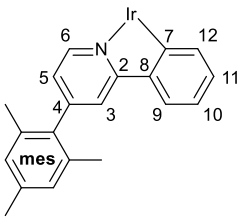

A/B

^{1}H NMR (700 MHz, CD_2Cl_2) δ (ppm) = 9.27 (d, *J* = 5.7 Hz, $2H_{A6}$), 8.44 (d, *J* = 5.6 Hz, $2H_{B6}$), 7.71 (s, $2H_{B3}$), 7.69 (s, $2H_{A3}$), 7.46 (d, *J* = 7.7 Hz, $2H_{B9}$), 7.35 (d, *J* = 7.7 Hz, $2H_{A9}$), 7.21 (dd, *J* = 5.8, 1.7 Hz, $2H_{A5}$), 7.05 (s, $2H_{mesAr}$), 7.04 (s, $4H_{mesAr}$), 7.01 (s, $2H_{mesAr}$), 6.94 (dd, *J* = 5.7, 1.7 Hz, $2H_{B5}$), 6.80 (t, *J* = 7.7 Hz, $2H_{B10}$), 6.70 (t, *J* = 7.3 Hz, $2H_{A10}$), 6.69 – 6.65 (m, $2H_{B11}$), 6.62 (t, *J* = 7.4 Hz, $2H_{A11}$), 6.41 (d, *J* = 7.8 Hz, $2H_{A12}$), 5.99 (d, *J* = 8.4 Hz, $2H_{B12}$), 2.37 (s, $6H_{mesMe}$), 2.36 (s, $6H_{mesMe}$), 2.29 (s, $6H_{mesMe}$), 2.21 (s, $6H_{mesMe}$), 2.13 (s, $6H_{mesMe}$), 2.09 (s, $6H_{mesMe}$); ^{19}F NMR {^{1}H} (376 MHz, CD_2Cl_2) δ (ppm) = -141.9 (dd, *J* = 25.2, 7.7 Hz, 2F), -145.1 – -145.2 (m, 2F), -155.9 (t, *J* = 21.6 Hz, 2F), -160.2 – -160.4 (m, 2F), -162.9 (ddd, *J* = 23.3, 21.0, 7.9 Hz, 2F); ^{13}C NMR (176 MHz, CD_2Cl_2) δ (ppm) = 168.1 (C_{A2}), 167.9 (C_{B2}), 151.9 (C_{A4}), 151.6 (C_{B4}), 150.8 (C_{A7}), 149.8 (C_{A6}), 148.4 (C_{B6}), 147.7 (C_{B7}), 144.7 (C_{B8}), 143.0 (C_{A8}), 135.0 – 135.8 ($C_{mes\ quart\ carbons}$), 131.8 (C_{B12}), 131.7 (C_{A12}), 129.1 (C_{B11}), 128.9 (C_{A11}), 128.4 (C_{mesAr}), 128.4# (C_{mesAr}), 123.9 (C_{B9}), 123.6 (C_{A9}), 123.1 (C_{A5}), 122.9 (C_{B5}), 121.8 (C_{B10}), 120.5 (C_{A3}), 119.9 (C_{B3}), 119.5 (C_{A10}), 20.8* (C_{mesMe}), 20.4 (C_{mesMe}), 20.3 (C_{mesMe}), 20.1 (C_{mesMe}), 20.0 (C_{mesMe}), Due to low solubility in organic solvents and extensive coupling to ^{19}F nuclei, some of the quaternary ^{13}C NMR signals could not be identified. All signals that could be clearly identified in the ^{13}C, ^{1}H–^{13}C HSQC and ^{1}H–^{13}C HMBC NMR spectra are reported. The spectra are included as Figures S23, S28 and S29. MS (MALDI–TOF): *m/z* 1892.3 [M^+]. Calcd. for $C_{94}H_{72}F_{10}Ir_2N_6O_2^+$: 1892.5; Anal. Calcd. for $C_{94}H_{72}F_{10}Ir_2N_6O_2$: C, 59.67; H, 3.84; N, 4.44, Calcd. for $C_{94}H_{72}F_{10}Ir_2N_6O_2 \cdot 0.4CH_2Cl_2$: C,

58.87; H, 3.81; N, 4.36. Found: C, 58.78; H, 3.73; N, 4.36. Single crystals suitable for X-ray diffraction were grown by vapour diffusion of hexane into a DCM solution of the complex. A second yellow band presumed to contain the *meso* (ΛΔ) diastereomer slowly eluted from the column after the *rac* (ΛΛ/ ΔΔ) diastereomer, but due to very low solubility it could not be isolated in an analytically pure form.

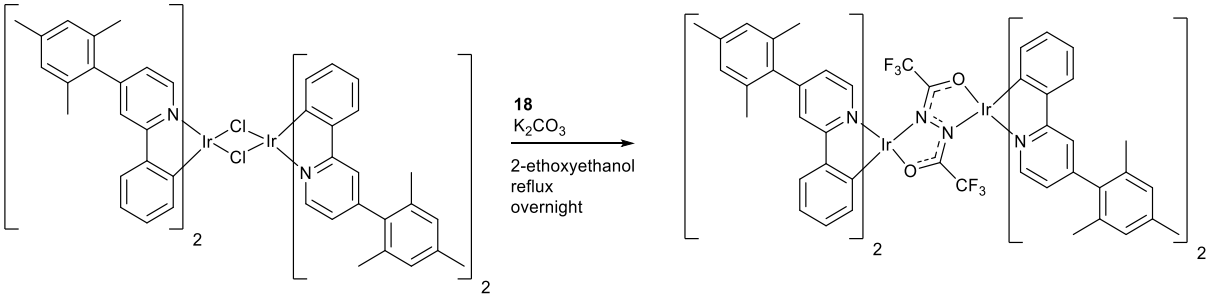

Complex *meso* **12.** Bis(trifluoromethyl)hydrazide (**18**) (43 mg, 0.19 mmol, 1.00 eq.), $[Ir(mesppy)_2\mu\text{-}Cl]_2$ (300 mg, 0.19 mmol, 1.00 eq.) and K_2CO_3 (80 mg, 0.70 mmol, 2.98 eq.) were added to 2-ethoxyethanol (15 mL) under and argon atmosphere and heated to reflux overnight. The reaction mixture was then cooled to room temperature and the solvent was removed under reduced pressure. The residue was then dissolved in DCM and suspended onto celite (*c.a.* 2 g) under reduced pressure, before being subjected to flash chromatography on silica gel (eluent: gradient *n*-hexane/ DCM sat. K_2CO_3 9:1–1:1 v/v). The glowing yellow band was collected and after removing the solvent under reduced pressure, the residue was dissolved in a minimal amount of DCM (*ca.* 5 mL). Addition of hexane (*ca.* 20 mL) followed by reducing the volume of the mixture to *ca.* 20 mL afforded complex *meso* **12** as a yellow precipitate which was isolated via filtration and washed with pentane (200 mg, 0.12 mmol, 61%). A single diastereomer (ΛΔ) was obtained.

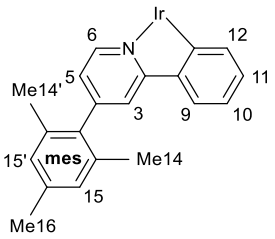

A/B

^{1}H NMR (700 MHz, THF-d_8) δ (ppm) = 8.74 (d, J = 5.6 Hz, $2H_{A6}$), 8.63 (d, J = 5.7 Hz, $2H_{B6}$), 7.84 (d, J = 1.8 Hz, $2H_{A3}$), 7.79 (d, J = 1.8 Hz, $2H_{B3}$), 7.56 (dd, J = 7.9, 1.3 Hz, $2H_{A9}$), 7.53 (dd, J = 7.9, 1.3 Hz, $2H_{B9}$), 7.25 (dd, J = 5.7, 1.9 Hz, $2H_{A5}$), 7.01 – 6.99 (m, $4H_{A15',B15'}$), 6.97 (s, $2H_{B15}$), 6.90 – 6.87 (m, $4H_{A15, B5}$), 6.70 (td, J = 7.6, 7.1, 1.2 Hz, $2H_{B10}$), 6.65 (ddd, J = 7.9, 6.9, 1.2 Hz, $2H_{A10}$), 6.57 (ddd, J = 8.2, 7.0, 1.3 Hz, $2H_{B11}$), 6.53 (ddd, J = 8.1, 6.9, 1.3 Hz, $2H_{A11}$), 6.30 (d, J = 7.8 Hz, $2H_{A12}$), 6.05 (dd, J = 7.9, 1.2 Hz, $2H_{B12}$), 2.35 (s, $6H_{BMe16}$), 2.32 (s, $6H_{AMe16}$), 2.18 (s, $6H_{AMe14'}$), 2.15 (s, $6H_{BMe14'}$), 1.91 (s, $6H_{BMe14}$), 1.86 (s, $6H_{AMe14}$); ^{19}F {^{1}H} NMR (376 MHz, CD_2Cl_2) δ (ppm) = -67.0 (s, 6F); ^{13}C NMR (176 MHz, THF-d_8) δ (ppm) = 170.8 (C_{A2}), 169.9 (C_{B2}), 152.5 (C_{B4}), 152.3 (C_{A4}), 150.6 (C_{B6}), 150.3 (C_{A7}), 149.4 (C_{A6}), 146.5 (C_{B7}), 145.2 (C_{B8}), 145.0 (C_{A8}), 138.7 ($C_{mes\ quart}$), 138.5 ($C_{mes\ quart}$), 137.3 – 135.9 ($C_{mes\ quart\ carbons}$), 134.6 (C_{A12}), 132.9 (C_{B12}), 130.4 (C_{B11}), 130.0 (C_{A11}), 130.0* ($C_{A15',B15'}$), 129.9 (C_{B15}), 129.8 (C_{A15}), 125.7 (C_{B9}), 125.4 (C_{A9}), 124.5 (C_{B5}), 124.13 (C_{A5}), 122.7 (C_{B10}), 121.8 (C_{B3}), 121.7 (C_{A3}), 121.2 (C_{A10}), 22.0* ($C_{A16,B16}$), 21.6 (C_{A14}), 21.5 (C_{B14}), 21.5 ($C_{A14'}$), 21.4 ($C_{B14'}$), Due to low solubility in organic solvents some of the quaternary ^{13}C NMR signals could not be identified. All signals that could be clearly identified in the ^{13}C, ^{1}H–^{13}C HSQC and ^{1}H–^{13}C HMBC NMR spectra are reported. The spectra are included as Figures S32, S36 and S37. MS (MALDI–TOF): *m/z* 1696.3 [M$^+$]. Calcd. for $C_{84}H_{72}F_6Ir_2N_6O_2^+$: 1696.5; Anal. Calcd. for $C_{84}H_{72}F_6Ir_2N_6O_2$: C, 59.49; H, 4.28; N, 4.96, Calcd. for $C_{84}H_{72}F_6Ir_2N_6O_2{\cdot}0.5CH_2Cl_2$: C, 58.38; H, 4.23; N, 4.83. Found: C, 58.04; H, 4.25; N,

4.71. Single crystals suitable for X-ray diffraction were grown by vapour diffusion of hexane into a THF solution of the complex.

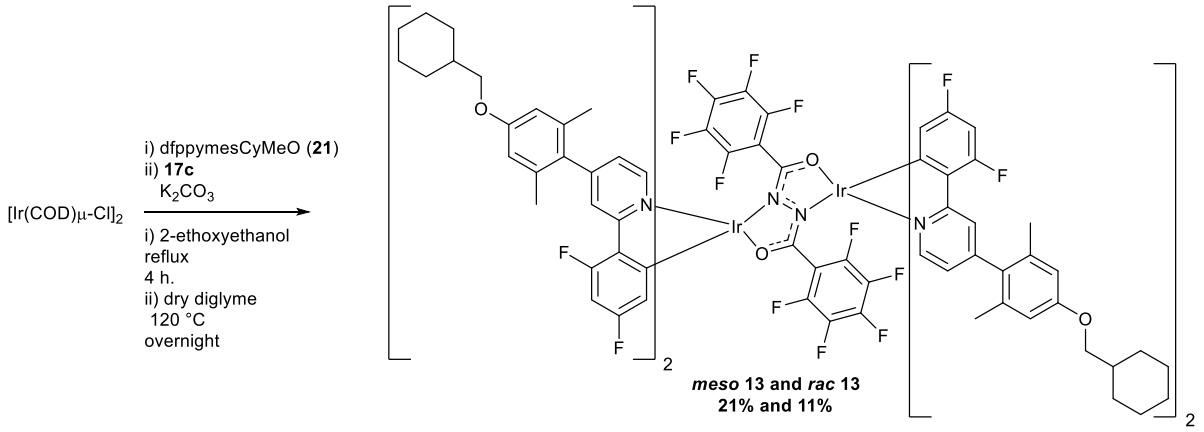

Complexes *meso* **13** and *rac* **13.** [Ir(COD)μ-Cl]$_2$ (200 mg, 0.30 mmol, 1.00 eq.) and 2-(2,4-difluorophenyl)-4-(2,6-dimethyl-4-(methylcyclohexyloxy)phenyl)pyridine (**21**) (534 mg, 1.32 mmol, 4.4 eq.) were added to 2-ethoxyethanol (10 mL) and heated to reflux under an argon atmosphere for 4 h. The reaction mixture was then cooled to room temperature and the solvent removed under reduced pressure. The residue was then dissolved in DCM (*ca.* 10 mL) and hexane was added (*ca*. 30 mL). The solvent volume was reduced to *ca.* 10 mL under reduced pressure. A yellow precipitate formed which was filtered and washed with pentane (*ca.* 20 mL) to isolate the intermediate μ-dichloro-bridged diiridium complex (463 mg, 0.22 mmol, 75%) which was used without further purification (^{1}H NMR data were consistent with the proposed structure – Figure S39). The obtained dichloro dimer was combined with *N,N'*-bis(pentafluorobenzoyl)hydrazide (**17c**) (94 mg, 0.22 mmol, 1.00 eq.) and K_2CO_3 (77 mg, 0.56 mmol, 2.50 eq.) and suspended in dry diglyme (15 mL) under argon. It was subsequently heated to 120 °C overnight. The reaction mixture was then cooled to room temperature and the solvent removed under reduced pressure. To the residue was added DCM (10 mL), and the resulting mixture was sonicated for 5 min. Hexane (30 mL) was then added, before the solvent volume was reduced to *ca.* 30 mL. The mixture was filtered to obtain a yellow powder and a yellow/orange filtrate. Both the filtrate and filtrand were retained.

Filtrand

The filtrand was further purified by flash chromatography on silica gel (eluent: *n*-hexane/ DCM sat. K_2CO_3 4:6 v/v). After evaporation of the column solvent, the residue was precipitated from DCM/ hexane, filtered and washed with pentane to afford the presumed *meso* (ΛΔ) diastereomer *(meso* **13***)* (150 mg, 0.06 mmol, 21% from [Ir(COD)μ-Cl]$_2$).

Filtrate

The filtrate was evaporated and the residue was refluxed in methanol (20 mL) for 5 min. The mixture was then cooled in a freezer (−18 °C) for 1 h before being filtered to obtain a yellow precipitate, which was further purified by flash chromatography on silica gel (eluent: *n*-hexane/ toluene 6:4 v/v). After evaporation of the column solvent, the residue was precipitated from DCM/ hexane, filtered and washed with pentane to afford *rac* **13** (80 mg, 0.03 mmol, 11% from [Ir(COD)μ-Cl]$_2$).

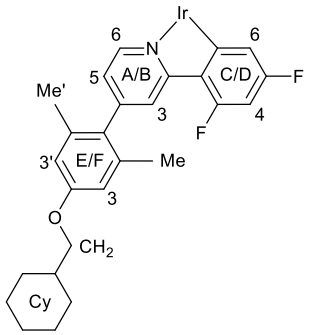

meso **13:** ^{1}H NMR (600 MHz, CD_2Cl_2) δ (ppm) = 8.93 (d, *J* = 5.8 Hz, $2H_{A6}$), 8.76 (d, *J* = 5.8 Hz, $2H_{B6}$), 8.10 (s, $2H_{A3}$), 8.01 (s, $2H_{B3}$), 7.34 (dd, *J* = 5.7, 1.8 Hz, $2H_{A5}$), 6.88 (dd, *J* = 5.8, 1.8 Hz, $2H_{B5}$), 6.78 – 6.72 (m, $6H_{E3,E3',F3'}$), 6.65 (bs, $2H_{F3}$), 6.38 – 6.32 (m, $2H_{C4}$), 6.31 – 6.25 (m, $2H_{D4}$), 5.66 (dd, *J* = 8.5, 2.0 Hz, $2H_{D6}$), 5.38 (dd, *J* = 8.9, 2.4 Hz, $2H_{C6}$), 3.85 (d, *J* = 6.4 Hz, $4H_{CH2}$), 3.81 (d, *J* = 6.4 Hz, $4H_{CH2}$), 2.18 (bs, $6H_{EMe/EMe'}$), 2.16 (bs, $6H_{FMe/FMe'}$), 1.98 −1.90 (m, $20H_{Cy,EMe/EMe',FMe/FMe'}$), 1.82 (td, *J* = 7.7, 3.7 Hz, $12H_{Cy}$), 1.76 (d, *J* = 11.7 Hz, $4H_{Cy}$), 1.41 – 1.32 (m, $8H_{Cy}$), 1.29 – 1.26 (m, $4H_{Cy}$), 1.18 – 1.09 (m, $8H_{Cy}$) The ^{1}H environments on rings E and F resolve due to restricted rotation. Exchange is observed in ^{1}H−^{1}H NOESY and ^{1}H−^{1}H ROESY experiments (Figures S47 and S48); ^{19}F NMR (376 MHz, CD_2Cl_2) δ (ppm) = -108.0 (d, *J* = 10.2 Hz, 2F), -108.3 (d, *J* = 10.1 Hz, 2F), -109.7 (d, *J* = 10.2 Hz, 2F), -110.0 (d, *J* = 10.2 Hz, 2F), -142.0 (d, *J* = 21.2 Hz, 2F), -143.4 (d, *J* = 20.5 Hz, 2F), -154.7 (t, *J* = 20.8 Hz, 2F), -161.1 (td, *J* = 22.4, 7.8 Hz, 2F), -161.7 (td, *J* = 23.9, 21.7, 7.5 Hz, 2F); ^{13}C NMR (176 MHz, CD_2Cl_2) δ (ppm) = 148.6 (C_{B6}), 147.7 (C_{A6}), 125.0 (C_{A3}), 124.9 (C_{B3}), 123.93 (C_{A5}), 123.59 (C_{B5}), 113.8 (C_{F3}), 113.7$^{\#}$ ($C_{F3',E3,E3'}$), 113.6 (C_{D6}), 113.5 (C_{C6}), 98.2 (C_{C4}), 96.0 (C_{D4}), 73.5 (C_{CH2}), 73.43 (C_{CH2}), 37.8* (C_{Cy}), 29.9* (C_{Cy}), 26.6* (C_{Cy}), 25.8* (C_{Cy}), 20.7 ($C_{FMe/FMe'}$), 20.6 ($C_{EMe/EMe'}$), 20.4 ($C_{FMe/FMe'}$), 20.3 ($C_{EMe/EMe'}$), Due to low solubility in organic solvents and extensive coupling to ^{19}F nuclei, some quaternary ^{13}C NMR signals could not be identified. All signals that could be clearly identified in the ^{13}C, ^{1}H–^{13}C HSQC and ^{1}H–^{13}C HMBC NMR spectra are reported. The spectra are included as Figures S41, S45 and S46. MS (MALDI–TOF): *m/z* 2428.6 [M^{+}]. Calcd. for $C_{118}H_{104}F_{18}Ir_2N_6O_6^{+}$: 2428.7; Anal. Calcd. for $C_{118}H_{104}F_{18}Ir_2N_6O_6$: C, 58.36; H, 4.32; N, 3.46, Calcd. for $C_{118}H_{104}F_{18}Ir_2N_6O_6{\cdot}0.3CH_2Cl_2$: C, 57.90; H, 4.30; N, 3.42. Found: C, 57.83; H, 4.34; N, 3.36.

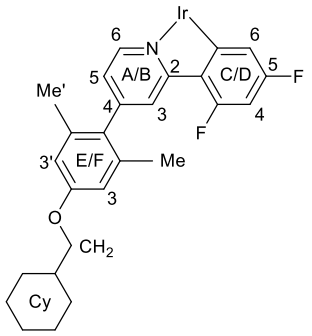

rac **13**: ^{1}H NMR (700 MHz, CD_2Cl_2, TMS) δ (ppm) = 9.18 (d, *J* = 5.8 Hz, $2H_{A6}$), 8.35 (d, *J* = 5.7 Hz, $2H_{B6}$), 8.08 (s, $4H_{A3,B3}$), 7.28 (d, *J* = 5.7 Hz, $2H_{A5}$), 7.01 – 6.98 (m, $2H_{B5}$), 6.76 – 6.71 (m, $8H_{E3,E3',F3,F3'}$), 6.35 (t, *J* = 10.5 Hz, $2H_{C4}$), 6.29 (t, *J* = 10.6 Hz, $2H_{D4}$), 5.84 (d, *J* = 8.7 Hz, $2H_{D6}$), 5.36 – 5.34 (m, $2H_{C6}$), 3.82 – 3.79 (m, $8H_{CH2}$), 2.30 (bs, $6H_{FMe/FMe'}$), 2.22 (bs, $6H_{EMe/EMe'}$), 2.11 (bs, $6H_{FMe/FMe'}$), 2.09 (bs, $6H_{EMe/EMe'}$), 1.89 (d, *J* = 12.8 Hz, $8H_{Cy}$), 1.79 (d, *J* = 13.8 Hz, $12H_{Cy}$), 1.73 (d, *J* = 12.8 Hz, $4H_{Cy}$), 1.34 (q, *J* = 13.1 Hz, $8H_{Cy}$), 1.29 – 1.22 (m, $4H_{Cy}$), 1.09 (q, *J* = 12.8 Hz, $8H_{Cy}$) The ^{1}H environments on rings E and F partially resolve due to restricted rotation. Exchange is suspected from the ^{1}H−^{1}H NOESY experiment (Figure S56); ^{19}F {^{1}H} NMR (376 MHz, CD_2Cl_2) δ (ppm) = -107.9 (d, *J* = 10.2 Hz, 2F), -108.5 (d, *J* = 10.2 Hz, 2F), -109.7 – -109.8 (m, 2F), -109.8 – -109.9 (m, 2F), -141.0 (d, *J* = 24.1 Hz, 2F), -144.5 (d, *J* = 22.6 Hz, 2F), -154.7 (t, *J* = 20.8 Hz, 2F), -159.9 – -160.2 (m, 2F), -161.9 (td, *J* = 22.8, 22.2, 7.7 Hz, 2F);

^{13}C NMR (176 MHz, CD_2Cl_2) δ (ppm) = 164.9 (C_{A2}), 164.4 (C_{B2}), 162.8 (d, *J* = 256 Hz, C_{D5}), 162.4 (d, *J* = 251 Hz, C_{C5}), 153.2 (C_{A4}), 153.1 (C_{B4}), 159.2* ($C_{E/F}$), 148.4 (C_{A6}), 148.1 (C_{B6}), 136.6* ($C_{E/F}$), 130.5* ($C_{E/F}$), 125.1 (C_{A3}), 124.7 (C_{B3}), 123.9 (C_{A5}), 123.7 (C_{B5}), 113.9 (C_{C6}), 113.7* ($C_{E/F}$), 113.7* ($C_{E/F}$), 113.6 (C_{D6}), 98.3 (C_{C4}), 95.9 (C_{D4}), 73.5* (C_{CH2}), 37.7* (C_{Cy}), 29.9* (C_{Cy}), 26.5* (C_{Cy}), 25.8*(C_{Cy}), 20.8 ($C_{EMe/EMe'}$), 20.6 ($C_{FMe/FMe'}$), 20.5 ($C_{FMe/FMe'}$), 20.5 ($C_{EMe/EMe'}$), Due to low solubility in organic solvents and extensive coupling to ^{19}F nuclei, some of the quaternary ^{13}C NMR signals could not be identified. All signals that could be clearly identified in the ^{13}C, ^{1}H–^{13}C HSQC and ^{1}H–^{13}C HMBC NMR spectra are reported. The spectra are included as Figures S50, S54 and S55. MS (MALDI–TOF): *m/z* 2428.6 [M^+]. Calcd. for $C_{118}H_{104}F_{18}Ir_2N_6O_6^+$: 2428.7; Anal. Calcd. for $C_{118}H_{104}F_{18}Ir_2N_6O_6$: C, 58.36; H, 4.32; N, 3.46, Calcd. for $C_{118}H_{104}F_{18}Ir_2N_6O_6 \cdot 0.5CH_2Cl_2$: C, 57.60; H, 4.28; N, 3.40. Found: C, 57.46; H, 4.32; N, 3.42. Crystals suitable for X-ray diffraction fell overnight from a saturated solution of the complex in CD_2Cl_2.

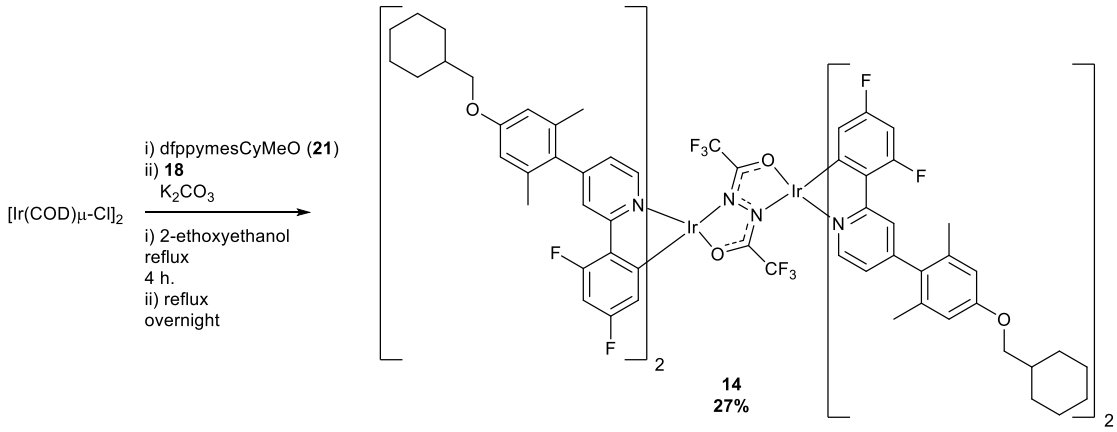

Complex 14. [Ir(COD)μ-Cl]$_2$ (94 mg, 0.14 mmol, 1.00 eq.) and 2-(2,4-difluorophenyl)-4-(2,6-dimethyl-4-(methylcyclohexyloxy)phenyl)pyridine (**21**) (250 mg, 0.62 mmol, 4.4 eq.) were added to 2-ethoxyethanol (5 mL) and heated to reflux under an argon atmosphere for 4 h to generate the μ-dichloro-bridged diiridium complex *in-situ*. The reaction mixture was then cooled to room temperature, before bis(trifluoromethyl)hydrazide (**18**) (34 mg, 0.14 mmol, 1.00 eq.), and K_2CO_3 (58 mg, 0.42 mmol, 3.00 eq.) were added. The reaction mixture was then heated to reflux overnight, before being cooled to room temperature and the solvent removed under reduced pressure. The residue was dissolved in DCM, suspended onto celite (*c.a.* 2 g) under reduced pressure and subjected to flash chromatography on silica gel (eluent: gradient *n*-hexane/ DCM sat. K_2CO_3 8:2–2:8 v/v). The yellow band was collected and the column solvent was removed under reduced pressure. The residue was heated to reflux in THF (25 mL) for 20 min and then hot filtered to obtain a yellow powder (25 mg, 0.01 mmol, 8%). A second crop was obtained by reducing the filtrate to 10 mL and repeating the process (60 mg, 0.03 mmol, 19%). The recovered solids from both filtrations were combined to afford complex (**14**) (85 mg, 0.04 mmol, 27%) as a single diastereomer.

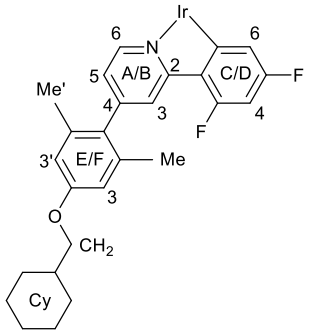

^{1}H NMR (700 MHz, CD_2Cl_2, TMS) δ (ppm) = 8.57 (d, *J* = 5.7 Hz, $2H_{A6}$), 8.42 (d, *J* = 5.7 Hz, $2H_{B6}$), 8.13 (s, $2H_{A3}$), 8.06 (s, $2H_{B3}$), 7.20 (dd, *J* = 5.7, 1.9 Hz, $2H_{A5}$), 6.79 (dd, *J* = 5.8, 1.9 Hz, $2H_{B5}$), 6.73 (bs, $2H_{E3}$), 6.72 (bs, $2H_{F3}$), 6.70 (bs, $2H_{F3'}$), 6.61 (bs, $2H_{E3'}$), 6.42 (ap. t, *J* = 10.2 Hz, $2H_{C4}$), 6.36 (ap. t, *J* = 10.6 Hz, $2H_{D4}$), 5.70 (dd, *J* = 9.1, 2.1 Hz,

$2H_{D6}$), 5.47 (dd, J = 9.0, 2.4 Hz, $2H_{C6}$), 3.82 (d, J = 6.4 Hz, $4H_{CH2}$), 3.79 (d, J = 6.1 Hz, $4H_{CH2}$), 2.17 (bs, $6H_{EMe/EMe'}$), 2.14 (bs, $6H_{FMe/FMe'}$), 1.92 (bs, $6H_{FMe/FMe'}$), 1.91 – 1.81 (m, $8H_{Cy}$), 1.84 (bs, $6H_{EMe/EMe'}$), 1.82 – 1.77 (m, $12H_{Cy}$), 1.74 (d, J = 13.0 Hz, $4H_{Cy}$), 1.39 – 1.31 (m, $8H_{Cy}$), 1.29 – 1.23 (m, $4H_{Cy}$), 1.13 – 1.09 (m, $8H_{Cy}$) The ^{1}H environments on rings E and F resolve due to restricted rotation. Exchange is suspected from the ^{1}H–^{1}H NOESY experiment (Figure S64); ^{19}F {^{1}H} NMR (376 MHz, CD_2Cl_2) δ (ppm) = -67.0 (s, $6F_{CF3}$), -107.6 (d, J = 10.2 Hz, $2F_{Ar}$), -109.4 (d, J = 9.8 Hz, $2F_{Ar}$), -109.6 (d, J = 10.2 Hz, $2F_{Ar}$), -111.2 – -111.3 (m, $2F_{Ar}$); ^{13}C NMR (176 MHz, CD_2Cl_2) δ (ppm) = 165.7 (C_{A2}), 164.6 (C_{B2}), 159.2 ($C_{E\ or\ F}$), 159.1 ($C_{E\ or\ F}$), 152.9 (C_{B4}), 152.7 (C_{A4}), 148.2 (C_{B6}), 146.9 (C_{A6}), 125.1 (C_{B3}), 124.9 (C_{A3}), 123.7 (C_{B5}), 123.3 (C_{A5}), 114.7 (C_{D6}), 113.7# ($C_{E3/E3'/F3'}$), 113.6 (C_{F3}), 113.6 (C_{C6}), 98.4 (C_{C4}), 96.5 (C_{D4}), 73.5 (C_{CH2}), 73.4 (C_{CH2}), 37.8* (C_{Cy}), 29.8* (C_{Cy}), 26.6* (C_{Cy}), 25.8* (C_{Cy}), 20.6 ($C_{EMe/EMe'}$), 20.6 ($C_{FMe/FMe'}$), 20.6 ($C_{FMe/FMe'}$), 20.5 ($C_{EMe/EMe'}$), Due to low solubility in organic solvents, some quaternary ^{13}C NMR signals could not be identified. All signals that could be clearly identified in the ^{13}C, ^{1}H–^{13}C HSQC and ^{1}H–^{13}C HMBC NMR spectra are reported. The spectra are included as Figures S58, S62 and S63. MS (MALDI–TOF): *m/z* 2232.2 [M$^+$]. Calcd. for $C_{108}H_{104}F_{14}Ir_2N_6O_6^+$: 2232.7.

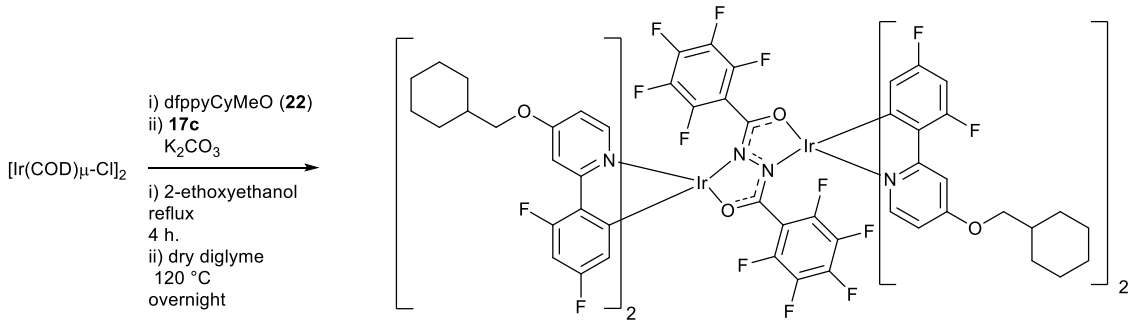

Complex 15. [Ir(COD)μ-Cl]$_2$ (200 mg, 0.30 mmol, 1.00 eq.) and 2-(2,4-difluorophenyl)-4-(methylcyclohexyloxy)phenyl pyridine (**22**) (366 mg, 1.21 mmol, 4.05 eq.) were added to 2-ethoxyethanol (15 mL) and heated to reflux under an argon atmosphere for 4 h. The reaction mixture was then cooled to room temperature and hexane was added (*ca.* 30 mL). The mixture was cooled in a fridge (*ca.* 3 °C) for 1 h. A yellow precipitate formed which was filtered and washed with pentane (*ca.* 20 mL) to isolate the intermediate μ-dichloro-bridged diiridium complex (403 mg, 0.24 mmol, 80%) which was used without further purification (^{1}H NMR data were consistent with the proposed structure – Figure S65). The obtained dichloro dimer was combined with *N,N'*-bis(pentafluorobenzoyl)hydrazide (**17c**) (102 mg, 0.24 mmol, 1.00 eq.) and K_2CO_3 (84 mg, 0.60 mmol, 2.50 eq.) and suspended in dry diglyme (15 mL) under argon. It was subsequently heated to 120 °C overnight. The reaction mixture was then cooled to room temperature and diluted with hexane (*ca.* 70 mL). A yellow precipitate formed which was filtered and washed with pentane (*ca.* 20 mL). The obtained solid was then dissolved in DCM and suspended onto celite (*c.a.* 2 g) under reduced pressure, before being subjected to flash chromatography on silica gel (eluent: *n*-hexane/ DCM sat. K_2CO_3 1:1 v/v). The faint yellow band was collected and after removing the solvent under reduced pressure, the residue was dissolved in minimal DCM (*ca.* 15 mL). Hexane was added (*ca.* 20 mL) and the volume was reduced to 20 mL After collecting the precipitate by filtration and washing with pentane complex **15** was obtained as a yellow solid (130 mg, 0.6 mmol, 22% from [Ir(COD)μ-Cl]$_2$). A single diastereomer was obtained.

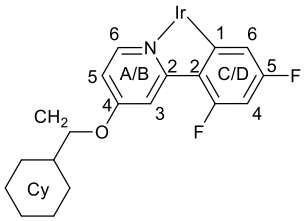

^{1}H NMR (700 MHz, CD_2Cl_2, TMS) δ (ppm)= 8.73 (d, *J* = 6.5 Hz, $2H_{A6}$), 7.94 (d, *J* = 6.5 Hz, $2H_{B6}$), 7.75 (t, *J* = 3.1 Hz, $2H_{A3}$), 7.72 (t, *J* = 2.9 Hz, $2H_{B3}$), 7.00 (dd, *J* = 6.5, 2.8 Hz, $2H_{A5}$), 6.72 (dd, *J* = 6.5, 2.7 Hz, $2H_{B5}$), 6.32 (ddd, *J* = 12.0, 9.0, 2.4 Hz, $2H_{C4}$), 6.24 (ddd, *J* = 11.9, 9.0, 2.4 Hz, $2H_{D4}$), 5.60 (dd, *J* = 9.0, 2.4 Hz, $2H_{D6}$), 5.42 (dd, *J* = 8.7, 2.4 Hz, $2H_{C6}$), 4.08 – 4.05 (m, $8H_{CH2}$), 2.03 – 1.93 (m, $12H_{Cy}$), 1.89 – 1.83 (m, $8H_{Cy}$), 1.80 – 1.74 (m, $4H_{Cy}$), 1.45 – 1.35 (m, $8H_{Cy}$), 1.29 – 1.26 (m, $4H_{Cy}$), 1.25 – 1.16 (m, $8H_{Cy}$); ^{19}F NMR (376 MHz, CD_2Cl_2) δ (ppm) = -108.7 (d, *J* = 10.1 Hz, 2F), -109.4 (d, *J* = 10.0 Hz, 2F), -111.0 (d, *J* = 10.1 Hz, 2F), -111.1 (d, *J* = 10.1 Hz, 2F), -140.4 (d, *J* = 24.5 Hz, 2F), -143.9 (d, *J* = 24.0 Hz, 2F), -155.3 (t, *J* = 20.8 Hz, 2F), -160.5 – -160.8 (m, 2F), -162.1 – -162.4 (m, 2F); ^{13}C NMR (176 MHz, CD_2Cl_2, TMS) δ (ppm) = 167.4 (C_{B2}), 167.2 ($C_{A4\ or\ B4}$), 165.7 (C_{A2}), 165.1 ($C_{A4\ or\ B4}$), 162.6 (d, *J* = 255 Hz, C_{D5}), 162.3 (d, *J* = 251 Hz, C_{C5}), 160.5 (d, *J* = 266 Hz, C_{D3}), 160.4 (d, *J* = 263 Hz, C_{C3}), 150.1 (C_{A6}), 148.7 (B_{B6}), 128. 7 (C_{C1}), 127.15 (C_{D1}), 114.1 (C_{C6}), 113.6 (C_{D6}), 109.7 (C_{A5}), 109.6 (C_{B5}), 108.8 (C_{A3}), 108.4 (C_{B3}), 97.9 (C_{C4}), 95.6 (C_{D4}), 74.3 (C_{CH2}), 74.25 (C_{CH2}), 37.50 (C_{Cy}), 37.44 (C_{Cy}), 29.75 (C_{Cy}), 29.68 (C_{Cy}), 26.39 (C_{Cy}), 26.36 (C_{Cy}), 25.74* (C_{Cy}), Due to low solubility in organic solvents and extensive coupling to ^{19}F nuclei, some of the quaternary ^{13}C NMR signals could not be reported. All signals that could be clearly identified in the ^{13}C, ^{1}H–^{13}C HSQC and ^{1}H–^{13}C HMBC NMR spectra are reported. The spectra are included as Figures S67, S70 and S71. MS (MALDI–TOF): *m/z* 2012.4 [M^+]. Calcd. for $C_{86}H_{72}F_{18}Ir_2N_6O_6^+$: 2012.3; Anal. Calcd. for $C_{86}H_{72}F_{18}Ir_2N_6O_6^+$: C, 51.34; H, 3.61; N, 4.18. Found: C, 51.23; H, 3.60; N, 4.15.

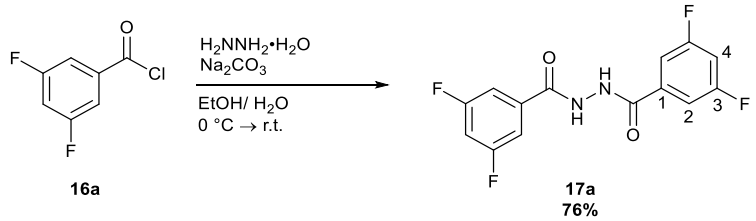

***N,N′*-Bis(3,5-difluorobenzoyl)hydrazide (17a).** 3,5-difluorobenzoyl chloride (**16a**) (5.00 g, 28.3 mmol, 2.10 eq.) was added dropwise under air to a stirred solution of hydrazine monohydrate (675 mg, 13.5 mmol, 1.00 eq.) in ethanol (10 mL), which was cooled in an ice bath to maintain the reaction temperature below 15 °C. Formation of a white precipitate was immediately observed. Once the addition was half complete, a further 30 mL of cold ethanol was added to facilitate stirring before a solution of Na_2CO_3 (1.50 g, 14.2 mmol, 1.05 eq.) in water (10 mL) was added dropwise alongside the remaining difluorobenzoyl chloride (**16a**). After the addition of the reagents was completed (*ca.* 20 min), the ice bath was removed and stirring was continued at room temperature for a further 30 min. The reaction mixture was poured into water (50 mL), allowed to settle for 1 h and filtered to collect the crude hydrazide as a white powder which was subsequently refluxed in ethanol (100 mL) for 10 min. The mixture was cooled to room temperature and then filtered to obtain *N,N′*-bis(3,5-difluorobenzoyl)hydrazide (**17a**) (3.19 g, 10.2 mmol, 76%). M.pt. 285–290 °C; ^{1}H NMR (400 MHz, DMSO-d_6) δ (ppm) = 10.84 (s, $2H_{N–H}$), 7.73 – 7.44 (m, $6H_{2+4}$); ^{13}C NMR (101 MHz, DMSO-d_6) δ (ppm) = 163.7 (t, *J* = 2.9 Hz, $C_{C=O}$), 162.8 (dd, *J* = 247.7, 12.7 Hz, C_3), 136.1 (t, *J* = 8.7 Hz, C_1), 111.7 – 111.2 (m, C_2), 108.1 (t, *J* = 25.9 Hz, C_4); ^{19}F{^{1}H} NMR (376 MHz, DMSO-d_6) δ (ppm) = -108.3 (s, 4F); HRMS (ASAP): *m/z* 313.0607 [MH^+]. Calcd. for $C_{14}H_9N_2O_2F_4^+$: 313.0600.

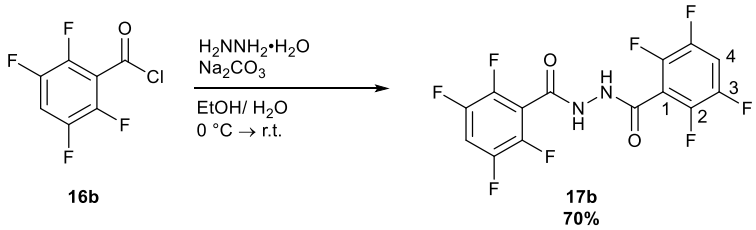

***N,N′*-Bis(2,3,5,6-tetrafluorobenzoyl)hydrazide (17b).** 2,3,5,6-tetrafluorobenzoyl chloride (**16b**) (5.00 g, 23.5 mmol, 2.13 eq.) was added dropwise under air to a stirred solution of hydrazine monohydrate (553 mg, 11.0 mmol, 1.00 eq.) in ethanol (10 mL), which was cooled in an ice bath to maintain the reaction temperature below 15 °C. Formation of a white precipitate was immediately observed. Once the addition was half complete, a solution of Na_2CO_3 (1.24 g, 11.7 mmol, 1.06 eq.) in water (10 mL) was added dropwise alongside the remaining 2,3,5,6-tetrafluorobenzoyl chloride (**16b**). After the addition of the reagents was completed (*ca.* 20 min), the ice bath was removed and stirring was continued at room temperature for a further 30 min. The reaction mixture was poured into water (50 mL), allowed to settle for 1 h and filtered to collect the crude hydrazide as a white powder (5.30 g, 13.8 mmol, 125%). The crude material was recrystallised twice from methanol/water and was obtained sufficiently pure for use in the next step (2.95 g, 7.68 mmol, 70%). M.pt. 265–269 °C; ^{1}H NMR (400 MHz, DMSO-d_6) δ (ppm) = 11.36 (s, $2H_{N-H}$), 8.22 – 8.01 (m, $2H_4$); ^{13}C NMR (101 MHz, DMSO-d_6) δ (ppm) = 156.7 ($C_{C=O}$), 147.2 – 141.8 (m, C_{2+3}), 115.8 (t, J = 20.5 Hz, $C_{1\ or\ 4}$), 109.3 (t, J = 23.5 Hz, $C_{1\ or\ 4}$); ^{19}F {^{1}H} NMR (376 MHz, DMSO-d_6) δ (ppm) = -137.9 – -138.1 (m, 4F), -141.5 – -141.6 (m, 4F); HRMS (ASAP): *m/z* 385.0224 [MH$^+$]. Calcd. for $C_{14}H_5N_2O_2F_8^+$: 385.0223.

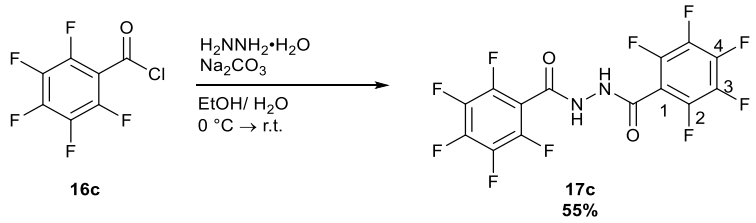

***N,N′*-Bis(pentafluorobenzoyl)hydrazide (17c).** Pentafluorobenzoyl chloride (**16c**) (5.00 g, 21.7 mmol, 2.13 eq.) was cautiously added dropwise under air to a stirred solution of hydrazine monohydrate (510 mg, 10.2 mmol, 1.00 eq.) in ethanol (10 mL), which was cooled in an ice bath to maintain the reaction temperature below 15 °C. Formation of a white precipitate was immediately observed. Once the addition was half complete, a further 20 mL of cold ethanol was added to facilitate stirring before a solution of Na_2CO_3 (1.15 g, 10.85 mmol, 1.06 eq.) in water (8 mL) was added dropwise alongside the remaining pentafluorobenzoyl chloride (**16c**). After the addition of the reagents was completed (*ca.* 20 min), the ice bath was removed and stirring was continued at room temperature for a further 30 min. The reaction mixture was poured into water (50 mL), allowed to settle for 1 h and filtered to collect the crude hydrazide as a white powder (3.58 g, 8.57 mmol, 84%). The crude material was recrystallised twice from methanol/water and was obtained sufficiently pure for use in the next step (2.36 g, 5.61 mmol, 55%). M.pt. 264–266 °C (lit. 270 °C[21]); ^{1}H NMR (400 MHz, DMSO-d_6) δ (ppm) = 11.41 (s, $2H_{N-H}$); ^{13}C NMR (101 MHz, DMSO-d_6) δ (ppm) = 156.0 ($C_{C=O}$), 145.4 – 136.0 (m, C_{2-4}), 110.5 (t, J = 21.3 Hz, C_1); ^{19}F{^{1}H} NMR (376 MHz, DMSO-d_6) δ (ppm) = -140.8 – -141.0 (m, $2F_{2\ or\ 3}$), -150.9 (t, J = 22.3 Hz, $1F_4$), -160.6 – -160.8 (m, $2F_{2\ or\ 3}$); HRMS (ASAP): *m/z* 421.0035 [MH$^+$]. Calcd. for $C_{14}H_3N_2O_2F_{10}^+$: 421.0035.

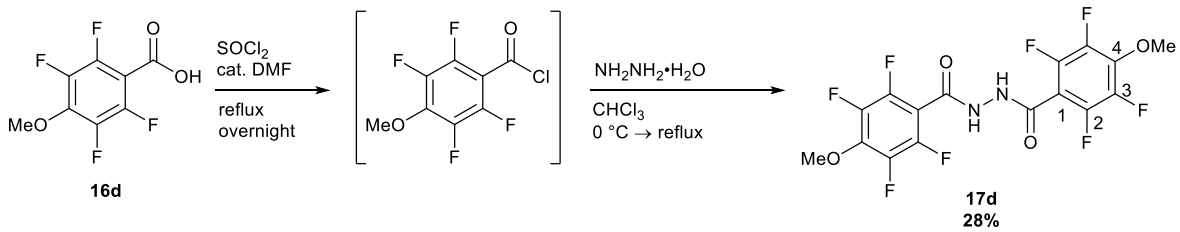

***N,N′*-Bis(2,3,5,6-tetrafluoro-4-methoxybenzoyl)hydrazide (17d).** 2,3,5,6-Tetrafluoro-4-methoxybenzoic acid (**16d**) (1.00 g, 4.46 mmol, 1.00 eq.) was heated to reflux in $SOCl_2$ (5 mL) with a drop of *N,N*-dimethylformamide overnight under argon. The solvent was then evaporated to obtain crude 2,3,5,6-tetrafluoro-4-methoxybenzoyl

chloride which was dissolved in dry chloroform (30 mL). Hydrazine monohydrate (0.1 mL, 2.09 mmol, 0.47 eq.) was added dropwise to the chloroform solution which was cooled in an ice bath to maintain the reaction temperature below 15 °C. Formation of a white precipitate was immediately observed. After the addition was completed (*ca.* 10 min), the ice bath was removed and the mixture was heated to reflux for 2 h. It was then diluted with *n*-hexane (50 mL), allowed to settle for 1 h and filtered to collect the crude hydrazide as a white powder (650 mg, 1.46 mmol, 70% based on hydrazine monohydrate). The crude material was recrystallised from ethanol and was obtained sufficiently pure for use in the next step (260 mg, 0.59 mmol, 28% based on hydrazine monohydrate). M.pt. 252–256 °C; ^{1}H NMR (400 MHz, DMSO-d_6) δ (ppm) = 11.18 (s, $2H_{N-H}$), 4.14 (s, $6H_{OMe}$); ^{13}C NMR (101 MHz, DMSO-d_6) δ (ppm) = 156.7 ($C_{C=O}$), 145.3 – 139.0 (m, C_{1-3}), 108.3 (t, J = 21 Hz, C_4), 62.8 (C_{OMe}); ^{19}F {^{1}H} NMR (376 MHz, DMSO-d_6) δ (ppm) = -142.4 – -142.5 (m, 4F), -156.9 – -157.2 (m, 4F); HRMS (ASAP): *m/z* 445.0422 [MH$^+$]. Calcd. for $C_{16}H_9N_2O_4F_8^+$: 445.0435.

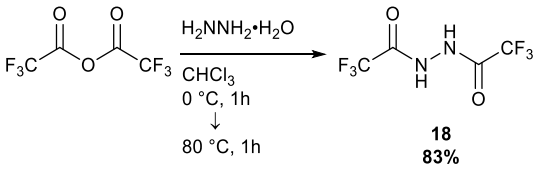

Bis(trifluoromethyl)hydrazide (18). Hydrazine monohydrate (2.5 mL, 51.5 mmol, 1.00 eq.) was added to dry chloroform (10 mL) under argon and cooled in an ice water bath to *ca.* 0 °C. Trifluoroacetic anhydride (21.8 mL, 155 mmol, 3.00 eq.) was then cautiously added to the mixture over the course of 1 h. A white precipitate immediately formed during the addition. Once approximately half had been added, further dry chloroform (10 mL) was added to facilitate stirring. Once the addition was complete, the mixture was refluxed under argon for 1 h, before being cooled to room temperature and filtered. The white precipitate was washed with hexane (*ca.* 50 mL) to obtain bis(trifluoromethyl)hydrazide (**18**) as a white powder (9.6 g, 43 mmol, 83%). Analytical data were in agreement with those previously reported.[22] ^{1}H NMR (400 MHz, Acetone-d_6) δ (ppm) = 10.00 – 11.00 (bs, 2H); ^{19}F {^{1}H} NMR (376 MHz, Acetone-d_6) δ (ppm) = -75.82 (s, 6F).

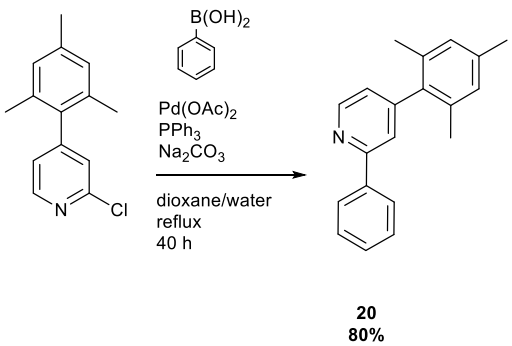

2-Phenyl-4-(2,4,6-trimethylphenyl)pyridine (20). 4-(2,4,6-Trimethylphenyl)-2-chloropyridine (3.36 g, 14.5 mmol, 1.00 eq.), phenyl boronic acid (2.65 g, 21.7 mmol, 1.50 eq.) and PPh_3 (912 mg, 3.48 mmol, 24 mol%) were combined in 1,4-dioxane (45 mL). A solution of Na_2CO_3 (6.14 g, 57.9 mmol, 4.00 eq.) in water (10 mL) was then added and the mixture was degassed for 30 min. $Pd(OAc)_2$ (195 mg, 0.87 mmol, 6 mol%) was then added and the mixture was degassed for a further 10 minutes, before being heated to reflux under argon overnight. The mixture was then allowed to cool to room temperature and evaporated to near-dryness. To the residue was added water (50 mL) and DCM (50 mL). The organic layer was separated and the aqueous later was extracted thrice more with DCM (50 mL). The organic extracts were combined, dried over $MgSO_4$ and evaporated under reduced pressure. The residue was passed through a short column of silica gel (eluent: EtOAc with *ca.* 0.5%

vol. NEt_3 as an additive) before being purified by distillation on a Kugelrohr apparatus (200 °C, *ca.* 9 × 10^{-2} mbar) to afford 2-phenyl-4-(2,4,6-trimethylphenyl)pyridine (**20**) as a faint yellow viscous oil (3.15 g, 11,52 mmol, 80%). Analytical data were in agreement with those previously reported.[23] ^{1}H NMR (400 MHz, $CDCl_3$) δ (ppm) = 8.77 (dd, *J* = 5.0, 0.9 Hz, 1H), 8.09 – 8.01 (m, 2H), 7.60 (dd, *J* = 1.5, 0.9 Hz, 1H), 7.55 – 7.43 (m, 3H), 7.09 (dd, *J* = 4.9, 1.5 Hz, 1H), 7.01 (d, *J* = 0.7 Hz, 2H), 2.38 (s, 3H), 2.08 (s, 6H).

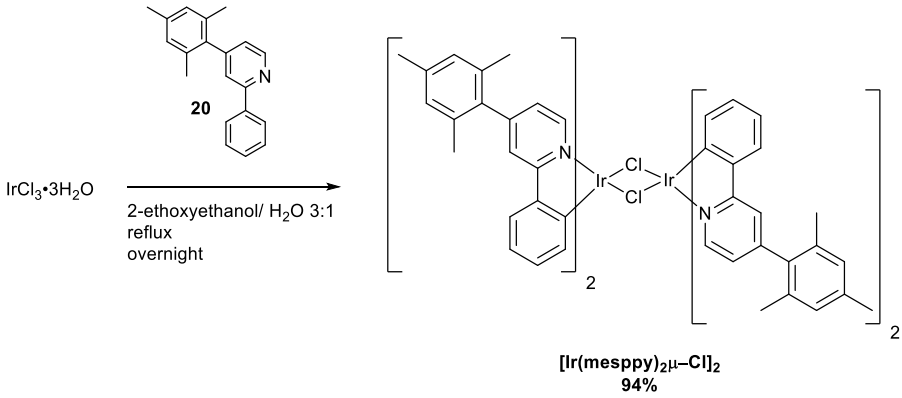

Tetrakis(2-phenyl-4-(2,4,6-trimethylphenyl)-pyridine-*C*^{2},*N*')(μ-dichloro)diiridium ([Ir(mesppy)$_2$μ-Cl]$_2$). $IrCl_3 \cdot 3H_2O$ (689 mg, 1.95 mmol, 1.00 eq.) and 2-phenyl-4(2,4,6-trimethylphenyl)-pyridine (**20**) (1.18 g, 4.32 mmol, 2.21 eq.) were added to a mixture of 2-ethoxyethanol (30 mL) and water (10 mL) and heated to reflux under an argon atmosphere for 24 h. The reaction mixture was then cooled to room temperature and poured into water (*ca.* 200 mL) and cooled in a fridge for 1 h. The formed yellow precipitate was then isolated via filtration and washed sequentially with water (*ca.* 50 mL), cold methanol (5 mL), cold *n*-hexane (3 × 20 mL) and cold *n*-pentane (3 × 20 mL) to afford tetrakis(2-phenyl-4-(2,4,6-trimethylphenyl)-pyridine-*C*^{2},*N*')(μ-dichloro)diiridium (**[Ir(mesppy)$_2$μ-Cl]$_2$).** as a yellow powder (1.42 g, 0.92 mmol, 94%). Analytical data were in agreement with those previously reported.[23] ^{1}H NMR (400 MHz, CD_2Cl_2) δ (ppm) = 9.70 (d, *J* = 5.9 Hz, 2H), 7.77 (d, *J* = 1.9 Hz, 2H), 7.54 (dd, *J* = 7.8, 1.4 Hz, 2H), 7.05 (d, *J* = 10.9 Hz, 4H), 6.89 – 6.82 (m, 4H), 6.71 (td, *J* = 7.5, 1.4 Hz, 2H), 5.95 (dd, *J* = 7.9, 1.1 Hz, 2H), 2.42 (s, 6H), 2.16 (s, 6H), 2.15 (s, 6H).

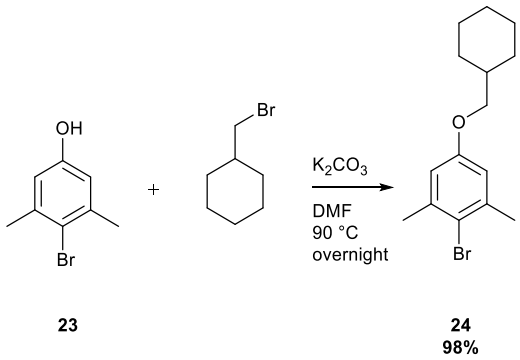

2-Bromo-5-(methylcyclohexyloxy)-*meta*-xylene (24). 2-Bromo-4-hydroxy-*meta*-xylene (**23**) (15.00 g, 74.6 mmol, 1.00 eq.) and K_2CO_3 (20.6 g, 149 mmol mmol, 2.00 eq.) were combined in *N*,*N*-dimethylformamide (100 mL) and heated to 80 °C for 10 min under argon. Bromo(methylcyclohexane) (15.6 mL, 112 mmol, 1.50 eq.) was then added in a single portion and the mixture was heated to 90 °C overnight. The reaction mixture was cooled to room temperature and poured into water (1 L). The mixture was extracted with EtOAc/ toluene 1:1 v/v (3 × 200 mL). The organic layers were combined and washed with HCl $_{(aq)}$ (1 M, 5 × 50 mL) before being dried over $MgSO_4$ and evaporated under reduced pressure to afford a brown oil. The residue was purified via flash chromatography on silica

gel (eluent: *n*-hexane). 2-Bromo-5-(methylcyclohexyloxy)-*meta*-xylene (**24**) eluted as a clear oil (21.7 g, 73.0 mmol, 98%). ^{1}H NMR (400 MHz, $CDCl_3$) δ (ppm) = 6.66 (s, 2H), 3.72 (d, *J* = 6.4 Hz, 2H), 2.40 (S, 6H), 1.93 – 1.67 (m, 6H), 1.39 – 1.17 (m, 3H), 1.05 (qd, *J* = 12.2, 3.4 Hz, 2H); ^{13}C NMR (101 MHz, $CDCl_3$) δ (ppm) = 157.8, 139.0, 117.9, 114.4, 73.6, 37.7, 29.9, 26.5, 25.8, 24.0; HRMS (ASAP): *m/z* 296.0779 [M^+]. Calcd. for $C_{15}H_{21}OBr^+$: 296.0776.

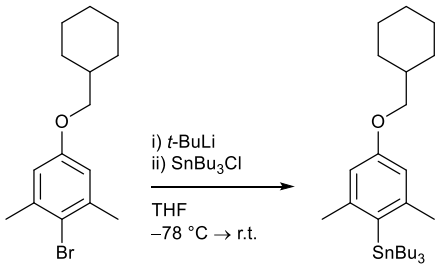

24 **25**

2-Tributylstannyl-5-(methylcyclohexyloxy)-*meta*-xylene (25). 2-Bromo-5-(methylcyclohexyloxy)-*meta*-xylene (**24**) (10.5 g, 33.6 mmol, 1.00 eq.) was dissolved in dry THF (250 mL) and cooled to –78 °C under argon. *t*-BuLi (1.7 M in pentane, 27 mL, 74.8 mmol, 2.22 eq.) was then added over 15 min, keeping the reaction temperature below –65 °C. The thick yellow mixture was then stirred at –78 °C for 45 min before the addition of tributyltin chloride (11.2 mL, 41.2 mmol, 1.23 eq.) over 5 min. The reaction was then warmed to room temperature overnight before being poured into hexane (200 mL). The mixture was washed with sat. $NH_4Cl_{(aq)}$ (3 × 50 mL) before being dried over $MgSO_4$, and the solvent removed under reduced pressure to afford 2-tributylstannyl-5-(methylcyclohexyloxy)-*meta*-xylene (**25**) as a pale yellow oil (17.0 g, 33.5 mmol, 100%) which was used without further purification. ^{1}H NMR (400 MHz, $CDCl_3$) δ (ppm) = 6.59 (s + (d, $^4J_{H–Sn}$ = 11.7 Hz), 2H), 3.74 (d, *J* = 6.3 Hz, 2H), 2.38 (s + (d, $^4J_{H–Sn}$ = 5.5 Hz), 6H), the aliphatic region (*ca*. 0.5–2 ppm) was not assigned due to the presence of alkyl tin impurities; HRMS (ASAP): *m/z* 505.2808 [MH^+]. Calcd. for $C_{27}H_{49}O^{116}Sn^+$: 505.2801.

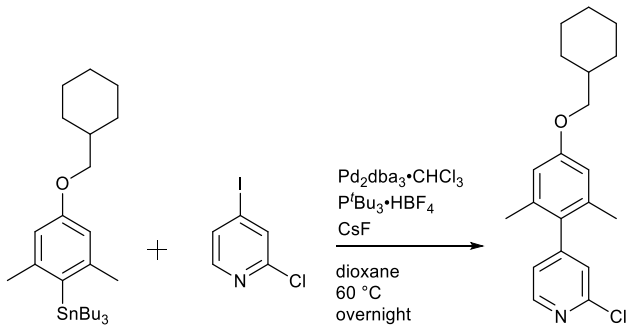

25 **26**
72%

2-Chloro-4-(2,6-dimethyl-4-(methylcyclohexyloxy)phenyl)pyridine (26). 2-Chloro-4-iodopyridine (3.00 g, 12.5 mmol, 1.00 eq.), 2-tributylstannyl-5-(methylcyclohexyloxy)-*meta*-xylene (**25**) (8.74 g, 17.2 mmol, 1.38 eq.) and tri-*tert*-butylphosphonium tetrafluoroborate (218 mg, 0.75 mmol, 6 mol%) were added to dry dioxane (50 mL) and the resulting mixture was degassed for 40 min. Pd_2dba_3•$CHCl_3$ (388 mg, 0.37 mmol, 3 mol%) was then added to the mixture, which was degassed for a further 10 min before the addition of CsF (4.18 g, 27.5 mmol, 2.20 eq.). The red

reaction mixture was subsequently stirred at room temperature for 2.5 h. Analysis of an aliquot by GC-MS at this point indicated that the desired reaction had not occurred. Further Pd_2dba_3•$CHCl_3$ (130 mg, 0.12 mmol, 1 mol%) and tri-*tert*-butylphosphonium tetrafluoroborate (73 mg, 0.25 mmol, 2 mol%) were added and the mixture was heated to 60 °C for 17 h, after which point analysis of an aliquot by GC-MS revealed complete consumption of 2-chloro-4-iodopyridine. The reaction mixture was cooled to room temperature, diluted with EtOAc (*ca.* 50 mL) and filtered through a plug of celite, which was subsequently washed with further EtOAc (2 × 50 mL). The combined filtrates were evaporated under reduced pressure and the residual crude product was purified via flash chromatography on silica gel (eluent: gradient EtOAc/ *n*-hexane 0:1–1:9 v/v with *ca.* 0.5% vol. NEt_3 as an additive) to obtain 2-chloro-4-(2,6-dimethyl-4-(methylcyclohexyloxy)phenyl)pyridine (**26**) as a brown oil (3.67 g, 11.1 mmol, 89%). Further purification by distillation on a Kugelrohr apparatus (*ca.* 110 °C, 0.1 mbar) afforded a colourless viscous oil which solidified upon standing (2.96 g, 8.97 mmol, 72%). M.pt. 72–75 °C; ^{1}H NMR (400 MHz, $CDCl_3$) δ (ppm) = 8.45 (dd, *J* = 5.0, 0.8 Hz, 1H), 7.18 (dd, *J* = 1.5, 0.7 Hz, 1H), 7.06 (dd, *J* = 5.0, 1.4 Hz, 1H), 6.68 (s, 2H), 3.78 (d, *J* = 6.4 Hz, 2H), 1.93 – 1.70 (m, 6H), 1.41 – 1.19 (m, 3H), 1.15 – 1.02 (m, 2H); ^{13}C NMR (101 MHz, $CDCl_3$) δ (ppm) = 159.0, 152.8, 151.8, 149.7, 136.5, 125.5, 124.1, 113.6, 73.4, 37.8, 29.9, 26.6, 25.8, 20.9; HRMS (ESI): *m/z* 330.1628 [MH^+]. Calcd. for $C_{20}H_{25}NOCl^+$: 330.1625.

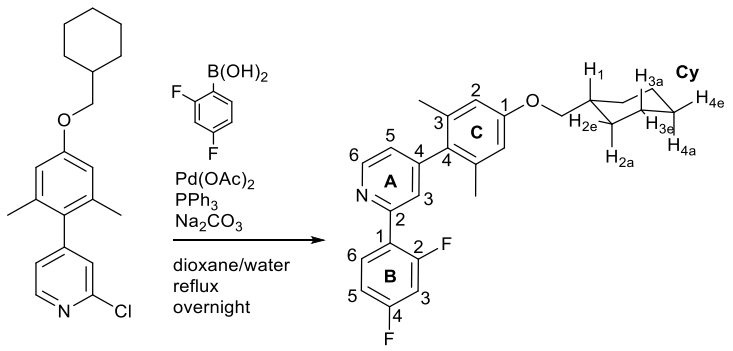

2-(2,4-Difluorophenyl)-4-(2,6-dimethyl-4-(methylcyclohexyloxy)phenyl)pyridine (21). 2-Chloro-4-(2,6-dimethyl-4-(methylcyclohexyloxy)phenyl)pyridine (**26**) (617 g, 1.87 mmol, 1.00 eq.), 2,4-difluorophenyl boronic acid (443 mg, 2.81 mmol, 1.50 eq.) and PPh_3 (20.5 mg, 0.45 mmol, 24 mol%) were combined in 1,4-dioxane (6 mL). A solution of Na_2CO_3 (795 mg, 7.48 mmol, 4.00 eq.) in water (2 mL) was then added and the mixture was degassed for 15 min. $Pd(OAc)_2$ (20.5 mg, 0.11 mmol, 6 mol%) was then added and the mixture was degassed for a further 5 minutes, before being heated to reflux under argon overnight. The mixture was then allowed to cool to room temperature and evaporated to near-dryness. To the residue was added water (30 mL) and DCM (40 mL). The organic layer was separated and the aqueous later was extracted twice more with DCM (40 mL). The organic extracts were combined, dried over $MgSO_4$ and evaporated under reduced pressure. The residue was purified by flash chromatography on silica gel (eluent: gradient EtOAc/ *n*- hexane 1:99–1:9 v/v with *ca.* 0.5% vol. NEt_3 as an additive). 2-(2,4-Difluorophenyl)-4-(2,6-dimethyl-4-(methylcyclohexyloxy)phenyl)pyridine (**21**) was obtained as a white tacky solid (678g, 1.66 mmol, 90%). M.pt. 117–118 °C; ^{1}H NMR (600 MHz, $CDCl_3$) δ (ppm) = 8.74 (dd, *J* = 5.0, 0.9 Hz, $1H_{A6}$), 8.07 (td, *J* = 8.8, 6.6 Hz, $1H_{B6}$), 7.57 (dd, *J* = 1.5, 0.9 Hz, $1H_{A3}$), 7.07 (dd, *J* = 5.0, 1.5 Hz, $1H_{A5}$), 7.02 (dddd, *J* = 8.8, 7.9, 2.6, 1.4 Hz, $1H_{B5}$), 6.90 (ddd, *J* = 11.3, 8.8, 2.6 Hz, $1H_{B3}$), 6.68 (s, $2H_{C2}$), 3.77 (d, *J* = 6.4 Hz, $2H_{CH2Cy}$), 2.06 (s, $6H_{CMe}$), 1.92 – 1.85 (m, $2H_{CyH2e}$), 1.85 – 1.81 (m, $1H_{CyH1}$), 1.77 (dt, *J* = 13.0, 3.4 Hz, $2H_{CyH3e}$), 1.74 – 1.68 (m, $1H_{CyH4e}$), 1.32 (qt, *J* = 12.6, 3.4 Hz, $2H_{CyH3a}$), 1.22 (qt, *J* = 12.7, 3.4 Hz, $1H_{CyH4a}$), 1.07 (qd, *J* = 12.4, 3.5 Hz,

2H_{CyH2a}); ^{13}C NMR (151 MHz, $CDCl_3$) δ (ppm) = 163.2 (dd, *J* = 250.9, 12.0 Hz, C_{B4}), 160.6 (dd, *J* = 252.8, 12.0 Hz, C_{B2}), 158.7 (C_{C1}), 152.6 (d, *J* = 2.6 Hz, C_{A2}), 149.9 (C_{A4}), 149.8 (C_{A6}), 136.7 (C_{C3}), 132.2 (dd, *J* = 9.7, 4.4 Hz, C_{B6}), 131.4 (C_{C4}), 125.7 (d, *J* = 9.4 Hz, C_{A3}), 123.9 (C_{A5}), 123.9 (dd, *J* = 12.0, 3,9 Hz, C_{B1}), 113.5 (C_{C2}), 111.9 (dd, *J* = 21.1, 3.6 Hz, C_{B5}), 104.4 (dd, *J* = 27.0, 25.3 Hz, C_{B3}), 73.4 (C_{CH2}), 37.7 (C_{Cy1}), 29.9 (C_{Cy2}), 26.5 (C_{Cy4}), 25.8 (C_{Cy3}), 21.0 (C_{Me}); ^{19}F {^{1}H} NMR (376 MHz, $CDCl_3$) δ (ppm) = -109.2 – -109.5 (m, 1F), -112.7 – - 112.8 (m, 1F); HRMS (ESI): *m/z* 408.2128 [MH^+]. Calcd. for $C_{26}H_{28}NOF_2^+$: 408.2139.

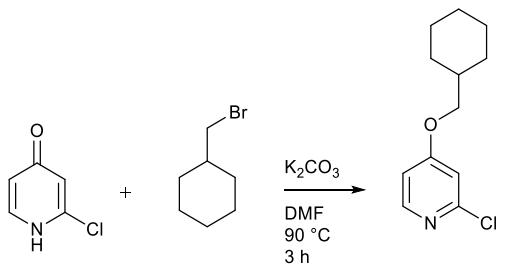

27 **28**
87%

4-(Methylcyclohexyloxy)-2-chloropyridine (28). 2-Chloro-4-pyridone (**27**) (5.00 g, 38.6 mmol, 1.00 eq.) and K_2CO_3 (10.7 g, 77.2 mmol, 2.00 eq.) were combined in *N,N*-dimethylformamide (50 mL) and heated to 80 °C for 10 min under argon. Bromo(methylcyclohexane) (8.1 mL, 57.9 mmol, 1.50 eq.) was then added in a single portion and the mixture was heated to 90 °C for a further 4 h. The reaction mixture was cooled to room temperature and poured into water (200 mL). The mixture was extracted with EtOAc/ toluene 1:1 v/v (4 × 100 mL). The organic layers were combined and washed with HCl $_{(aq)}$ (1 M, 5 × 50 mL) before being dried over $MgSO_4$ and evaporated under reduced pressure to afford a brown oil. The residue was purified via flash chromatography on silica gel (eluent: EtOAc/ *n*-hexane 3:7 v/v) to obtain 4-(methylcyclohexyloxy)-2-chloropyridine (**28**) as a waxy white solid (7.55 g, 33.4 mmol, 87%). M.pt. 54–55 °C; ^{1}H NMR (400 MHz, $CDCl_3$) δ (ppm) = 8.19 (d, *J* = 5.8 Hz, 1H), 6.84 (d, *J* = 2.2 Hz, 1H), 6.75 (dd, *J* = 5.8, 2.3 Hz, 1H), 3.81 (d, *J* = 6.1 Hz, 2H), 1.93 – 1.59 (m, 6H), 1.40 – 1.15 (m, 3H), 1.14 – 0.99 (m, 2H); ^{13}C NMR (101 MHz, $CDCl_3$) δ (ppm) = 167.0, 152.5, 150.1, 110.1, 109.9, 73.9, 37.3, 29.7, 26.3, 25.7; HRMS (ESI): *m/z* 226.1001 [MH^+]. Calcd. for $C_{12}H_{17}NOCl^+$: 226.0999.

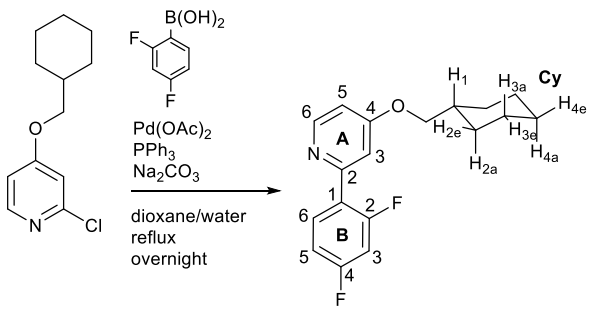

28 **22**
100%

2-(2,4-Difluorophenyl)-4-(methylcyclohexyloxy)pyridine (22). 4-(Methylcyclohexyloxy)-2-chloropyridine (**28**) (2.00 g, 8.86 mmol, 1.00 eq.), 2,4-difluorophenyl boronic acid (2.10 g, 13.29 mmol, 1.50 eq.) and PPh_3 (558 mg, 2.13 mmol, 24 mol%) were combined in 1,4-dioxane (32 mL). A solution of Na_2CO_3 (3.76 g, 35.4 mmol, 4.00 eq.) in

water (12 mL) was then added and the mixture was degassed for 30 min. $Pd(OAc)_2$ (120 mg, 0.53 mmol, 6 mol%) was then added and the mixture was degassed for a further 10 min, before being heated to reflux under argon overnight. The mixture was then allowed to cool to room temperature and evaporated to near-dryness. To the residue was added water (50 mL) and DCM (50 mL). The organic layer was separated and the aqueous later was extracted twice more with DCM (50 mL). The organic extracts were combined, dried over $MgSO_4$ and evaporated under reduced pressure. The residue was purified by flash chromatography on silica gel (eluent: EtOAc/ *n*- hexane 4:6 v/v with *ca.* 0.5% vol. NEt_3 as an additive). 2-(2,4-Difluorophenyl)-4-(methylcyclohexyloxy)pyridine (**22)** was obtained as a faint yellow oil which solidified on standing (2.68 g, 8.83 mmol, 100%). M.pt. 66–68 °C; ^{1}H NMR (600 MHz, $CDCl_3$) δ (ppm) = 8.49 (d, *J* = 5.7 Hz, $1H_{A6}$), 7.97 (td, *J* = 8.8, 6.6 Hz, $1H_{B6}$), 7.24 (ap. t, *J* = 2.4 Hz, $1H_{A3}$), 6.98 (tdd, *J* = 7.8, 2.5, 1.0 Hz, $1H_{B5}$), 6.90 (ddd, *J* = 11.3, 8.8, 2.5 Hz, $1H_{B3}$), 6.77 (dd, *J* = 5.7, 2.4 Hz, $1H_{A5}$), 3.84 (d, *J* = 6.3 Hz, $2H_{CH2Cy}$), 1.89 – 1.85 (m, $2H_{CyH2e}$), 1.84 – 1.81 (m, $1H_{CyH1}$), 1.78 (dt, *J* = 12.9, 3.4 Hz, $2H_{CyH3e}$), 1.73 – 1.69 (m, $1H_{CyH4e}$), 1.31 (qt, *J* = 12.7, 3.4 Hz, $2H_{CyH3a}$), 1.21 (qt, *J* = 12.8, 3.4 Hz, $1H_{CyH4a}$), 1.07 (qd, *J* = 12.7, 3.6 Hz, $2H_{CyH2a}$); ^{13}C NMR (151 MHz, $CDCl_3$) δ (ppm) = 165.7 (C_{A4}), 163.08 (dd, *J* = 250.7, 12.1 Hz, C_{B4}), 160.45 (dd, *J* = 252.4, 11.9 Hz, C_{B2}), 153.9 (d, *J* = 2.4 Hz, C_{A2}), 150.7 (C_{A6}), 132.1 (dd, *J* = 9.6, 4.5 Hz, C_{B6}), 123.9 (dd, *J* = 11.6, 3.8 Hz, C_{B1}), 111.7 (dd, *J* = 21.0, 3.7 Hz, C_{B5}), 110.9 (d, *J* = 9.1 Hz, C_{A3}), 109.0 (C_{A5}), 104.3 (dd, *J* = 27.1, 25.3 Hz, C_{B3}), 73.4 (C_{CH2}), 37.4 (C_{Cy1}), 29.8 (C_{Cy2}), 26.4 (C_{Cy4}), 25.7 (C_{Cy3}); ^{19}F{^{1}H} NMR (376 MHz, $CDCl_3$) δ (ppm) = -109.4 (d, *J* = 8.5 Hz, 1F), -112.7 (d, *J* = 8.5 Hz, 1F); HRMS (ESI): *m/z* 304.1517 [MH^+]. Calcd. for $C_{18}H_{20}NOF_2^+$: 304.1513.

Copies of NMR Spectra

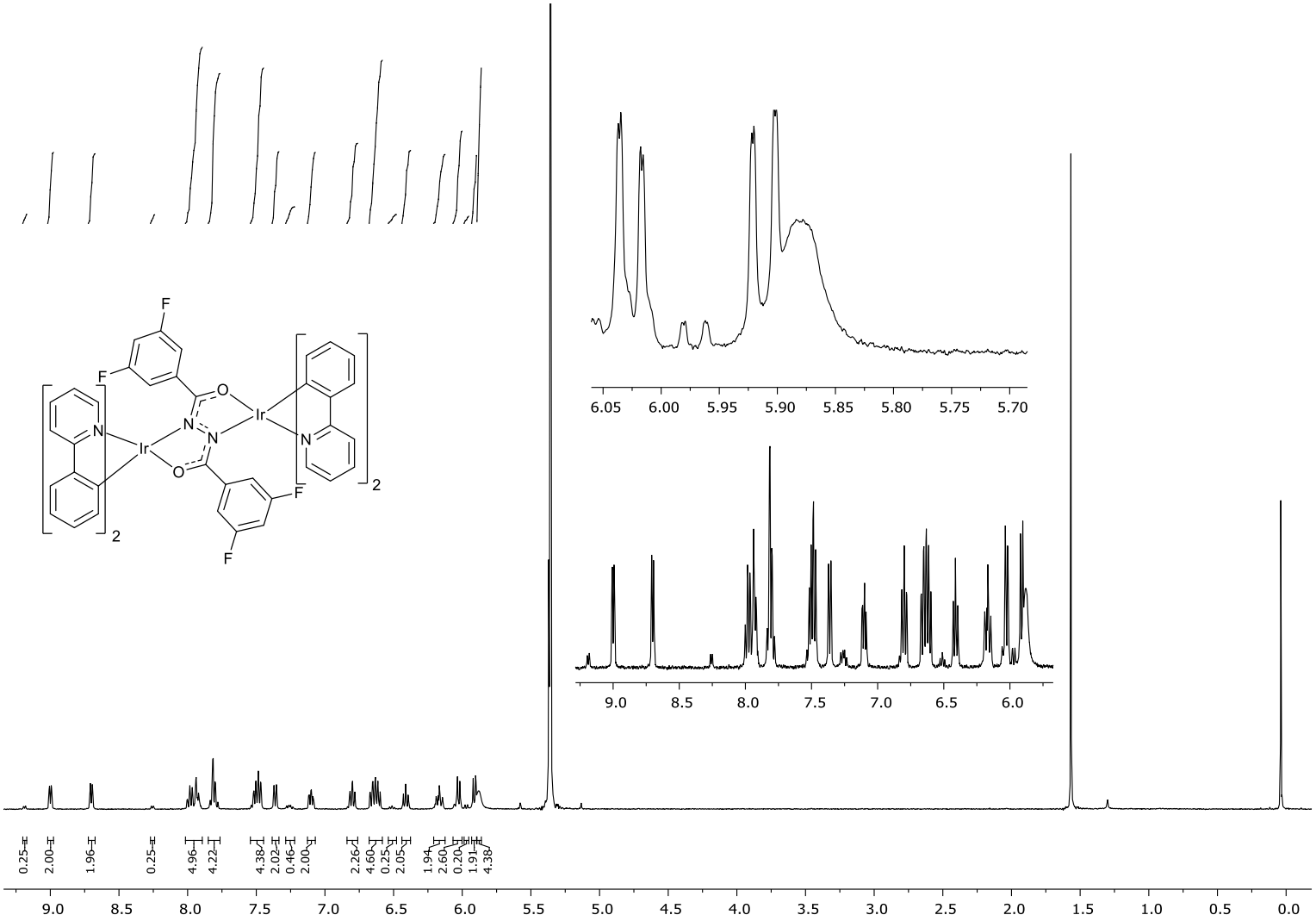

Figure S1. ^{1}H NMR spectrum (600 MHz) of **7** in CD_2Cl_2 (TMS).

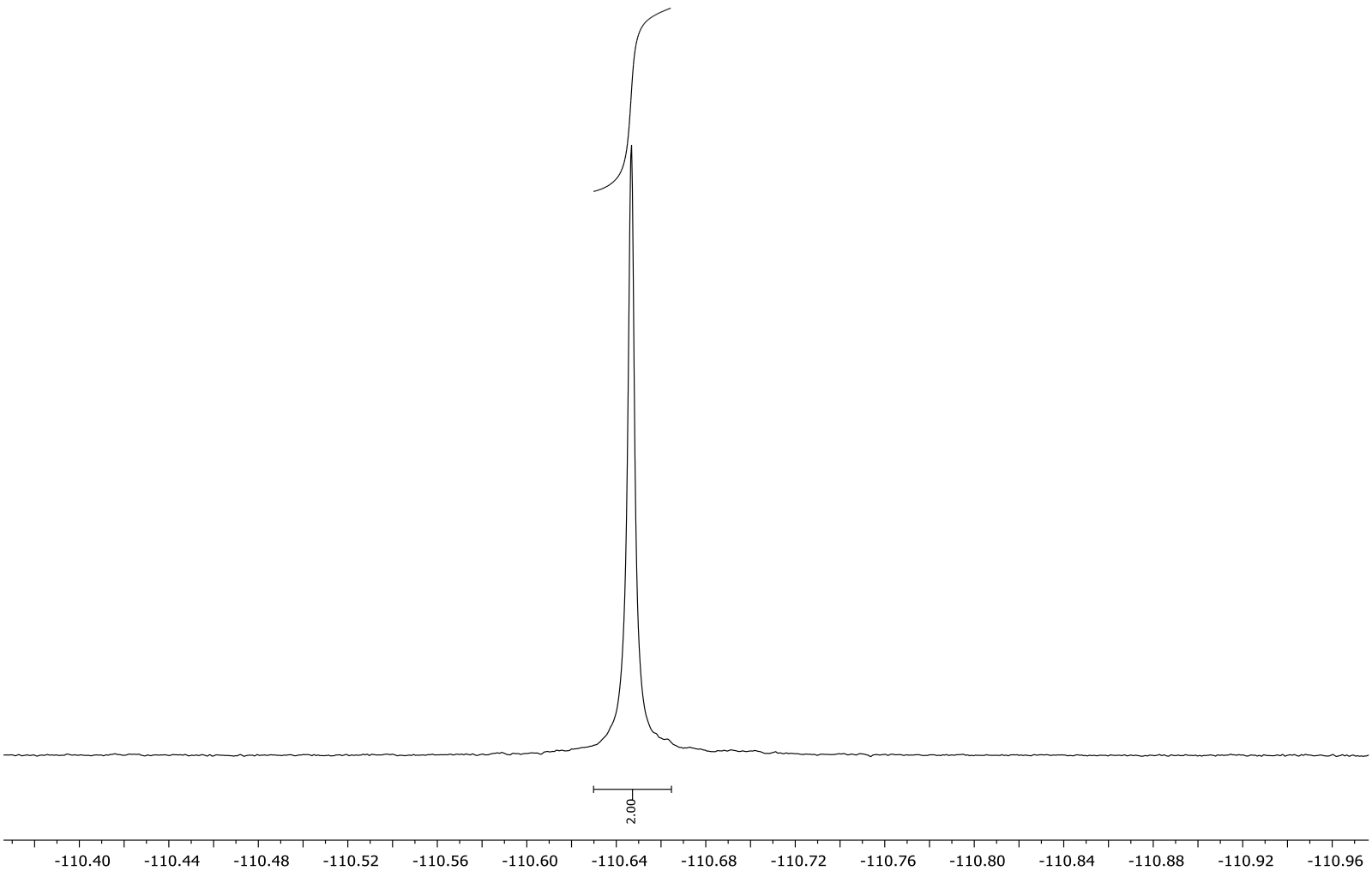

Figure S2. $^{19}F\{^{1}H\}$ NMR spectrum (376 MHz) of **7** in CD_2Cl_2.

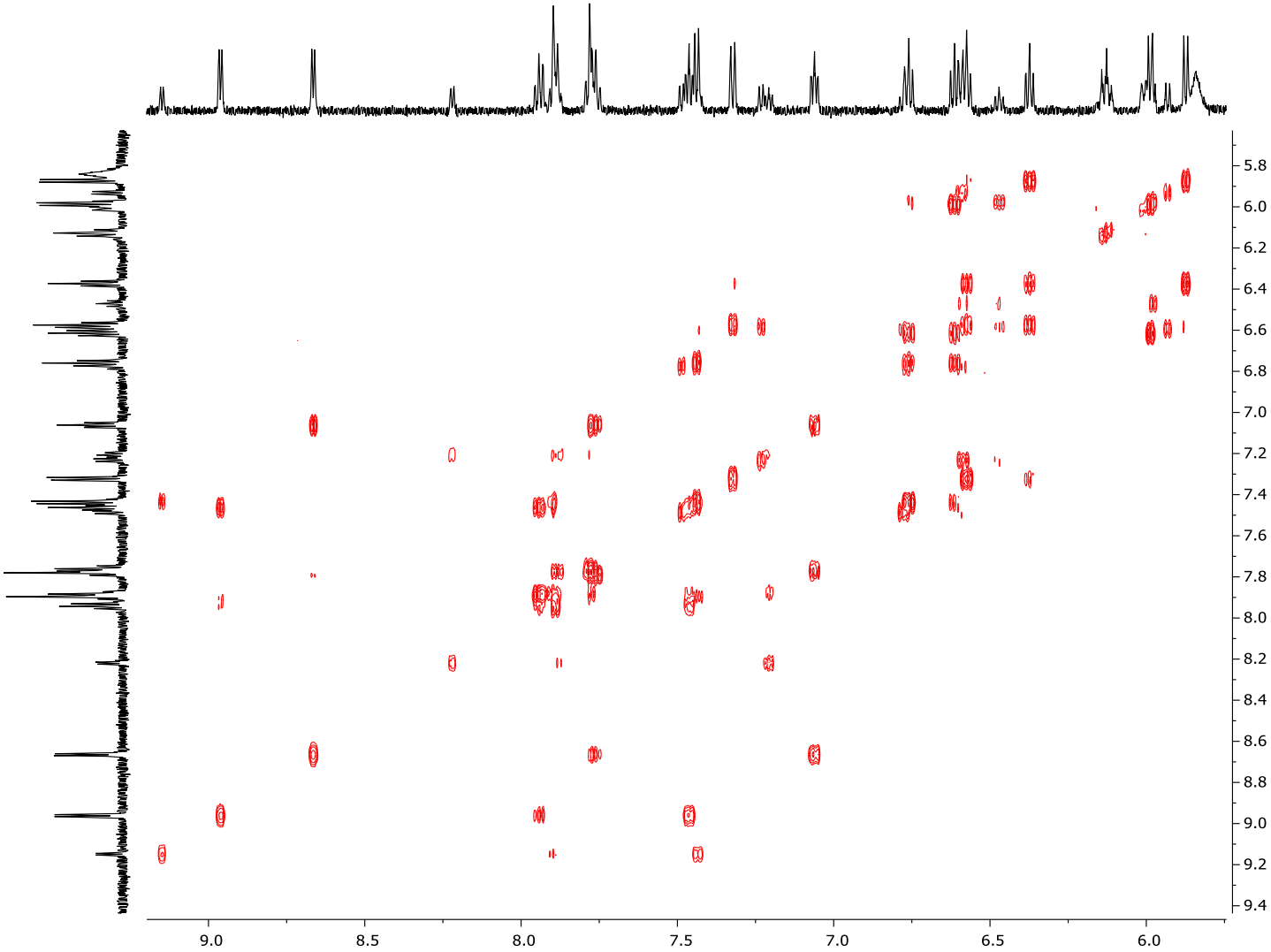

Figure S3. Expansion of the aromatic region of the ^{1}H–^{1}H COSY NMR spectrum of **7** in CD_2Cl_2 (TMS).

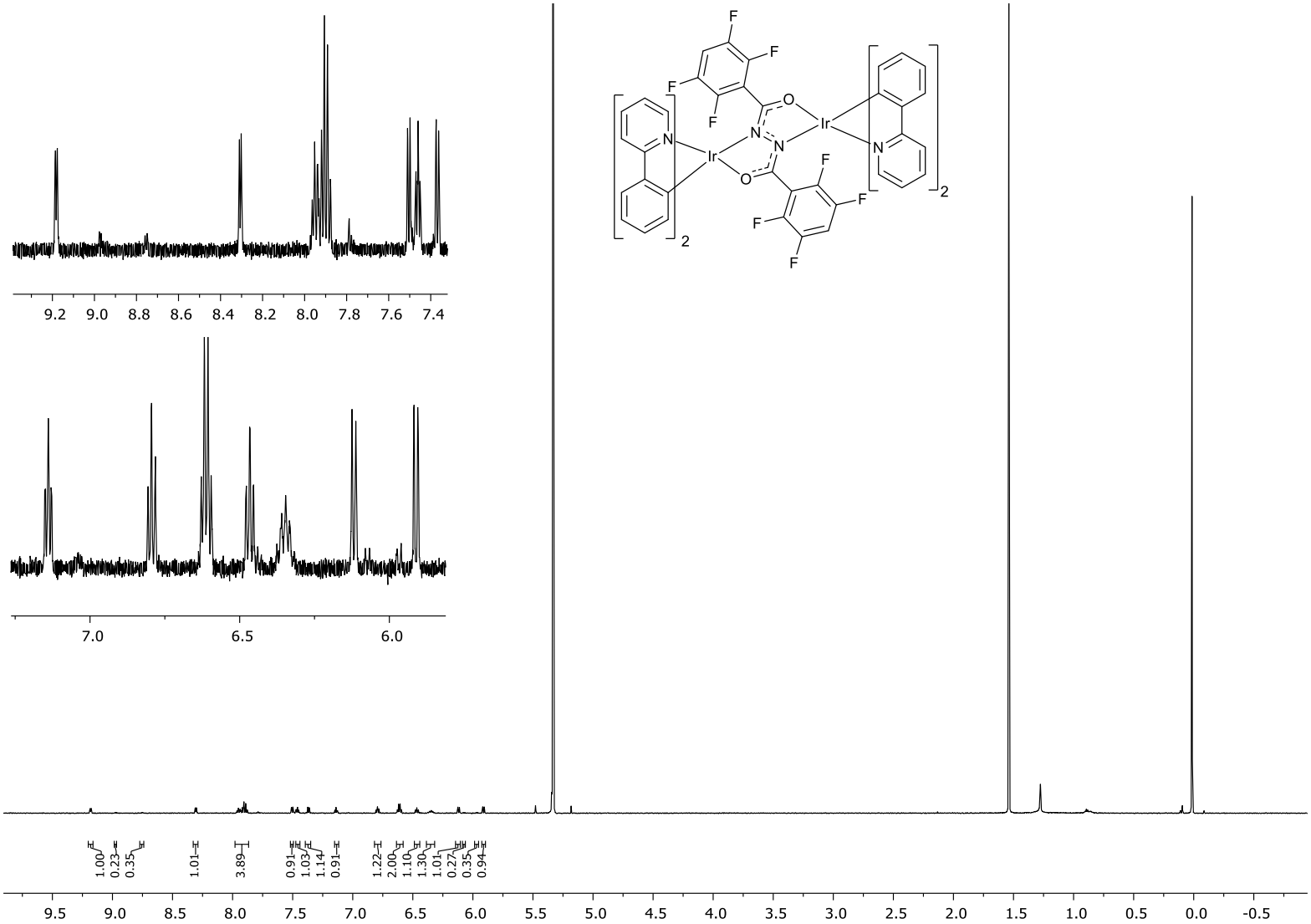

Figure S4. ^{1}H NMR spectrum (600 MHz) of **8** in CD_2Cl_2 (TMS).

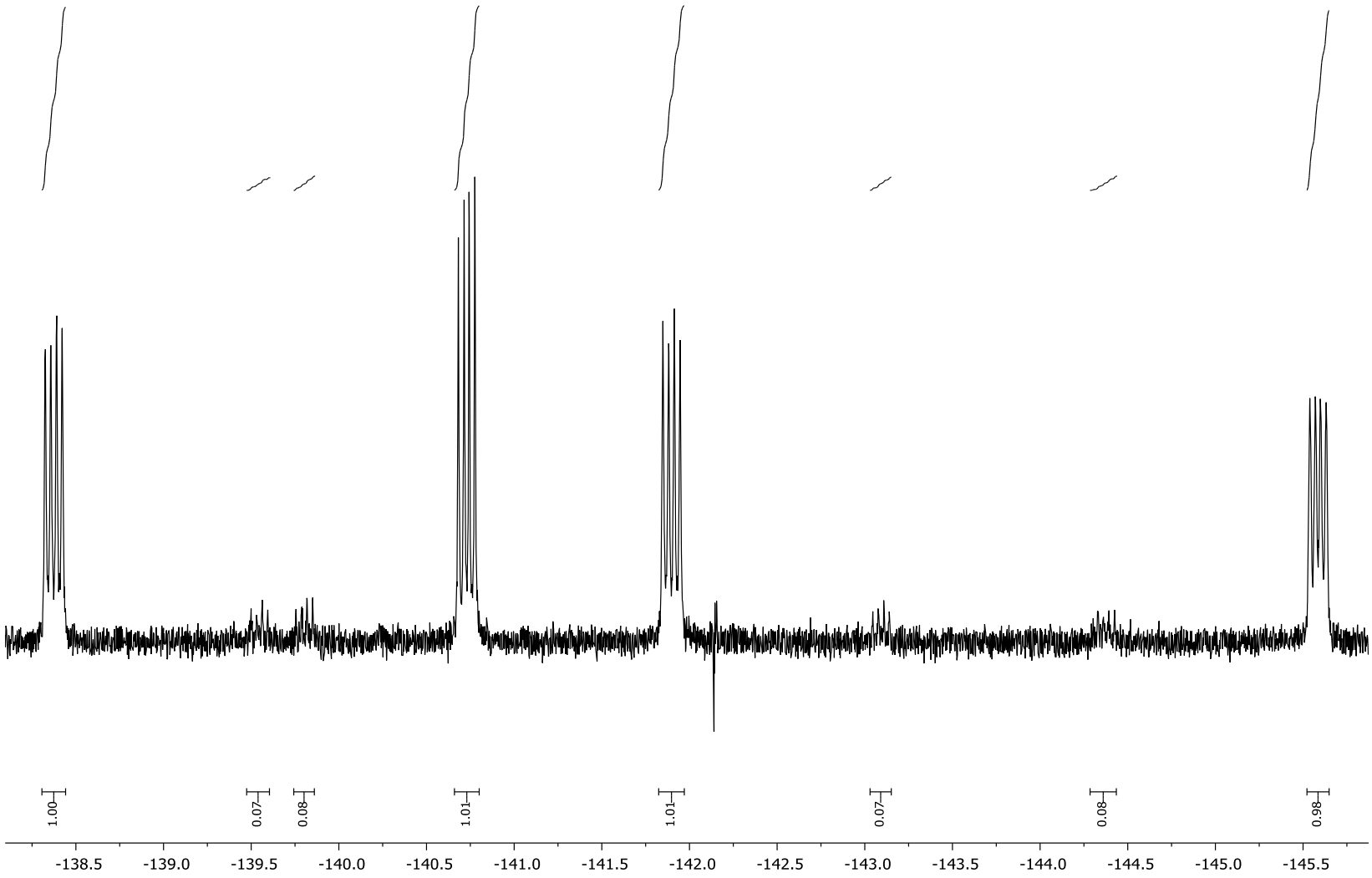

Figure S5. $^{19}F\{^{1}H\}$ NMR spectrum (376 MHz) of **8** in CD_2Cl_2.

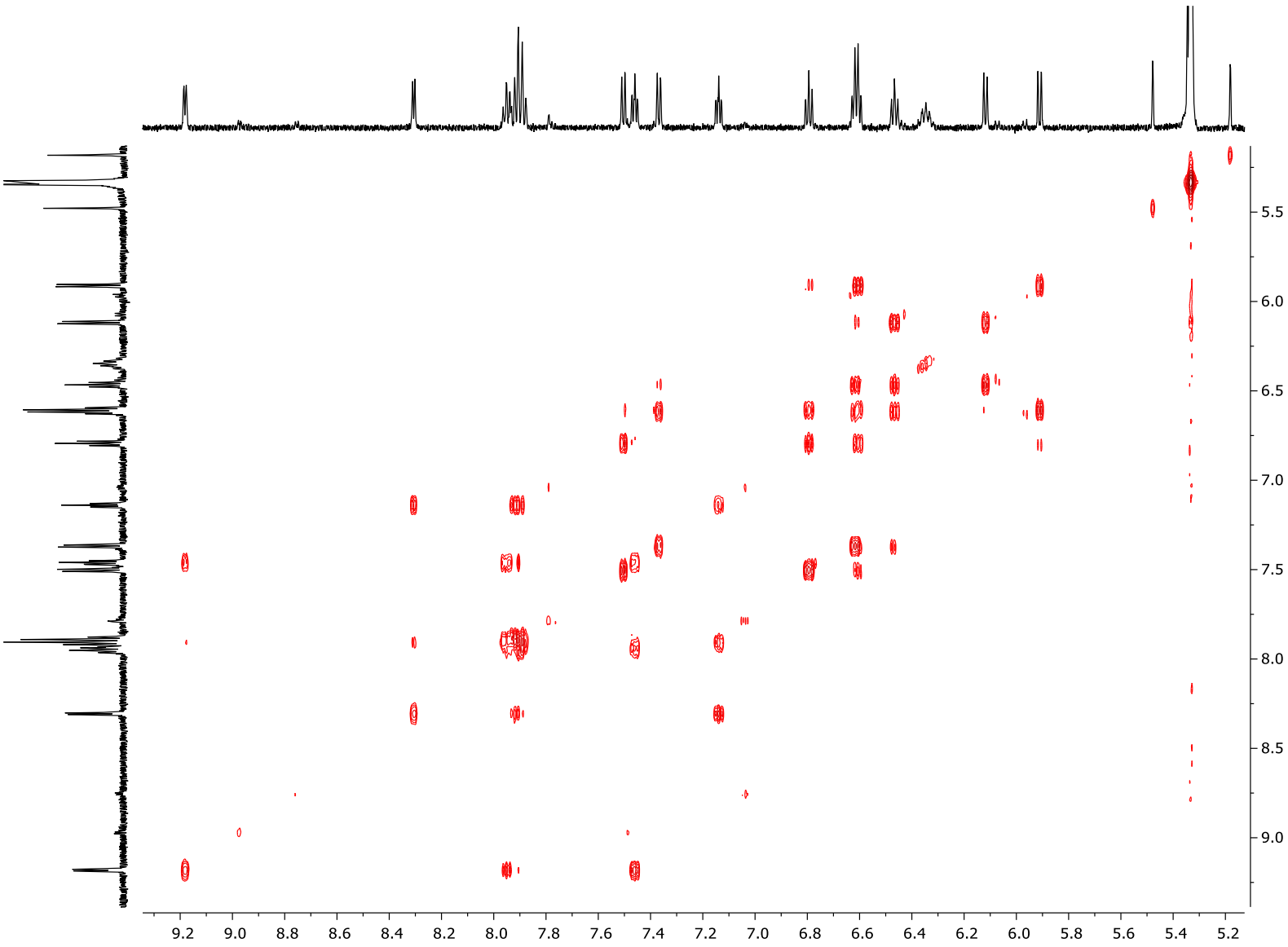

Figure S6. Expansion of the aromatic region of the ^{1}H–^{1}H COSY NMR spectrum of **8** in CD_2Cl_2 (TMS).

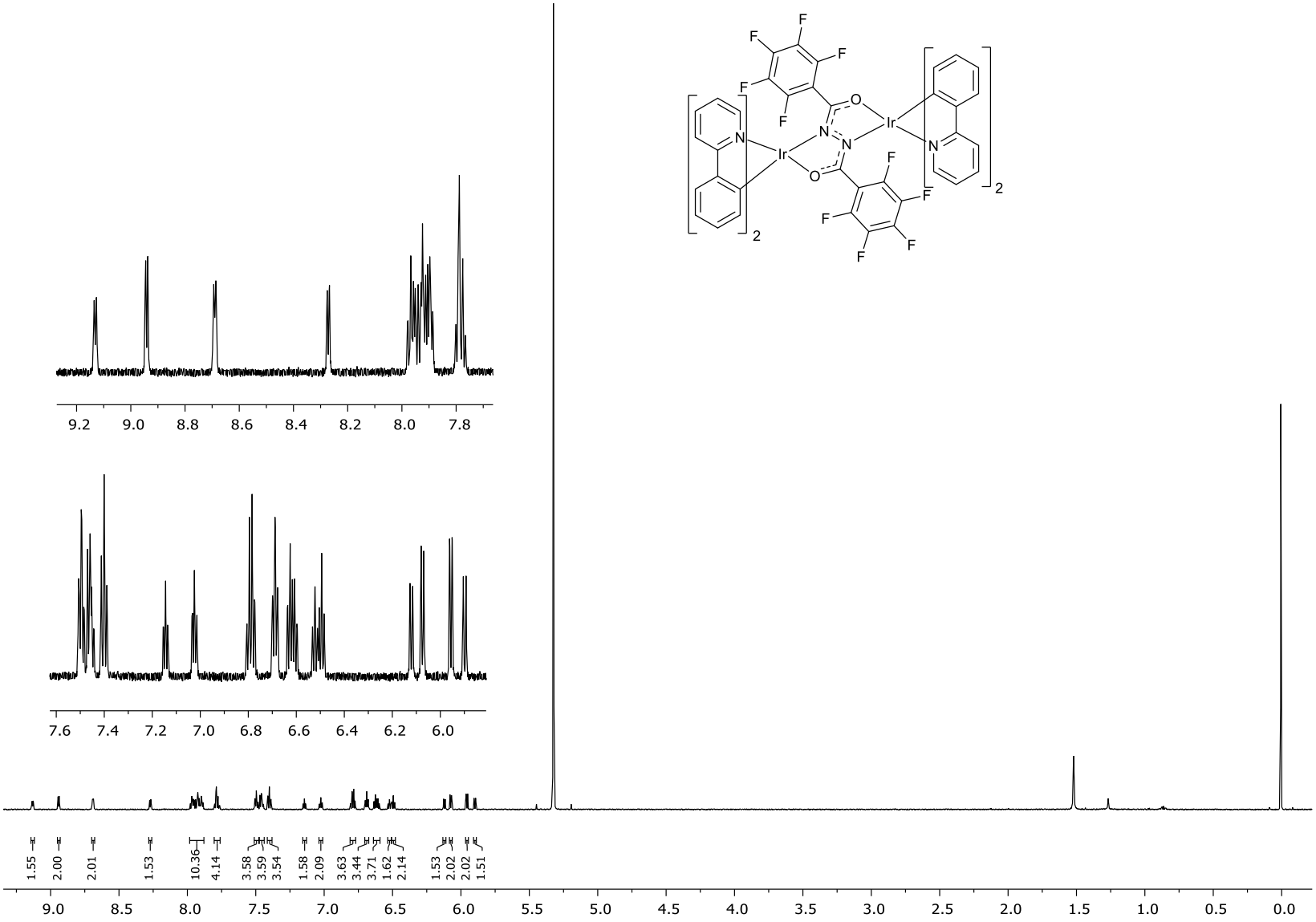

Figure S7. ^{1}H NMR spectrum (700 MHz) of **9** in CD_2Cl_2 (TMS).

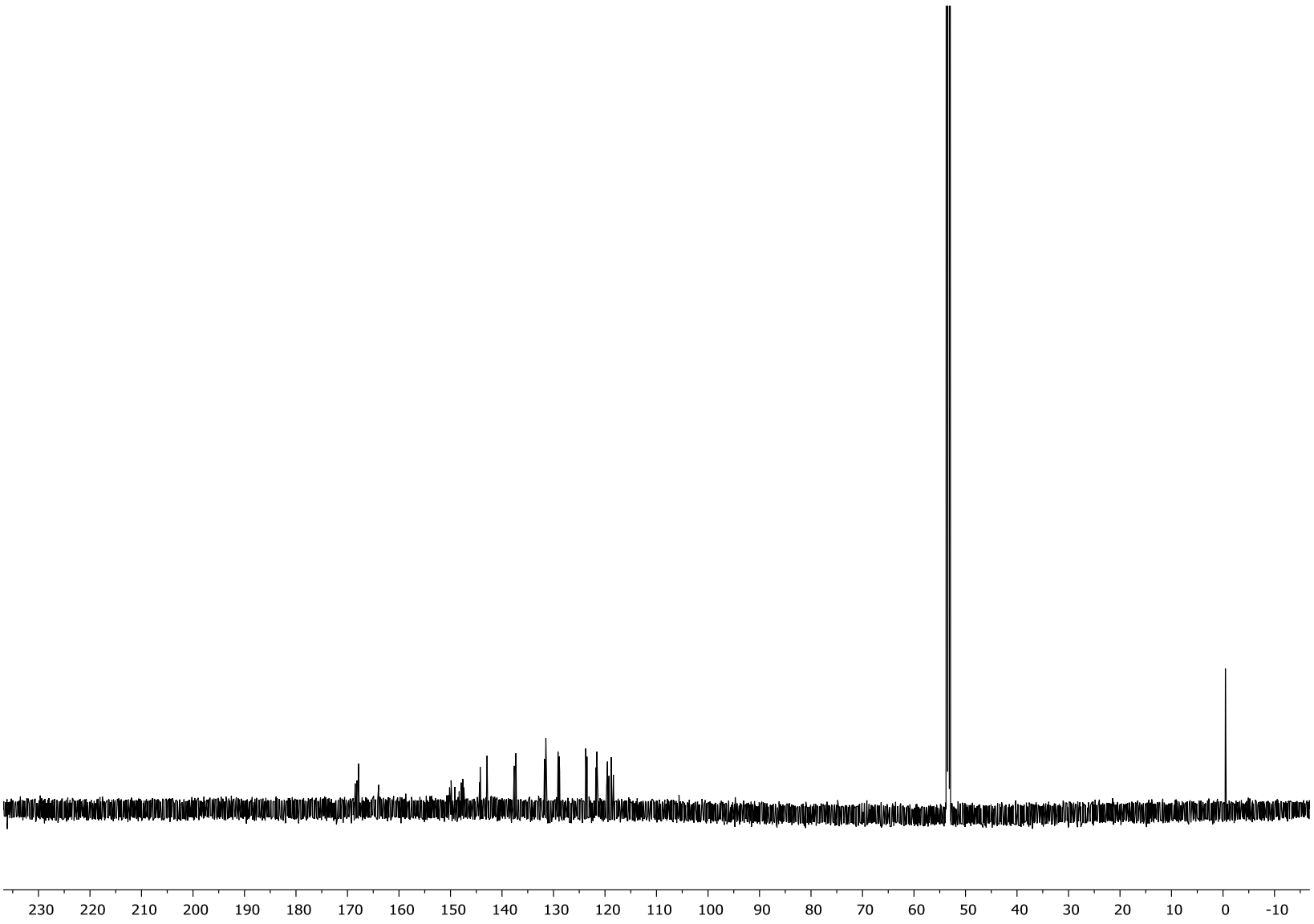

Figure S8. ^{13}C NMR spectrum (151 MHz) of **9** in CD_2Cl_2 (TMS).

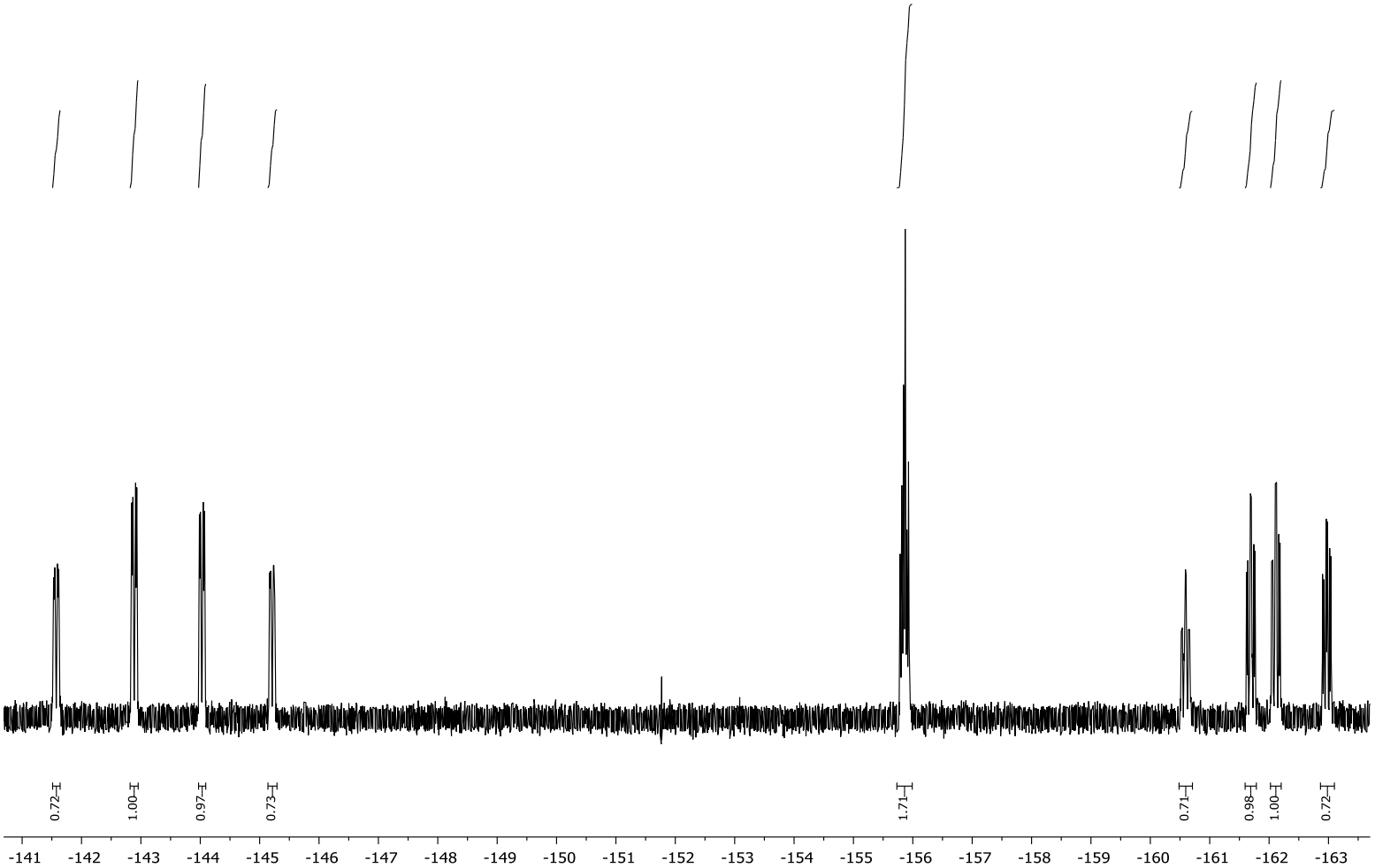

Figure S9. $^{19}F\{^{1}H\}$ NMR spectrum (376 MHz) of **9** in CD_2Cl_2.

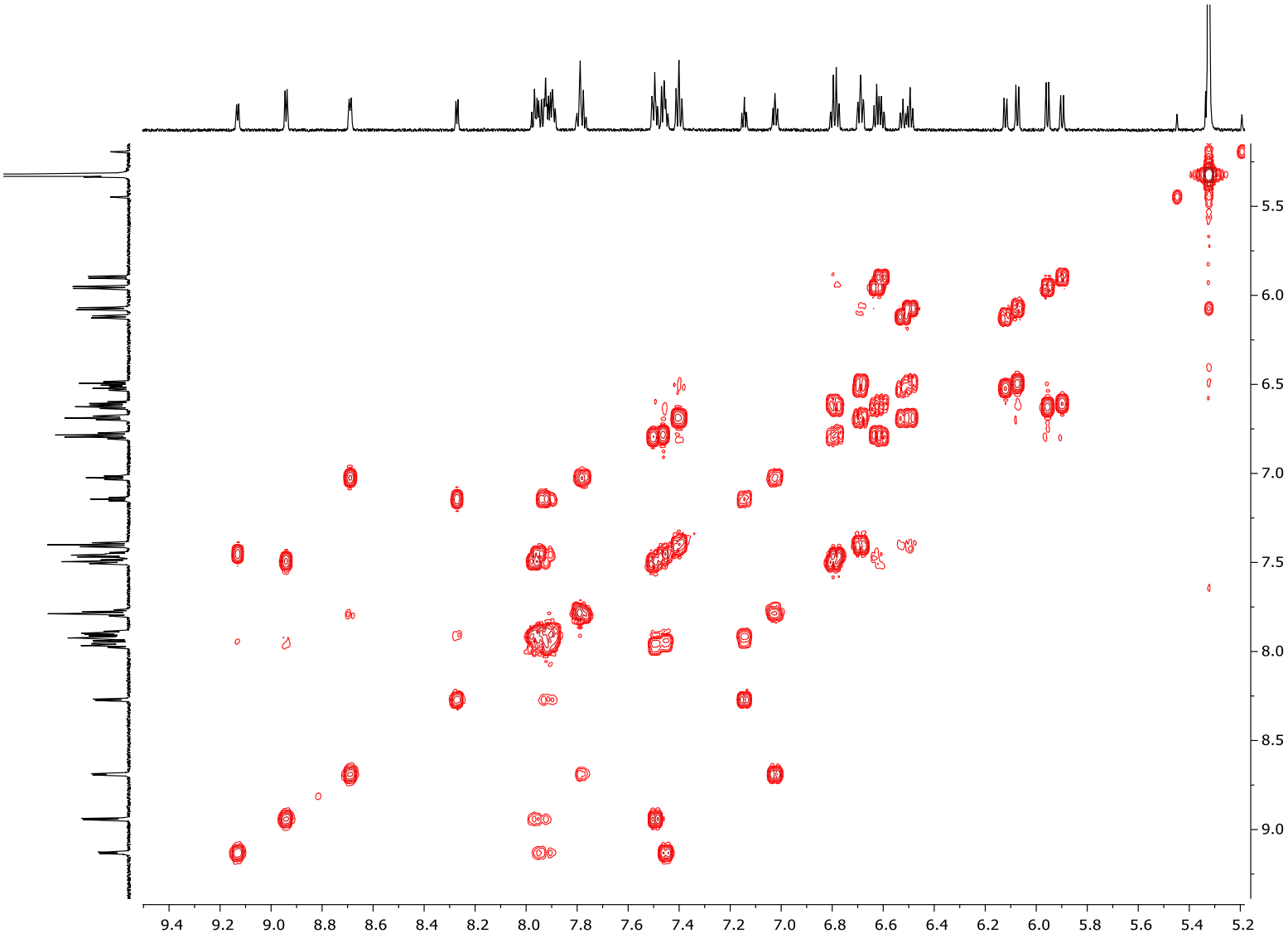

Figure S10. Expansion of the aromatic region of the ^{1}H–^{1}H COSY NMR spectrum of **9** in CD_2Cl_2 (TMS).

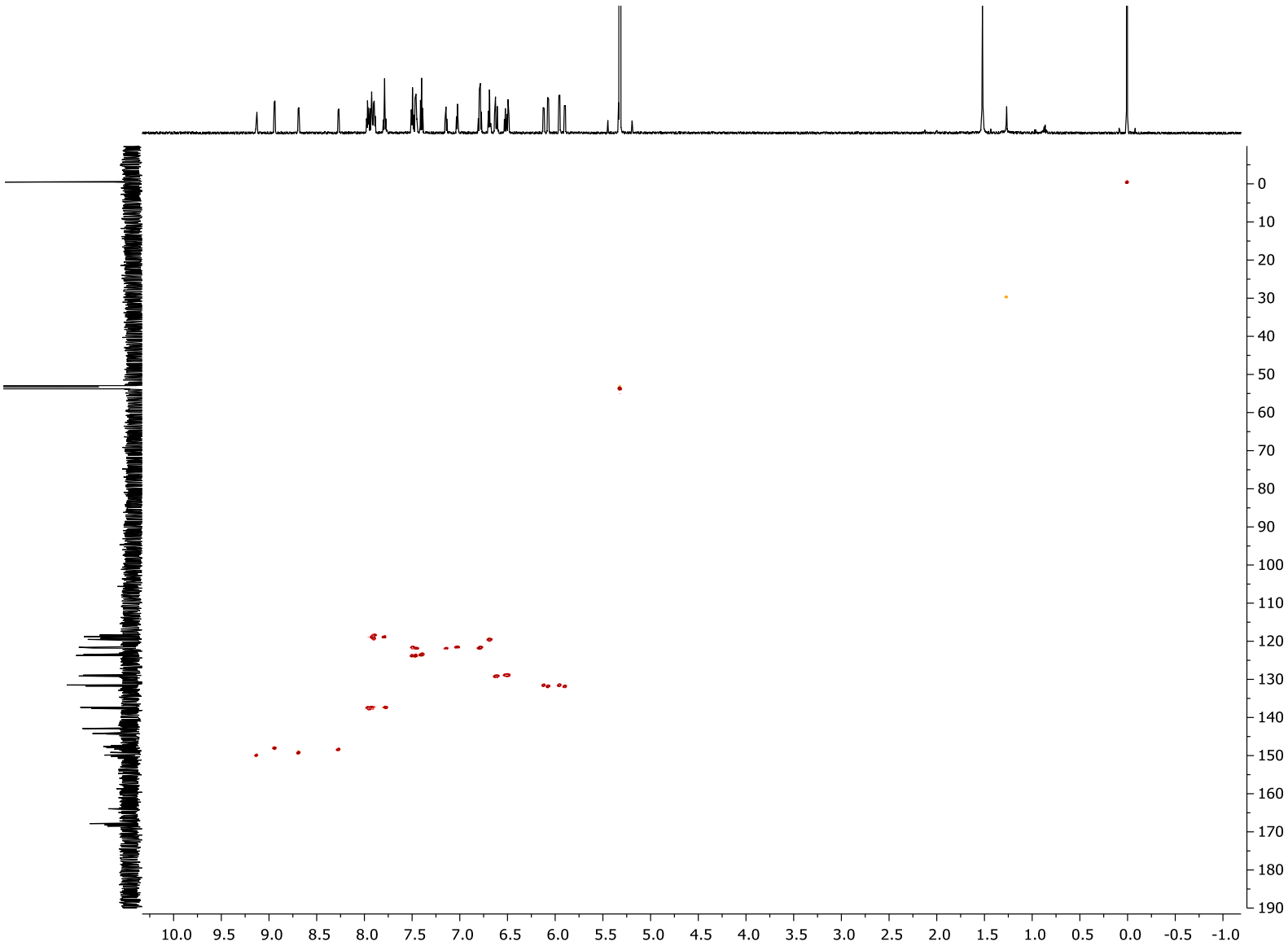

Figure S11. ^{1}H–^{13}C HSQC NMR spectrum of **9** in CD_2Cl_2.

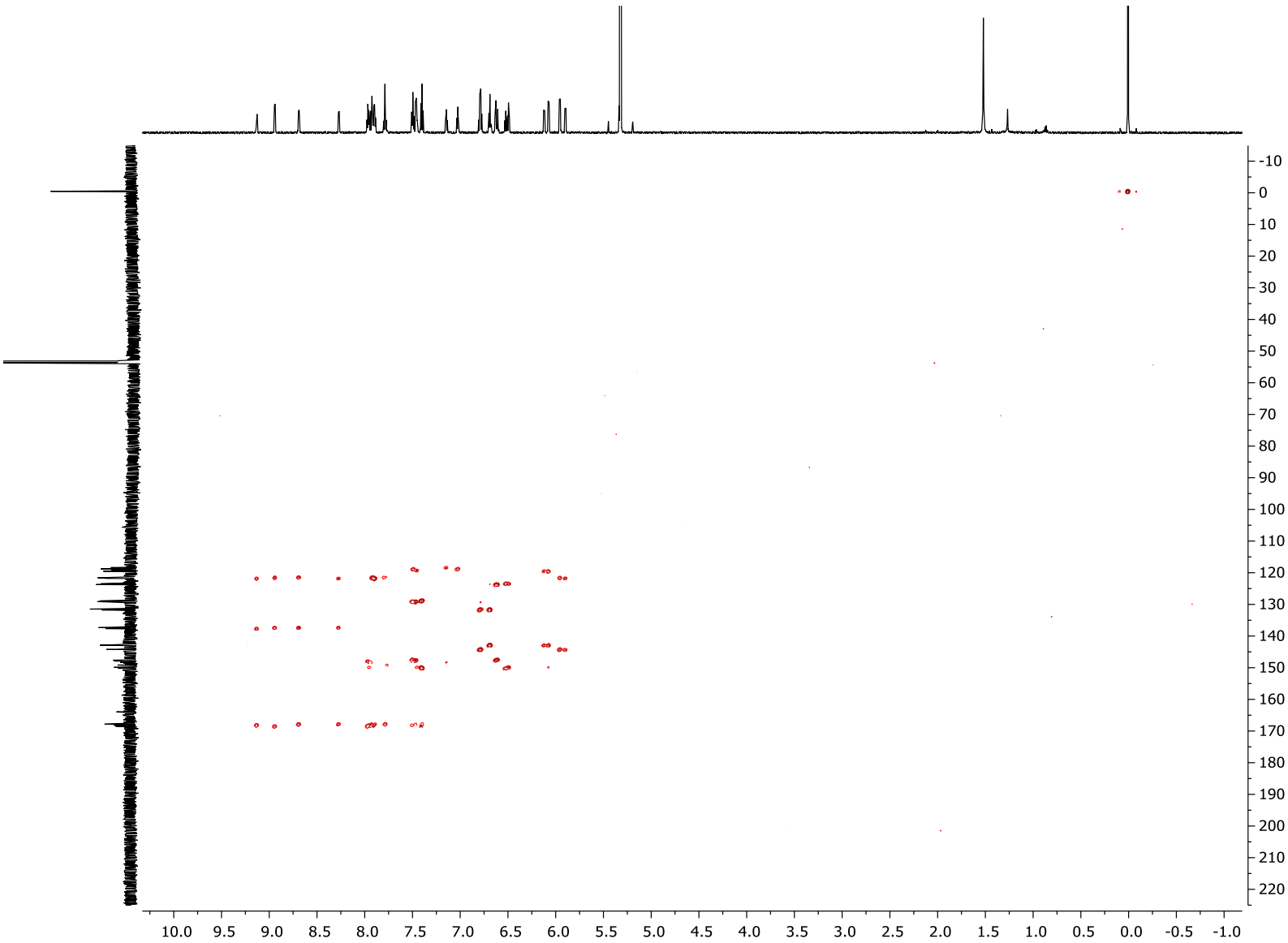

Figure S12. $^{1}H–^{13}C$ HMBC NMR spectrum of **9** in CD_2Cl_2.

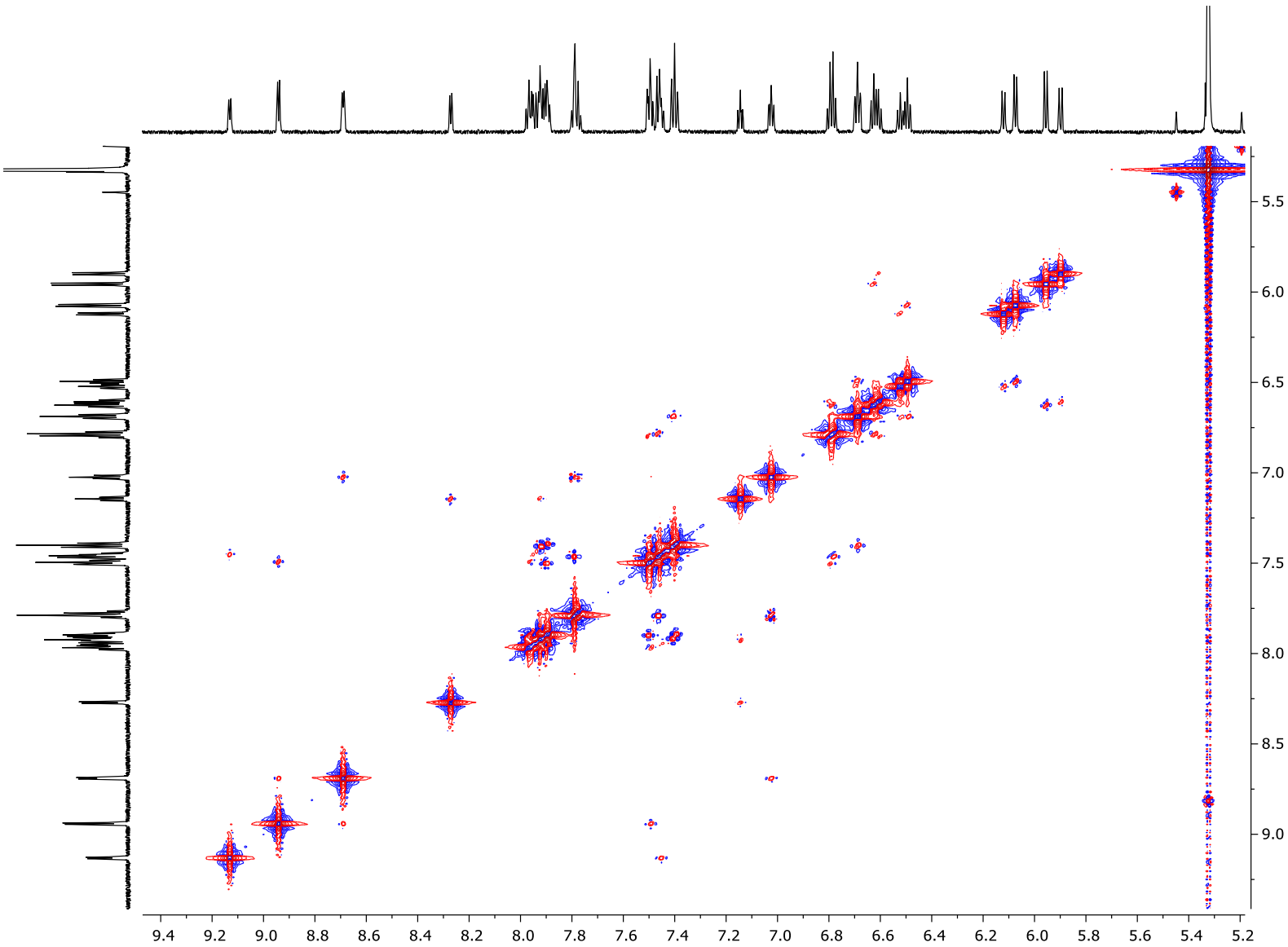

Figure S13. Aromatic region of the ^{1}H–^{1}H NOESY NMR spectrum of **9** in CD_2Cl_2.

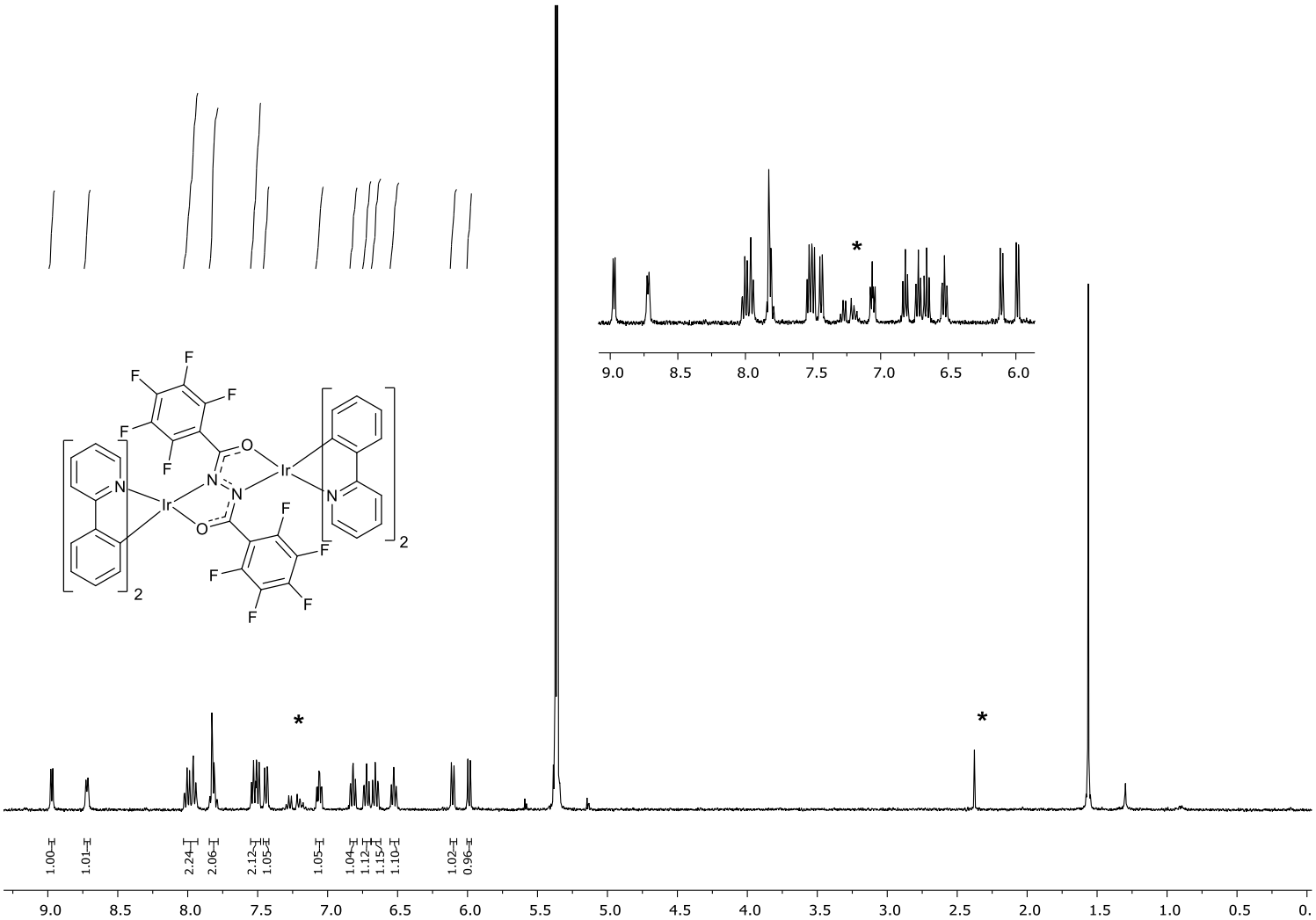

Figure S14. ^{1}H NMR spectrum (700 MHz) of *meso* **9** in CD_2Cl_2.* = Peaks from residual toluene.

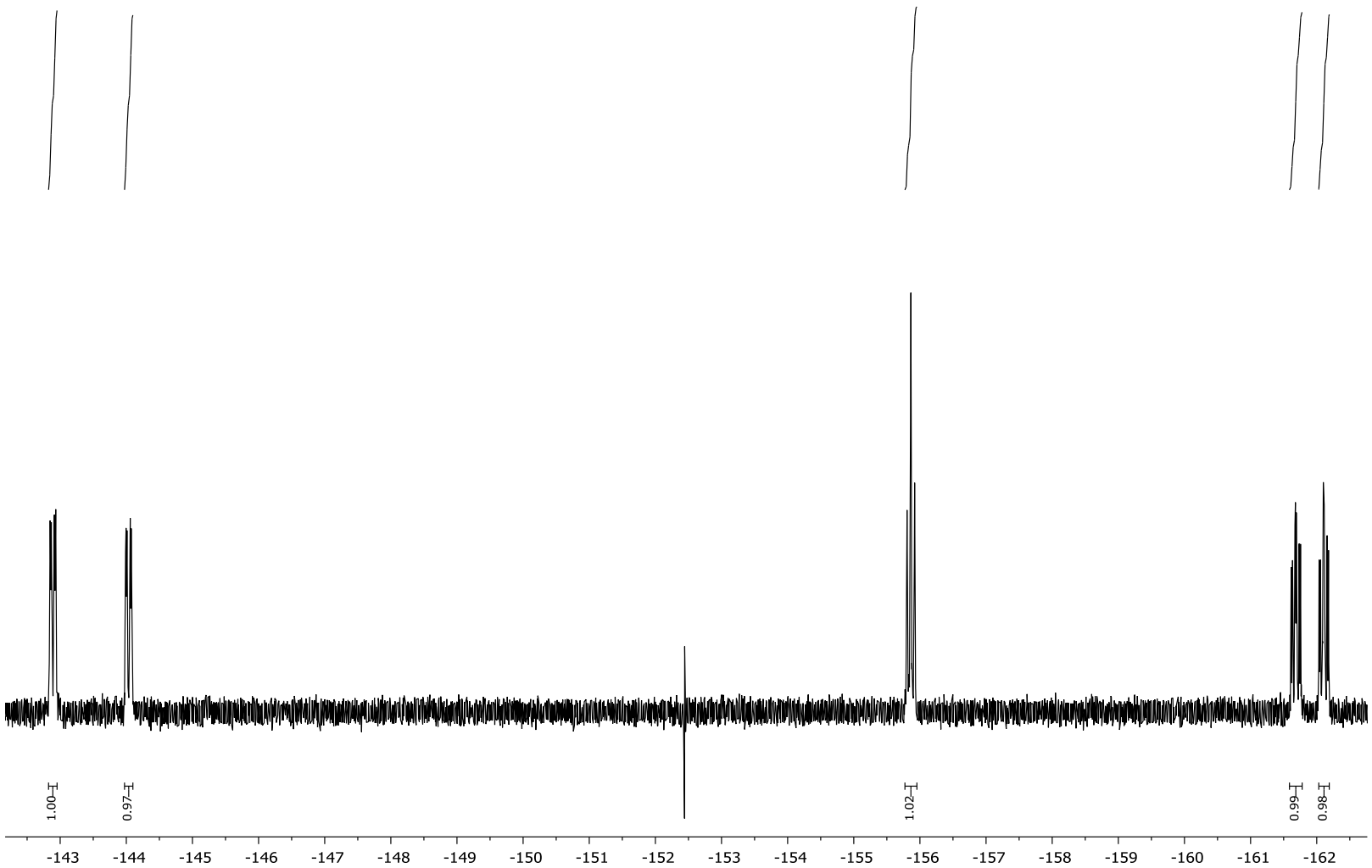

Figure S15. $^{19}F\{^{1}H\}$ NMR spectrum (376 MHz) of *meso* **9** in CD_2Cl_2.

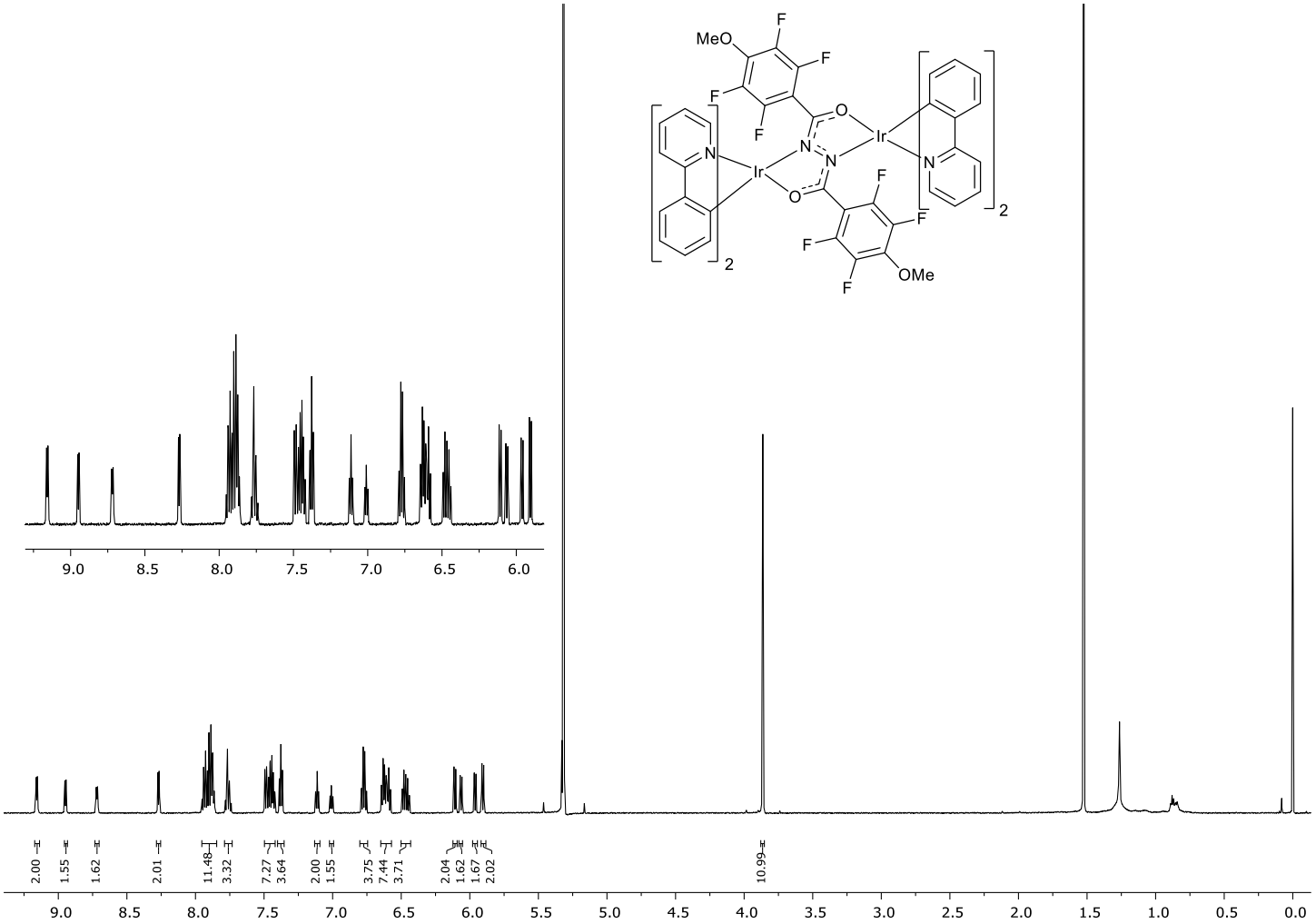

Figure S16. ^{1}H NMR spectrum (600 MHz) of **10** in CD_2Cl_2 (TMS).

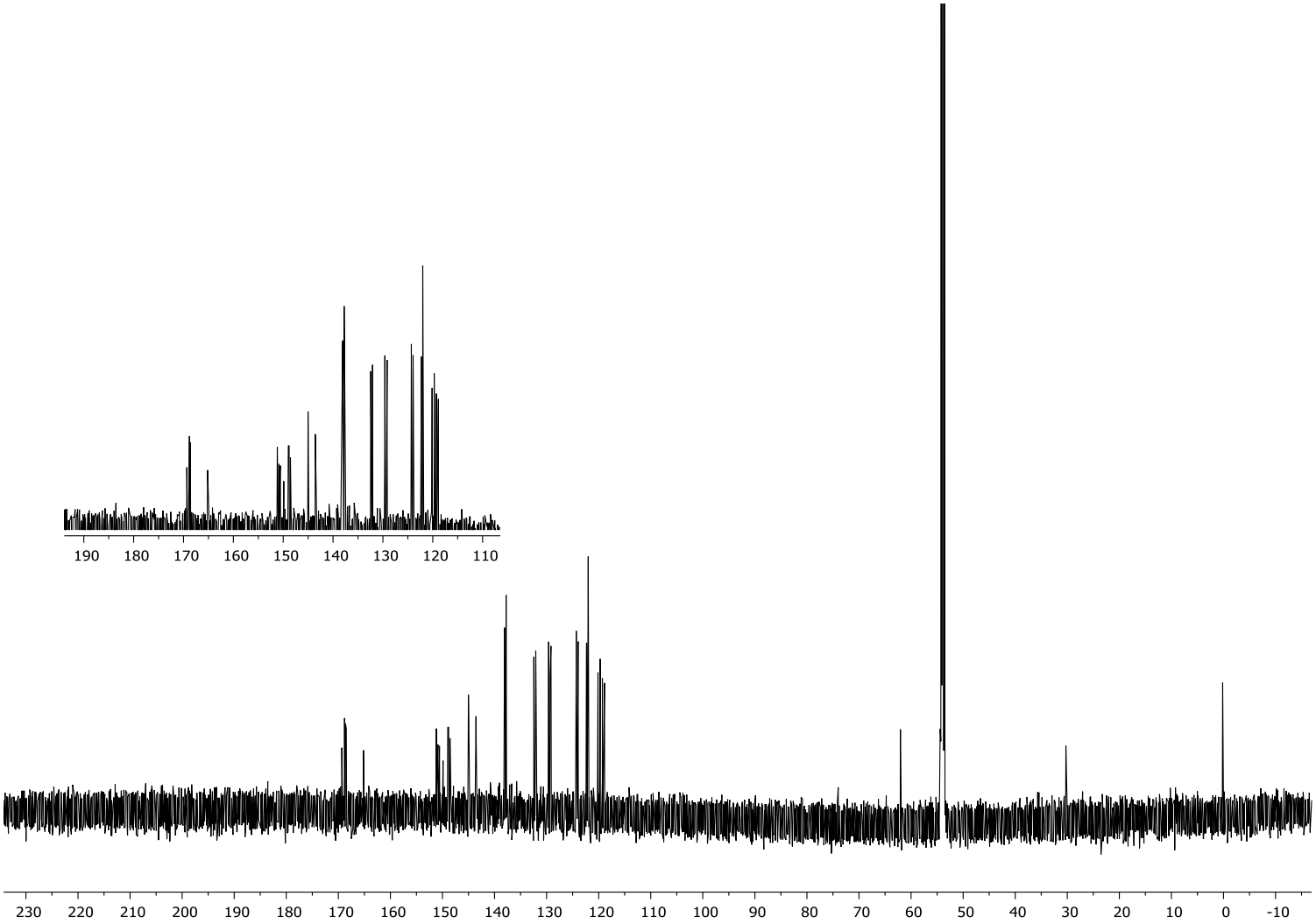

Figure S17. ^{13}C NMR spectrum (151 MHz) of **10** in CD_2Cl_2 (TMS).

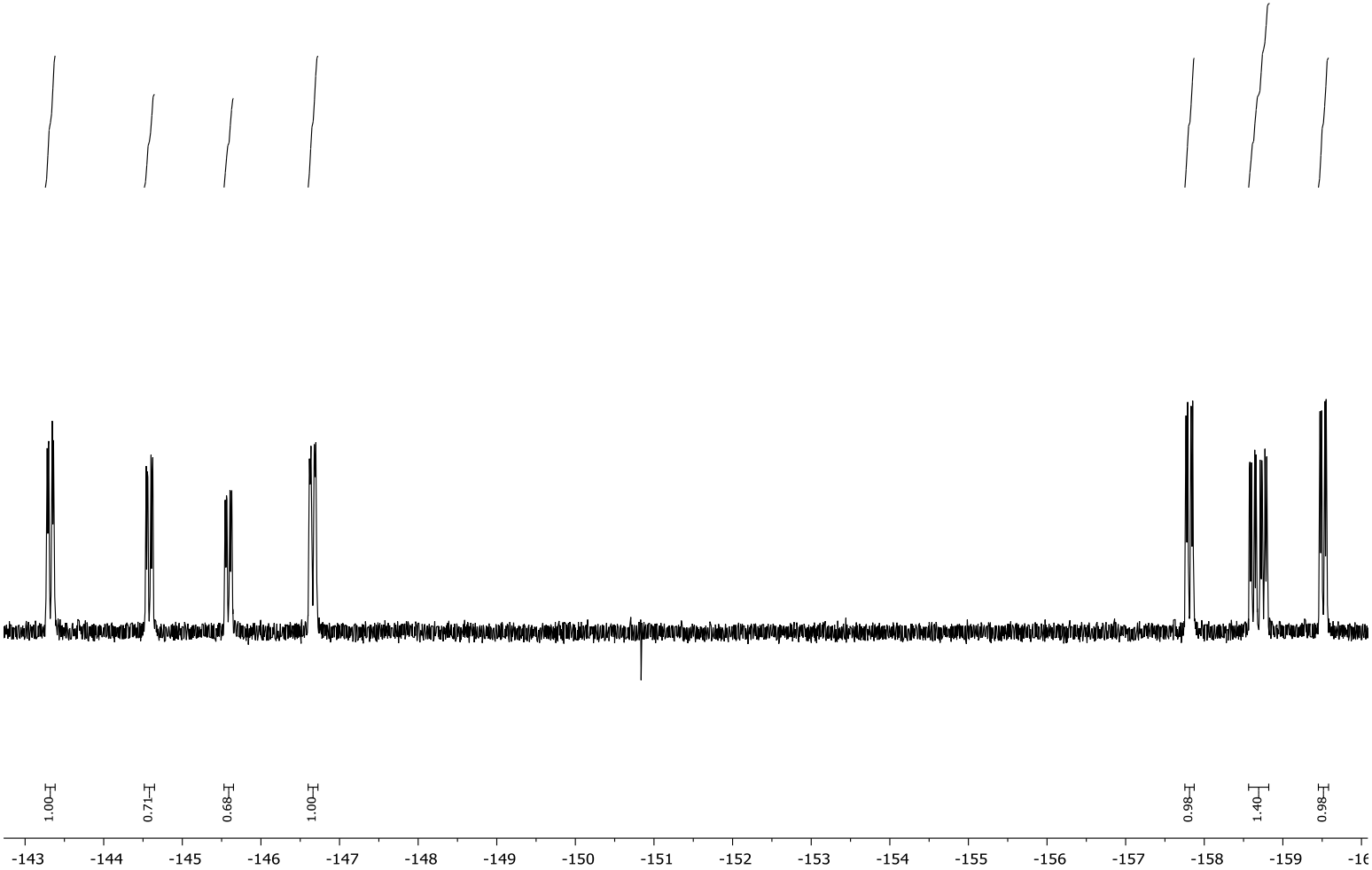

Figure S18. $^{19}F\{^{1}H\}$ NMR spectrum (376 MHz) of **10** in CD_2Cl_2.

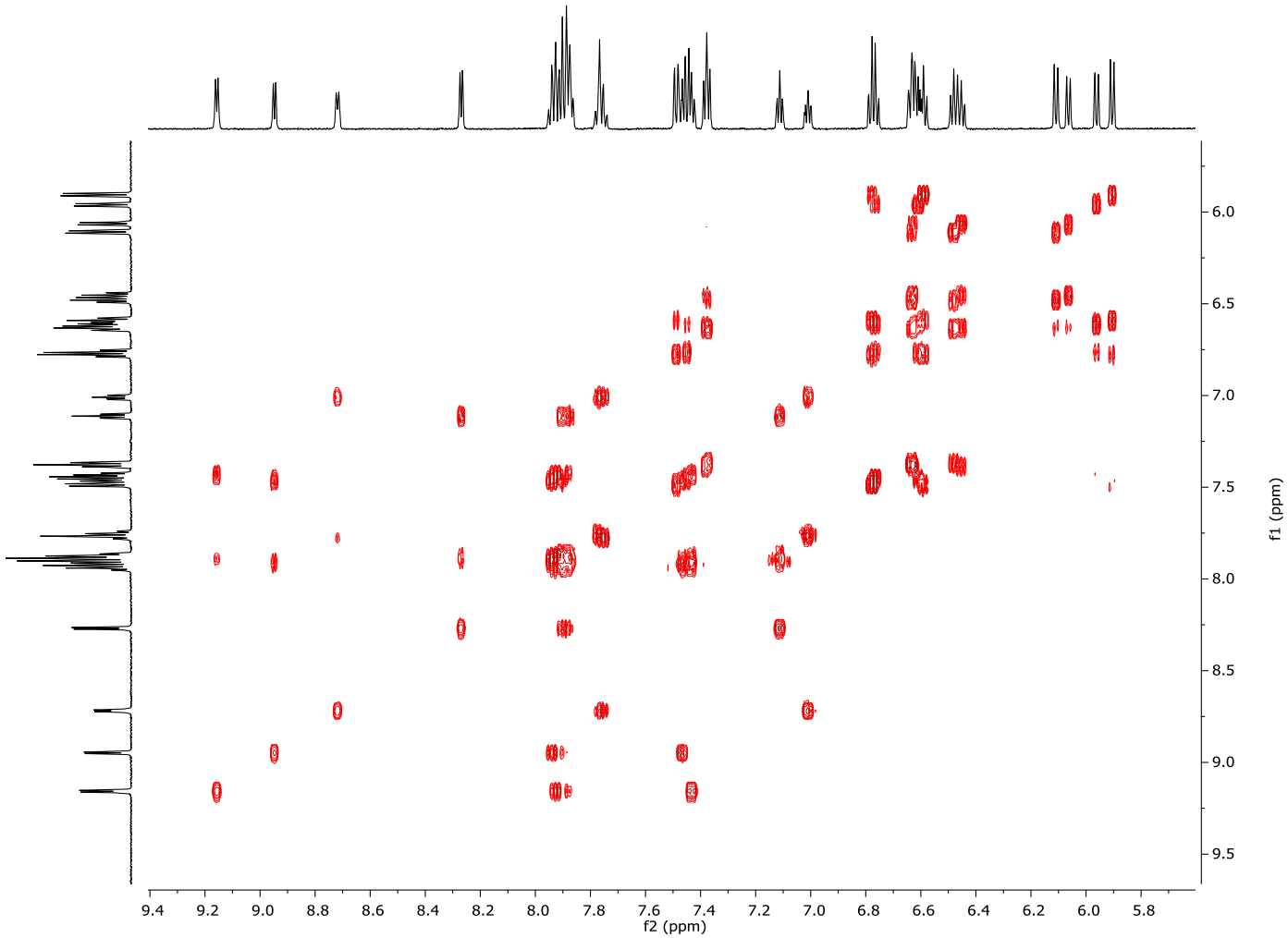

Figure S19. Expansion of the aromatic region of the ^{1}H–^{1}H COSY NMR spectrum of **10** in CD_2Cl_2 (TMS).

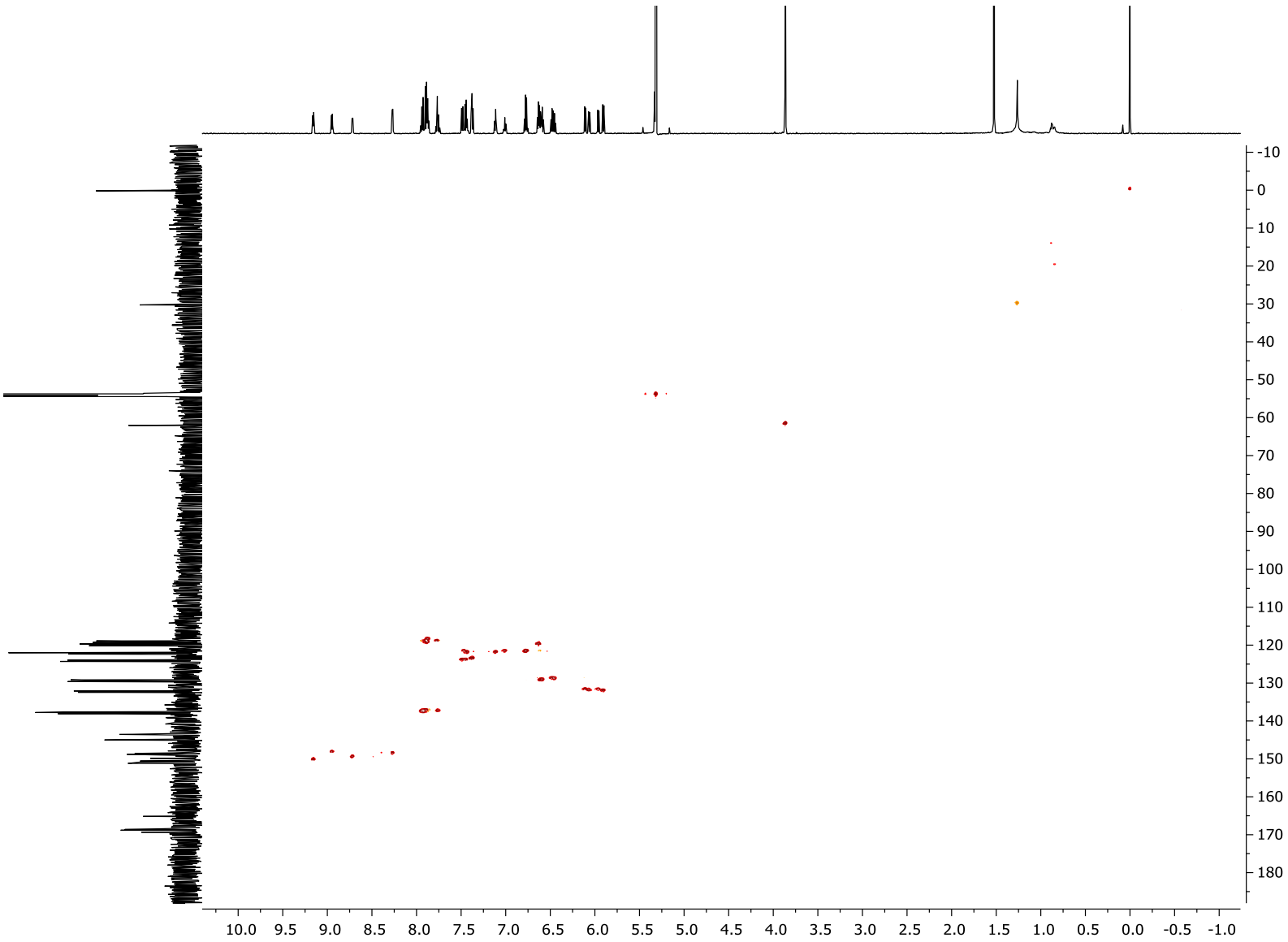

Figure S20. $^{1}H–^{13}C$ HSQC NMR spectrum of **10** in CD_2Cl_2.

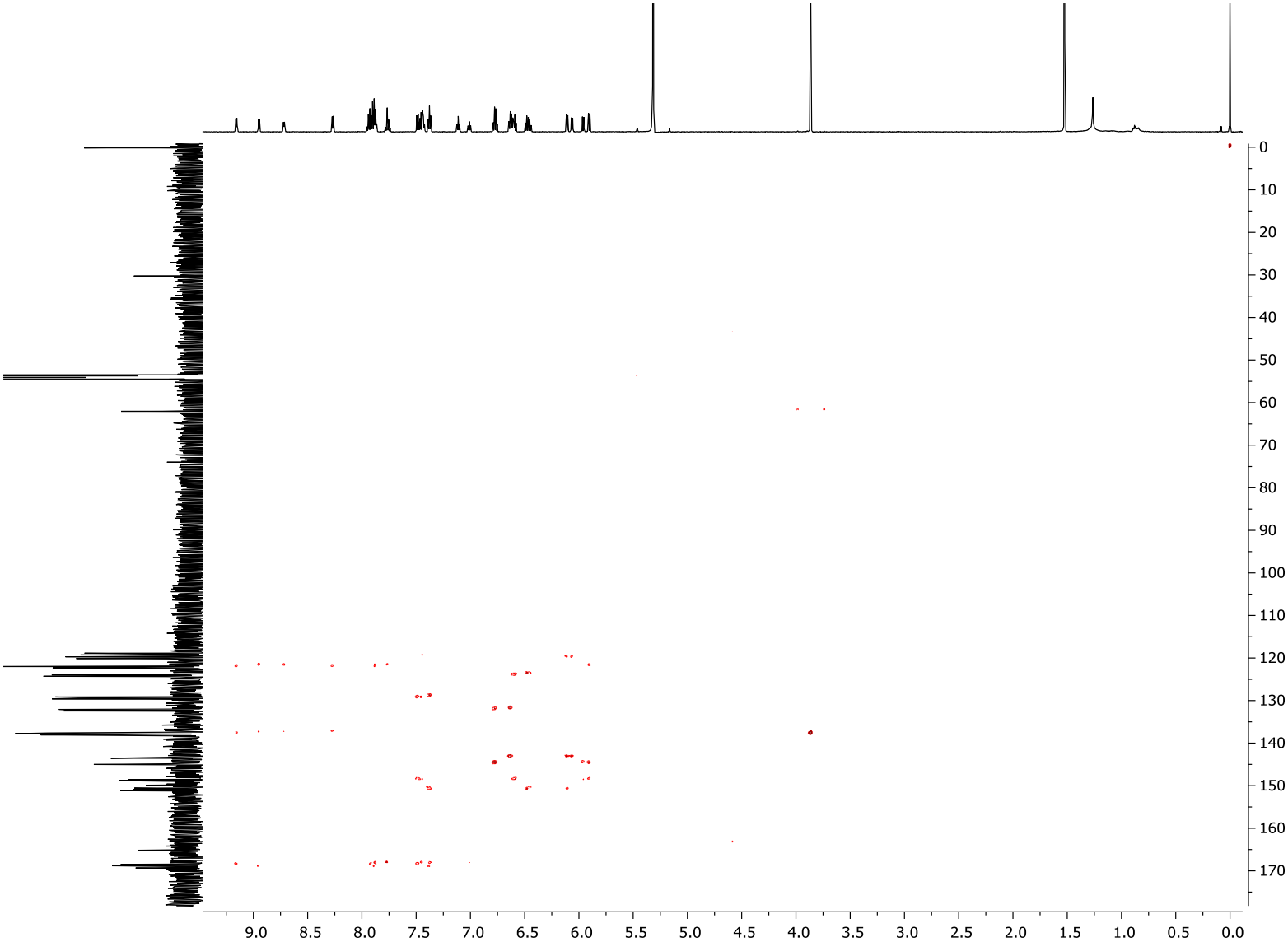

Figure S21. ^{1}H–^{13}C HMBC NMR spectrum of **10** in CD_2Cl_2.

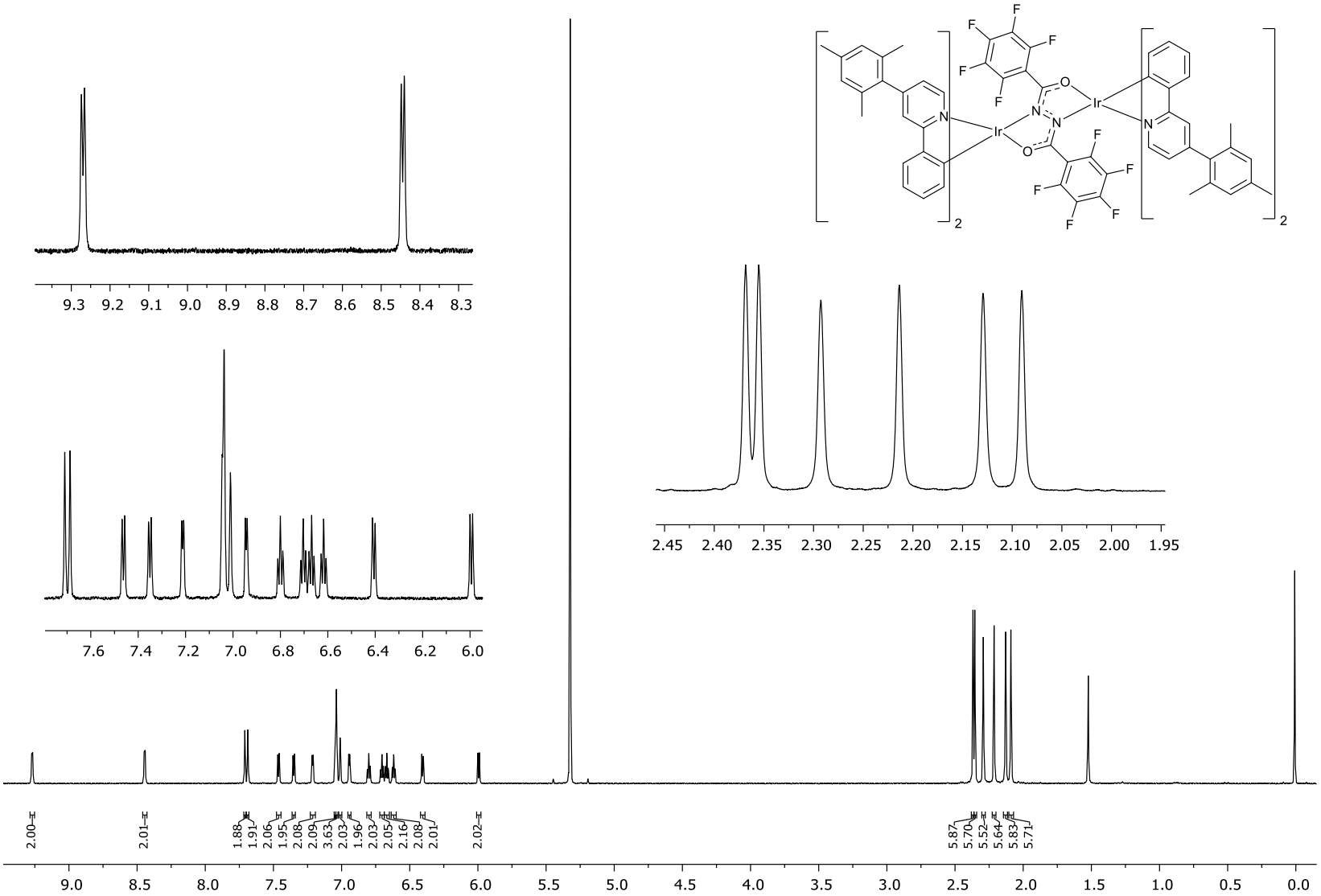

Figure S22. ^{1}H NMR spectrum (700 MHz) of *rac* **11** in CD_2Cl_2 (TMS).

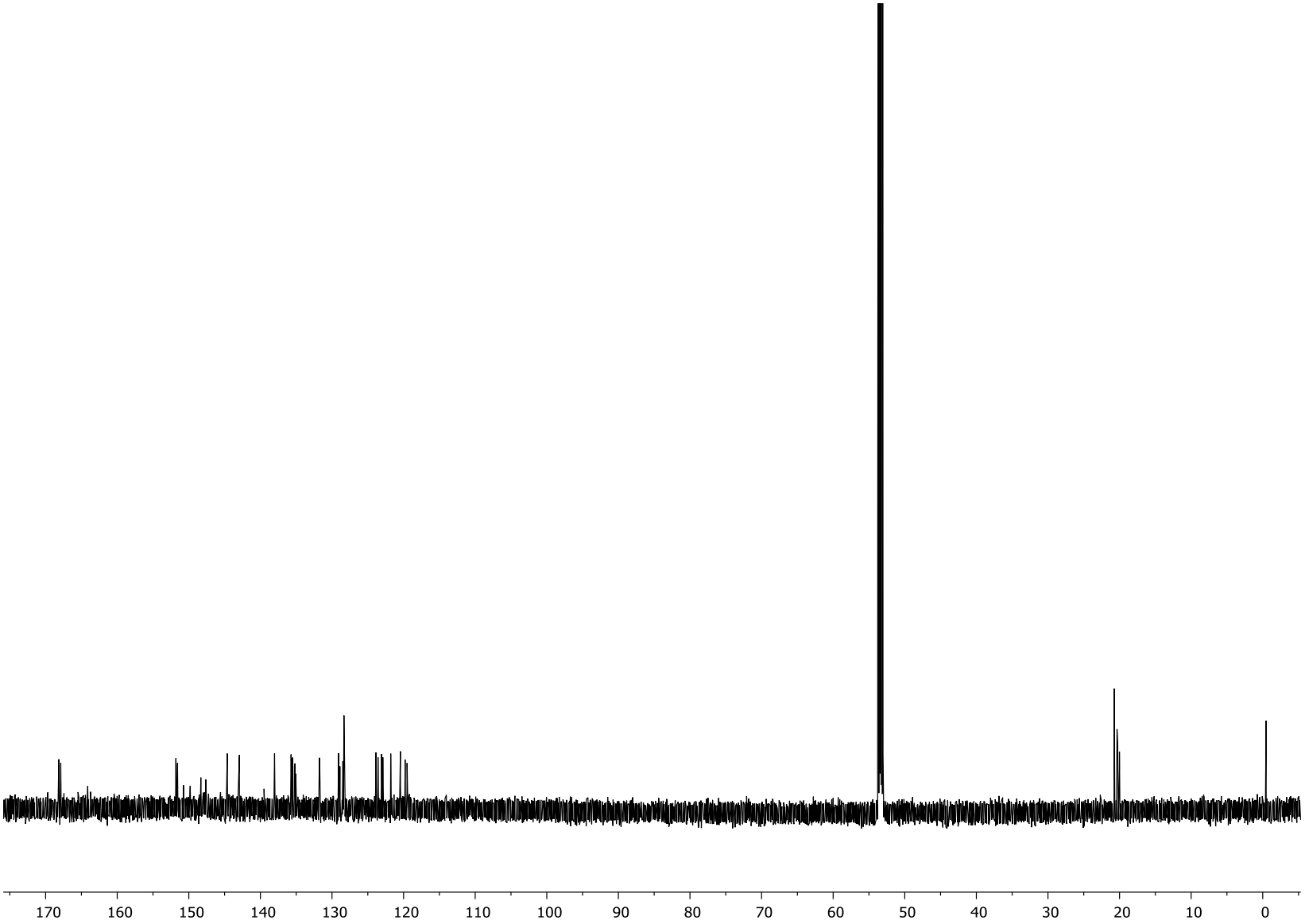

Figure S23. ^{13}C NMR spectrum (151 MHz) of *rac* **11** in CD_2Cl_2 (TMS).

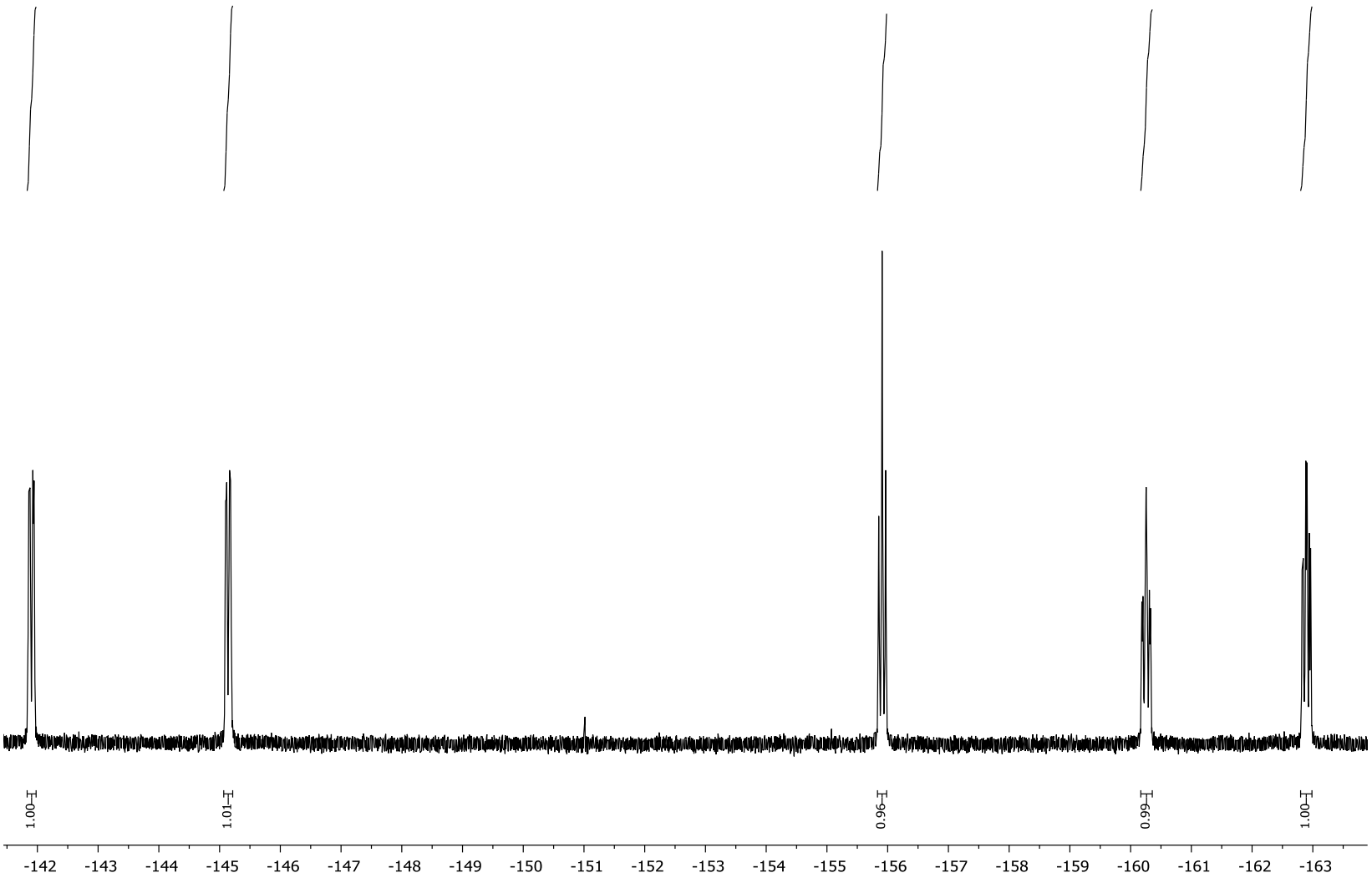

Figure S24. $^{19}F\{^{1}H\}$ NMR spectrum (376 MHz) of *rac* **11** in CD_2Cl_2

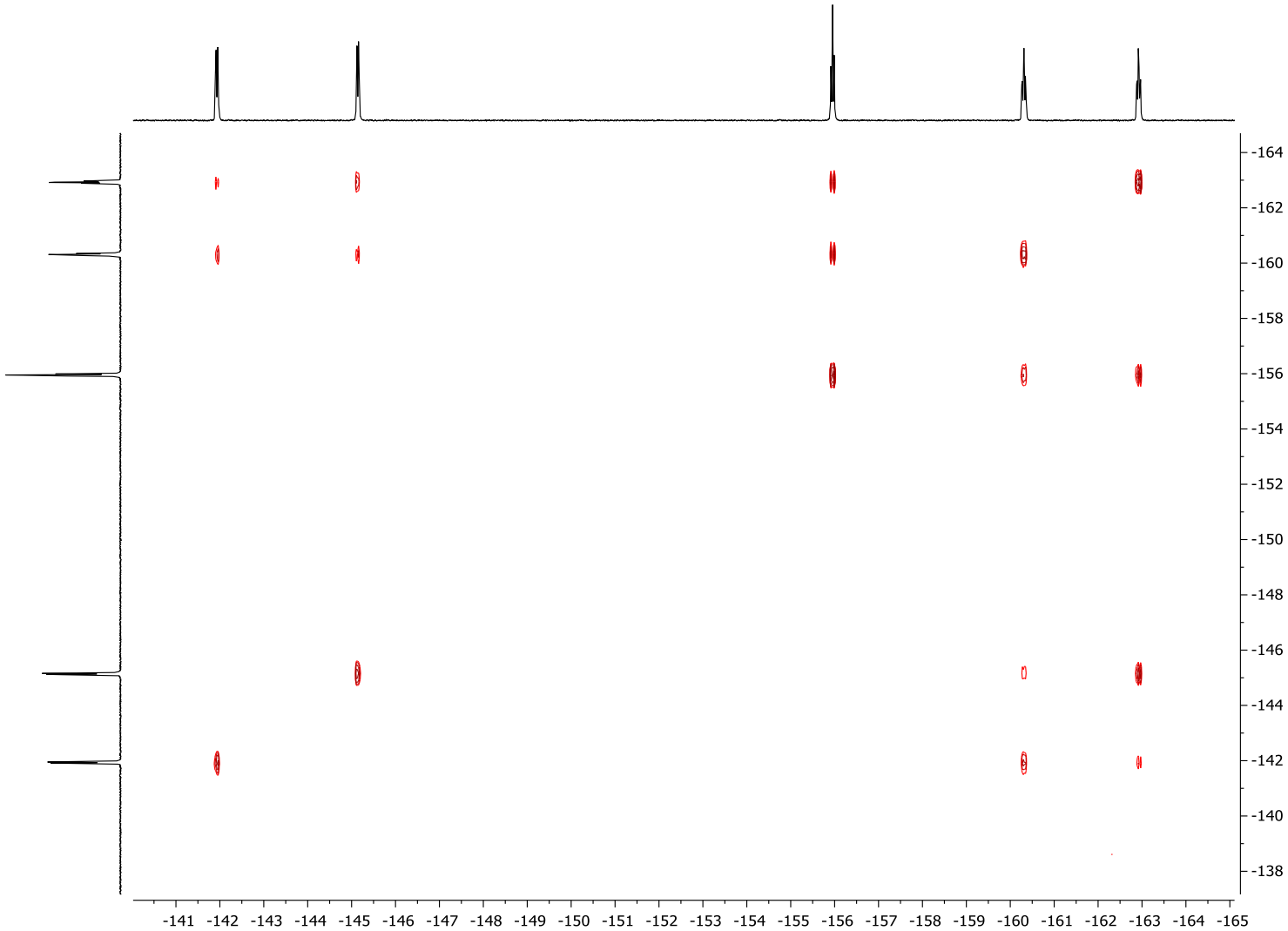

Figure S25. ^{19}F–^{19}F COSY NMR spectrum of *rac* **11** in CD_2Cl_2.

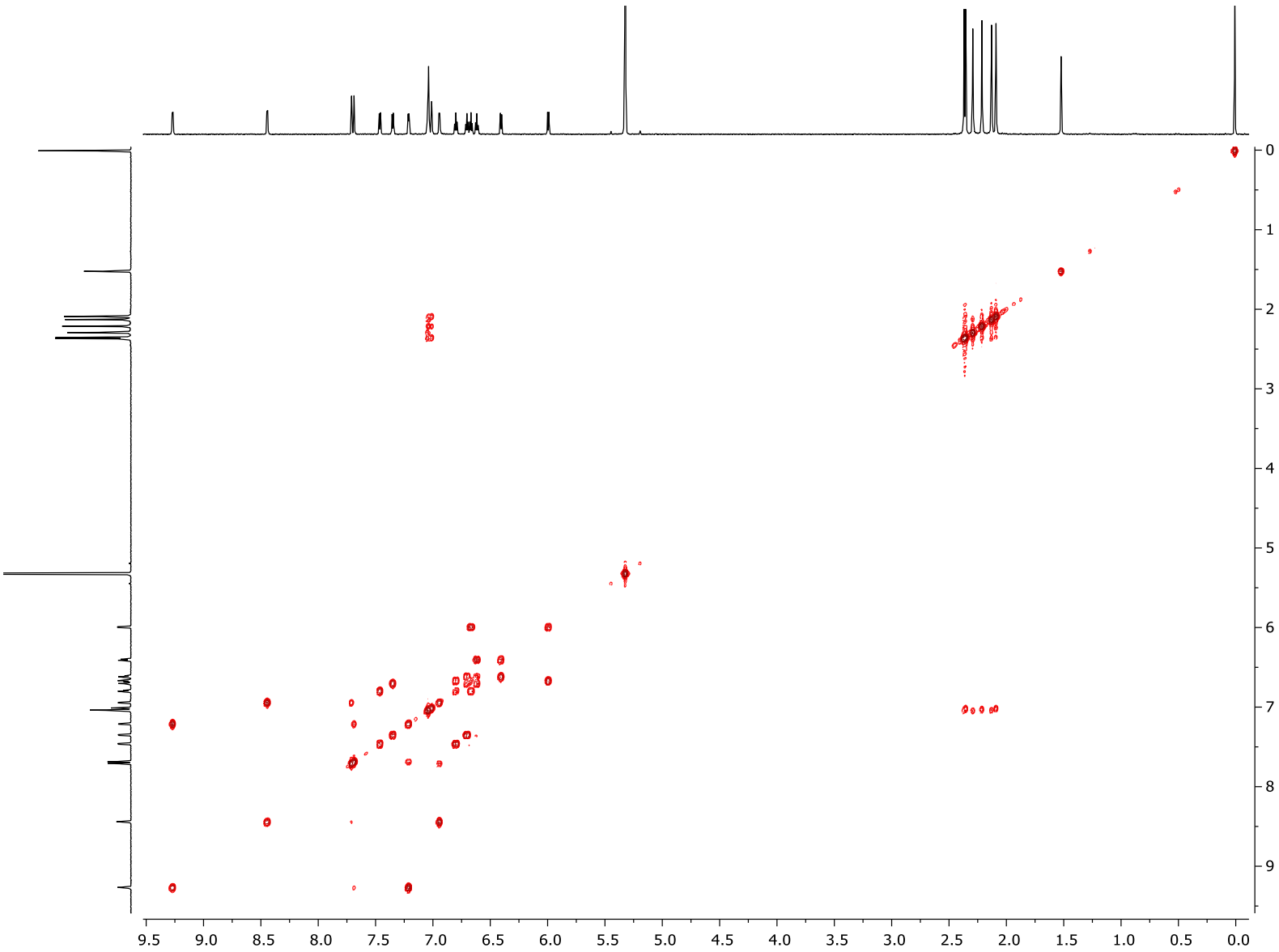

Figure S26. ^{1}H–^{1}H COSY NMR spectrum of *rac* **11** in CD_2Cl_2 (TMS).

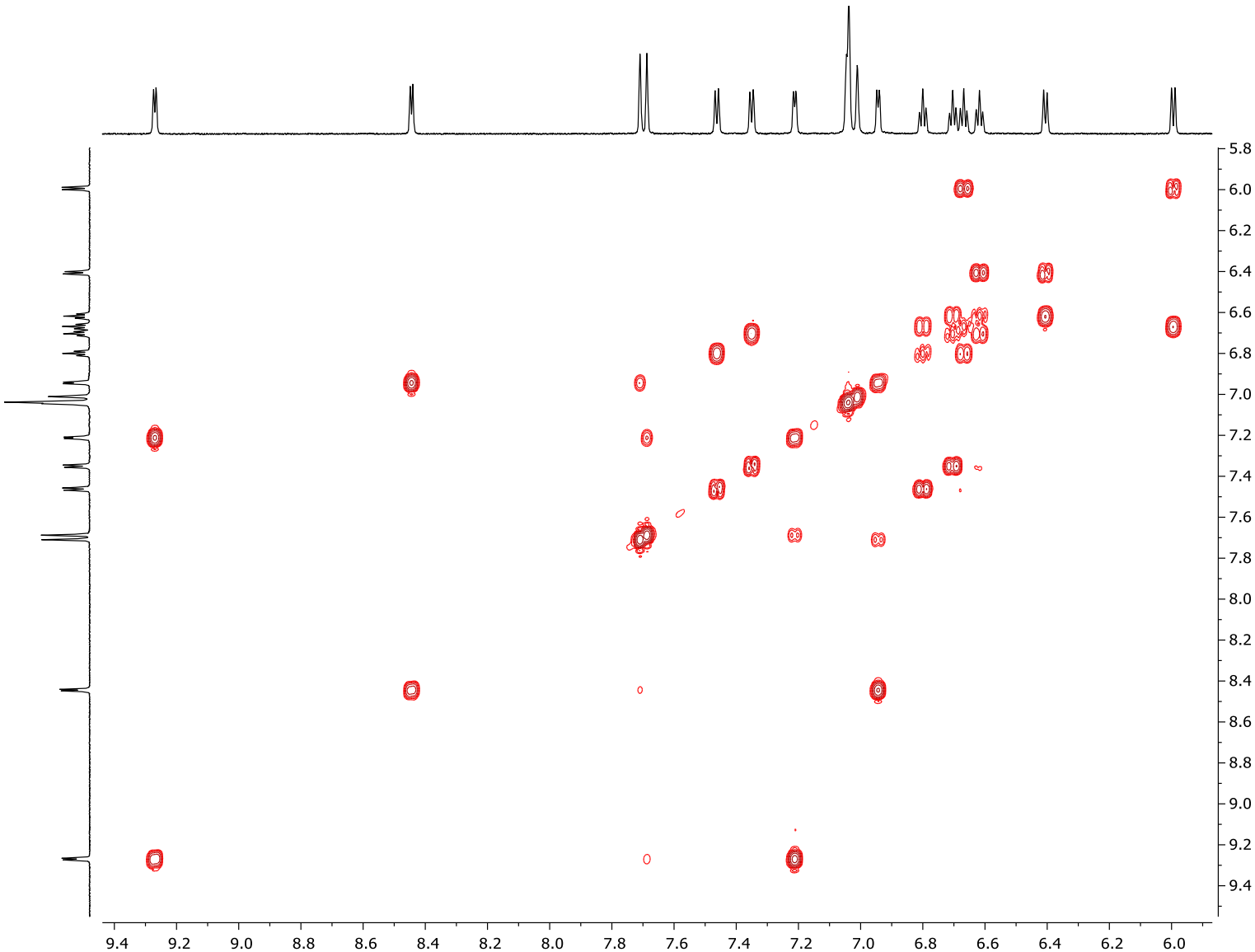

Figure S27. Expansion of the aromatic region of the ^{1}H–^{1}H COSY NMR spectrum of *rac* **11** in CD_2Cl_2 (TMS).

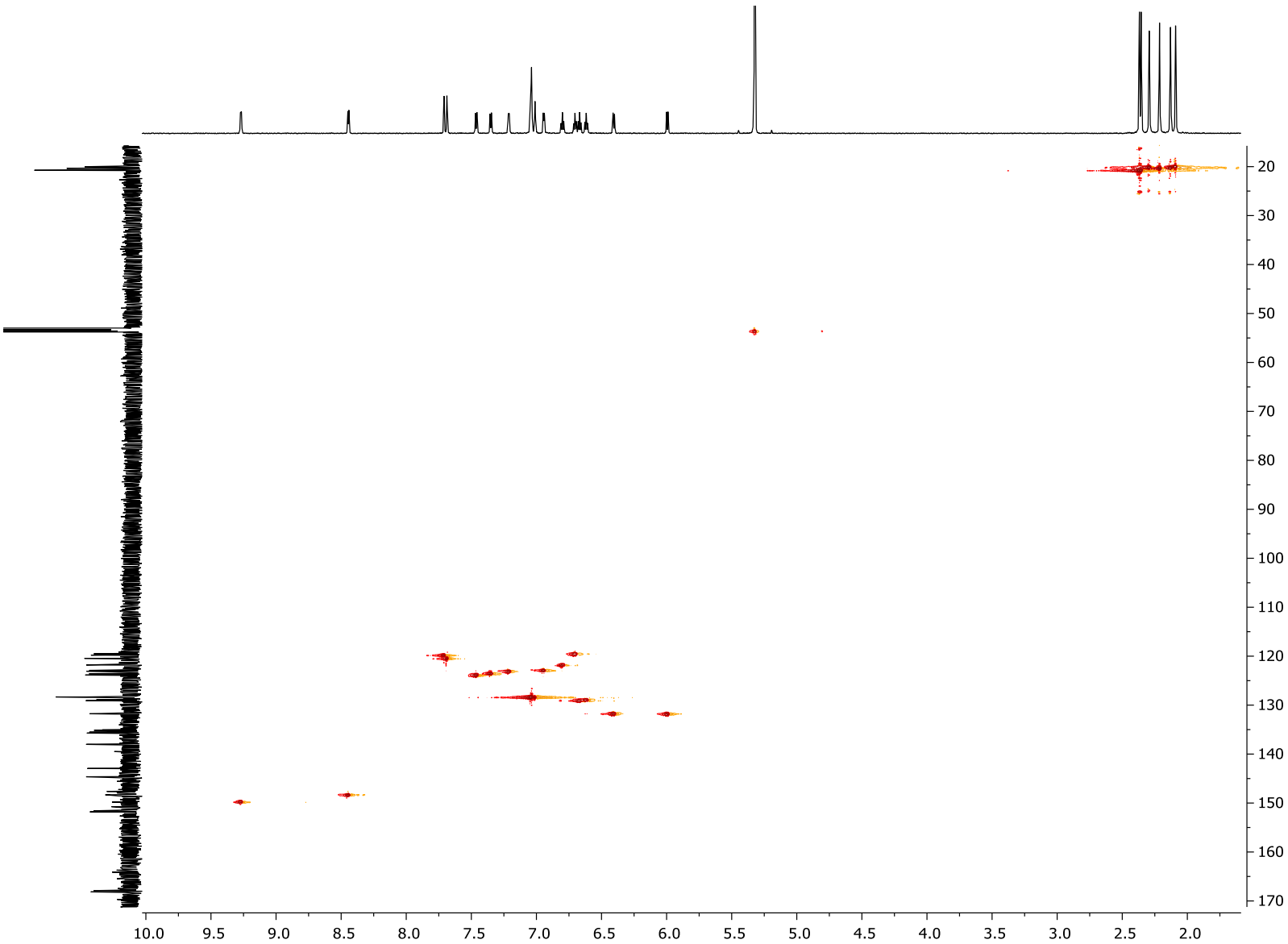

Figure S28. ^{1}H–^{13}C HSQC NMR spectrum of *rac* **11** in CD_2Cl_2 (TMS).

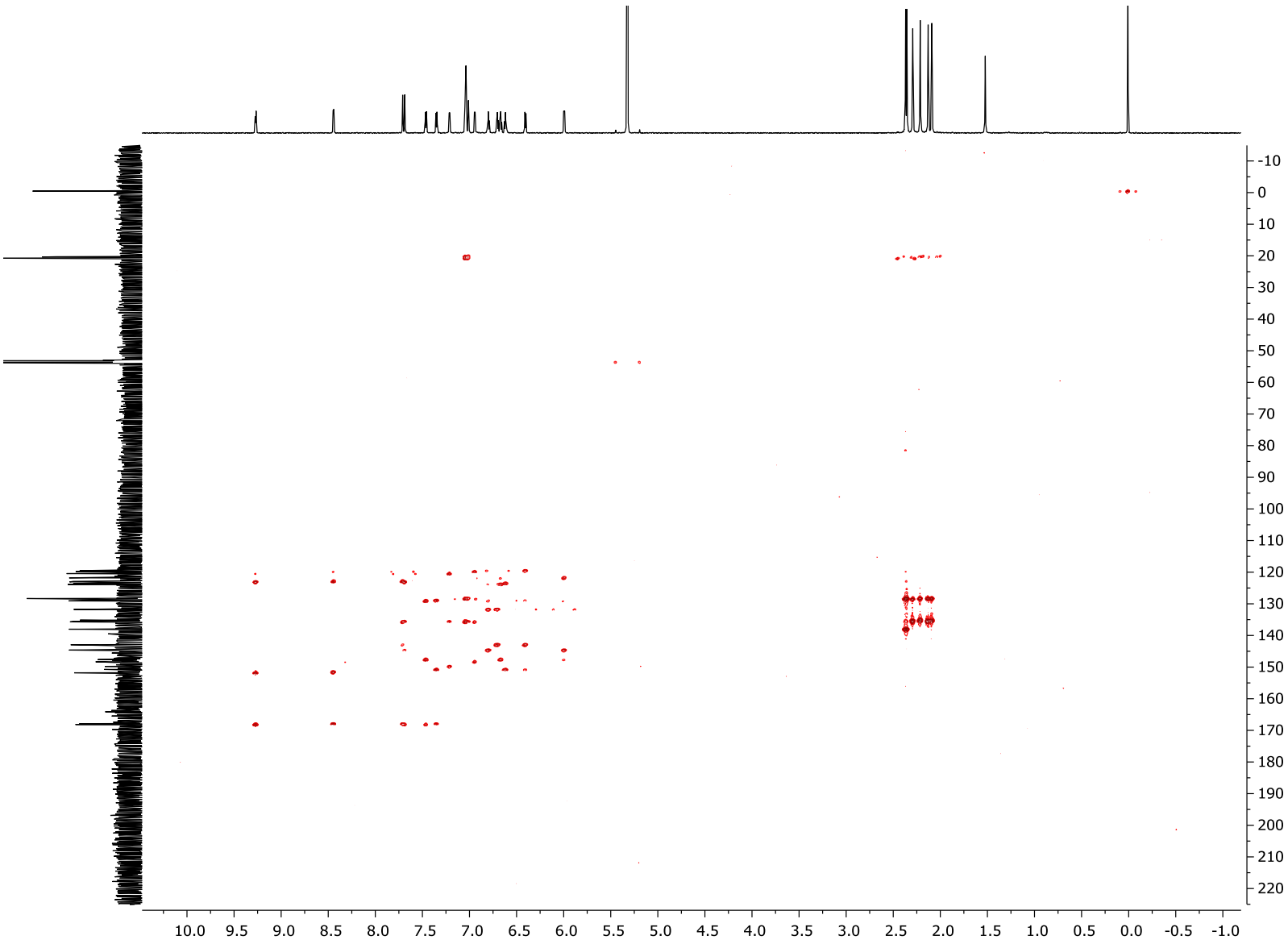

Figure S29. ^{1}H–^{13}C HMBC NMR spectrum of *rac* **11** in CD_2Cl_2 (TMS).

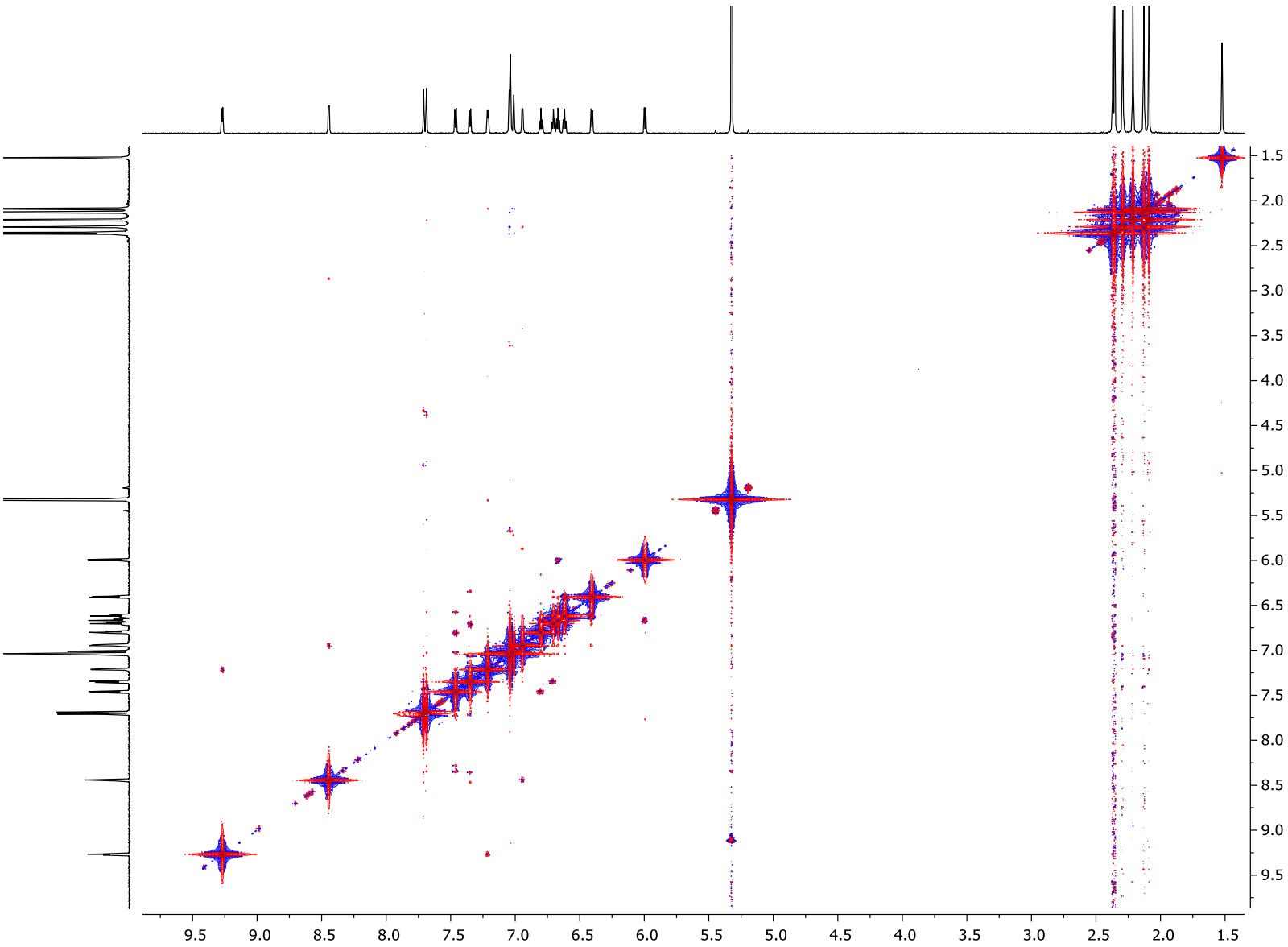

Figure S30. ^{1}H–^{1}H NOESY NMR spectrum of *rac* **11** in CD_2Cl_2 (TMS).

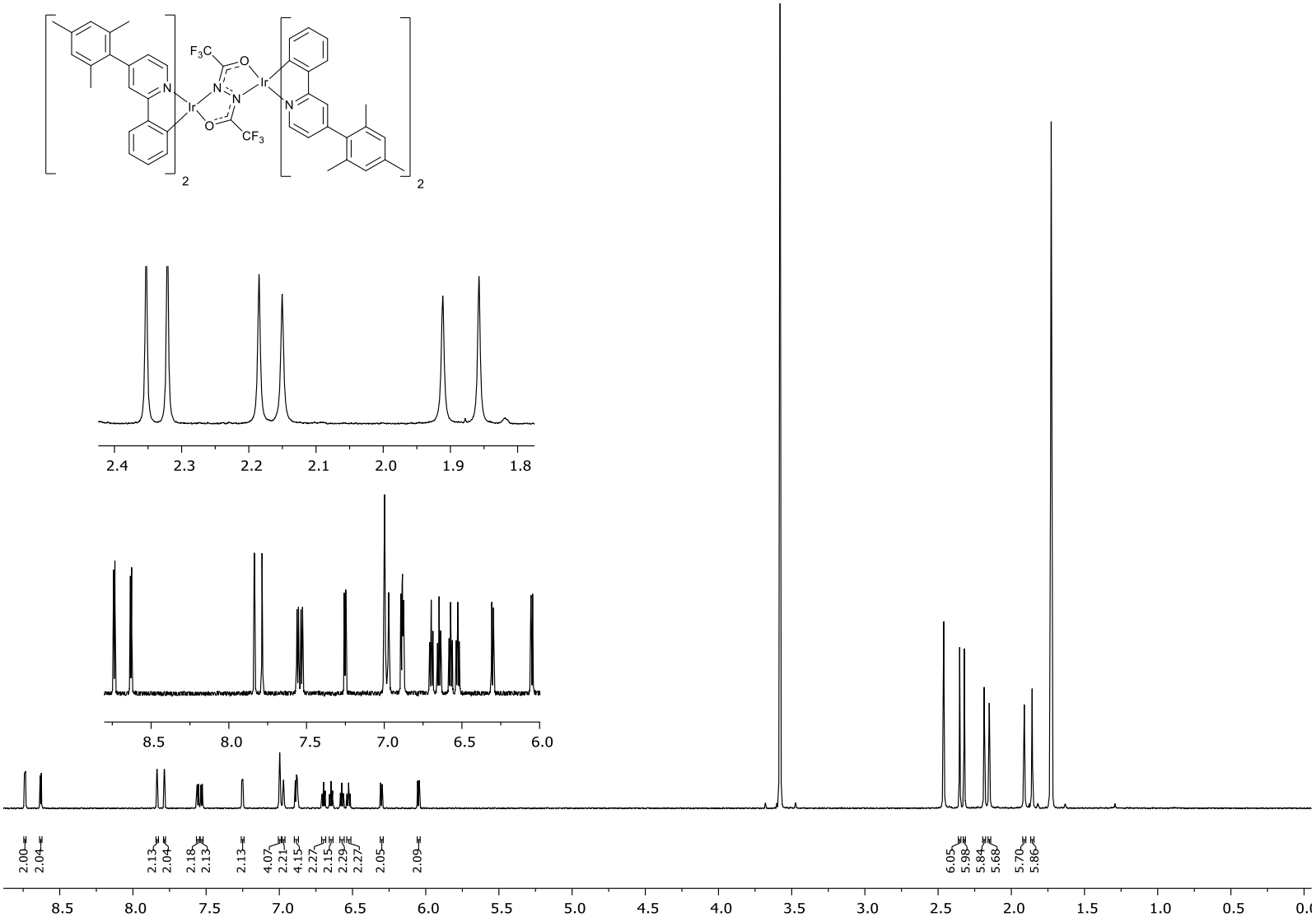

Figure S31. ^{1}H NMR spectrum (700 MHz) of *meso* **12** in THF-d_8.

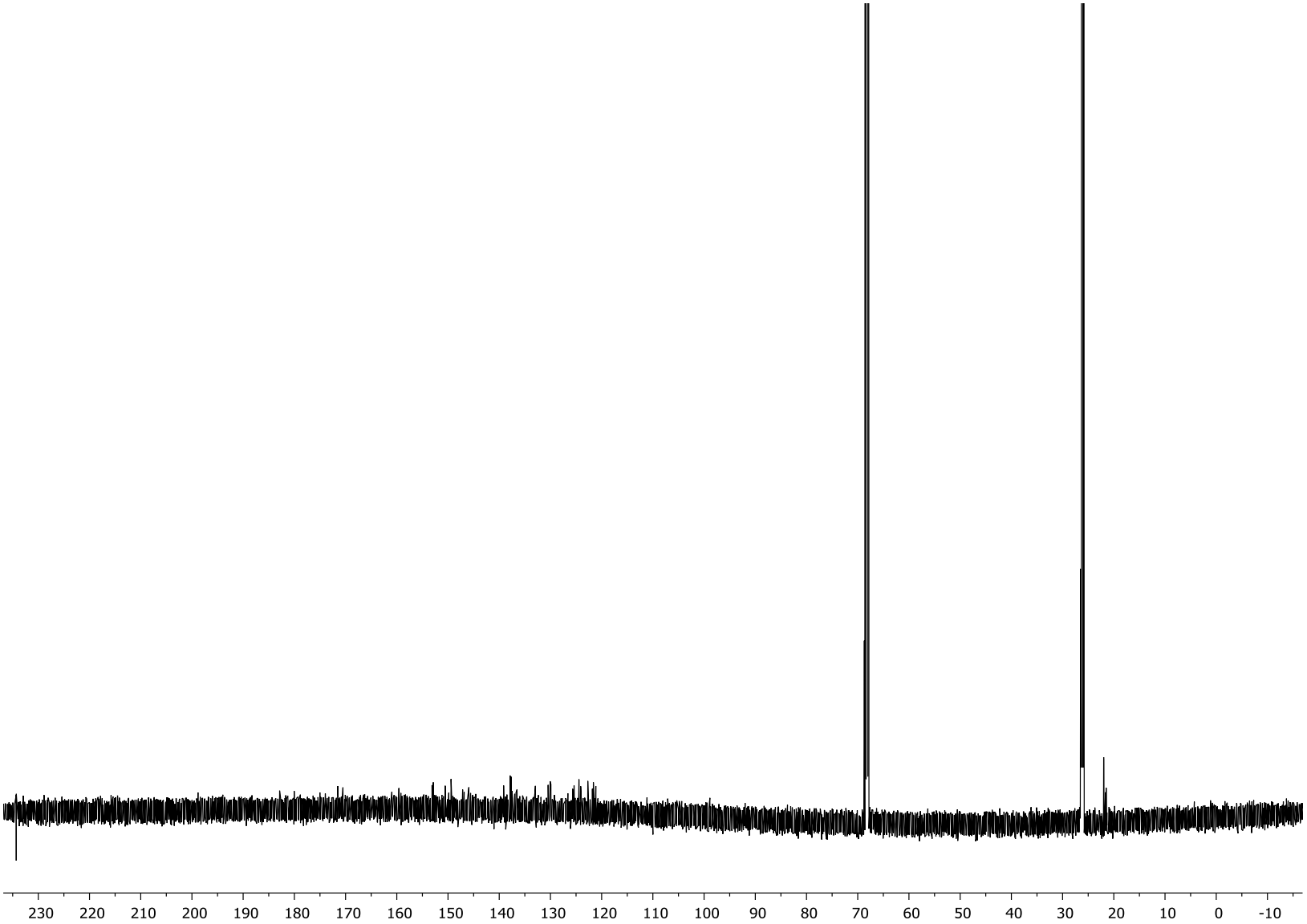

Figure S32. ^{13}C NMR spectrum (151 MHz) of *meso* **12** in THF-d_8.

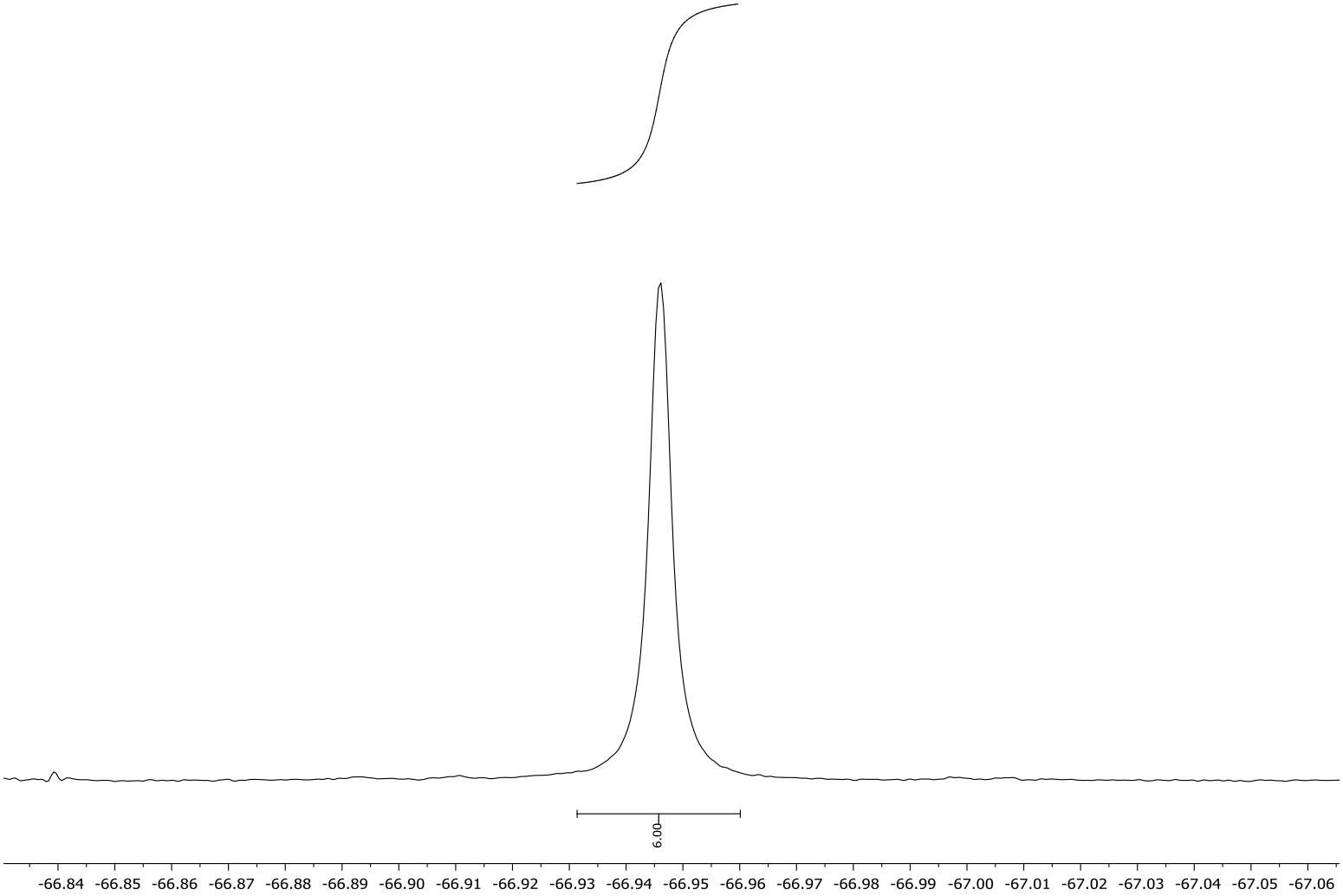

Figure S33. $^{19}F\{^{1}H\}$ NMR spectrum (376 MHz) of *meso* **12** in THF-d_8.

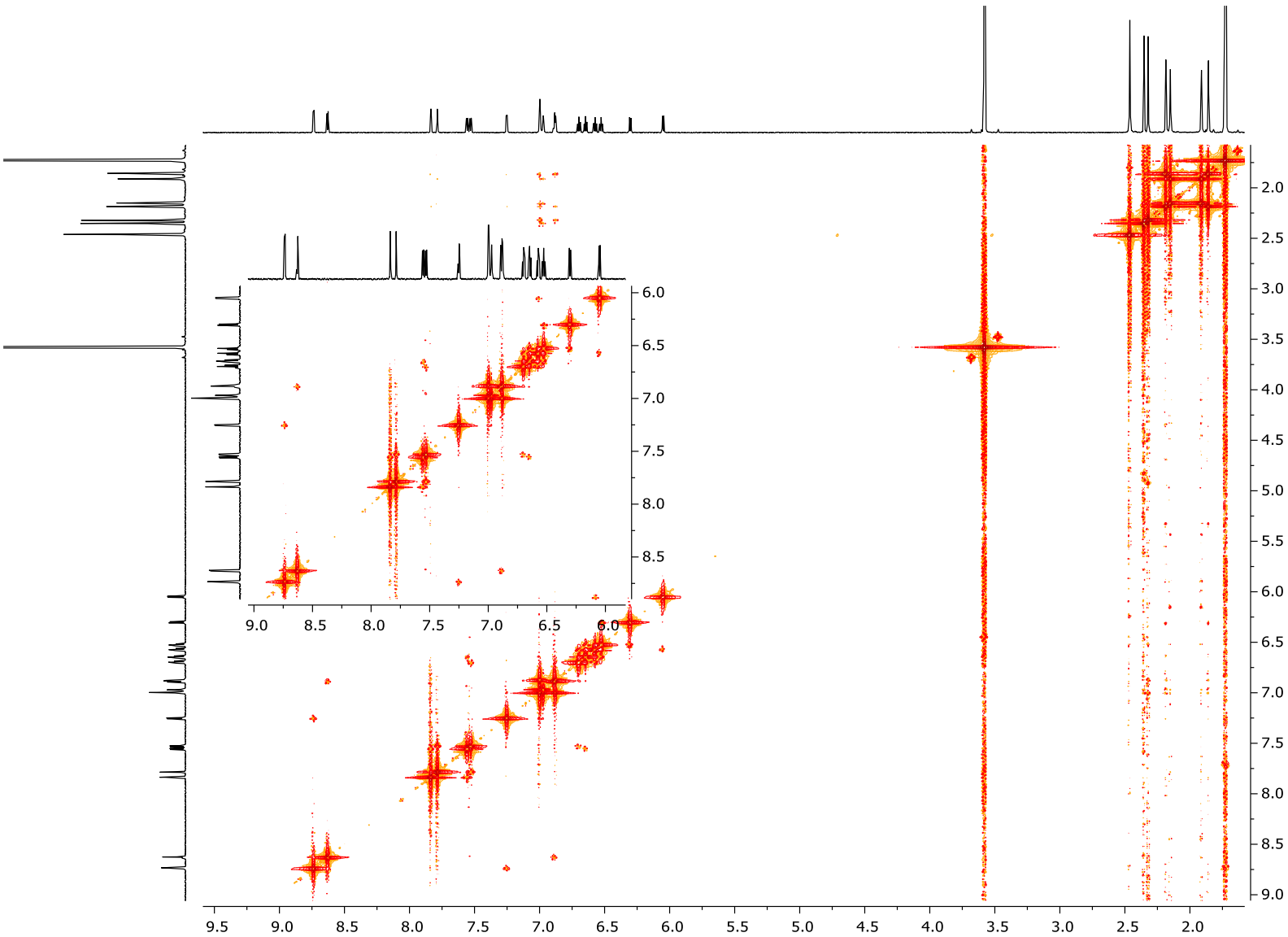

Figure S34. ^{1}H–^{1}H COSY NMR spectrum of *meso* **12** in THF-d_8.

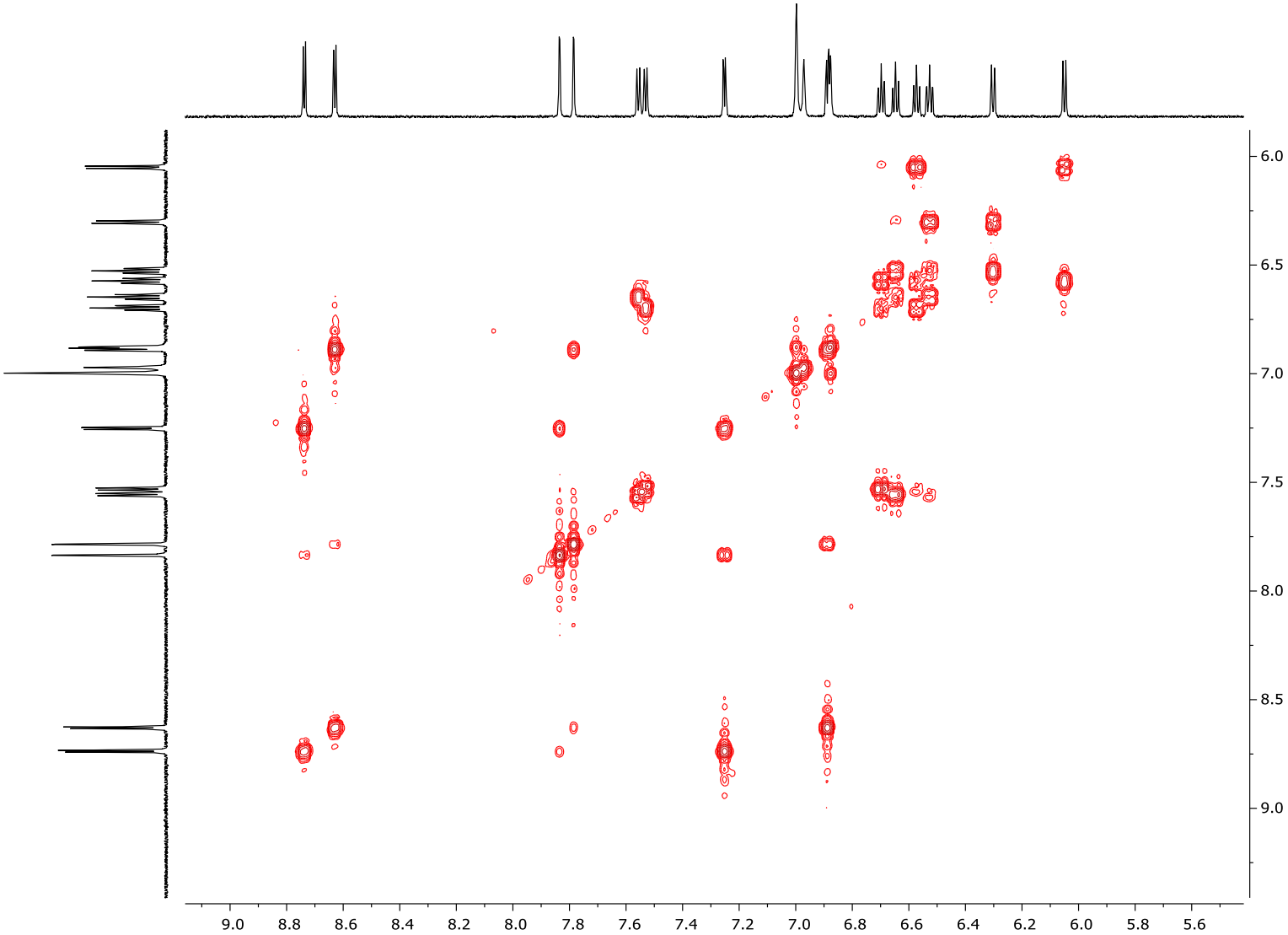

Figure S35. Expansion of the aromatic region of the ^{1}H–^{1}H COSY NMR spectrum of *meso* **12** in THF-d_8.

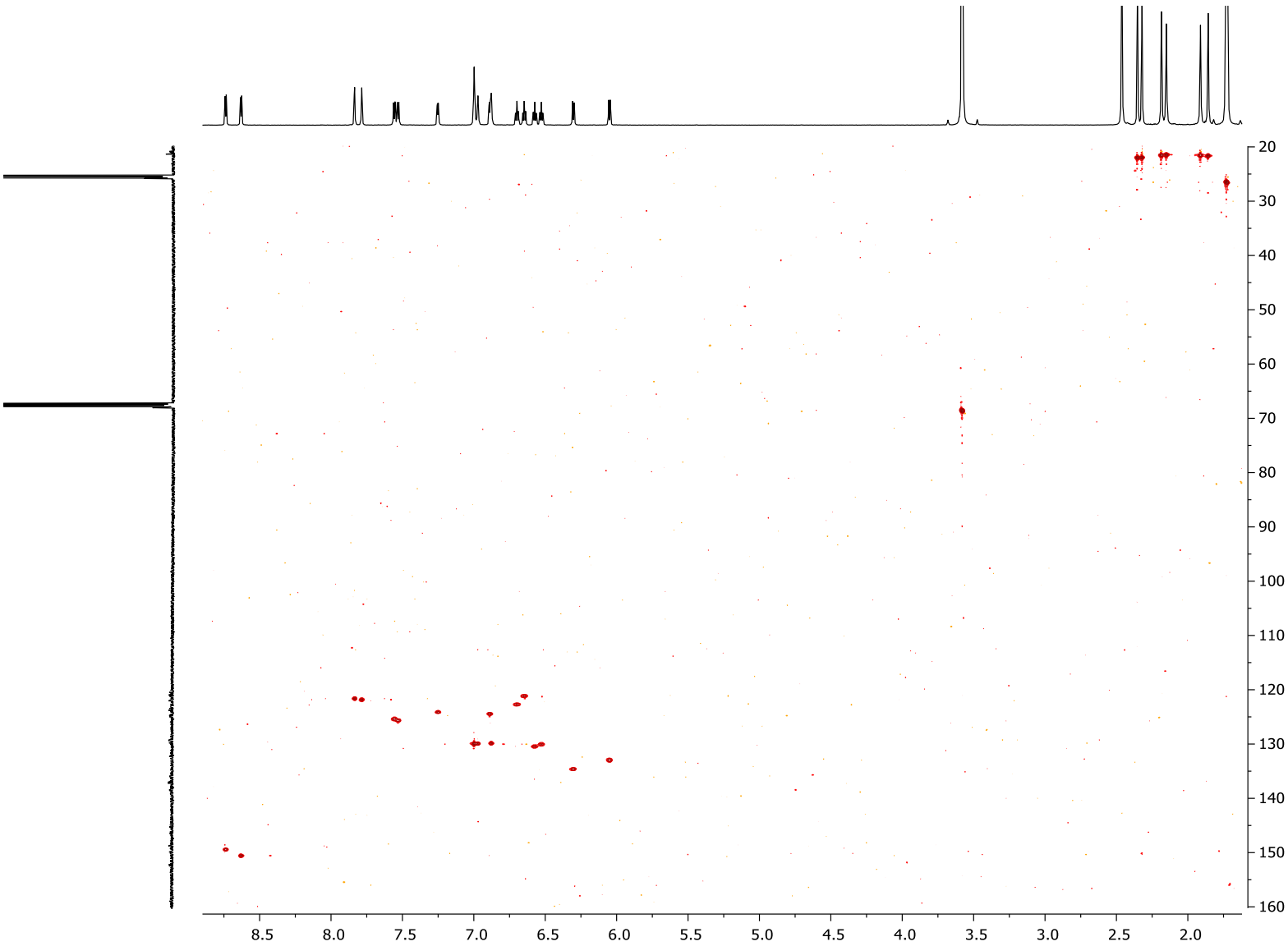

Figure S36. ^{1}H–^{13}C HSQC NMR spectrum of *meso* **12** in THF-d_8.

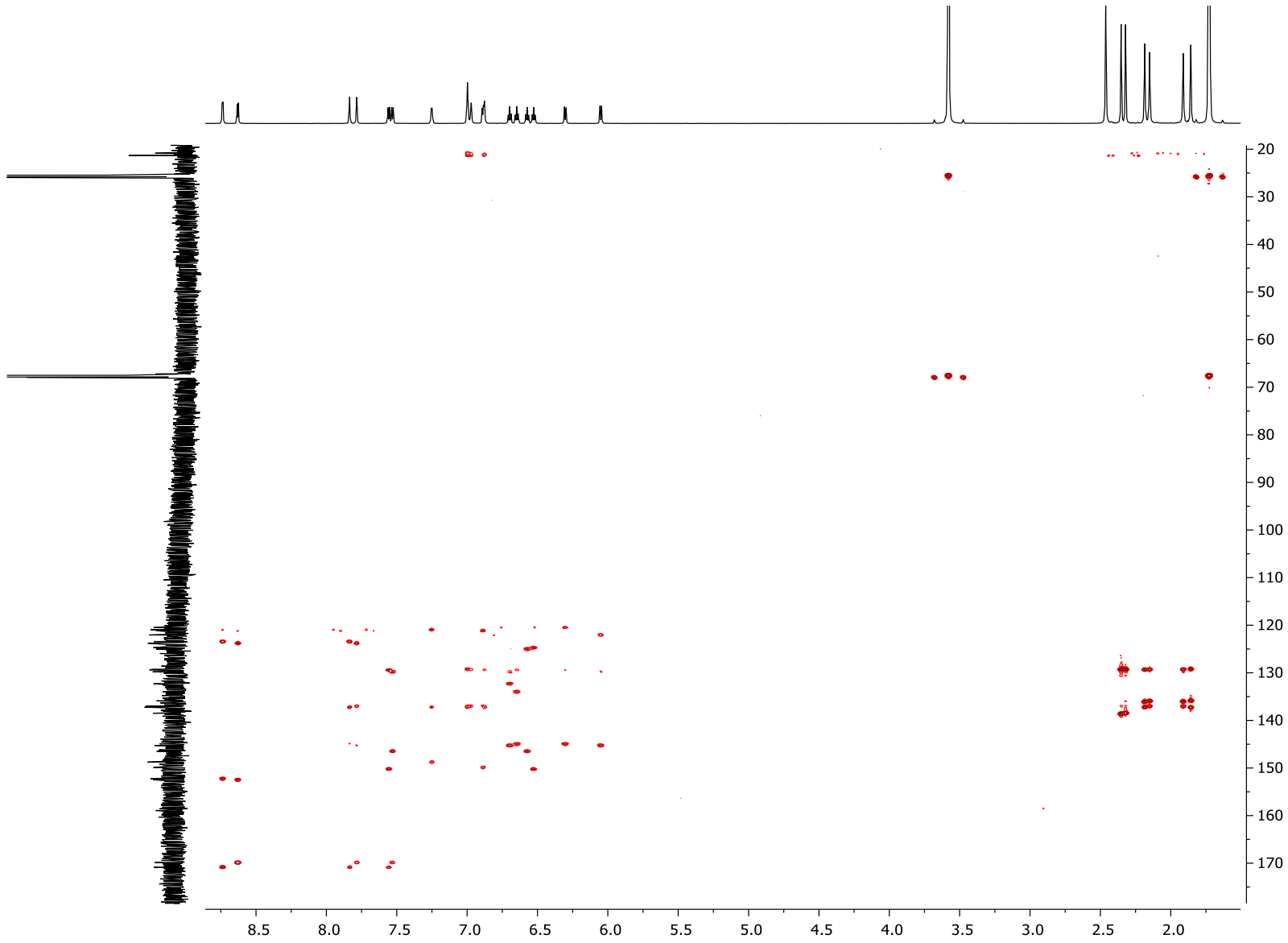

Figure S37. ^{1}H–^{13}C HMBC NMR spectrum of *meso* **12** in THF-d_8.

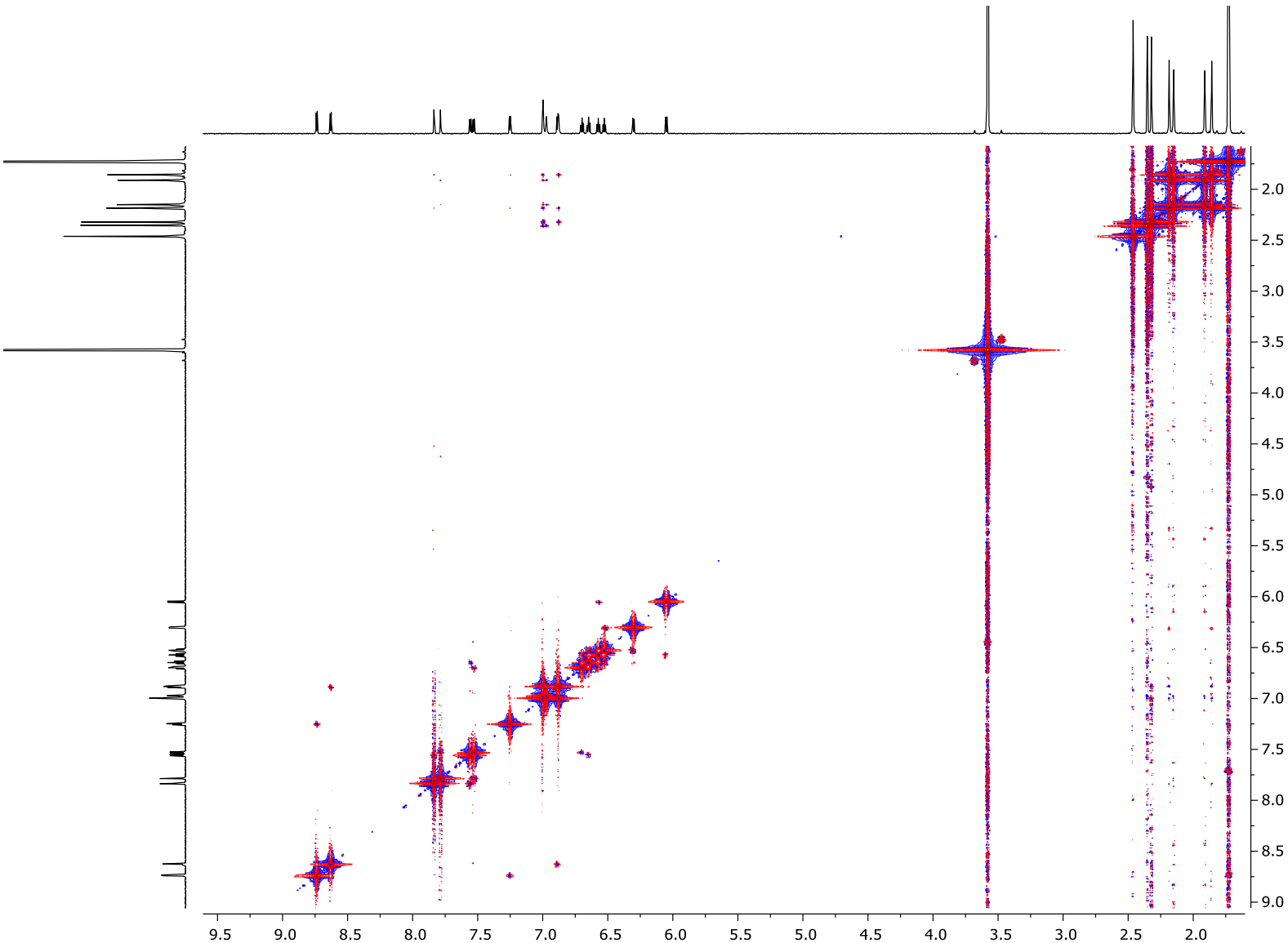

Figure S38. ^{1}H–^{1}H NOESY NMR spectrum of *meso* **12** in THF-d_8.

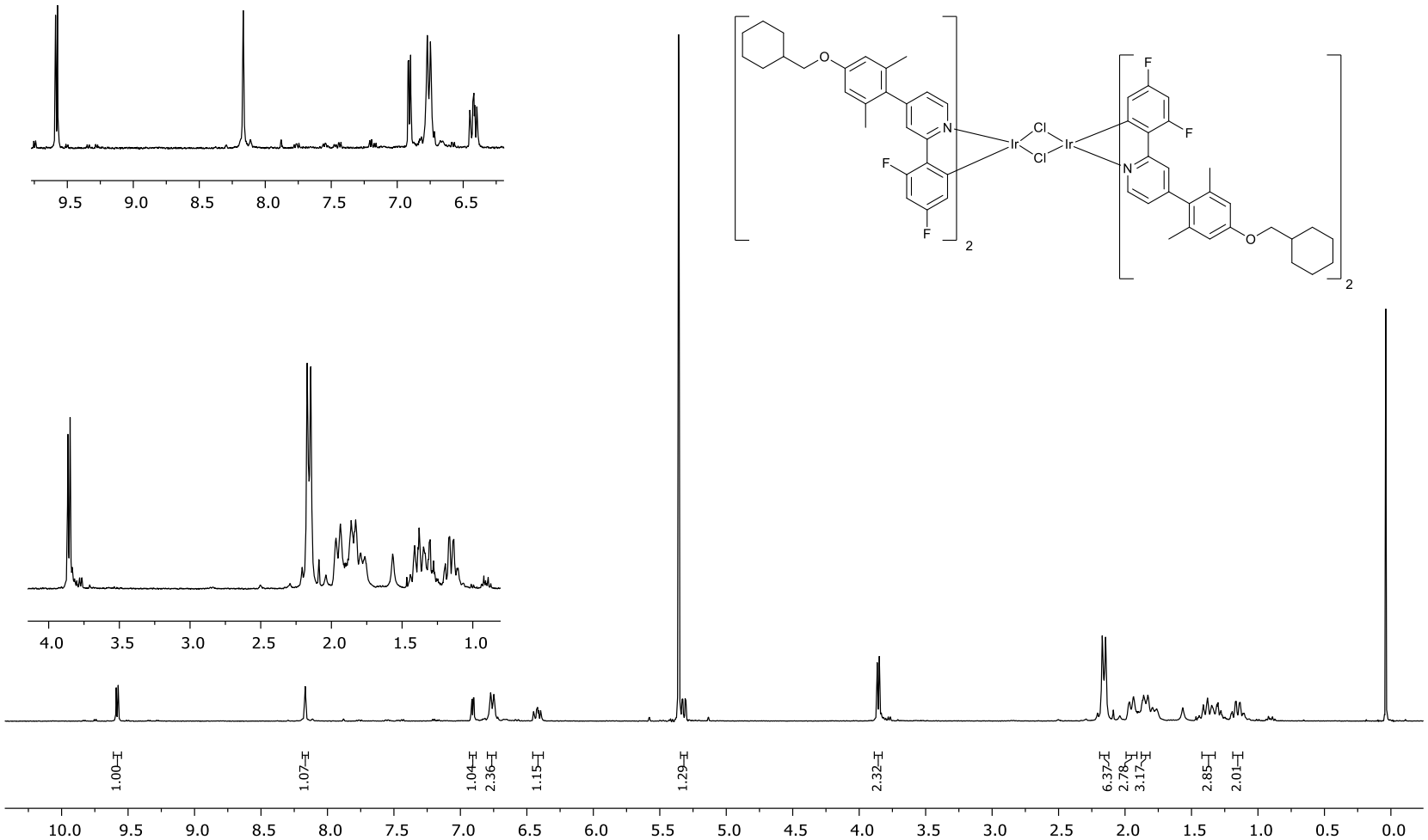

Figure S39. ^{1}H NMR spectrum (400 MHz) of the μ–dichloro dimer isolated as an intermediate in the synthesis of complex **13** in CD_2Cl_2 (TMS).

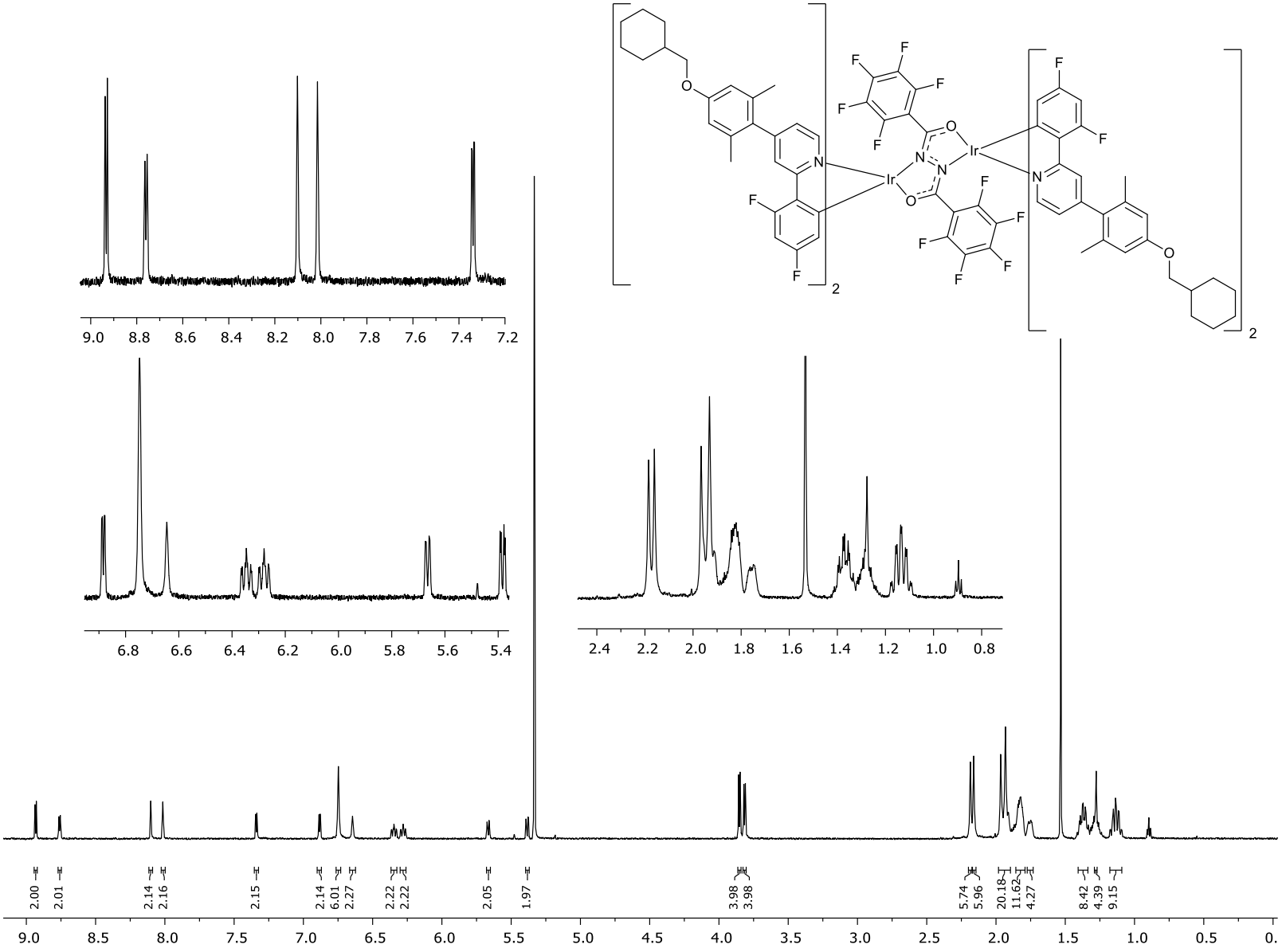

Figure S40. ^{1}H NMR spectrum (600 MHz) of *meso* **13** in CD_2Cl_2.

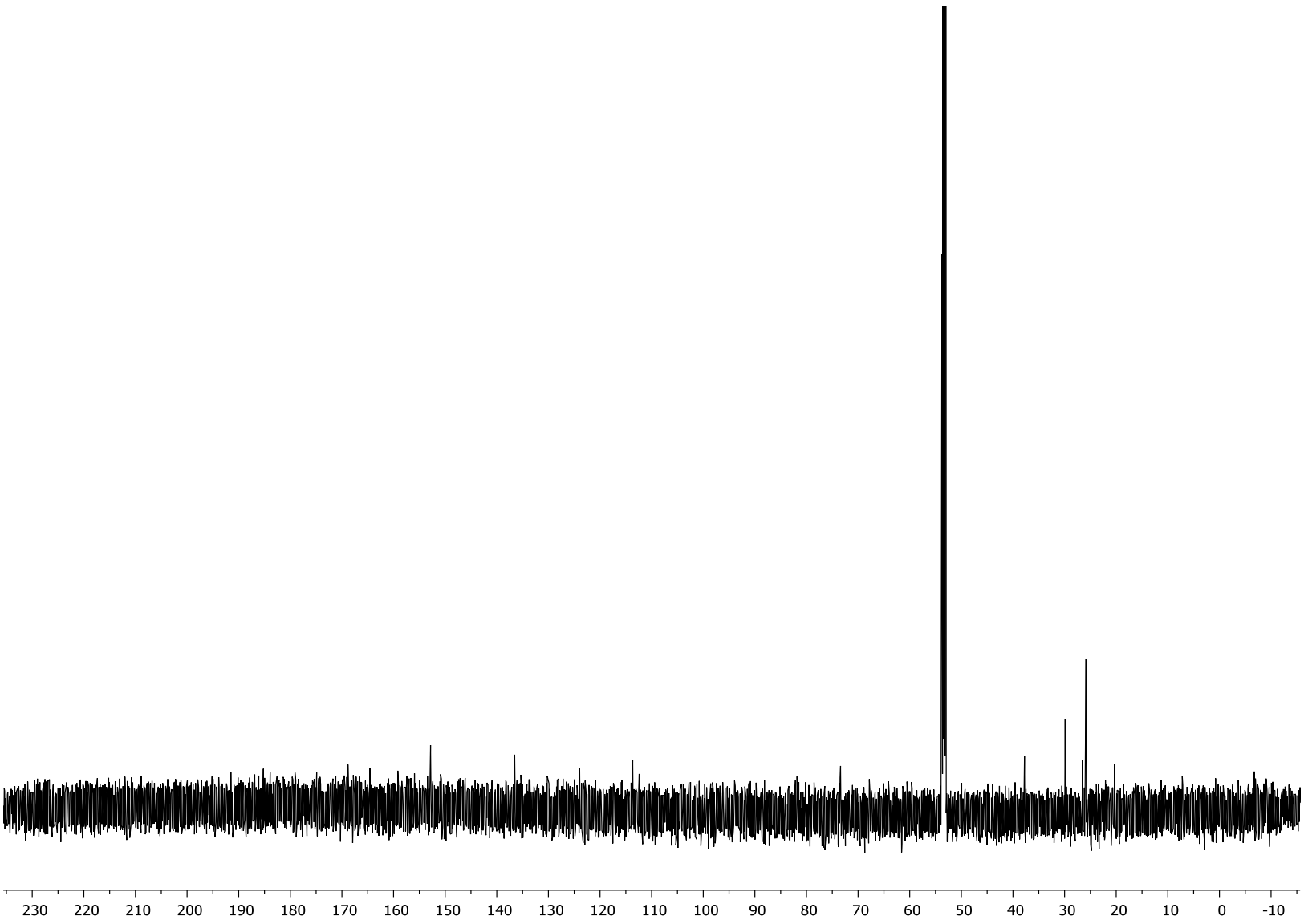

Figure S41. ^{13}C NMR spectrum (151 MHz) of *meso* **13** in CD_2Cl_2.

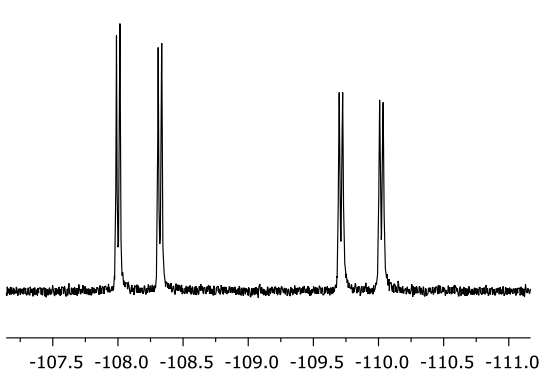

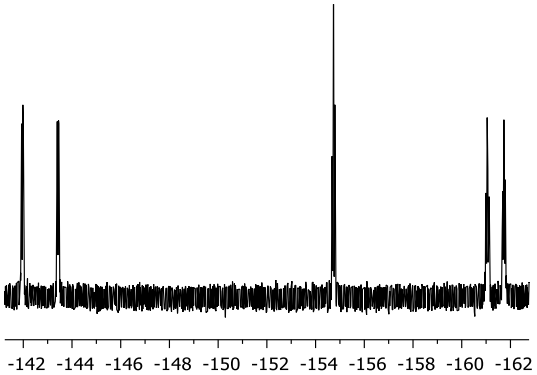

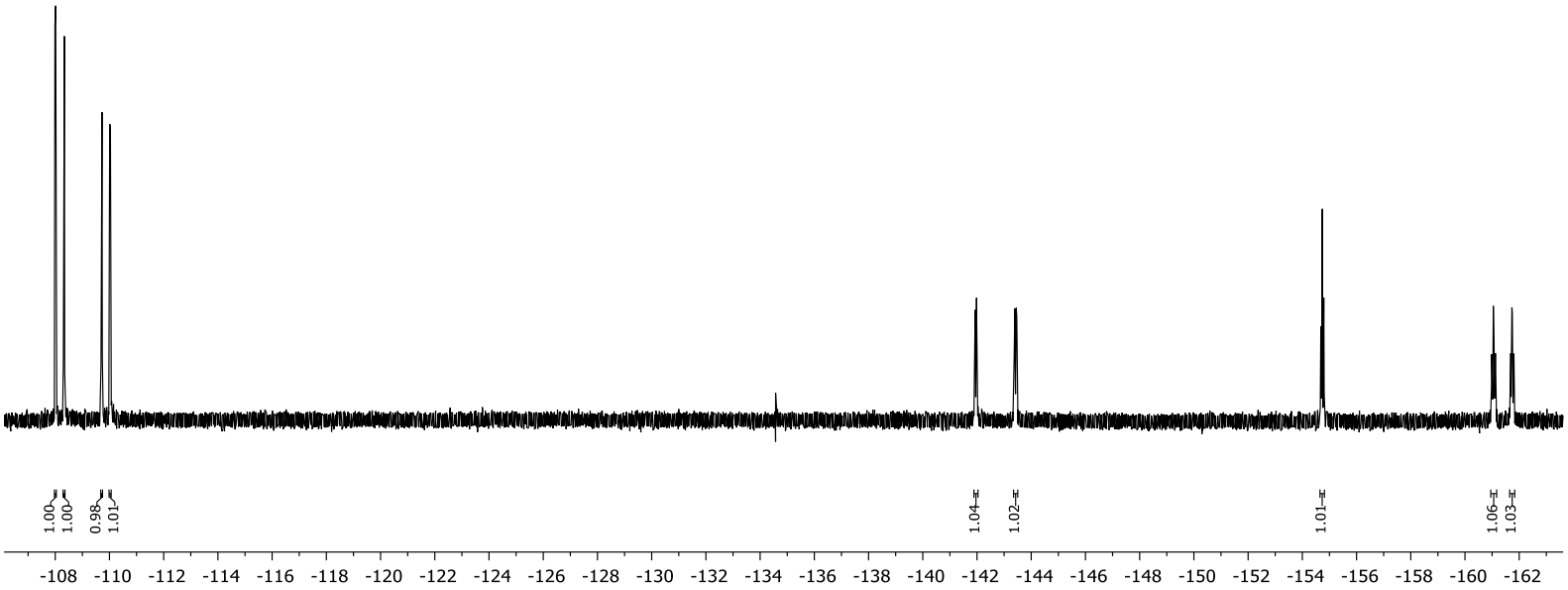

Figure S42. $^{19}F\{^{1}H\}$ NMR spectrum (376 MHz) of *meso* **13** in CD_2Cl_2**.**

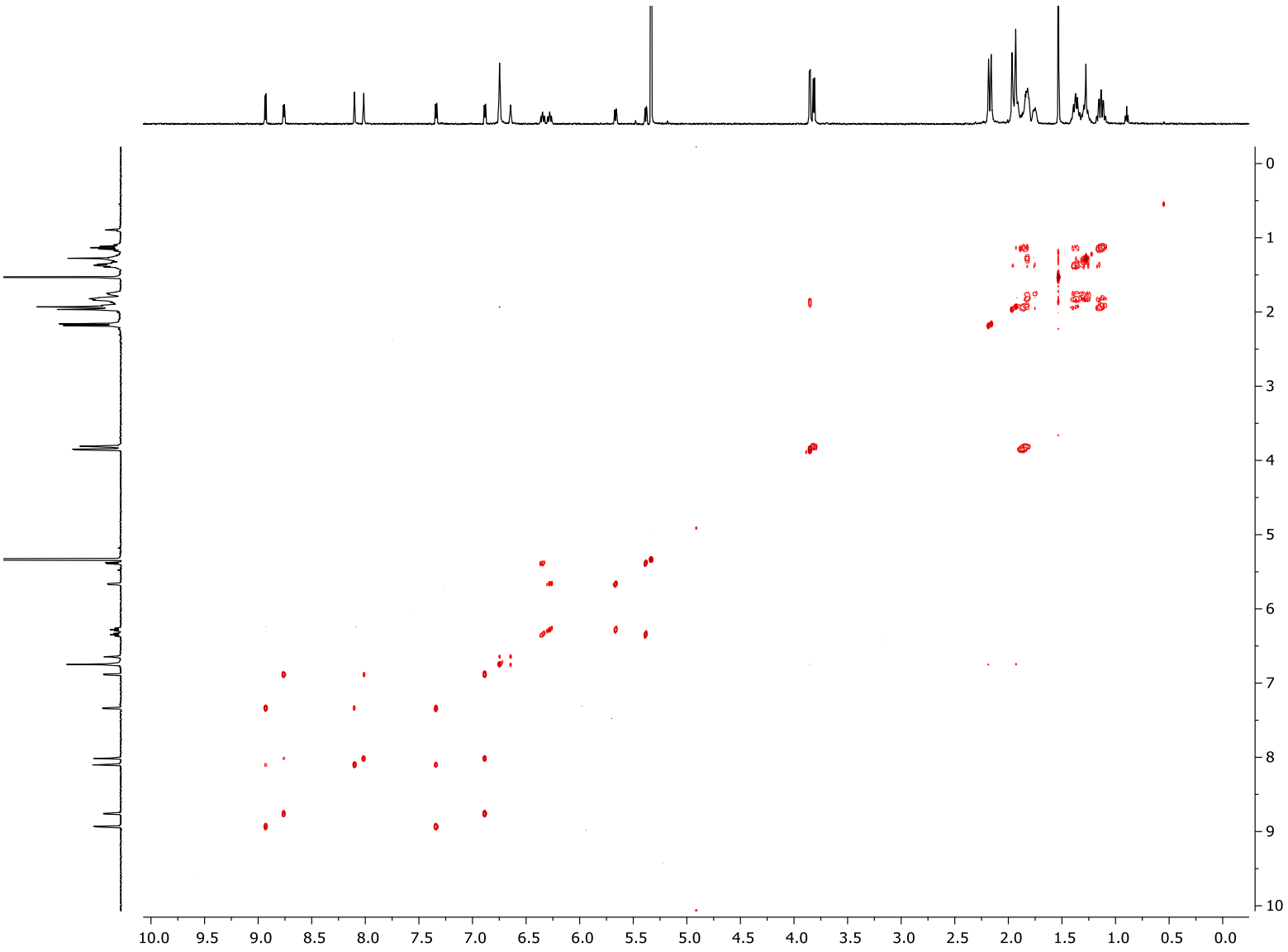

Figure S43. ^{1}H–^{1}H COSY NMR spectrum of *meso* **13** in CD_2Cl_2.

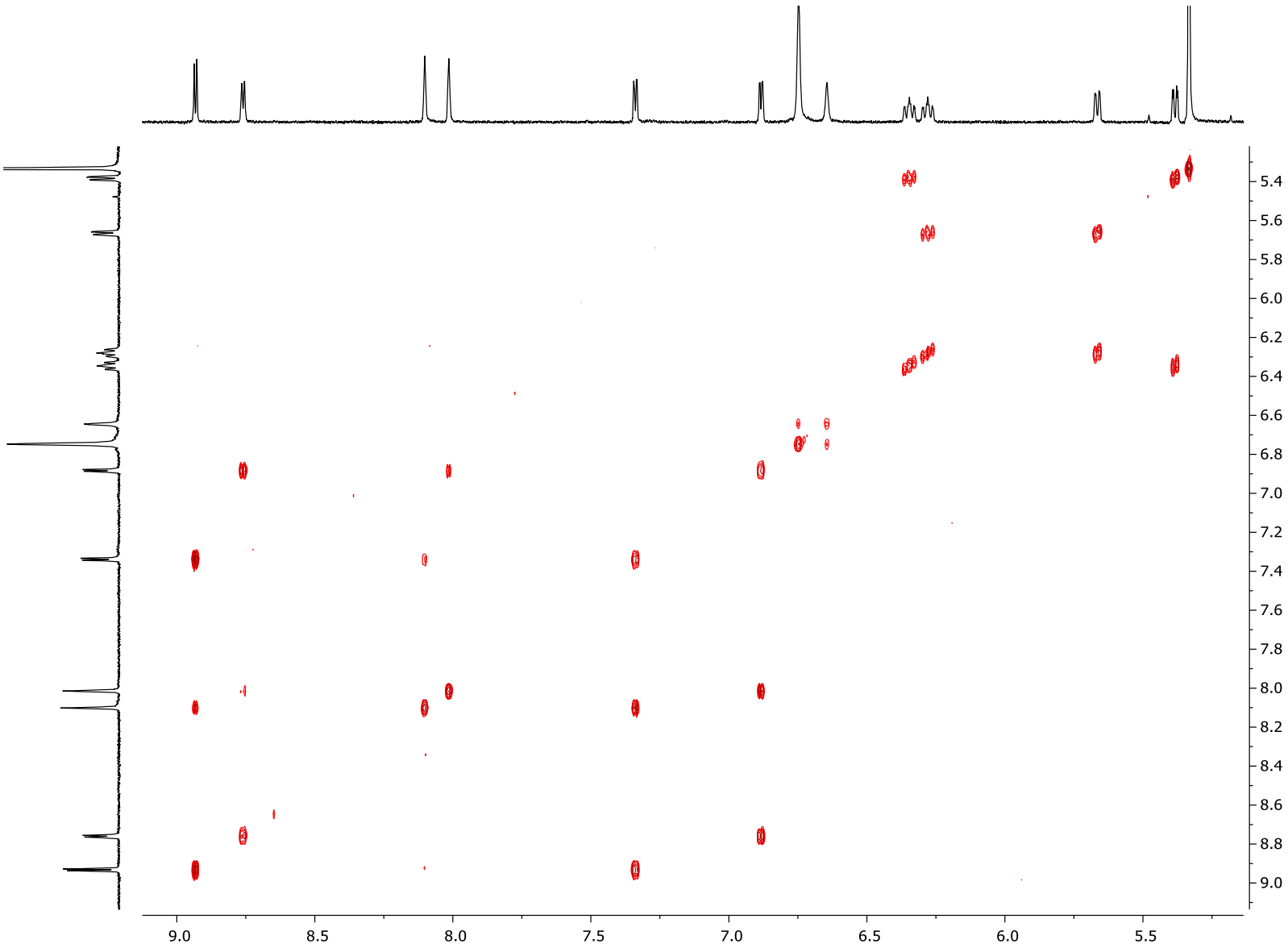

Figure S44. Expansion of the aromatic region of the ^{1}H–^{1}H COSY NMR spectrum of *meso* **13** in CD_2Cl_2.

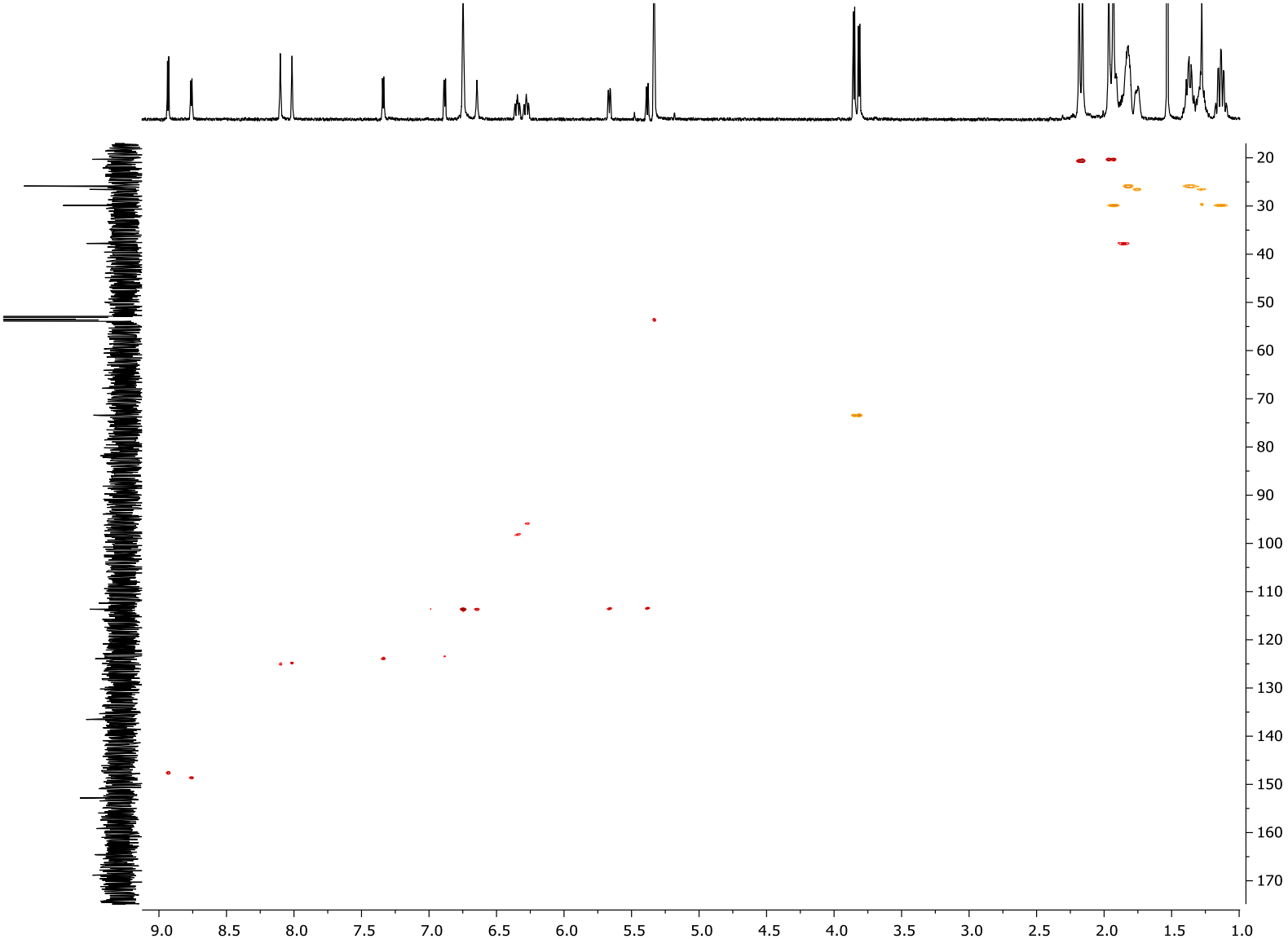

Figure S45. ^{1}H–^{13}C HSQC NMR spectrum of *meso* **13** in CD_2Cl_2.

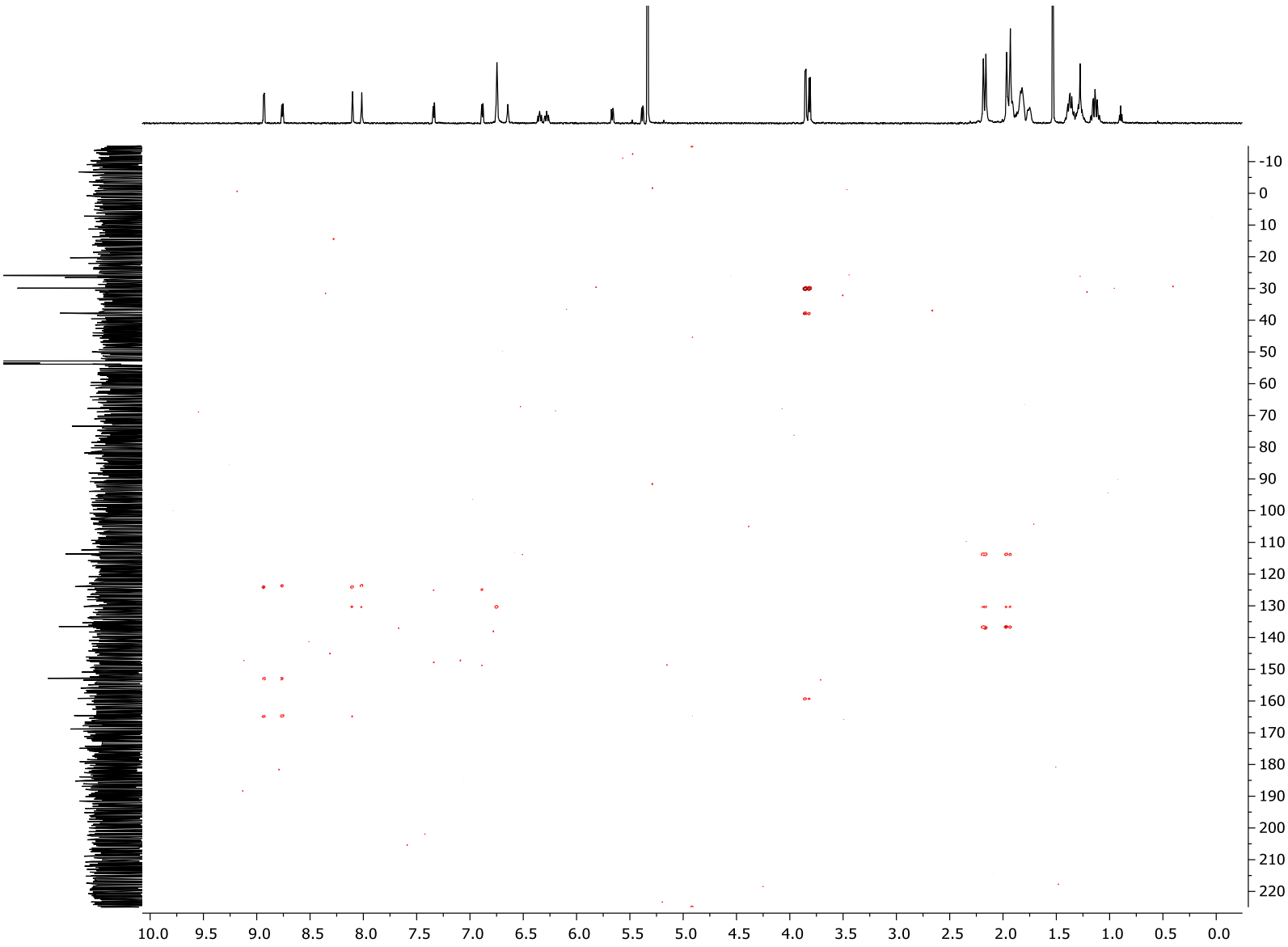

Figure S46. $^{1}H–^{13}C$ HMBC NMR spectrum of *meso* **13** in CD_2Cl_2.

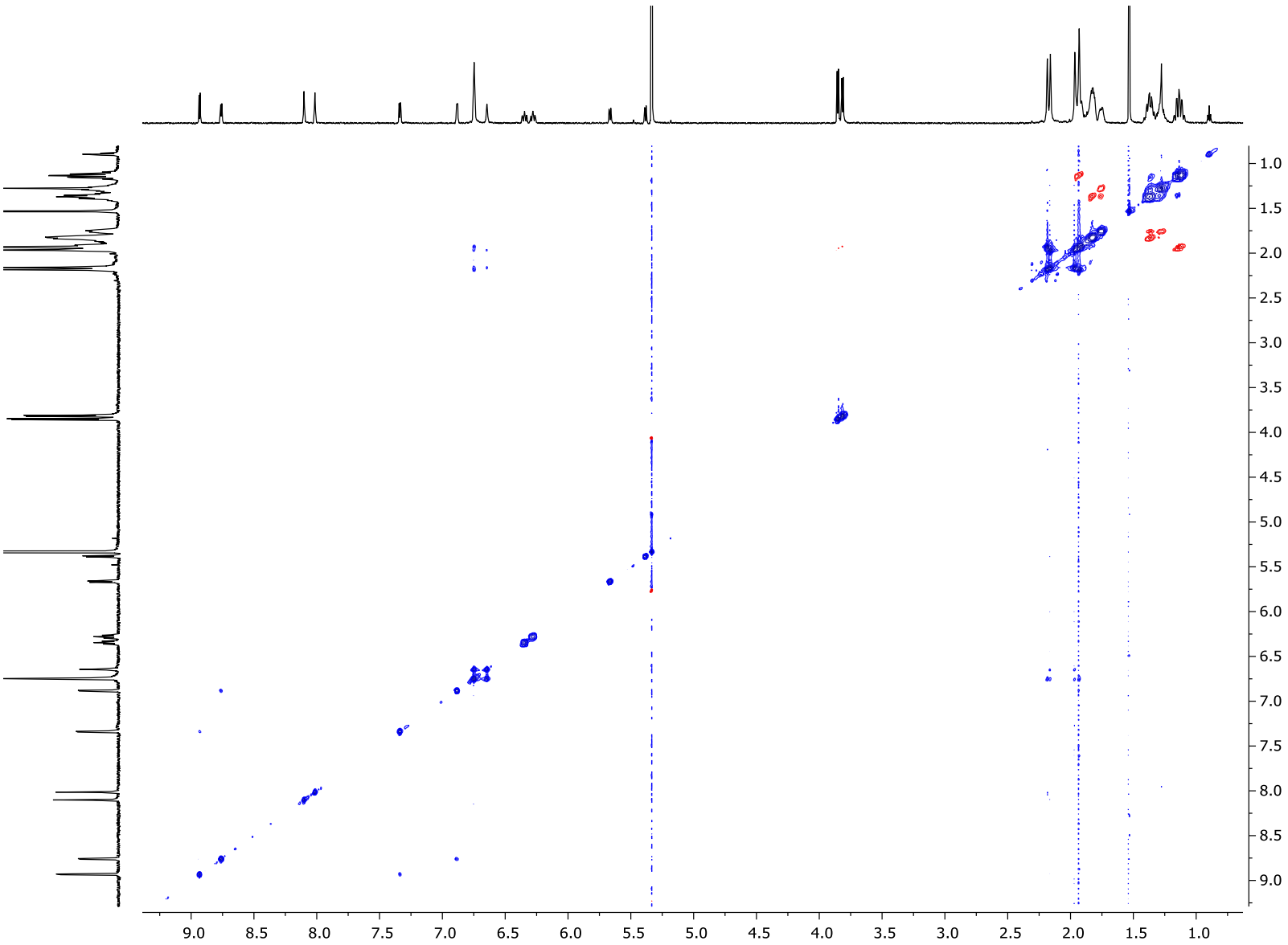

Figure S47. ^{1}H–^{1}H NOESY NMR spectrum of *meso* **13** in CD_2Cl_2.

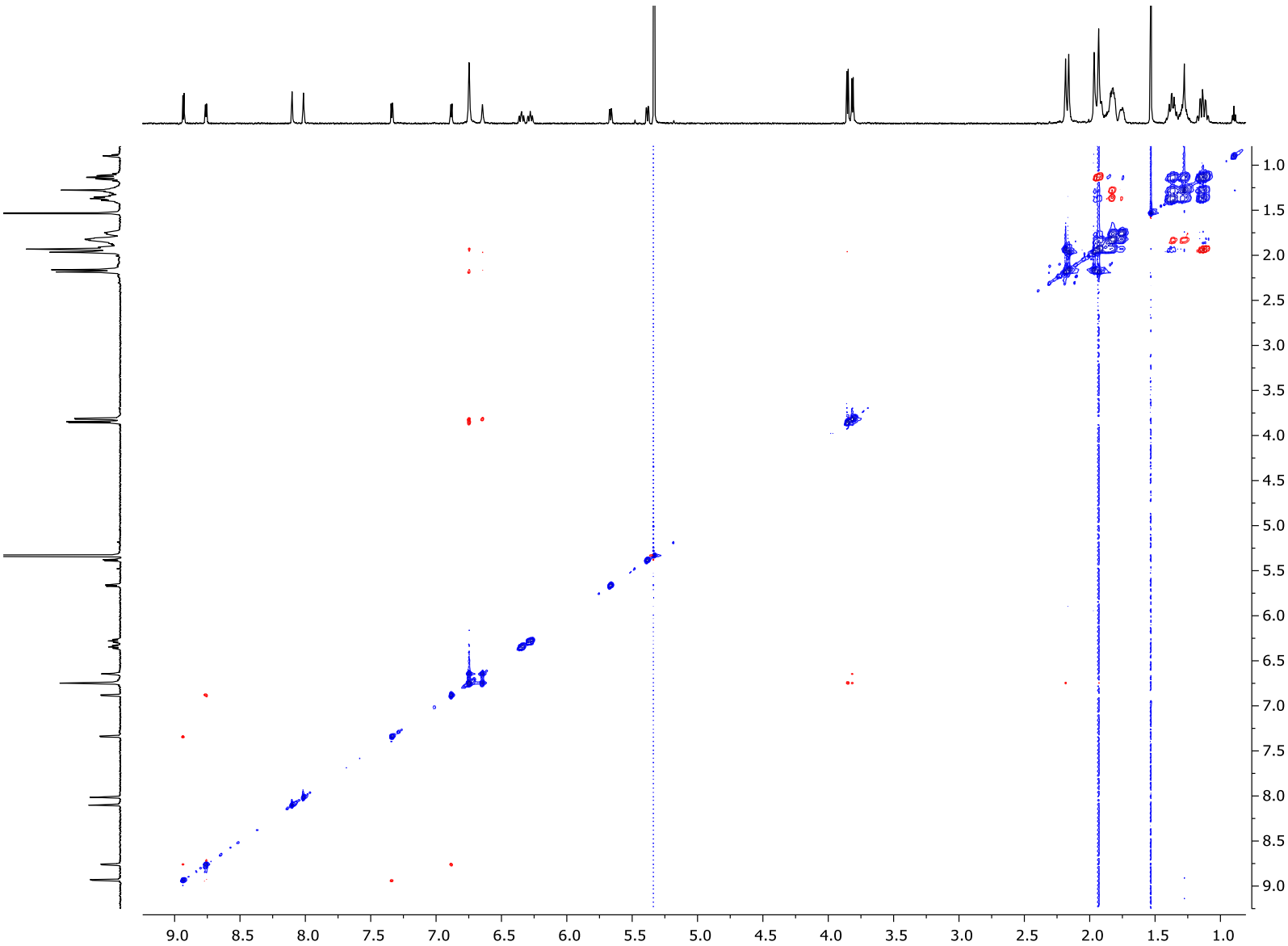

Figure S48. ^{1}H–^{1}H ROESY NMR spectrum of *meso* **13** in CD_2Cl_2.

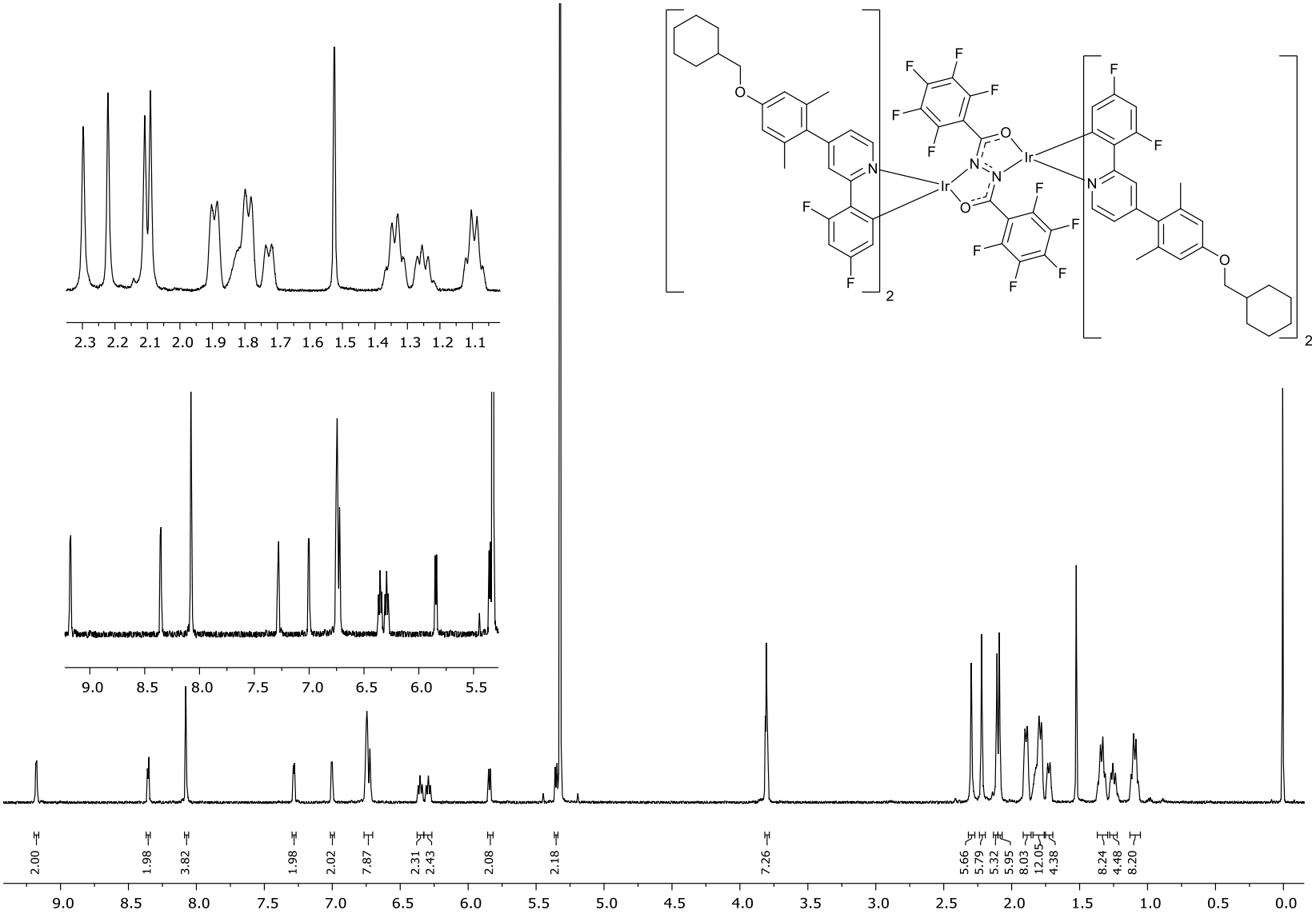

Figure S49. ^{1}H NMR spectrum (700 MHz) of *rac* **13** in CD_2Cl_2 (TMS).

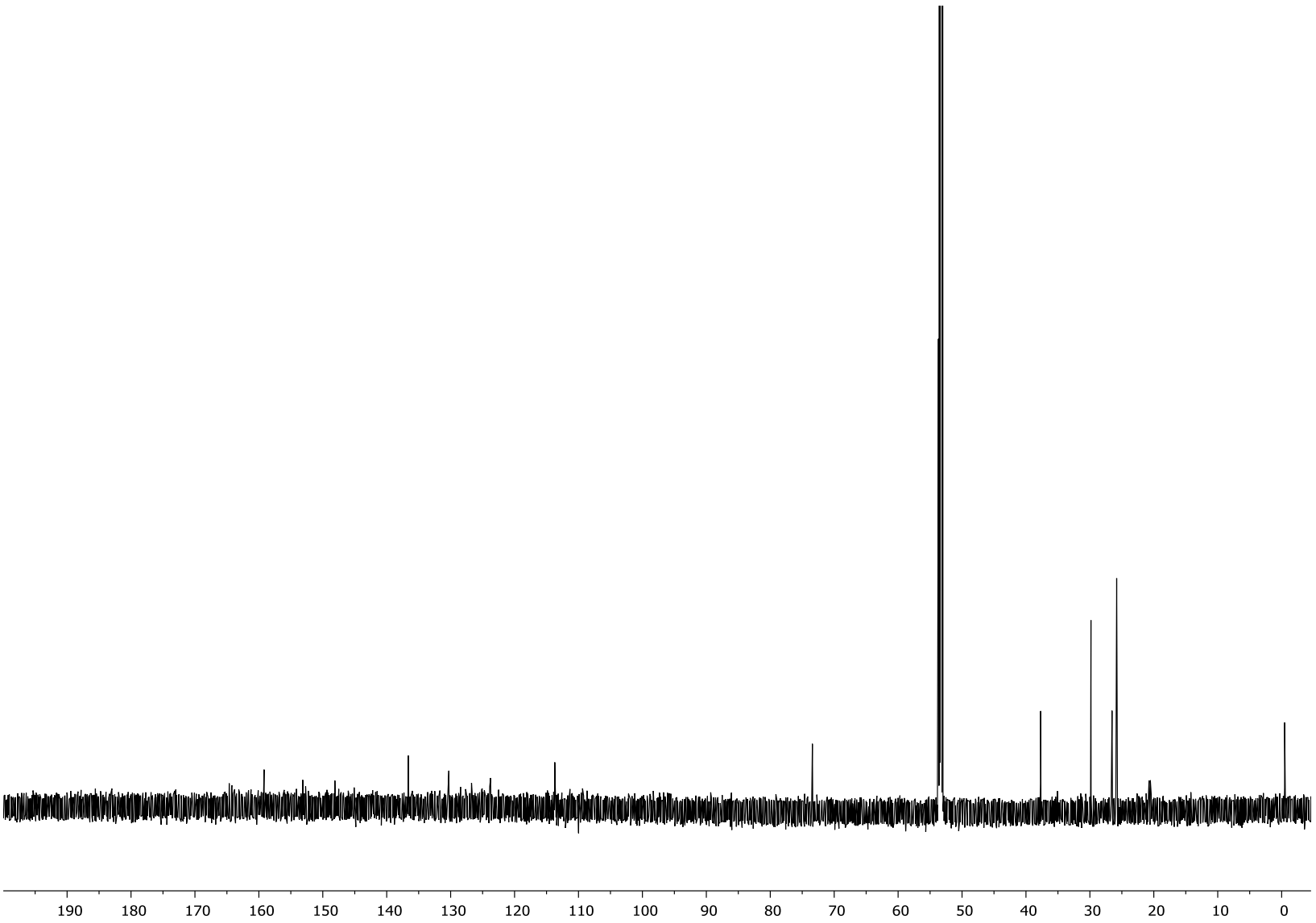

Figure S50. ^{13}C NMR spectrum (151 MHz) of *rac* **13** in CD_2Cl_2 (TMS).

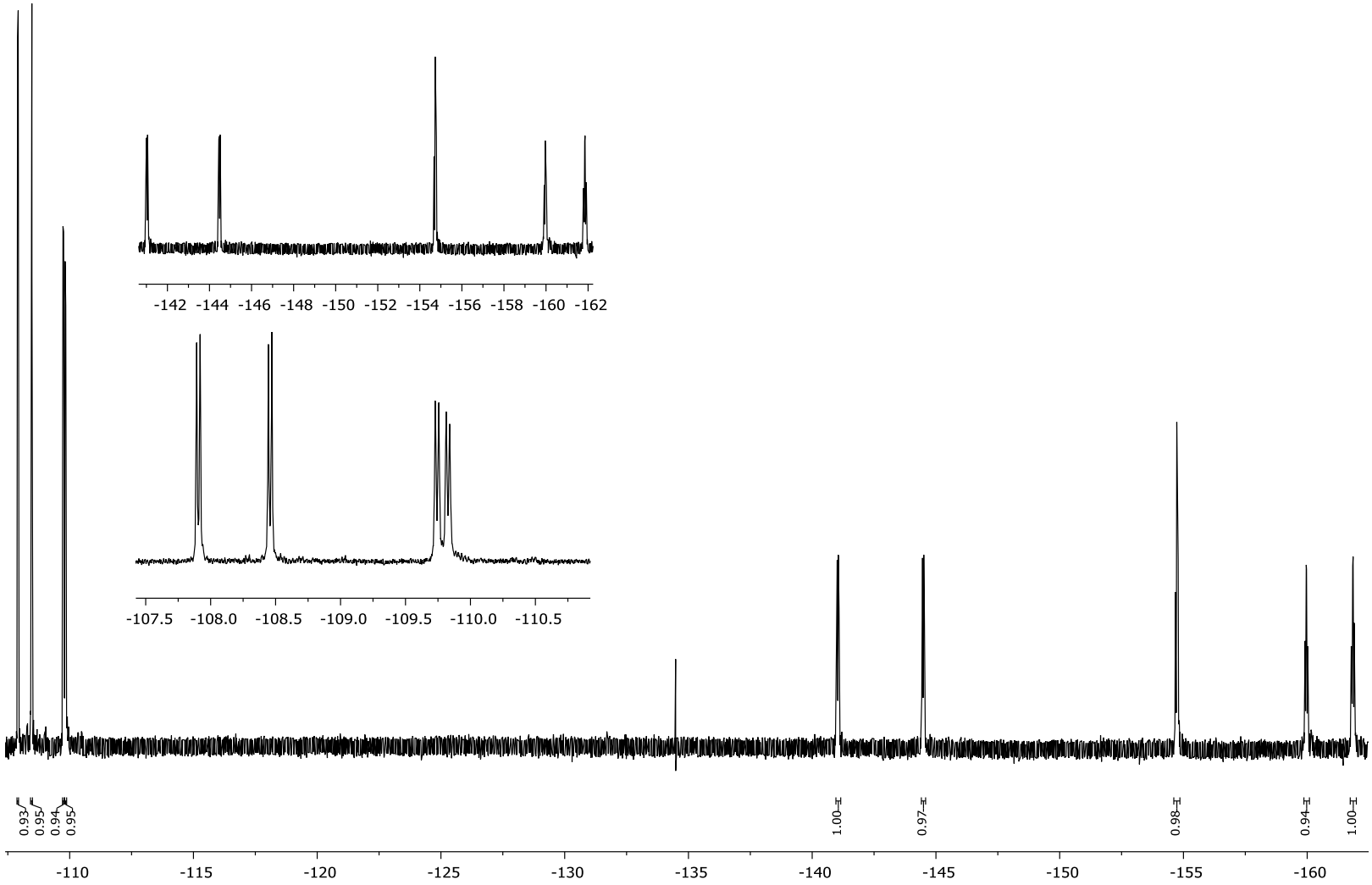

Figure S51. $^{19}F\{^{1}H\}$ NMR spectrum (376 MHz) of *rac* **13** in CD_2Cl_2**.**

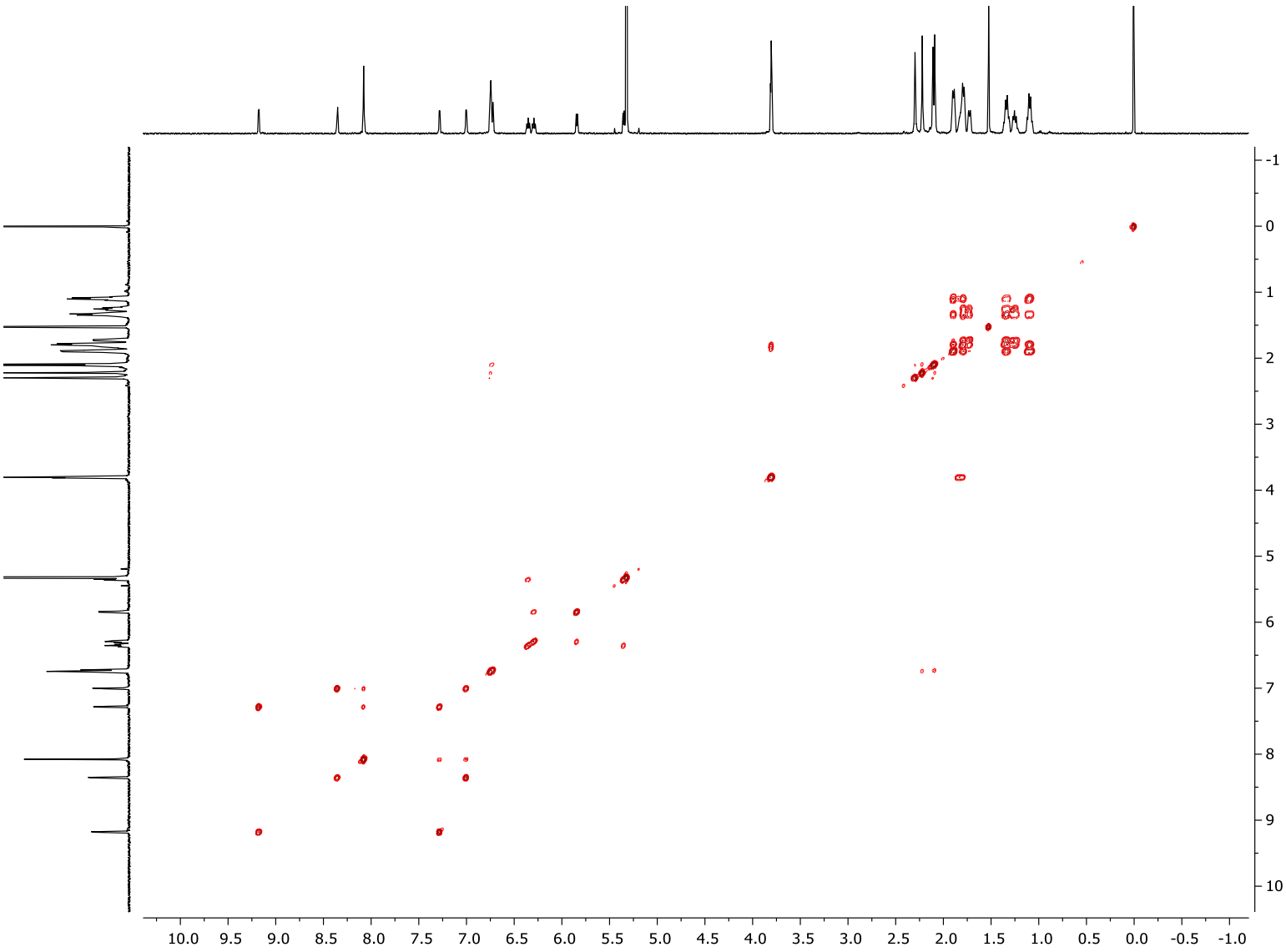

Figure S52. ^{1}H–^{1}H COSY NMR spectrum of *rac* **13** in CD_2Cl_2 (TMS).

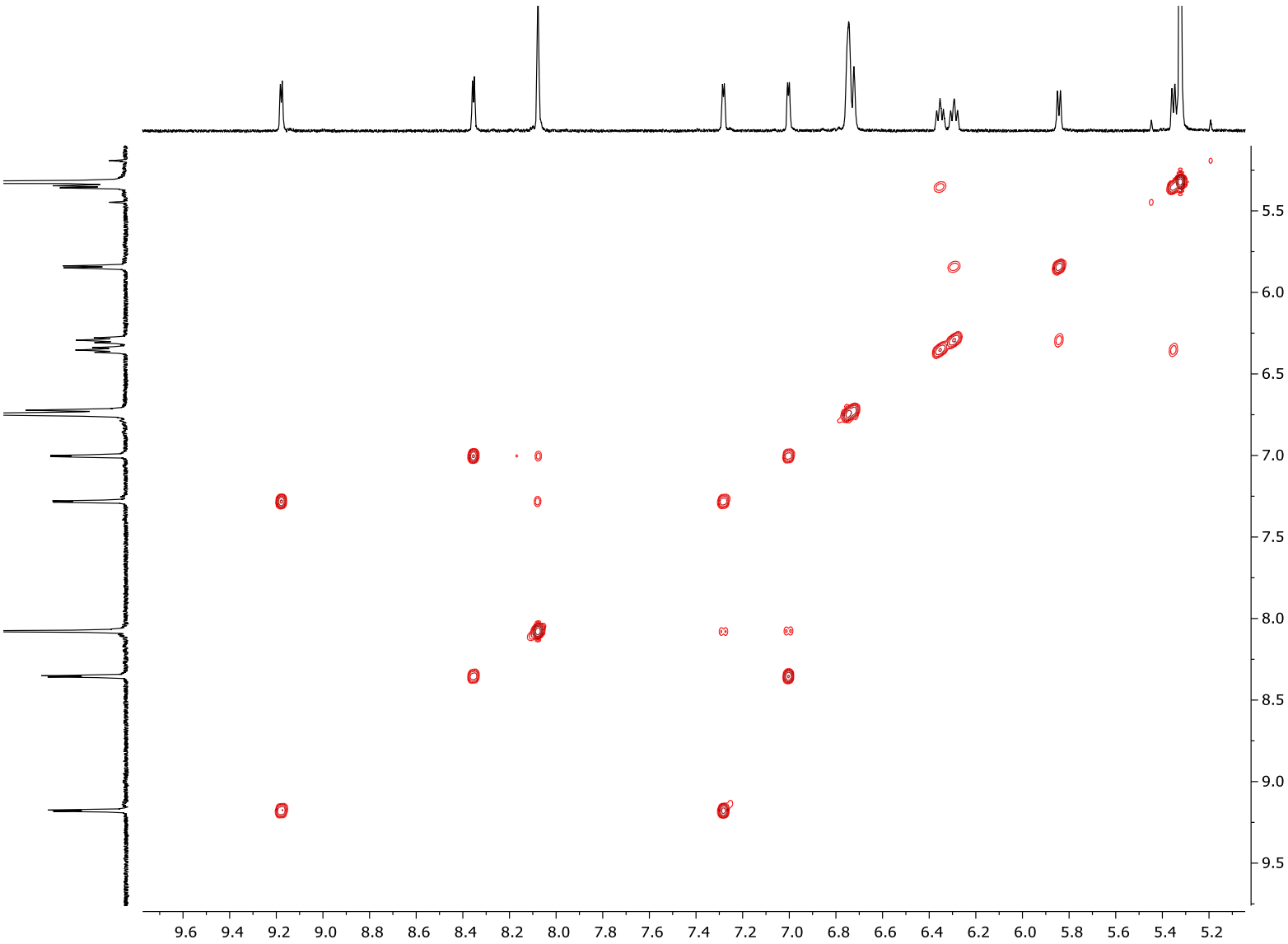

Figure S53. Expansion of the aromatic region of the ^{1}H–^{1}H COSY NMR spectrum of *rac* **13** in CD_2Cl_2 (TMS).

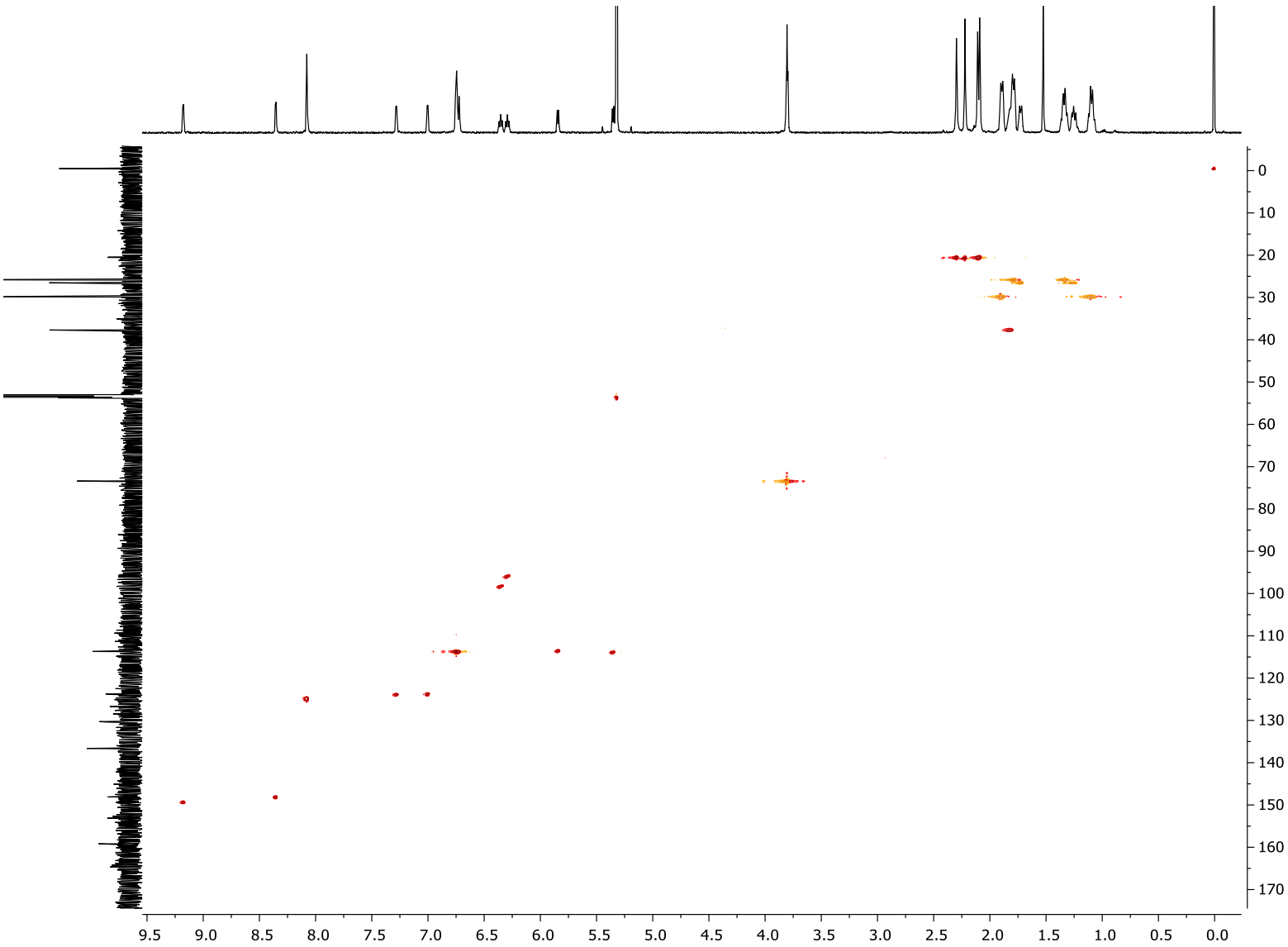

Figure S54. ^{1}H–^{13}C HSQC NMR spectrum of *rac* **13** in CD_2Cl_2 (TMS).

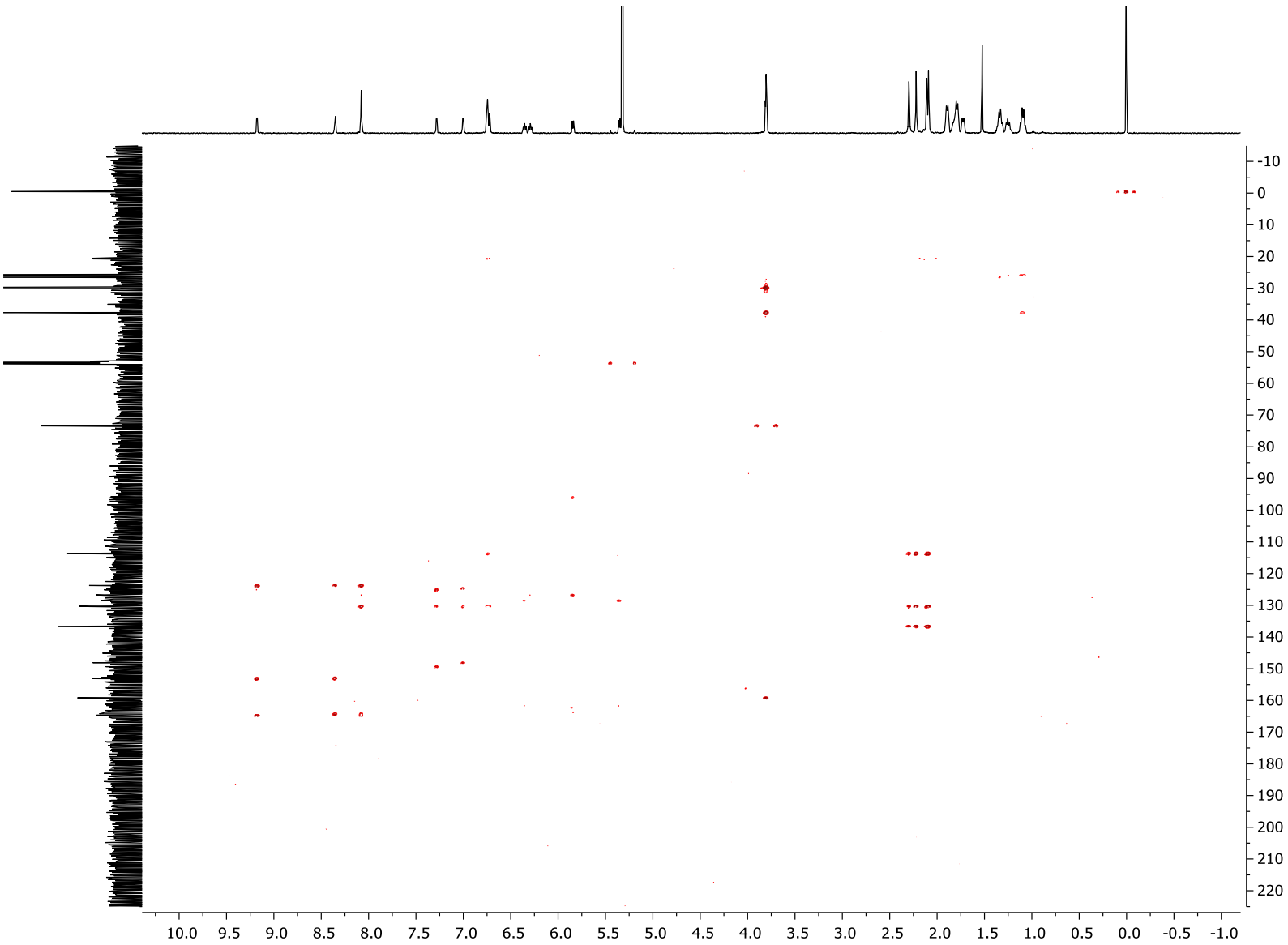

Figure S55. ^{1}H–^{13}C HMBC NMR spectrum of *rac* **13** in CD_2Cl_2 (TMS).

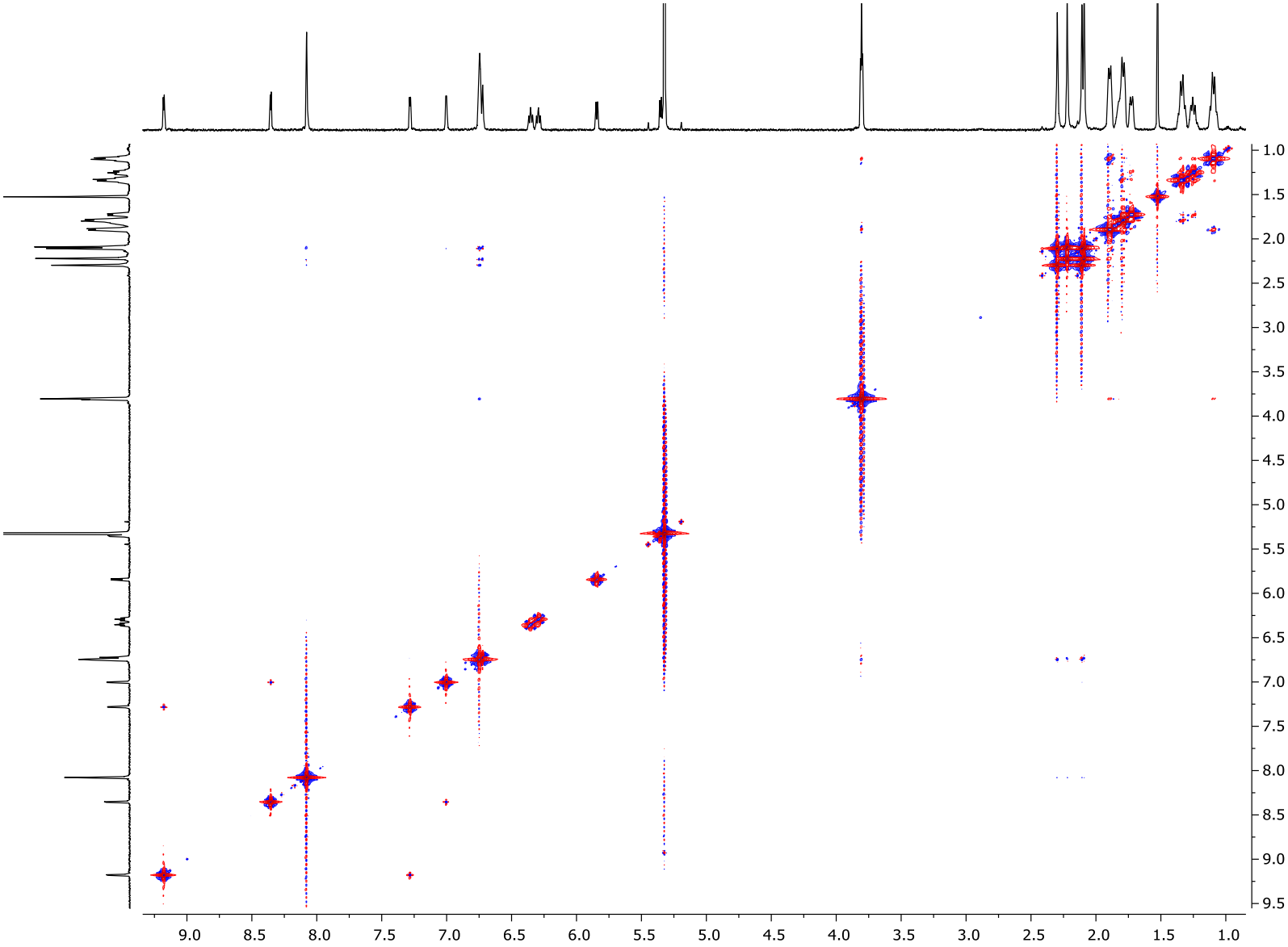

Figure S56. ^{1}H–^{1}H NOESY NMR spectrum of *rac* **13** in CD_2Cl_2 (TMS).

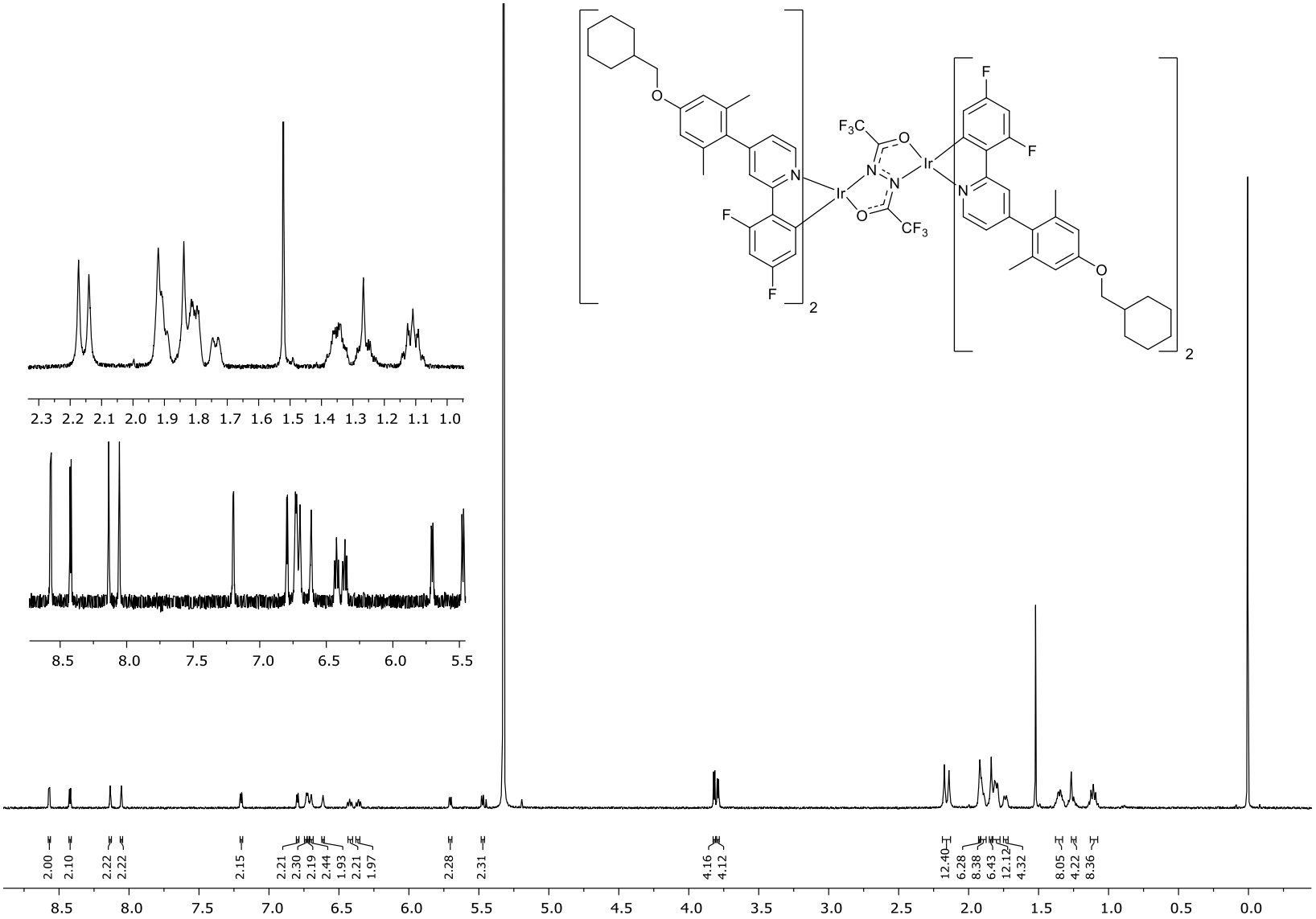

Figure S57. ^{1}H NMR spectrum (700 MHz) of **14** in CD_2Cl_2 (TMS).

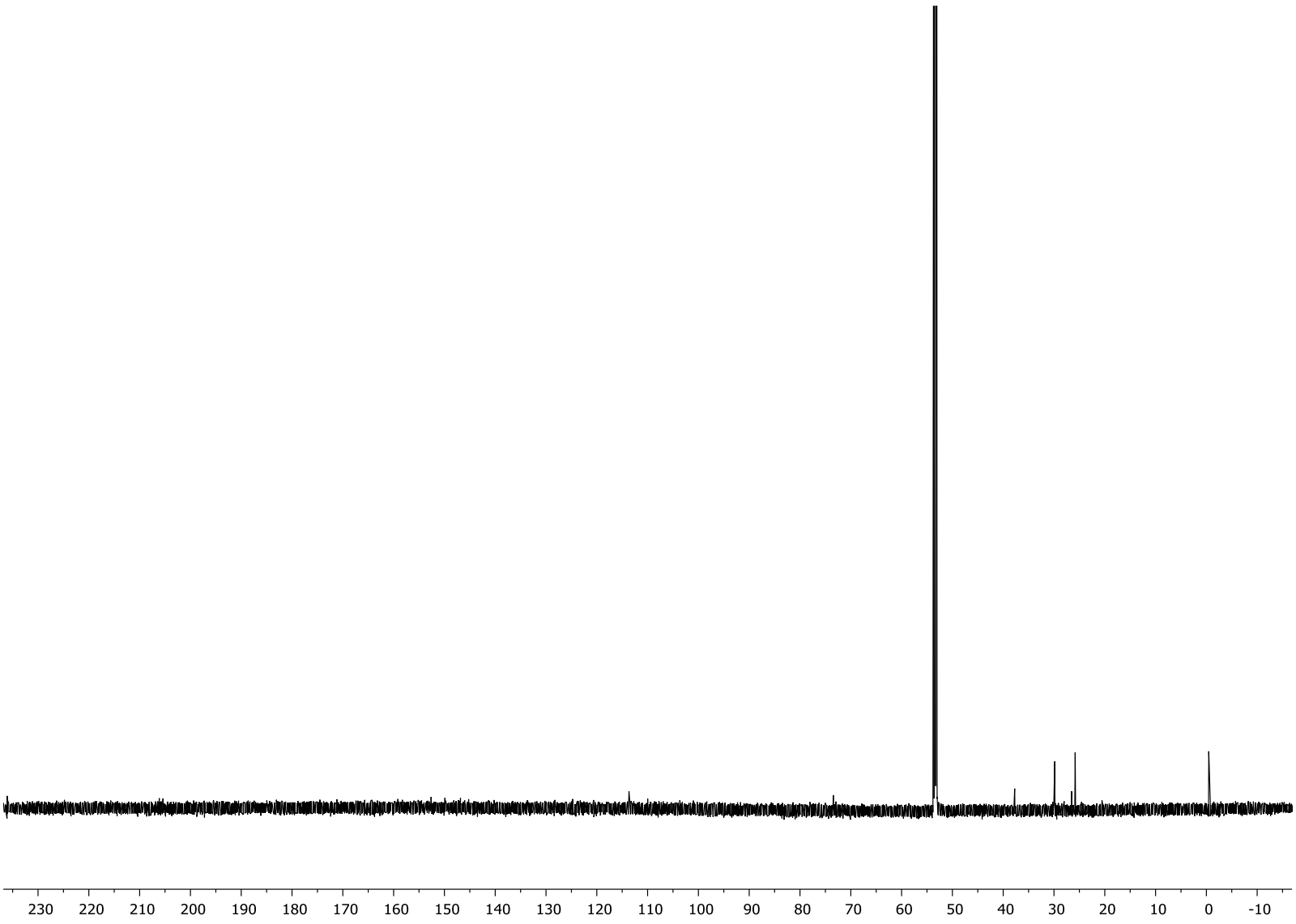

Figure S58. ^{13}C NMR spectrum (151 MHz) of **14** in CD_2Cl_2 (TMS).

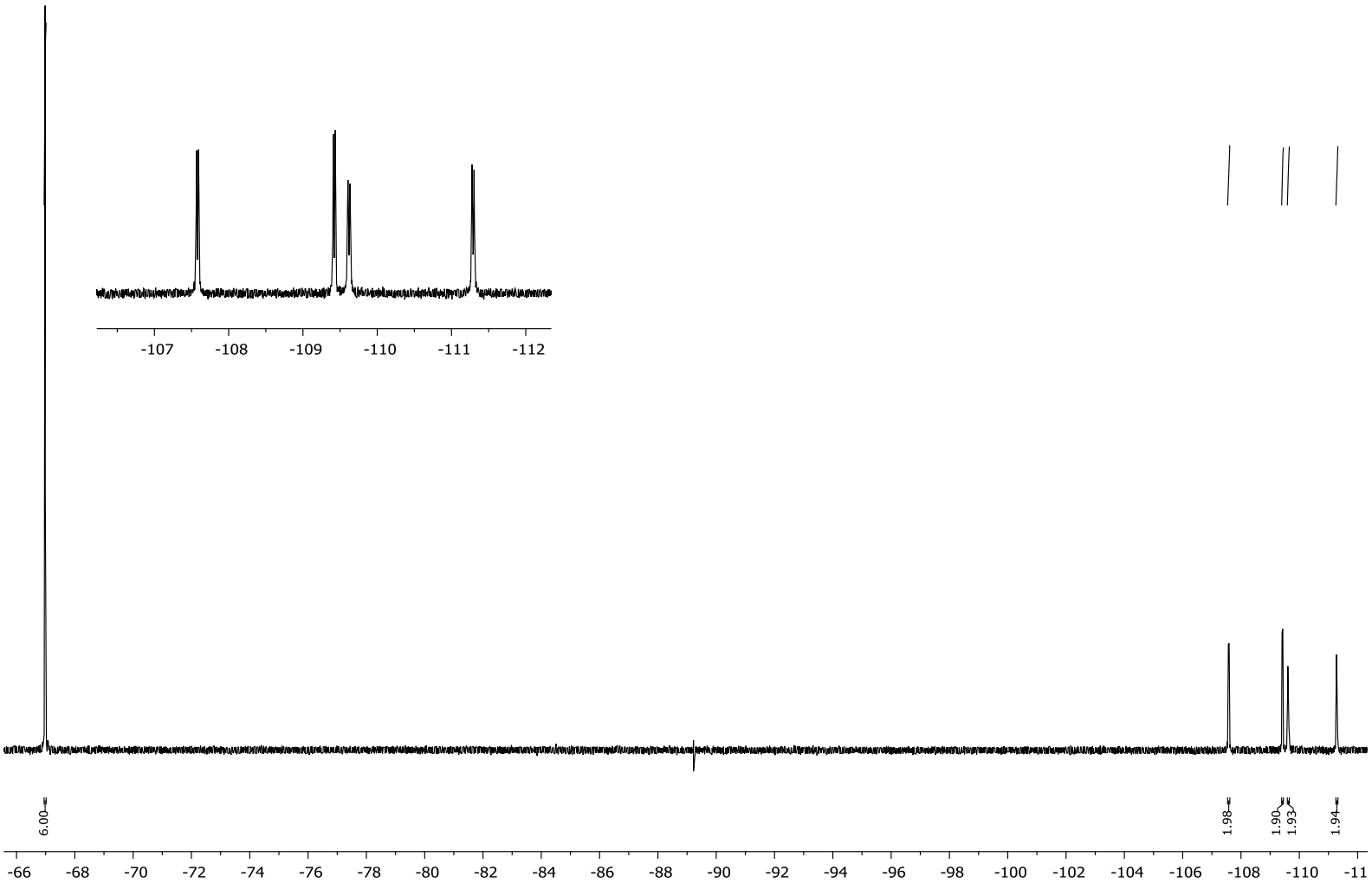

Figure S59. $^{19}F\{^{1}H\}$ NMR spectrum (376 MHz) of **14** in CD_2Cl_2.

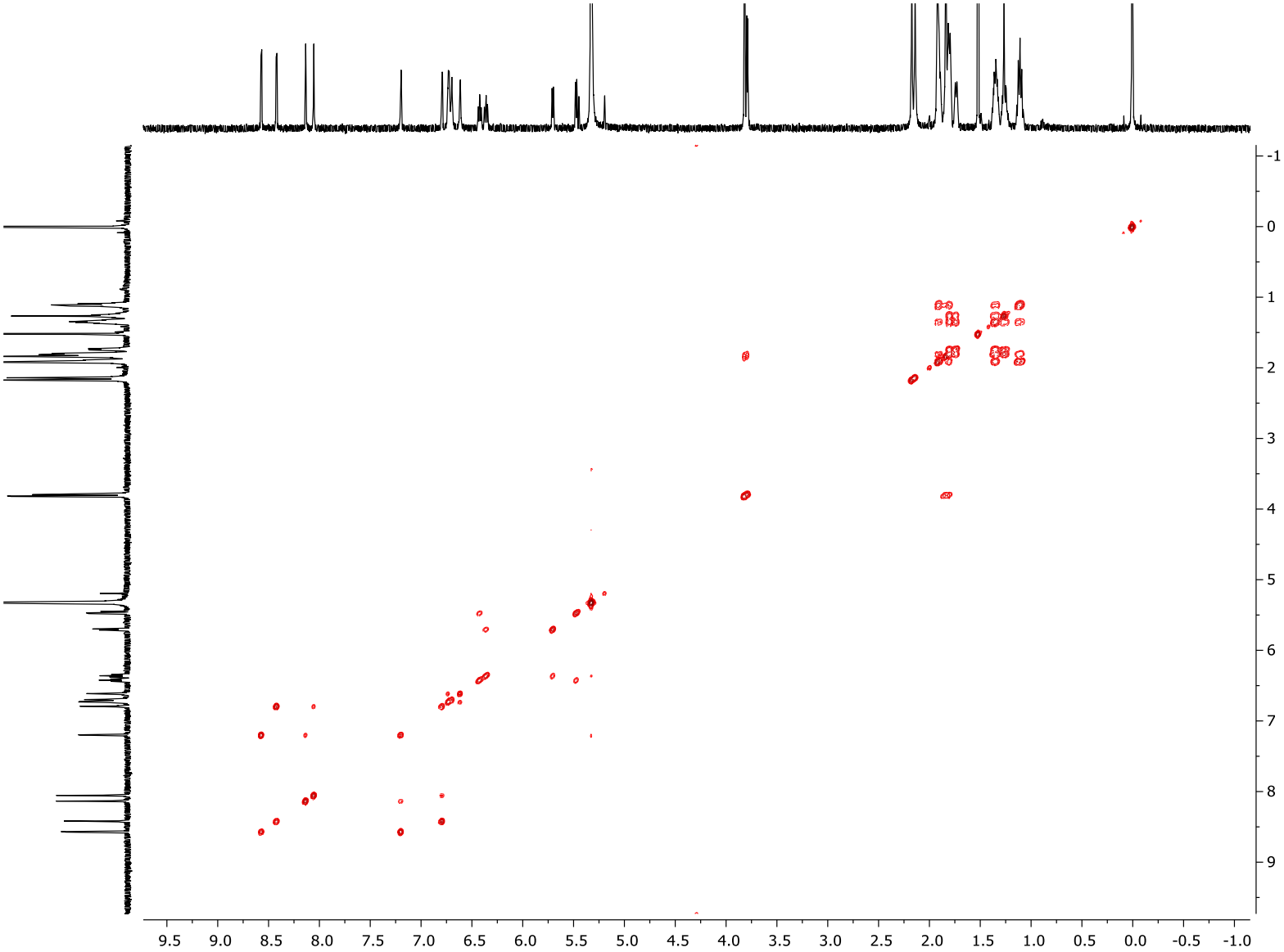

Figure S60. ^{1}H–^{1}H COSY NMR spectrum of **14** in CD_2Cl_2 (TMS).

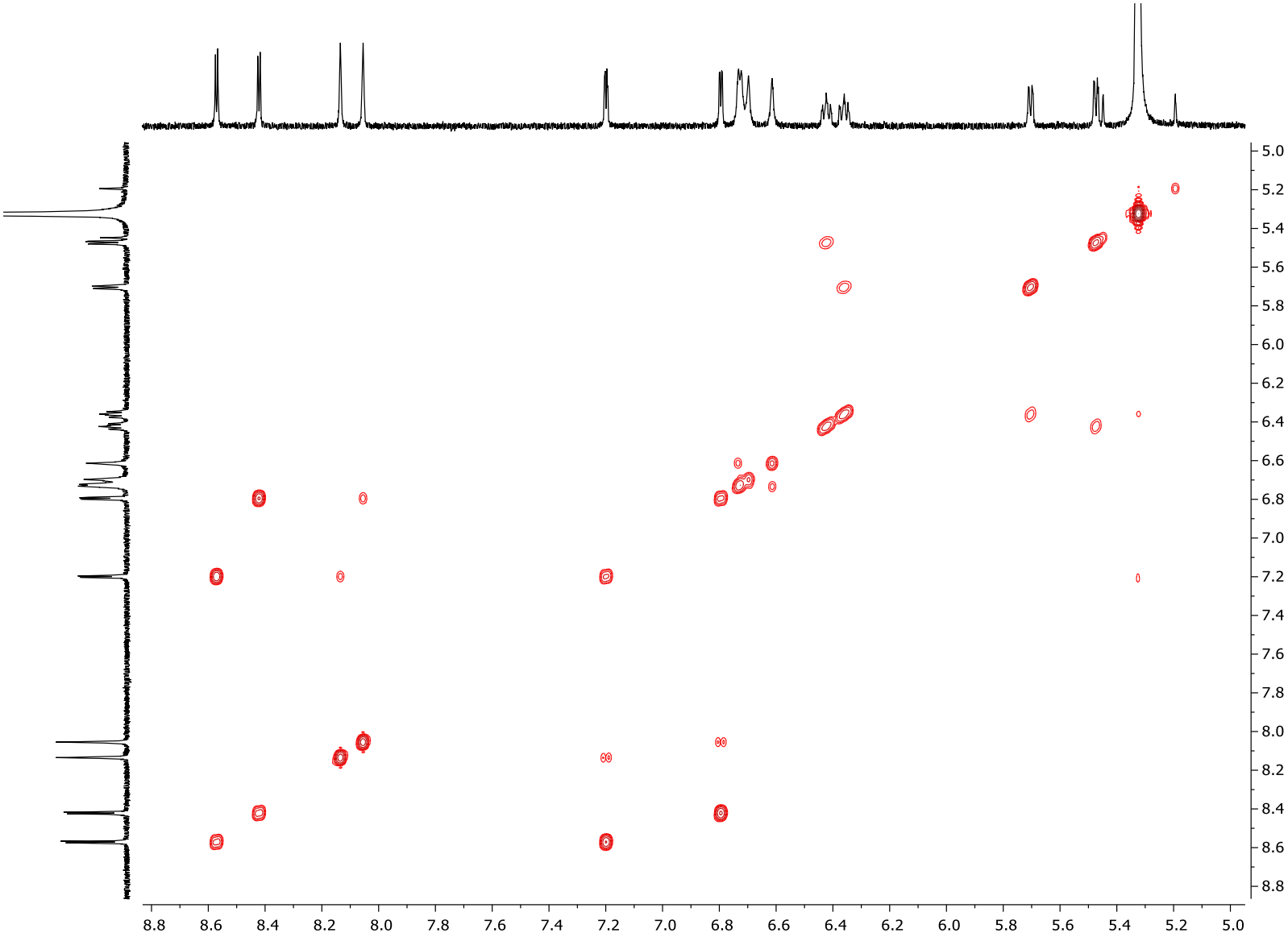

Figure S61. Expansion of the aromatic region of the ^{1}H–^{1}H COSY NMR spectrum of **14** in CD_2Cl_2 (TMS).

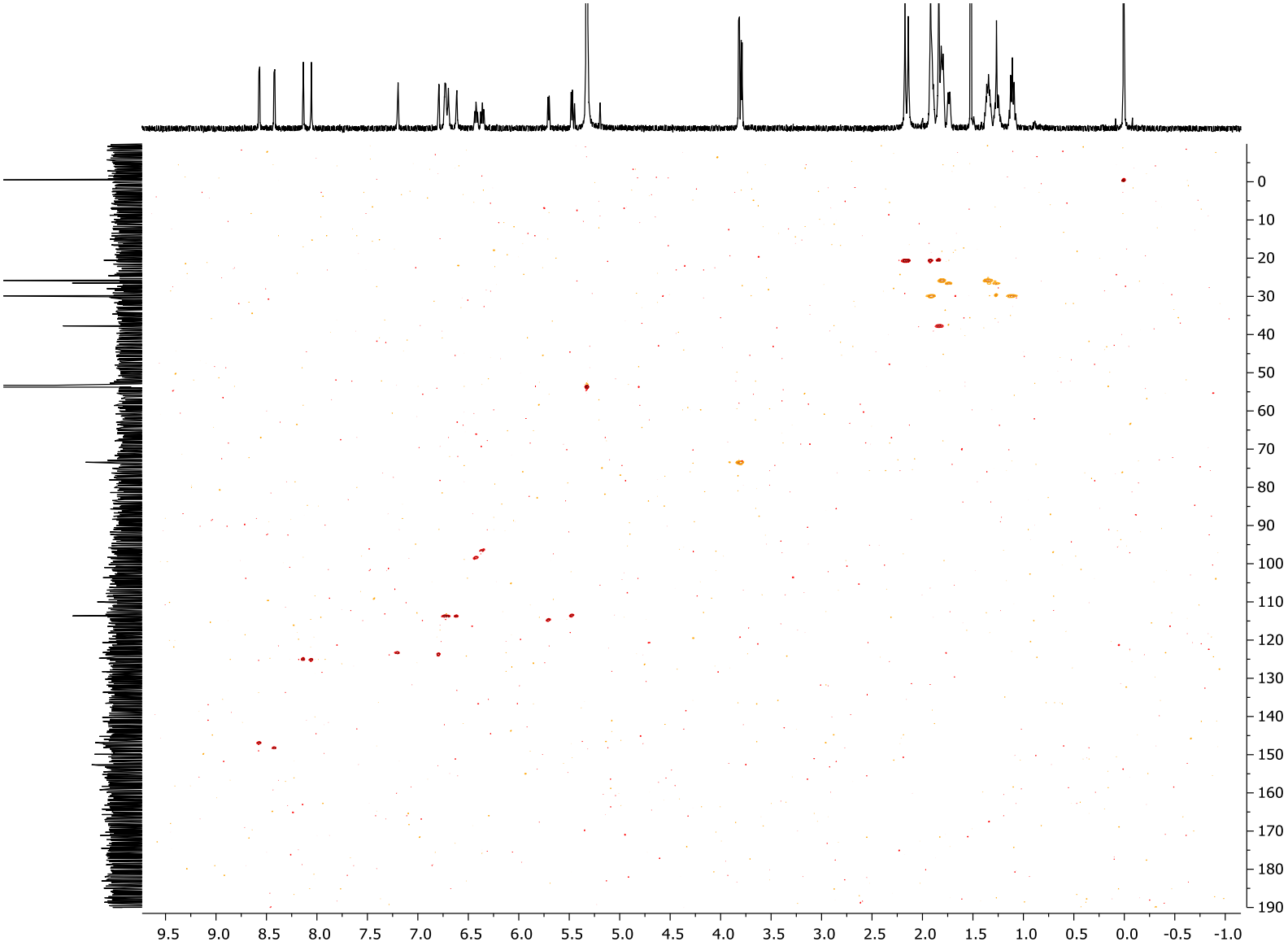

Figure S62. $^{1}H–^{13}C$ HSQC NMR spectrum of **14** in CD_2Cl_2 (TMS).

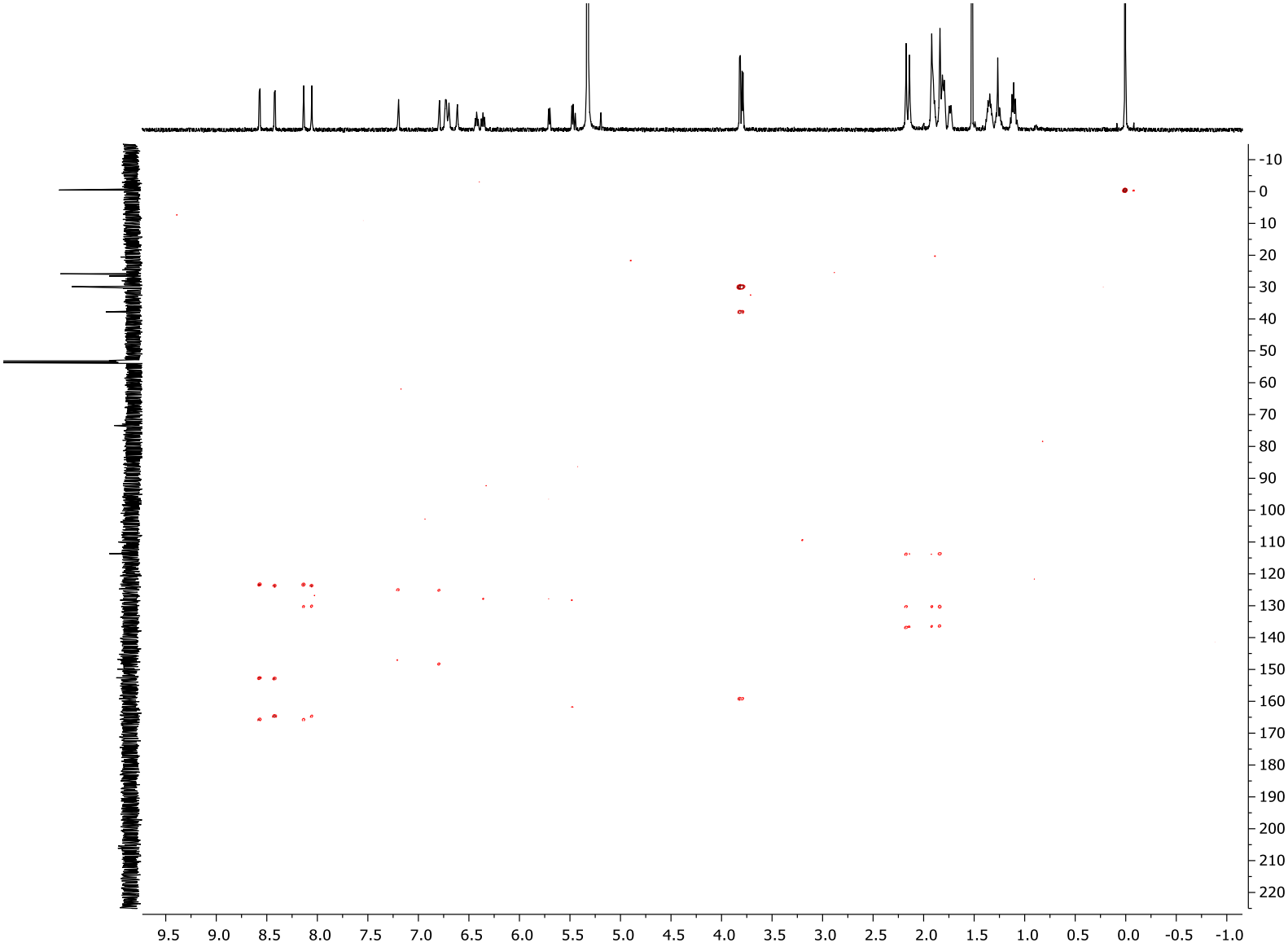

Figure S63. ^{1}H–^{13}C HMBC NMR spectrum of **14** in CD_2Cl_2 (TMS).

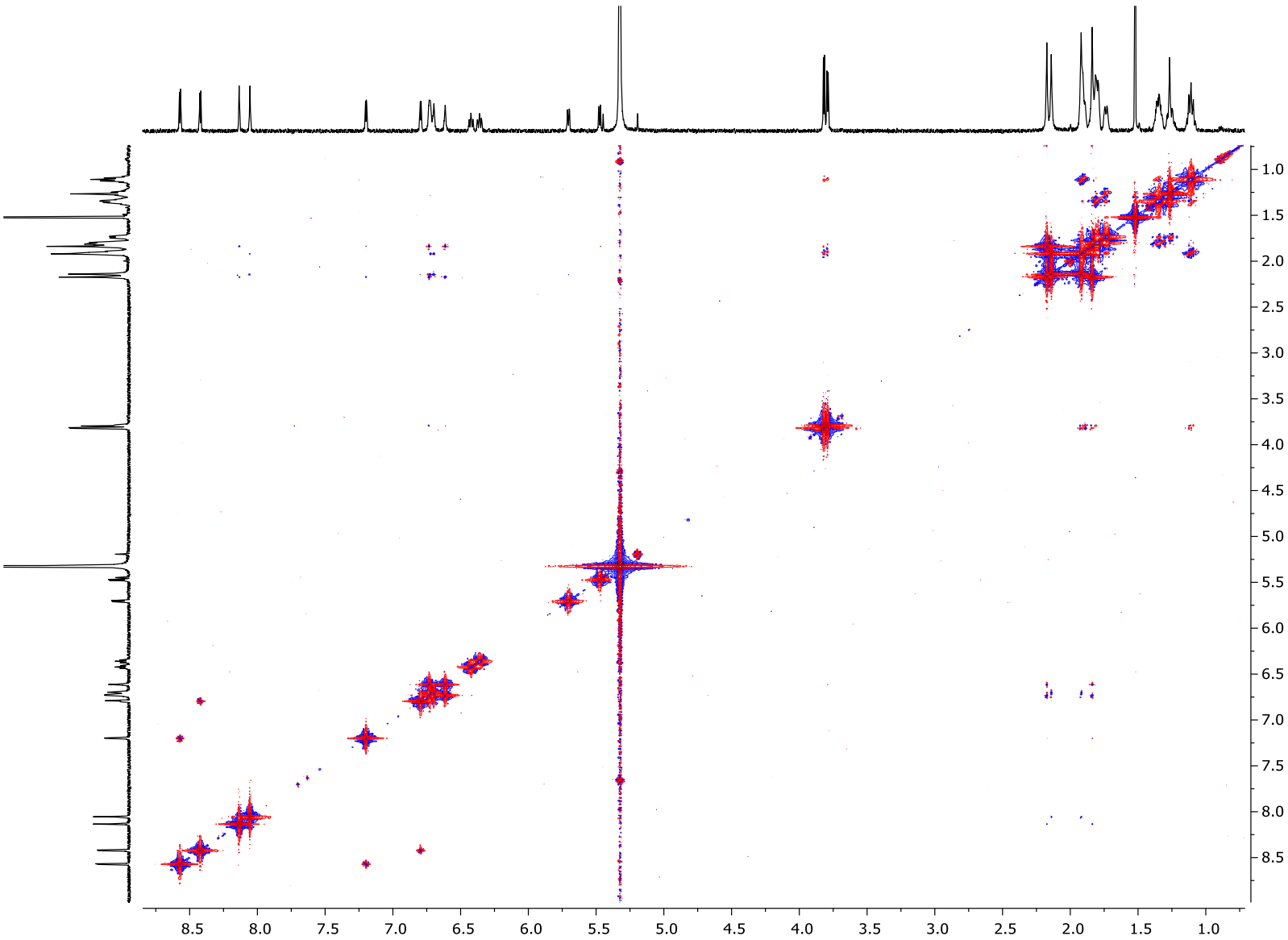

Figure S64. ^{1}H–^{1}H NOESY NMR spectrum of **14** in CD_2Cl_2 (TMS).

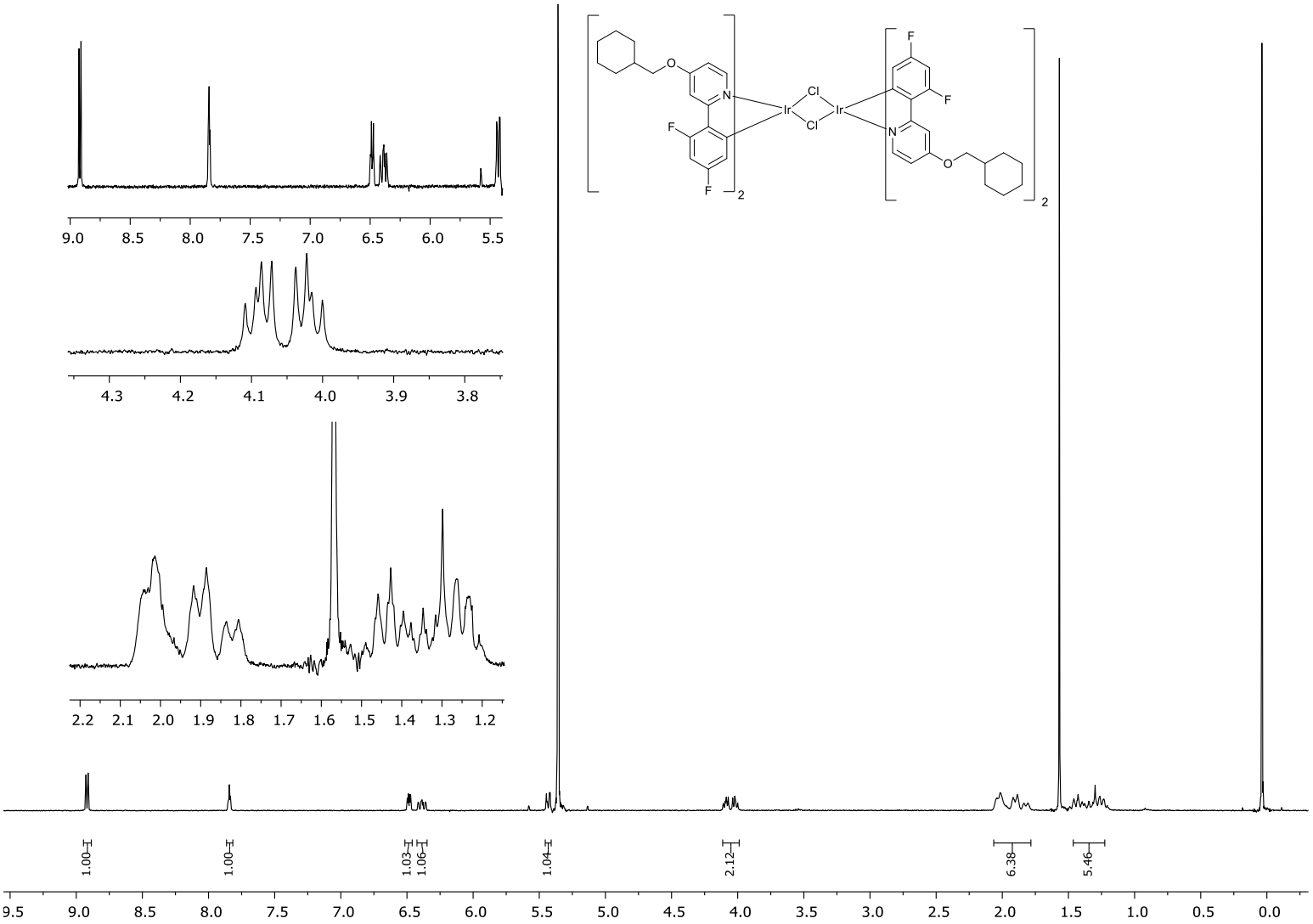

Figure S65. ^{1}H NMR spectrum (400 MHz) of the μ–dichloro dimer isolated as an intermediate in the synthesis of complex **15** in CD_2Cl_2 (TMS).

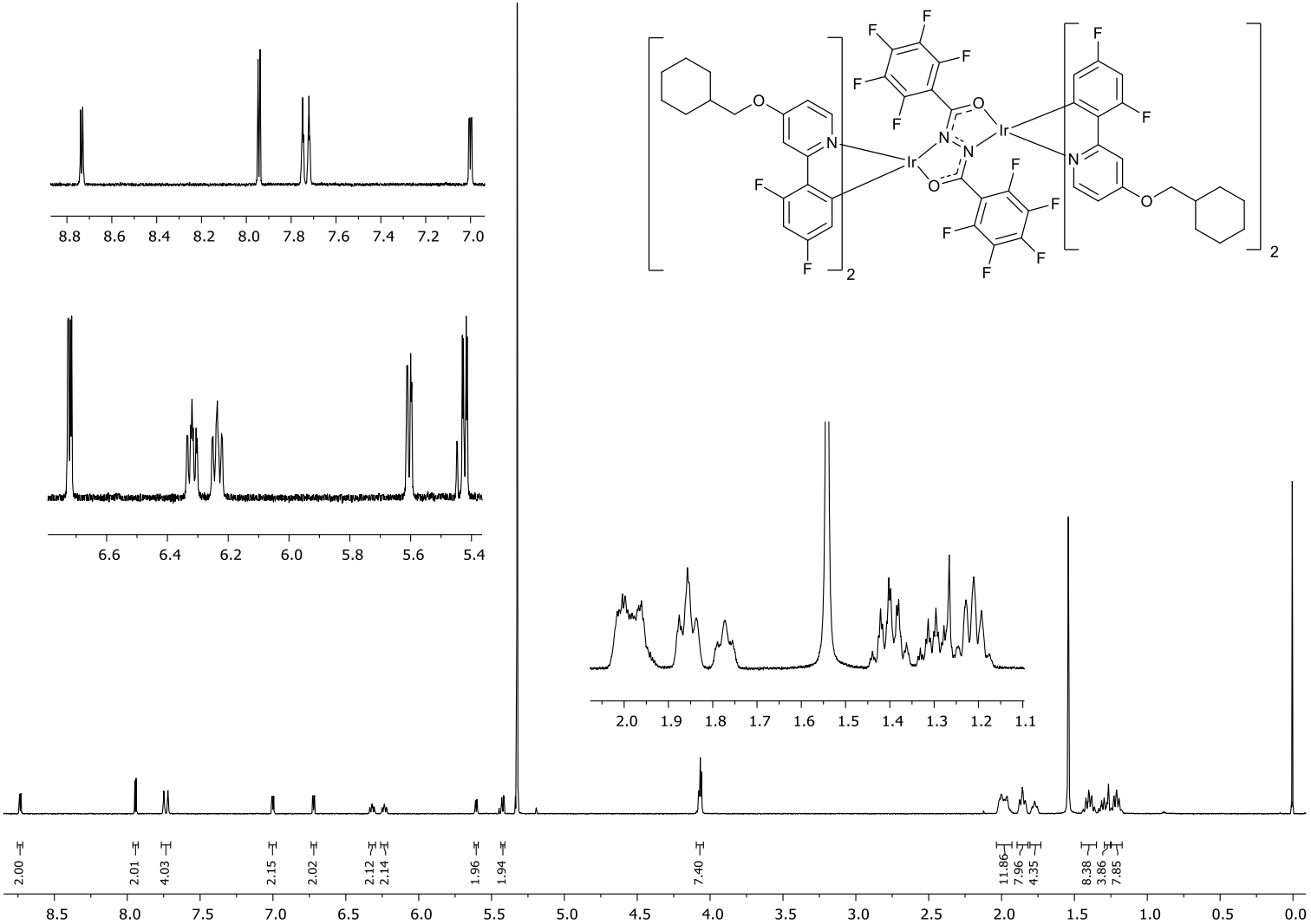

Figure S66. ^{1}H NMR spectrum (700 MHz) of **15** in CD_2Cl_2 (TMS).

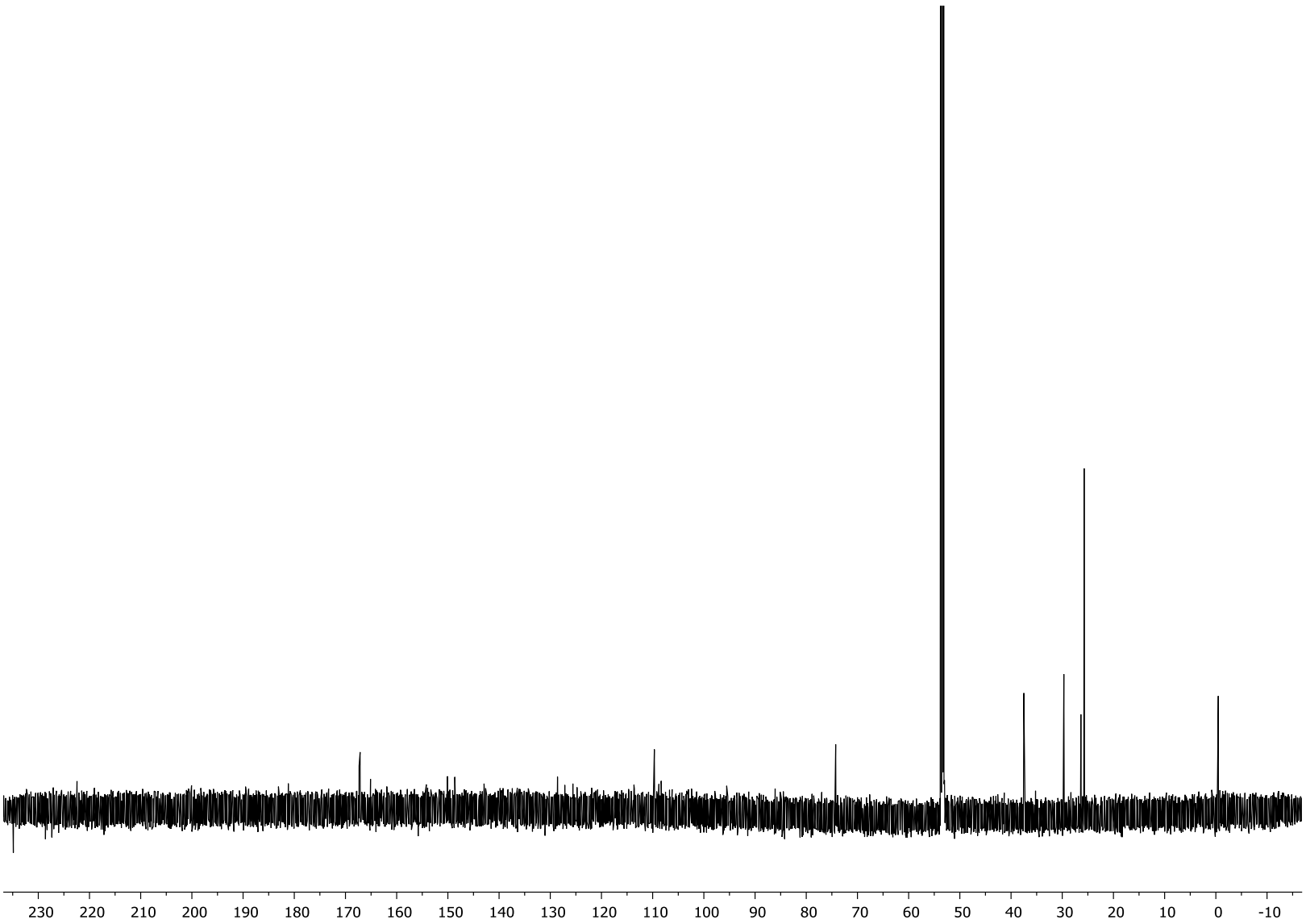

Figure S67. ^{13}C NMR spectrum (151 MHz) of **15** in CD_2Cl_2 (TMS).

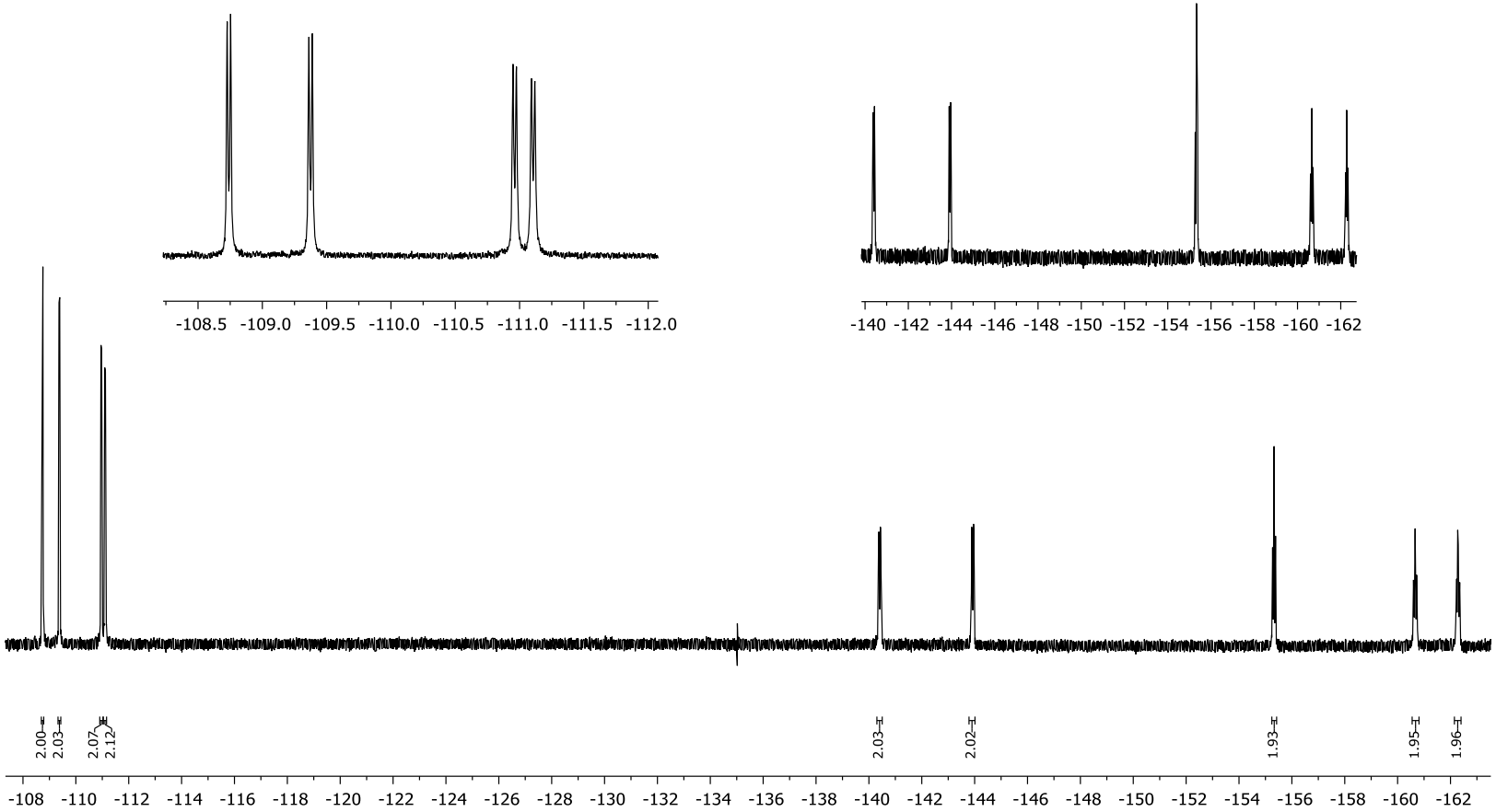

Figure S68. $^{19}F\{^{1}H\}$ NMR spectrum (376 MHz) of **15** in CD_2Cl_2.

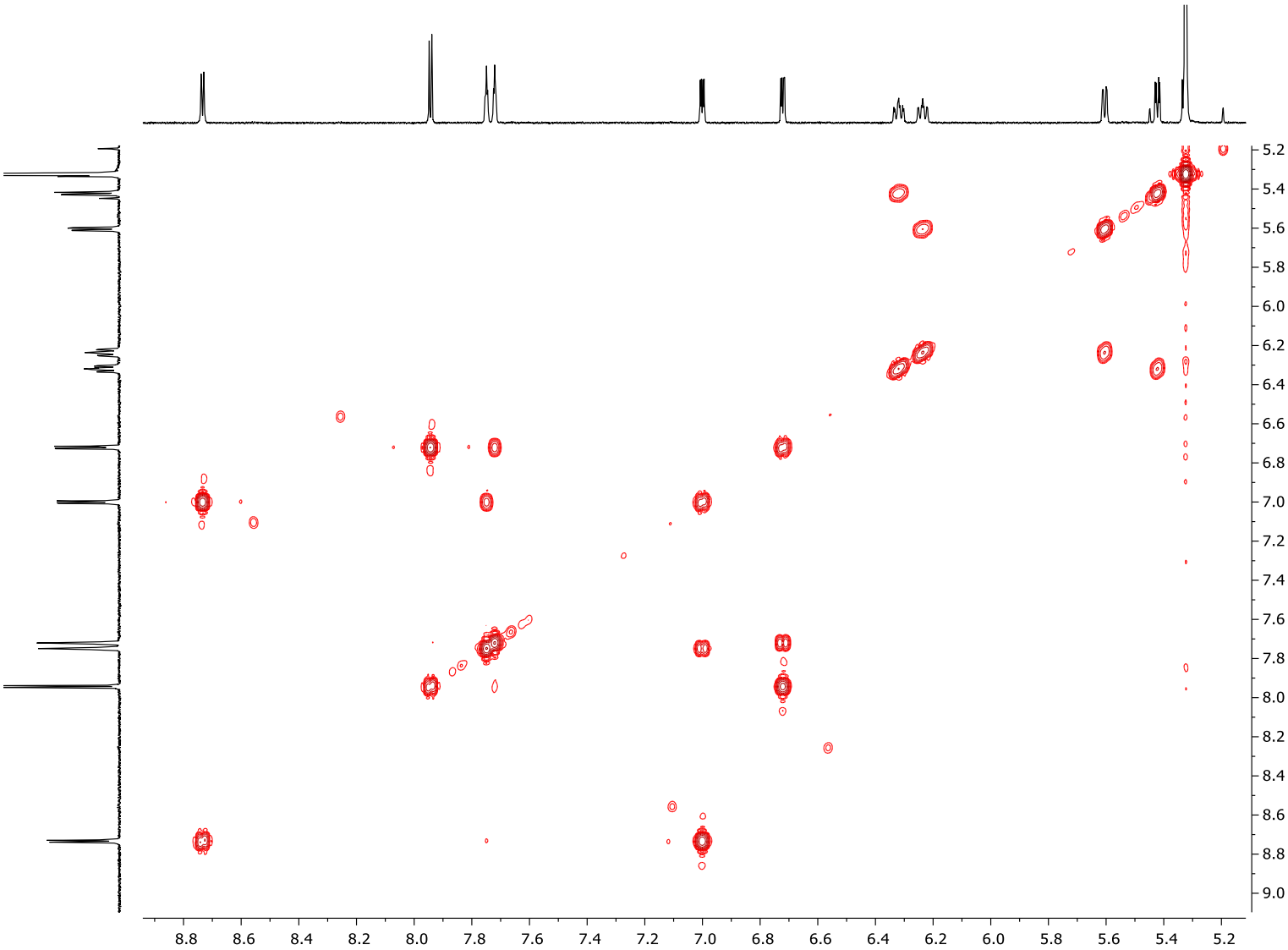

Figure S69. Expansion of the aromatic region of the ^{1}H–^{1}H COSY NMR spectrum of **15** in CD_2Cl_2 (TMS).

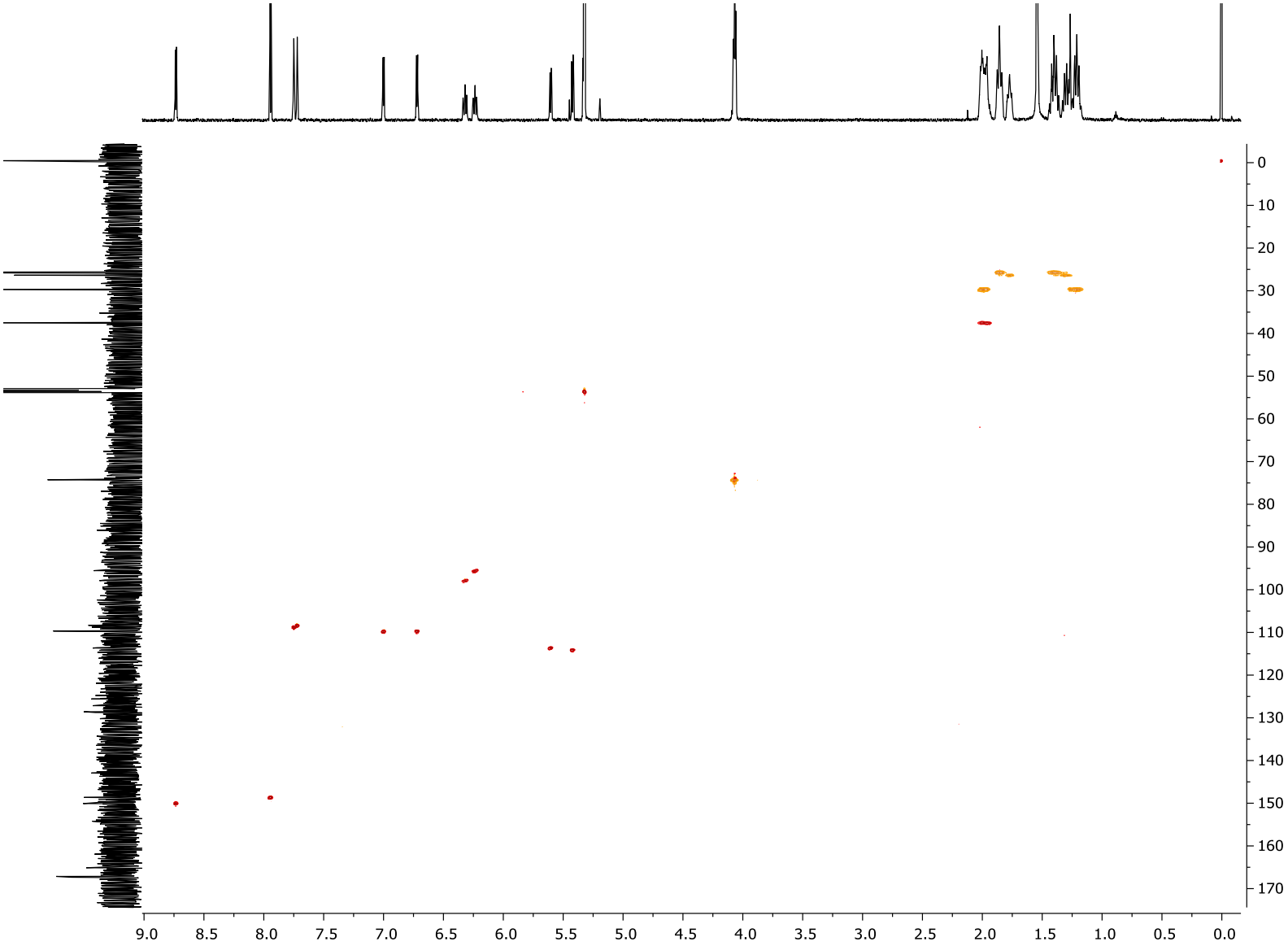

Figure S70. ^{1}H–^{13}C HSQC NMR spectrum of **15** in CD_2Cl_2 (TMS).

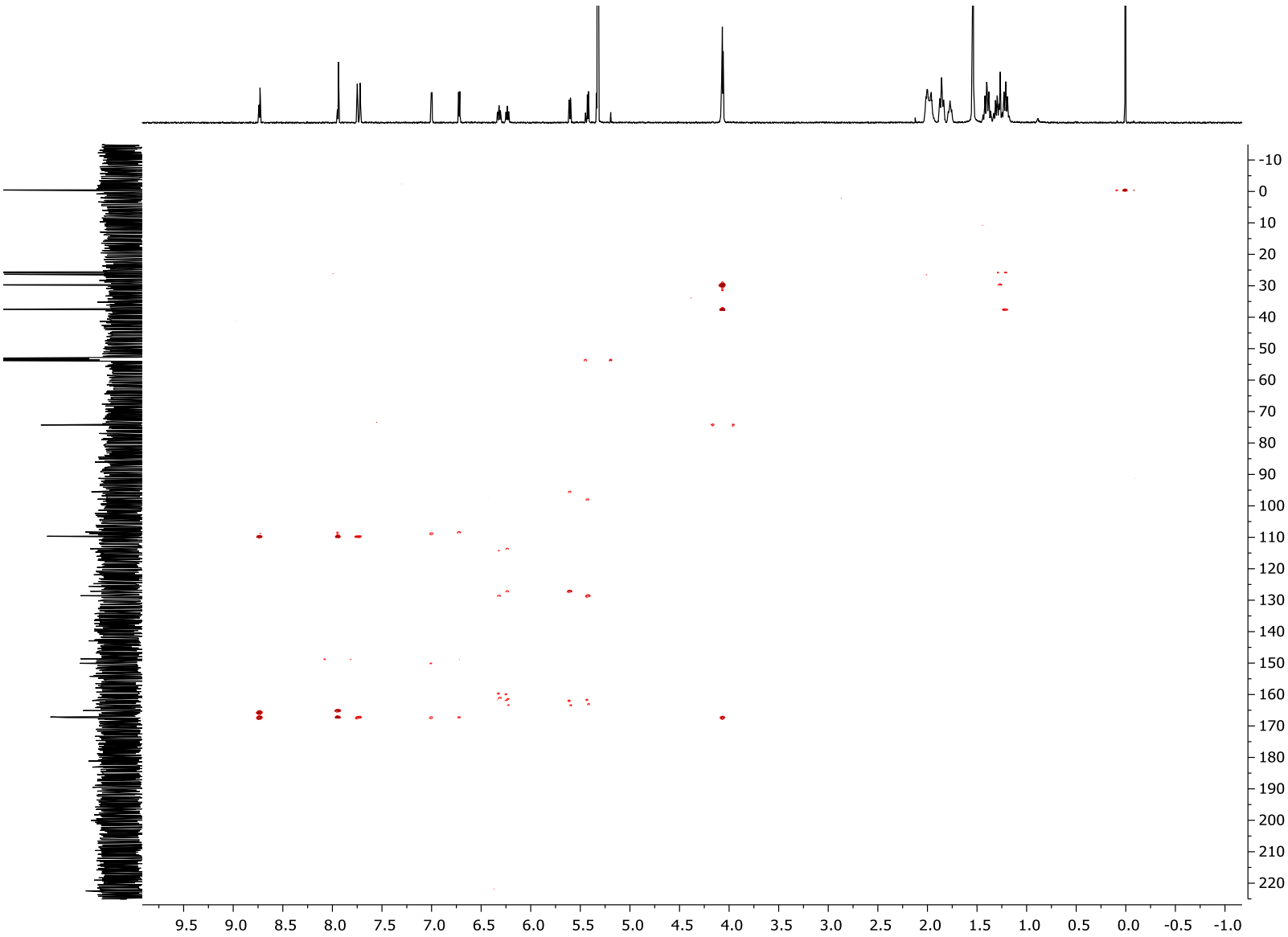

Figure S71. $^{1}H–^{13}C$ HMBC NMR spectrum of **15** in CD_2Cl_2 (TMS).

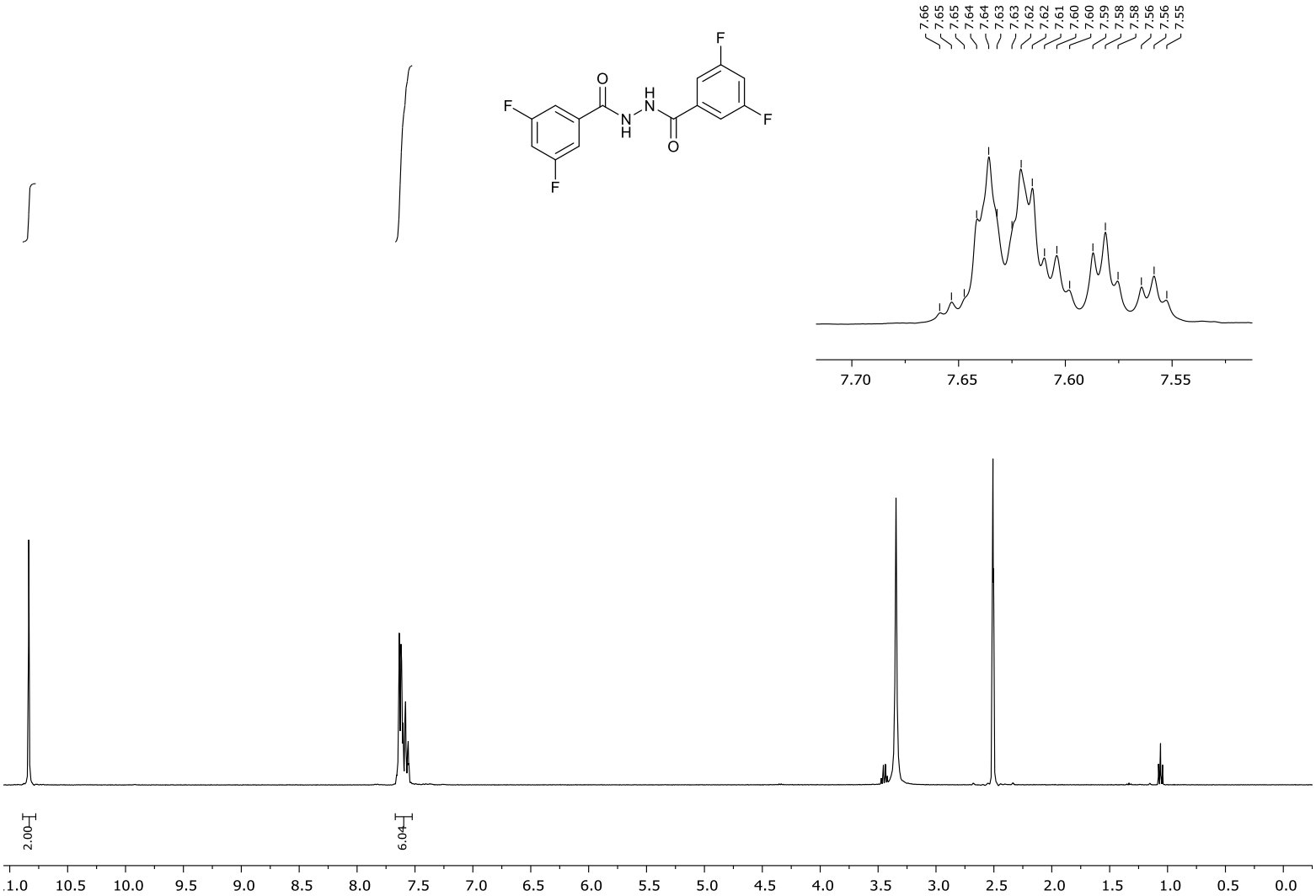

Figure S72. ^{1}H NMR spectrum (400 MHz) of **17a** in DMSO-d_6.

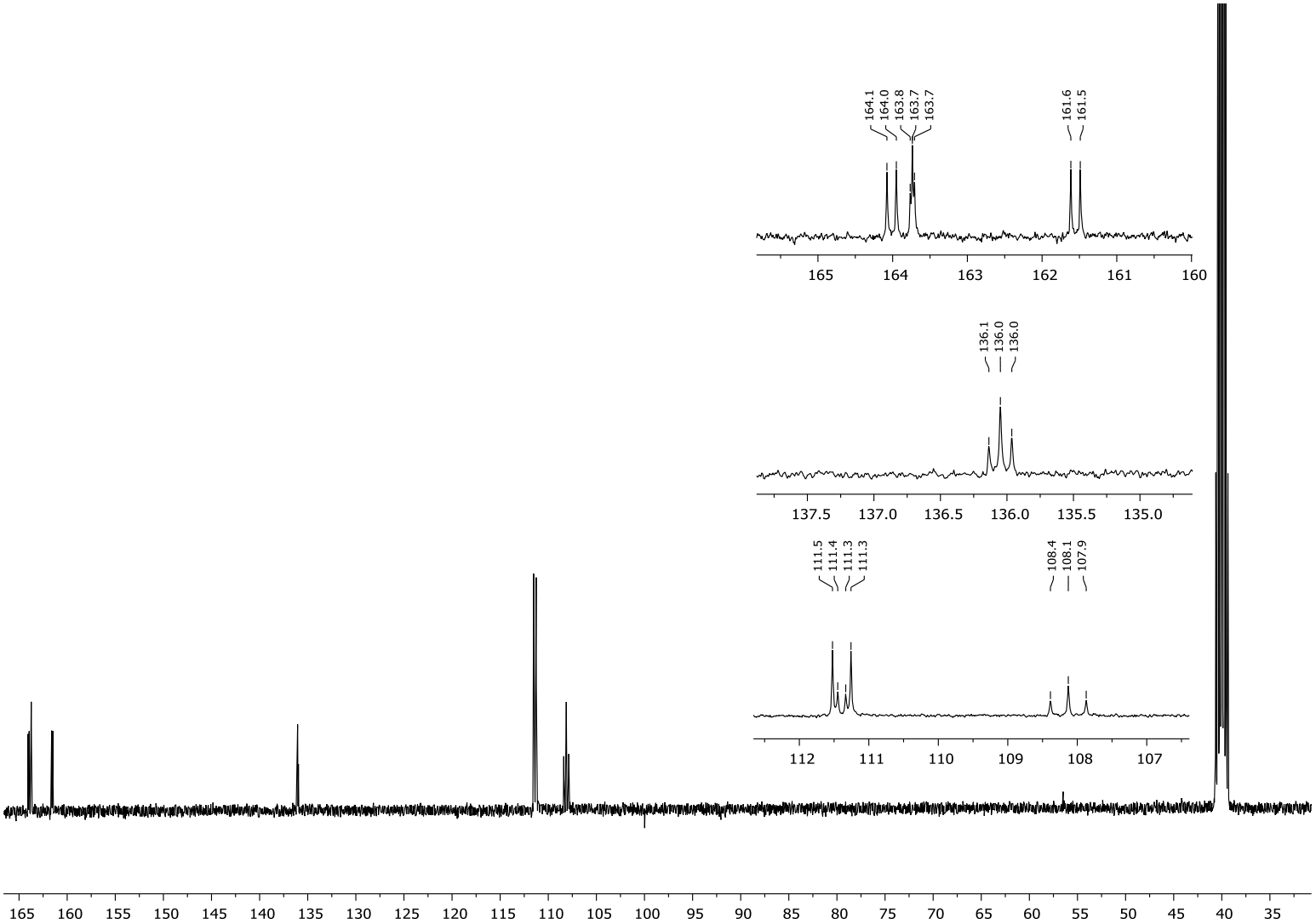

Figure S73. ^{13}C NMR spectrum (101 MHz) of **17a** in DMSO-d_6.

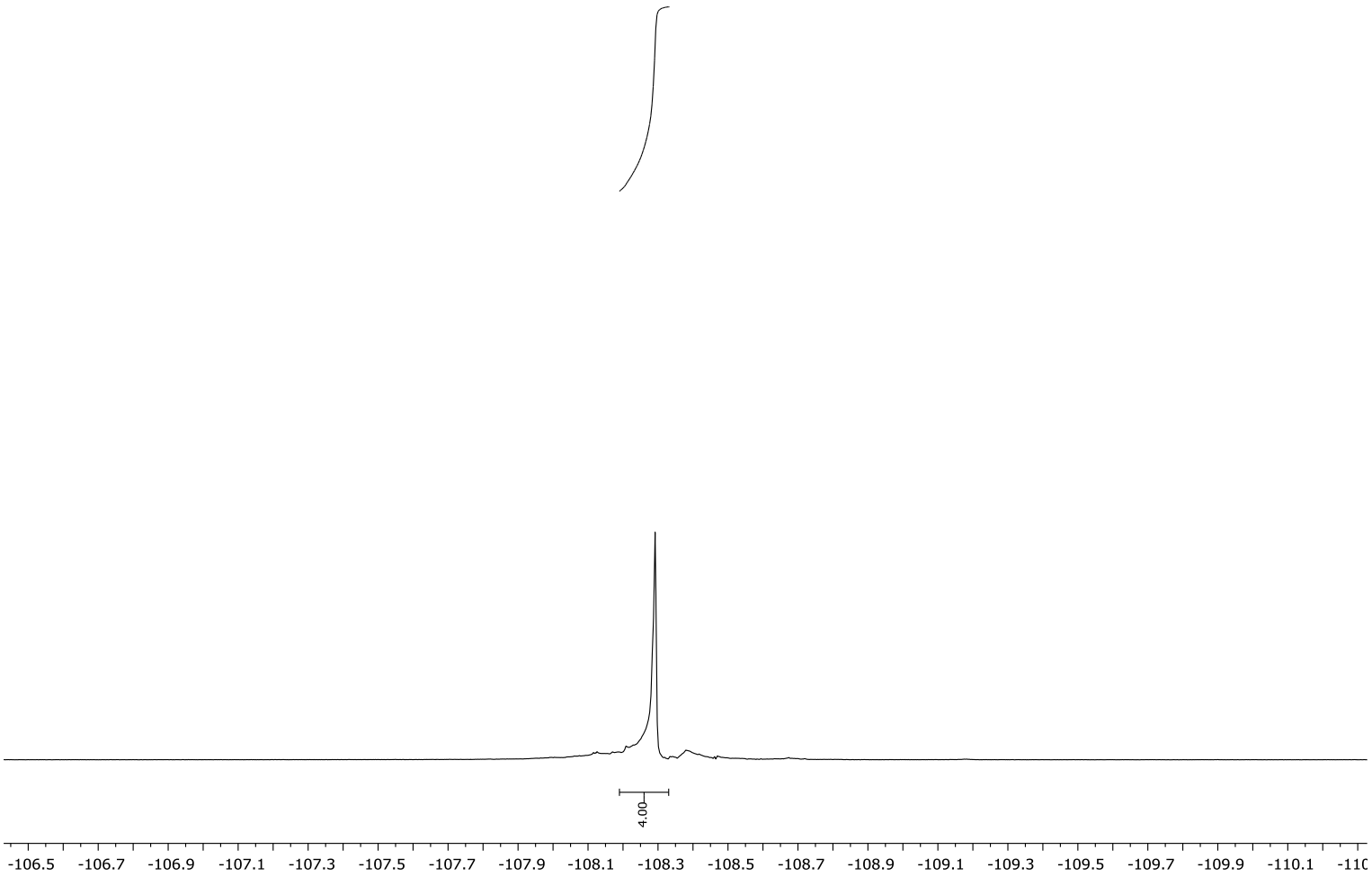

Figure S74. $^{19}F\{^{1}H\}$ NMR spectrum (376 MHz) of **17a** in DMSO-d_6.

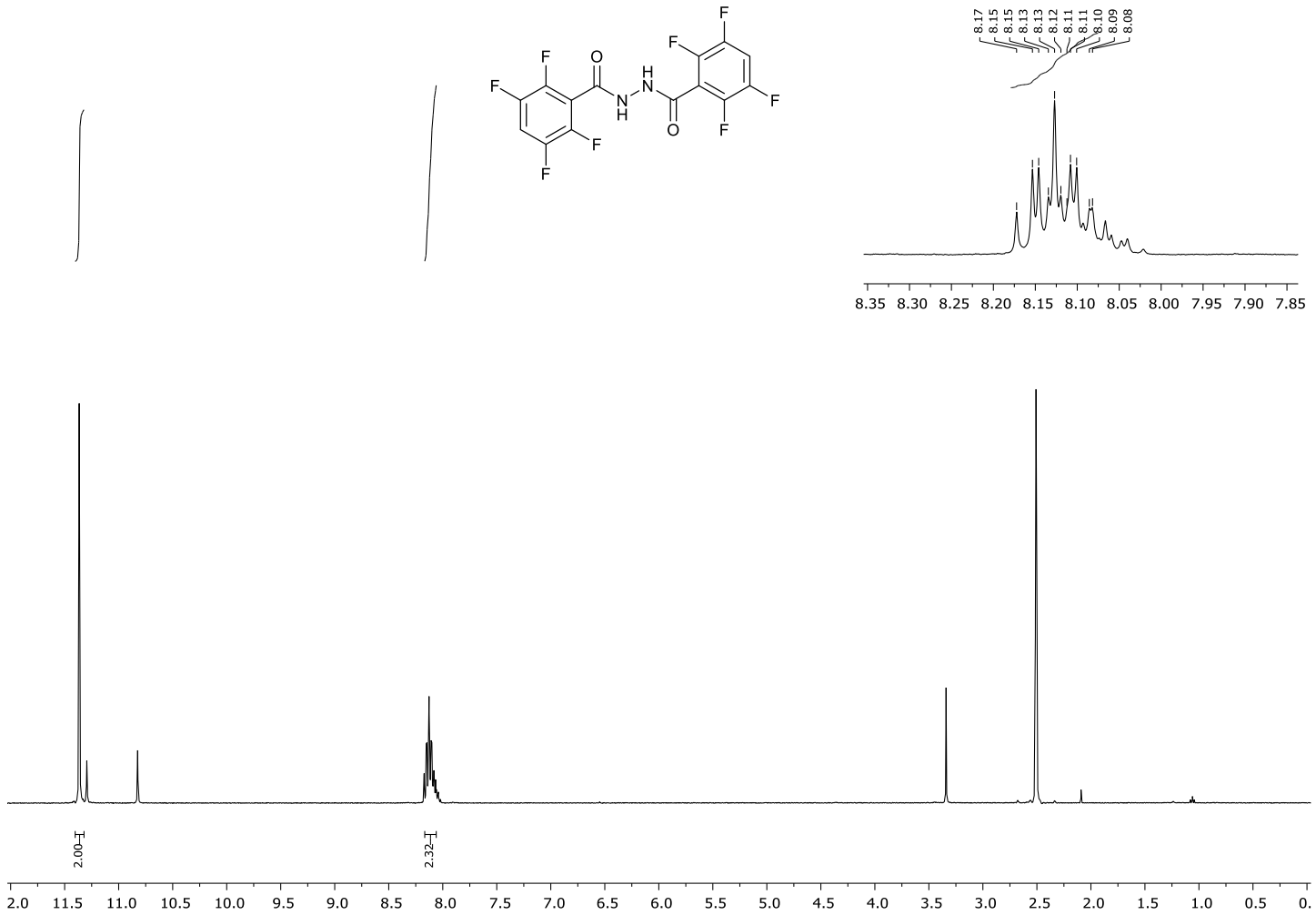

Figure S75. ^{1}H NMR spectrum (400 MHz) of **17b** in DMSO-d_6.

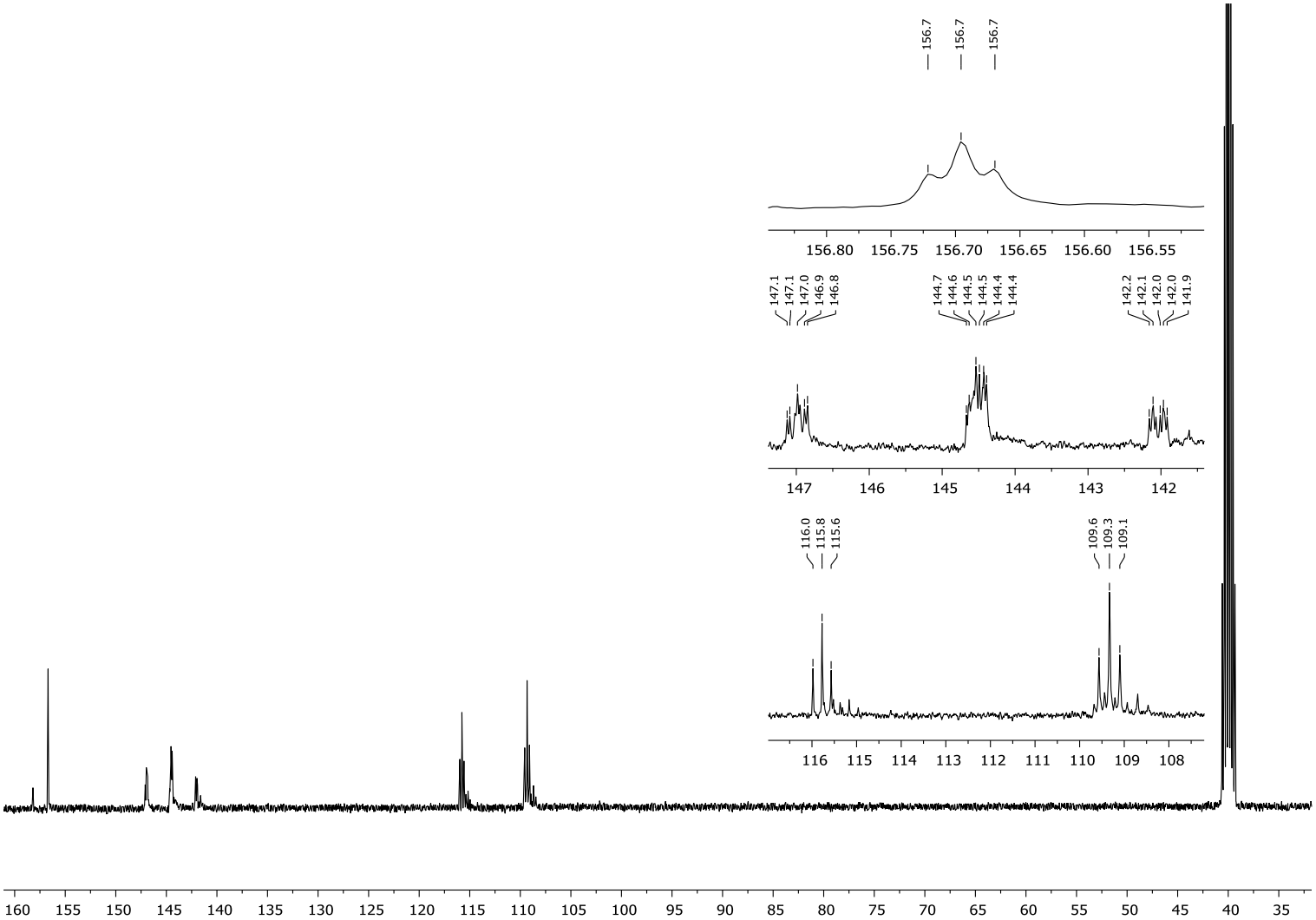

Figure S76. ^{13}C NMR spectrum (101 MHz) of **17b** in DMSO-d_6.

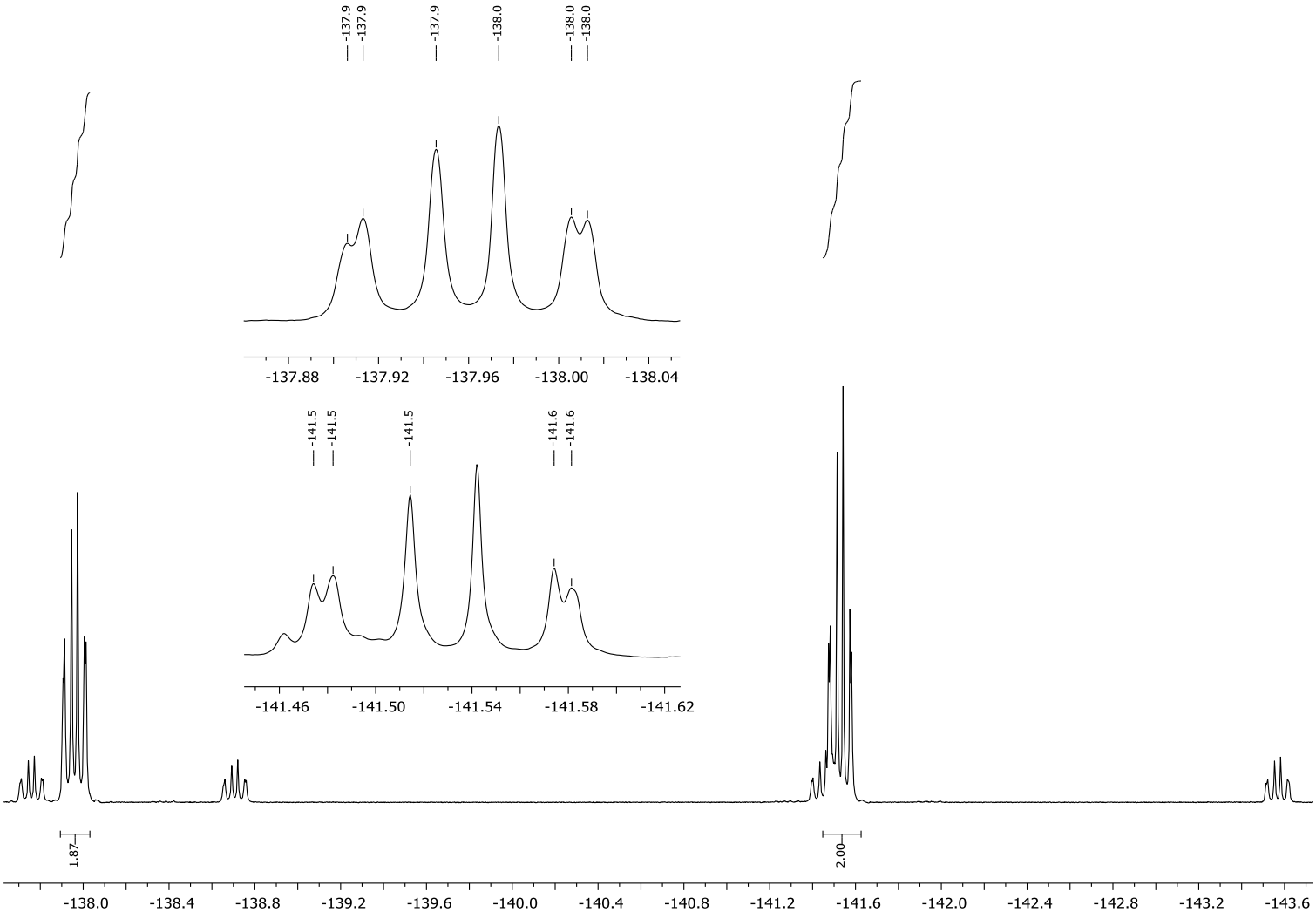

Figure S77. $^{19}F\{^{1}H\}$ NMR spectrum (376 MHz) of **17b** in DMSO-d_6.

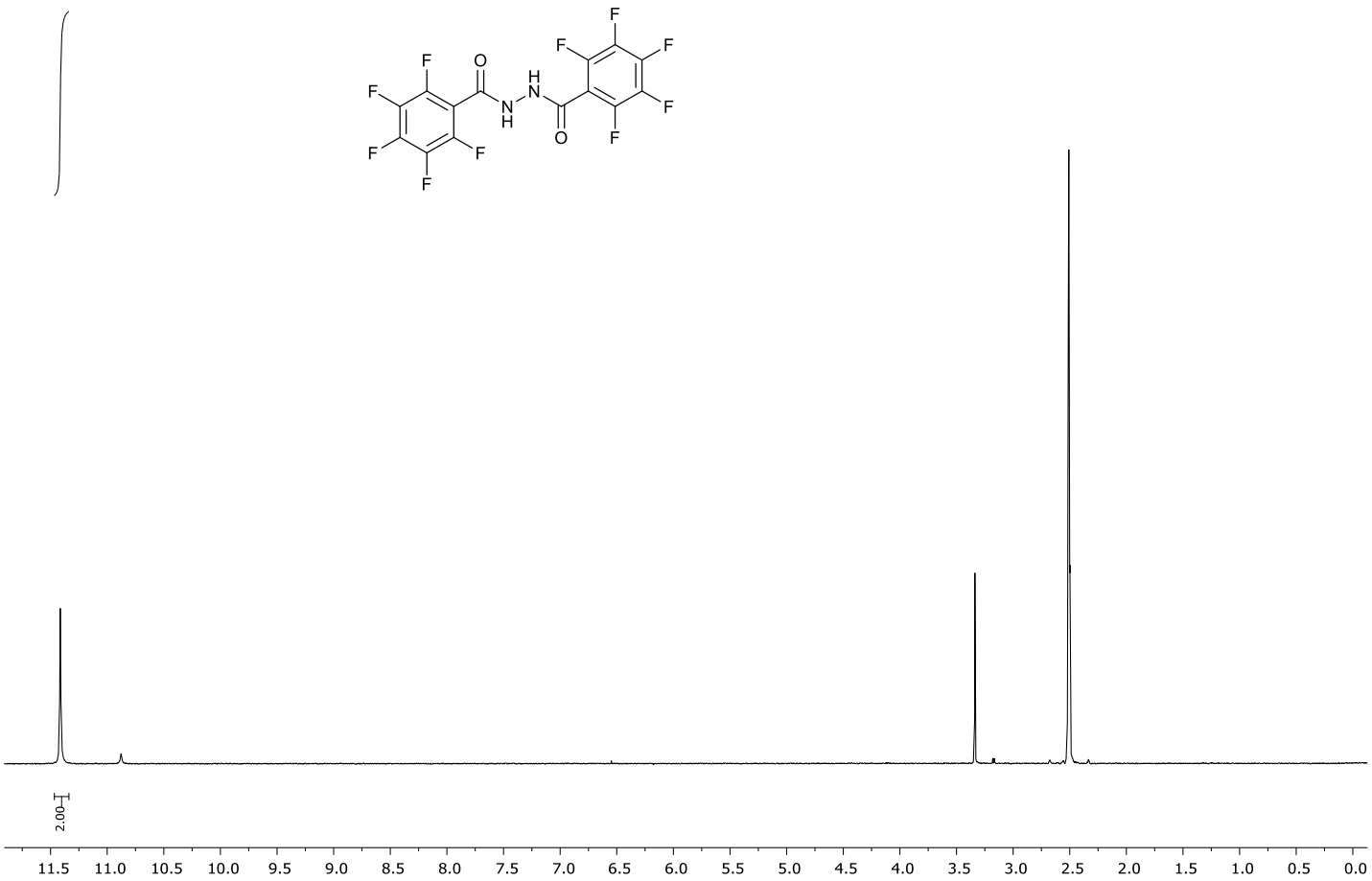

Figure S78. ^{1}H NMR spectrum (400 MHz) of **17c** in DMSO-d_6.

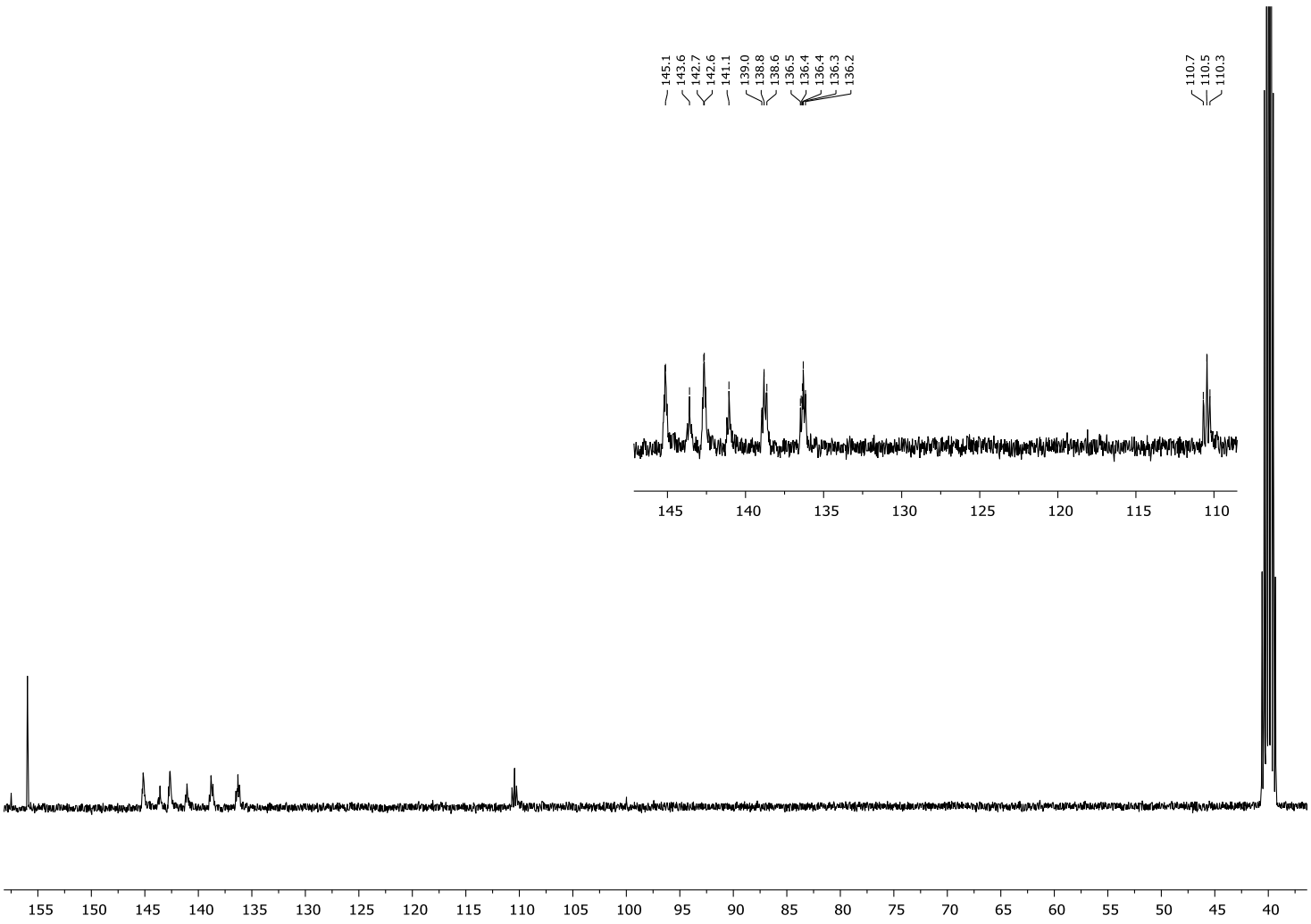

Figure S79. ^{13}C NMR spectrum (101 MHz) of **17c** in DMSO-d_6.

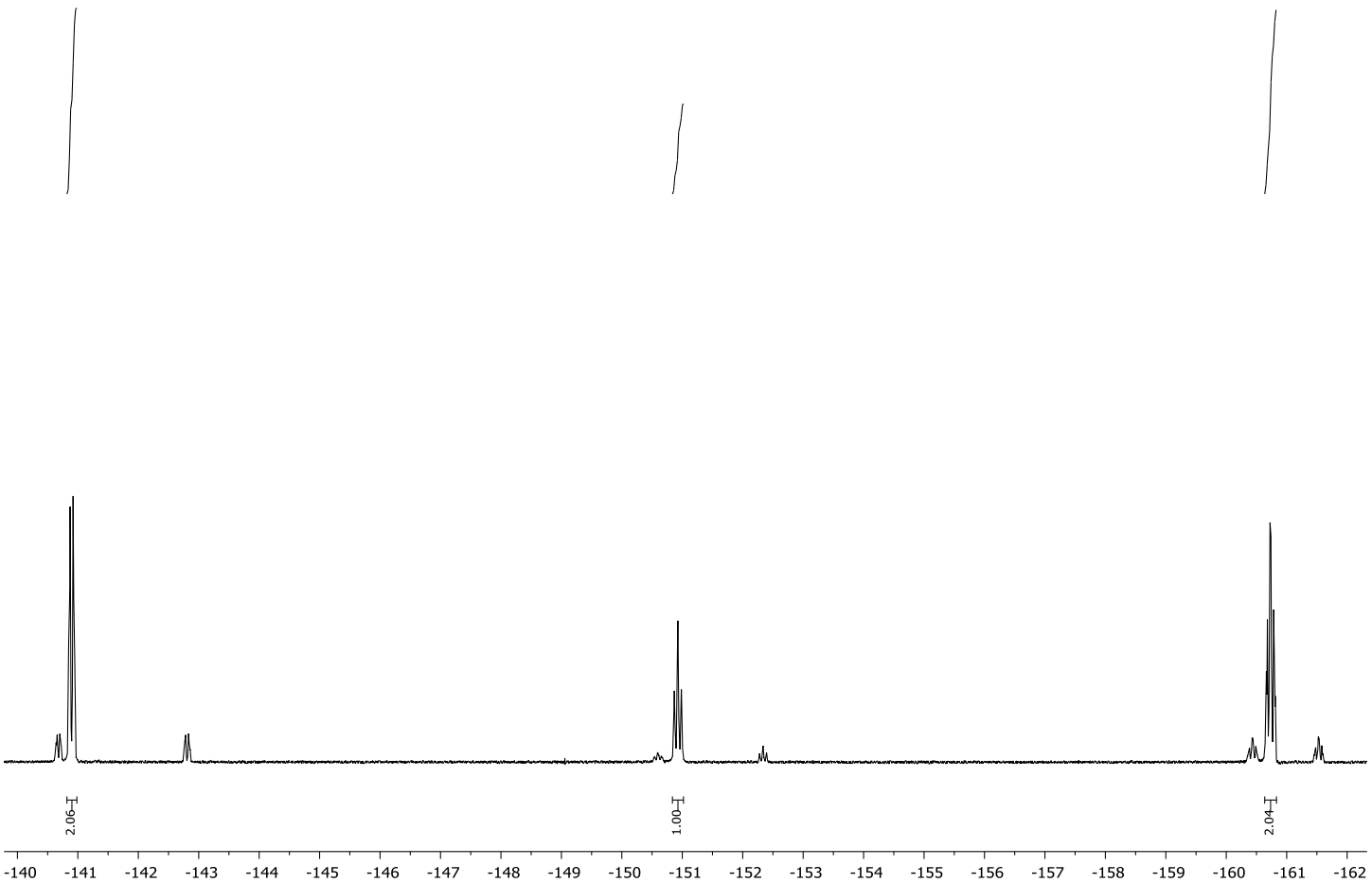

Figure S80. $^{19}F\{^{1}H\}$ NMR spectrum (376 MHz) of **17c** in DMSO-d_6.

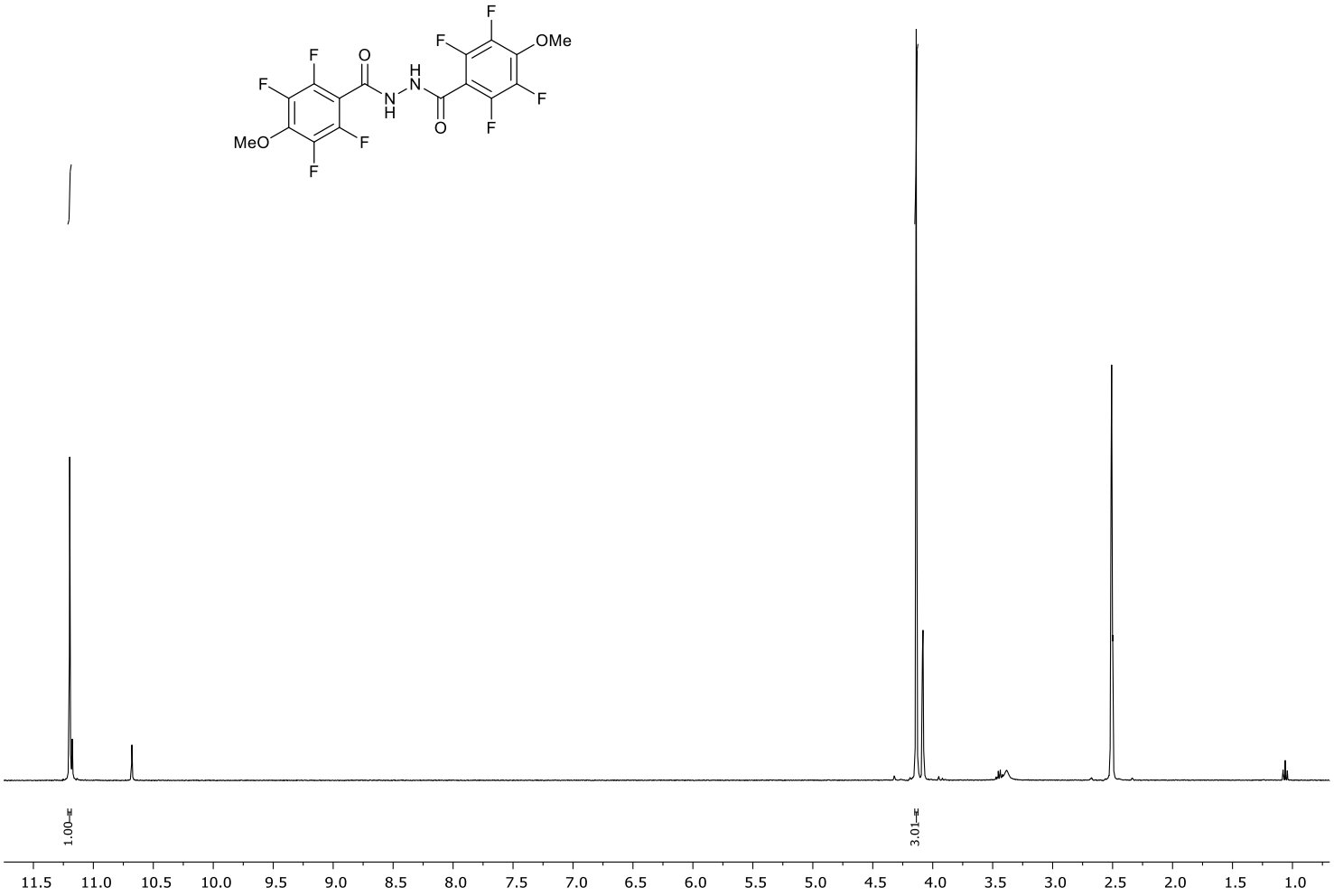

Figure S81. ^{1}H NMR spectrum (400 MHz) of **17d** in DMSO-d_6.

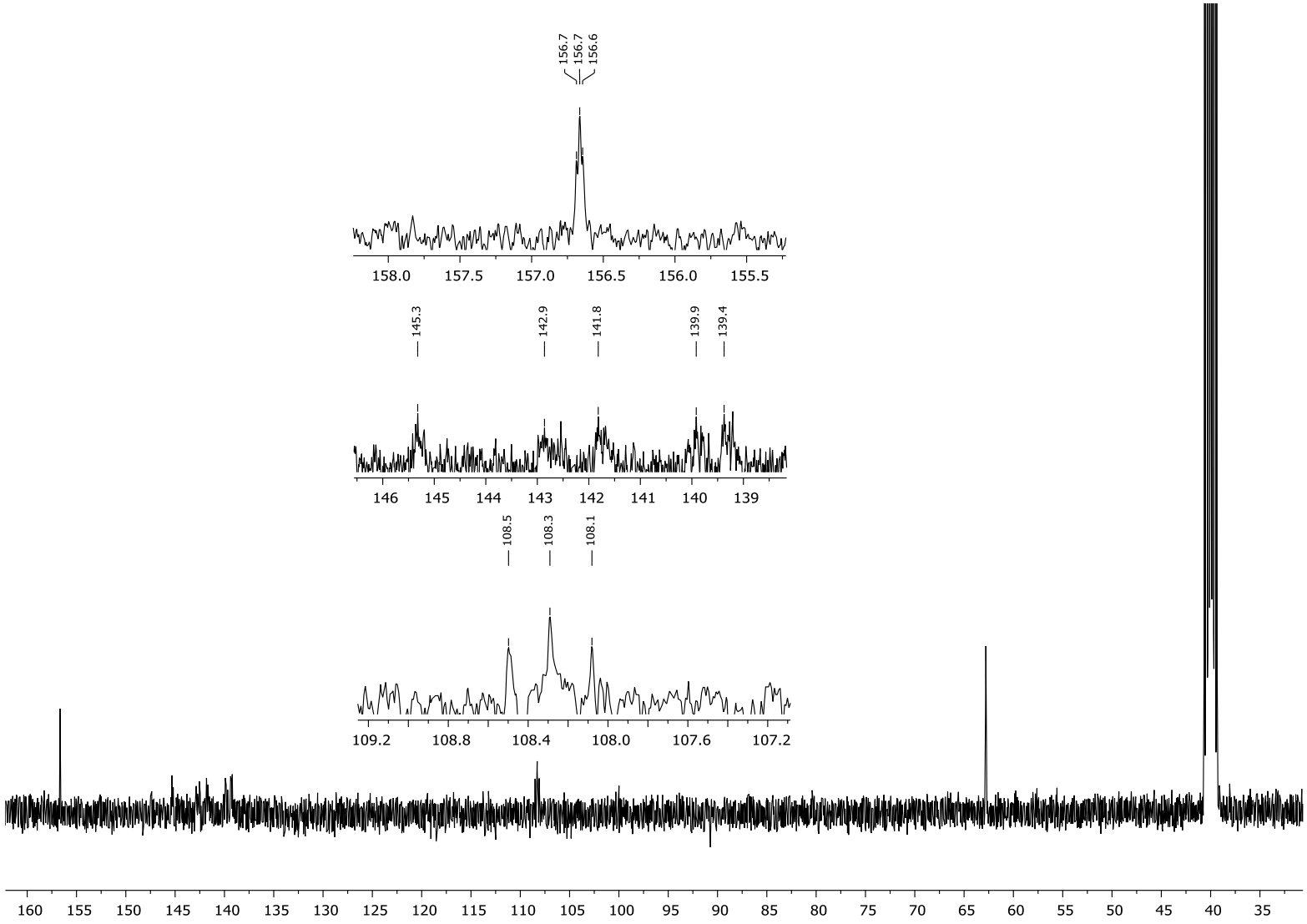

Figure S82. ^{13}C NMR spectrum (101 MHz) of **17d** in DMSO-d_6.

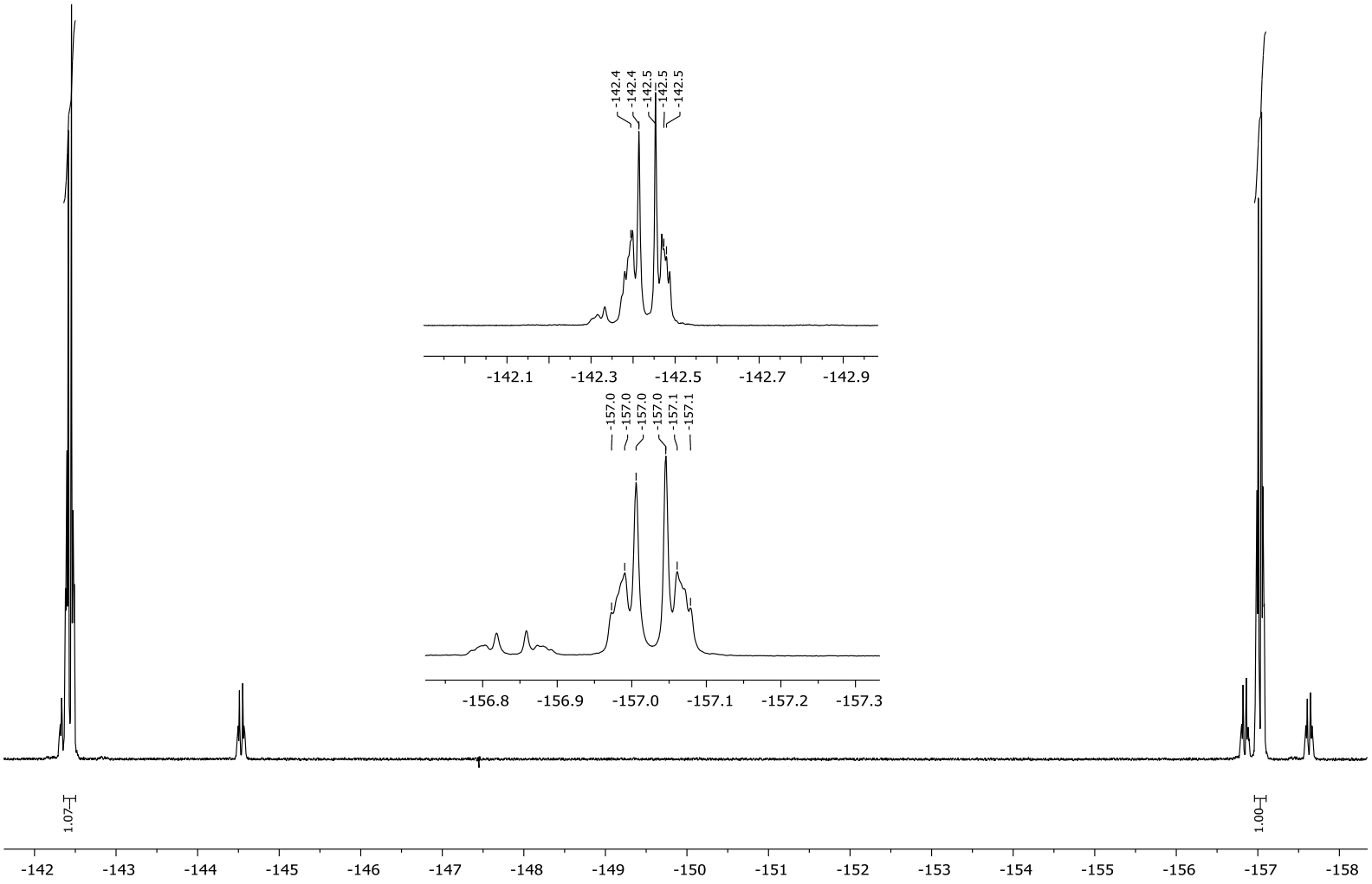

Figure S83. $^{19}F\{^{1}H\}$ NMR spectrum (376 MHz) of **17d** in DMSO-d_6.

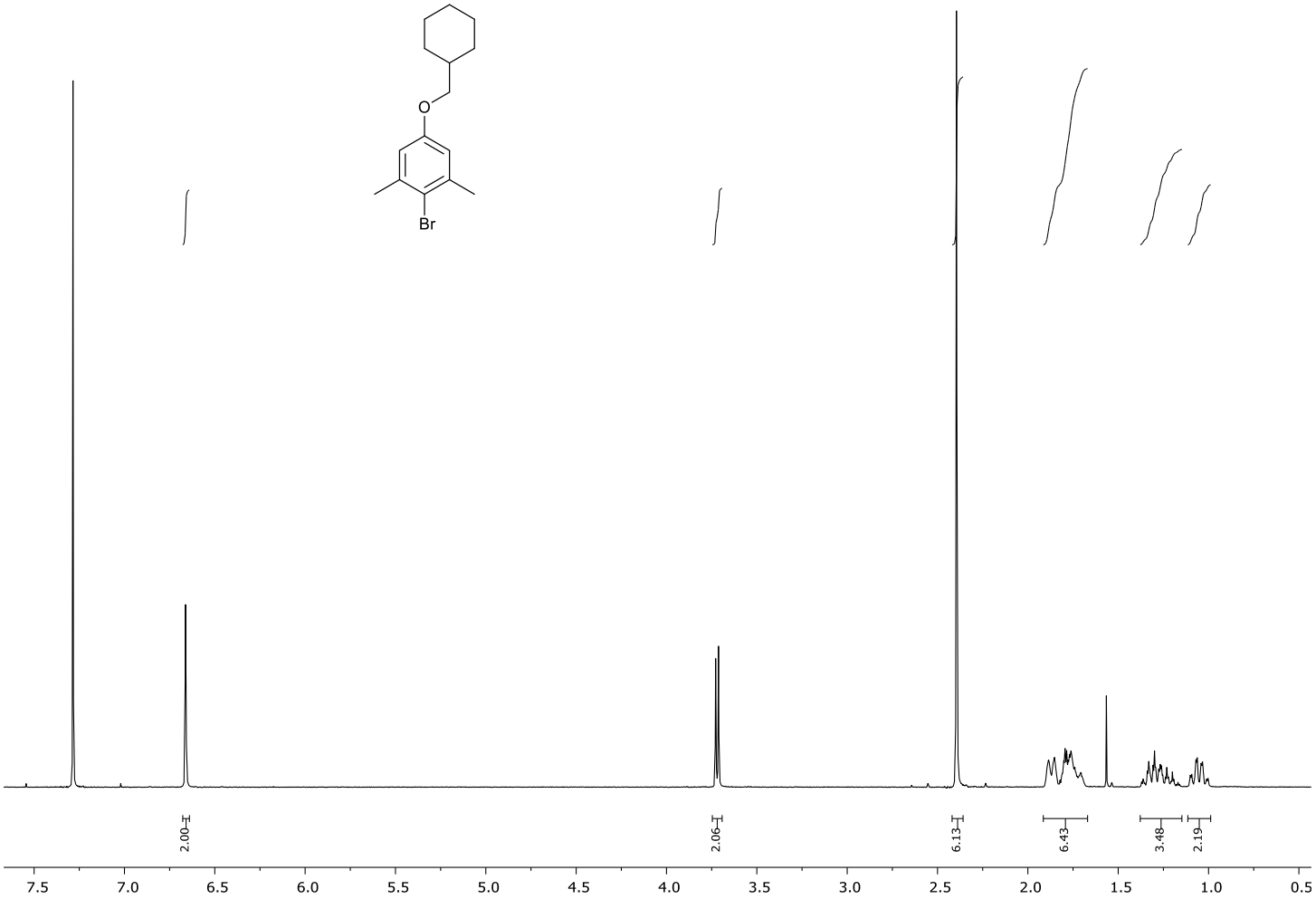

Figure S84. ^{1}H NMR spectrum (400 MHz) of **24** in $CDCl_3$.

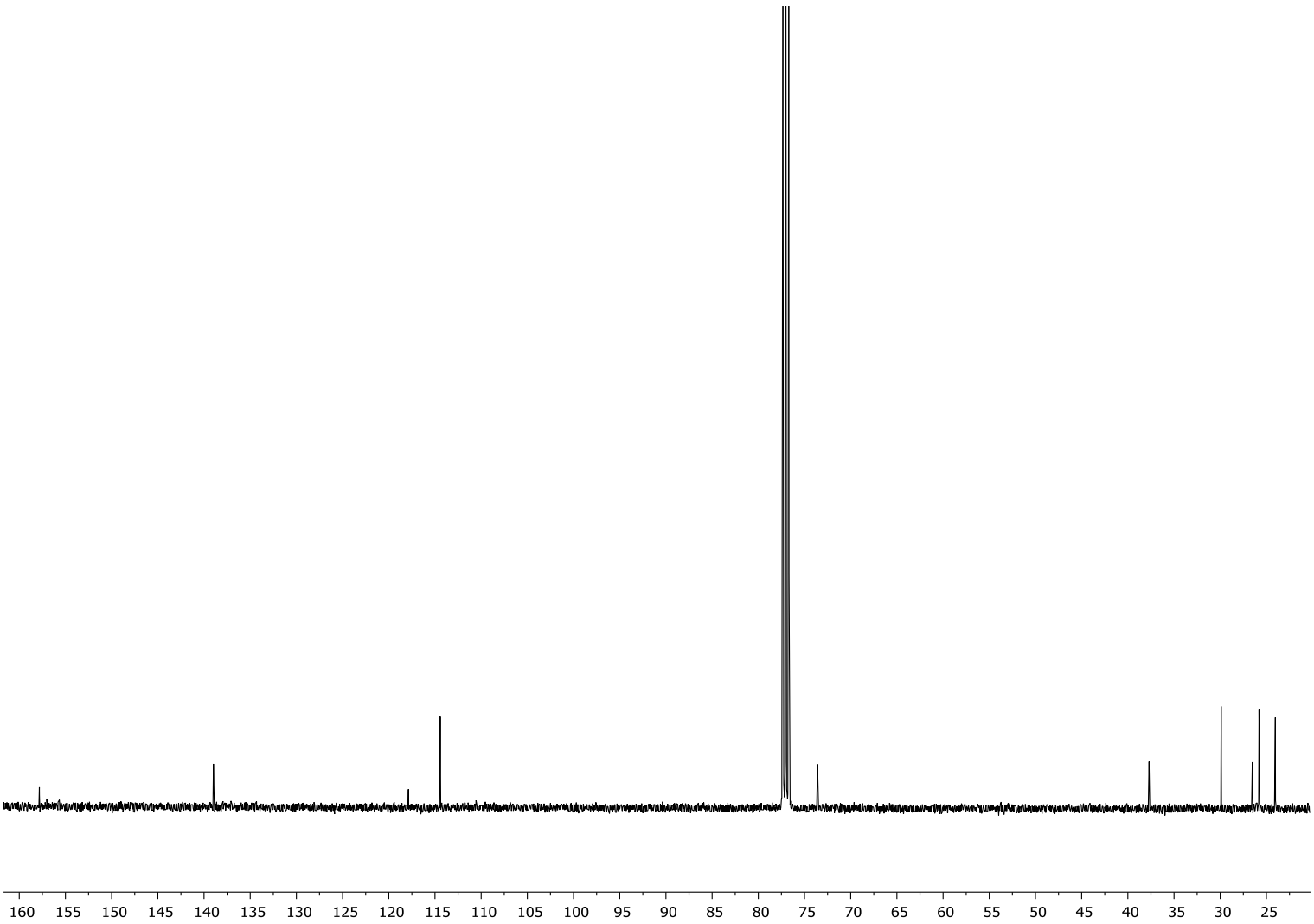

Figure S85. ^{13}C NMR spectrum (101 MHz) of **24** in $CDCl_3$.

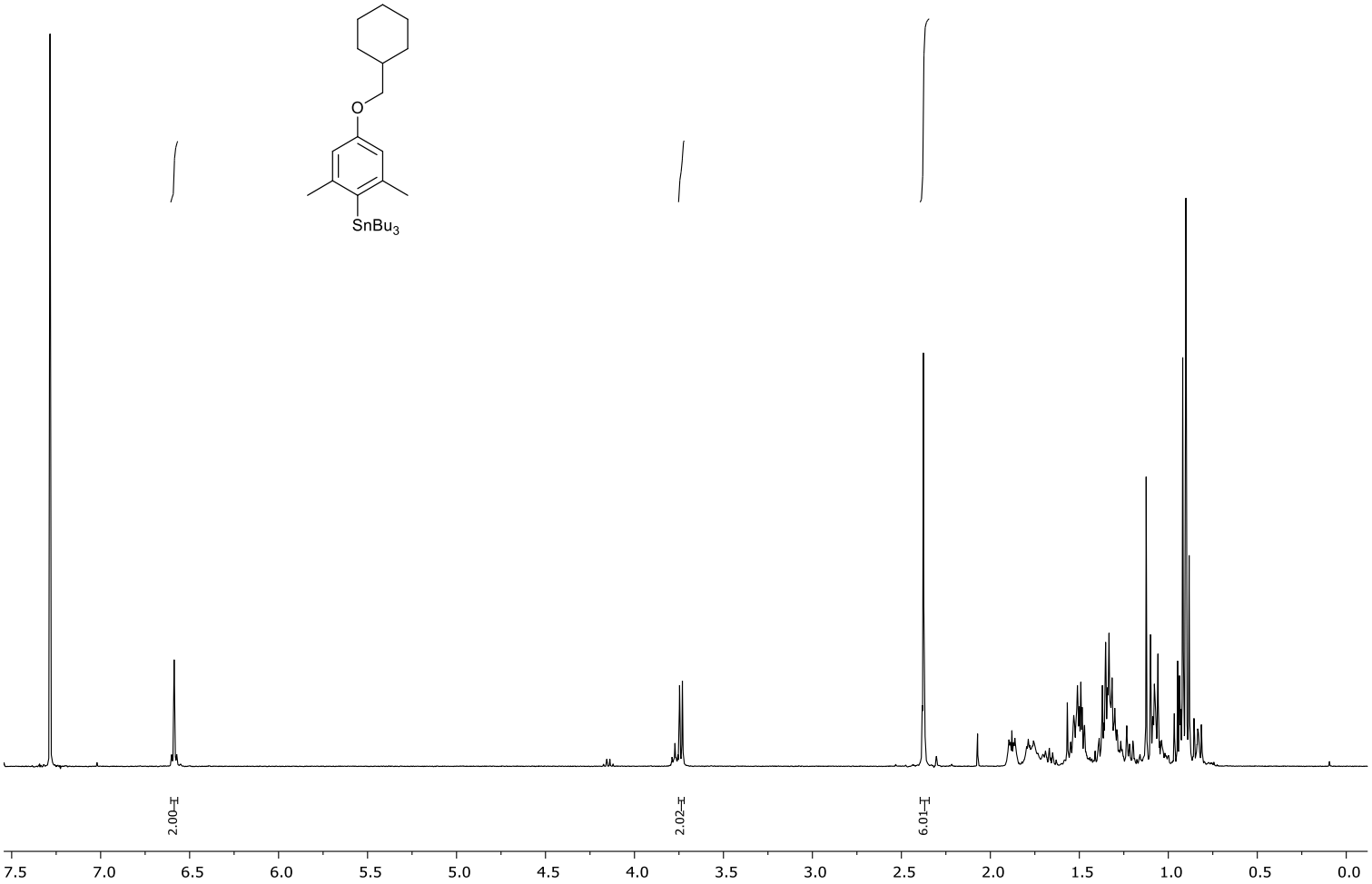

Figure S86. ^{1}H NMR spectrum (400 MHz) of **25** in $CDCl_3$.

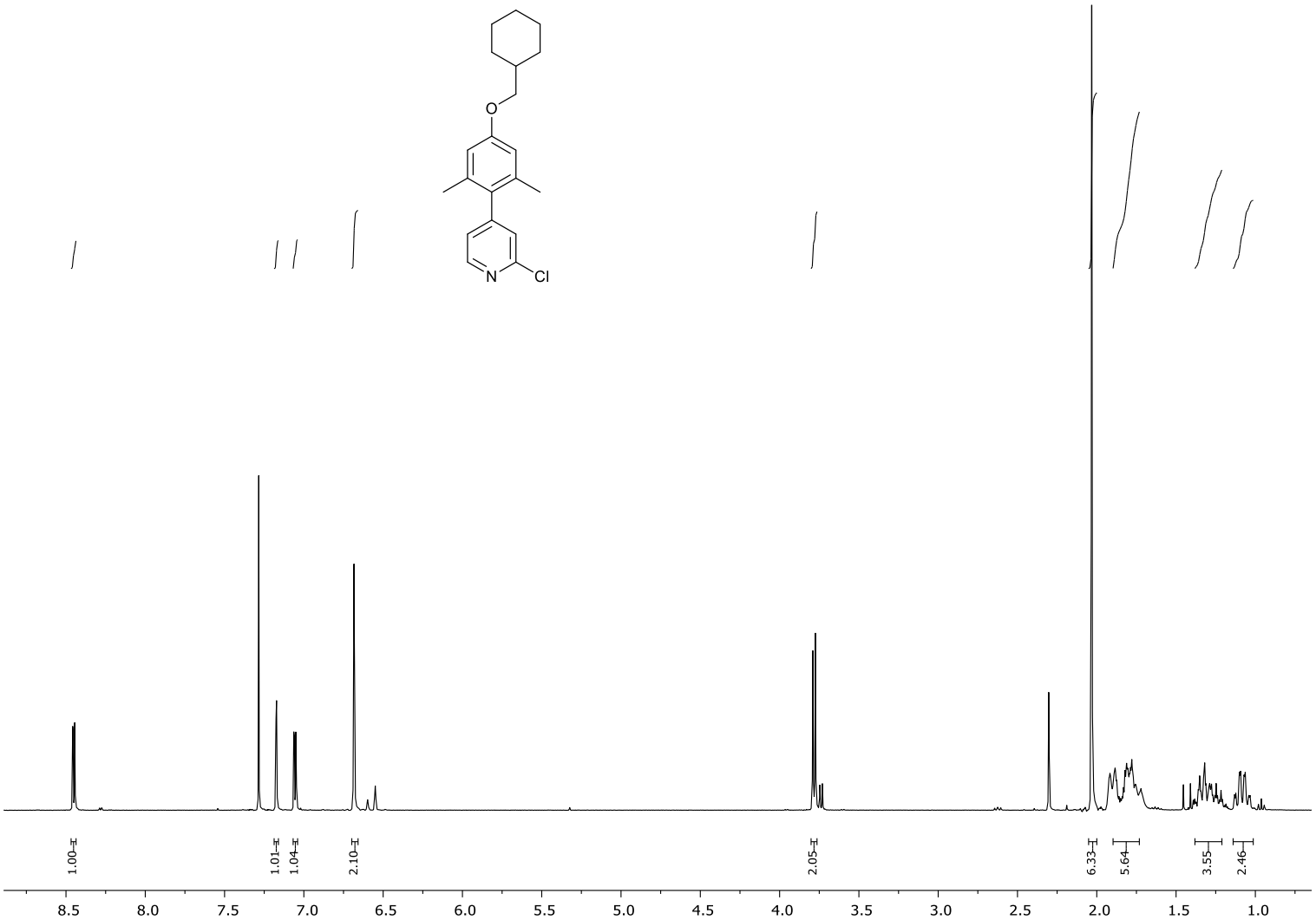

Figure S87. ^{1}H NMR spectrum (400 MHz) of **26** in $CDCl_3$.

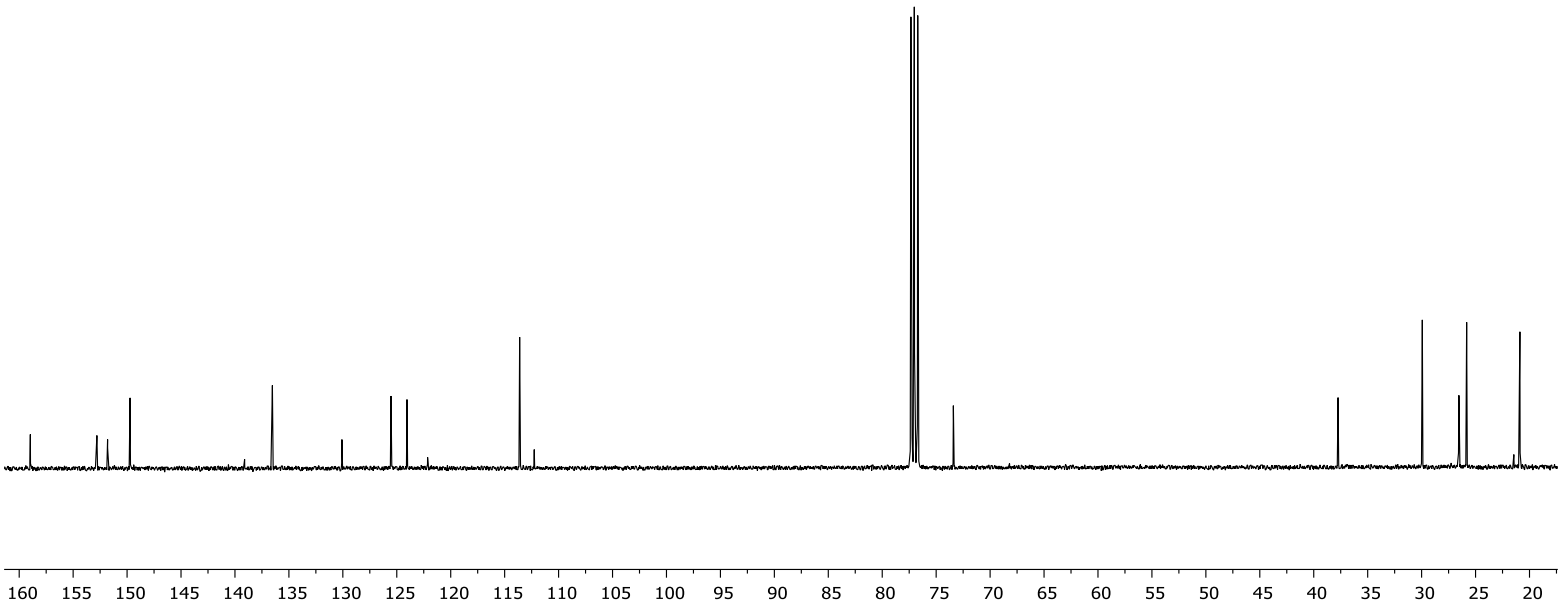

Figure S88. ^{13}C NMR spectrum (101 MHz) of **26** in $CDCl_3$.

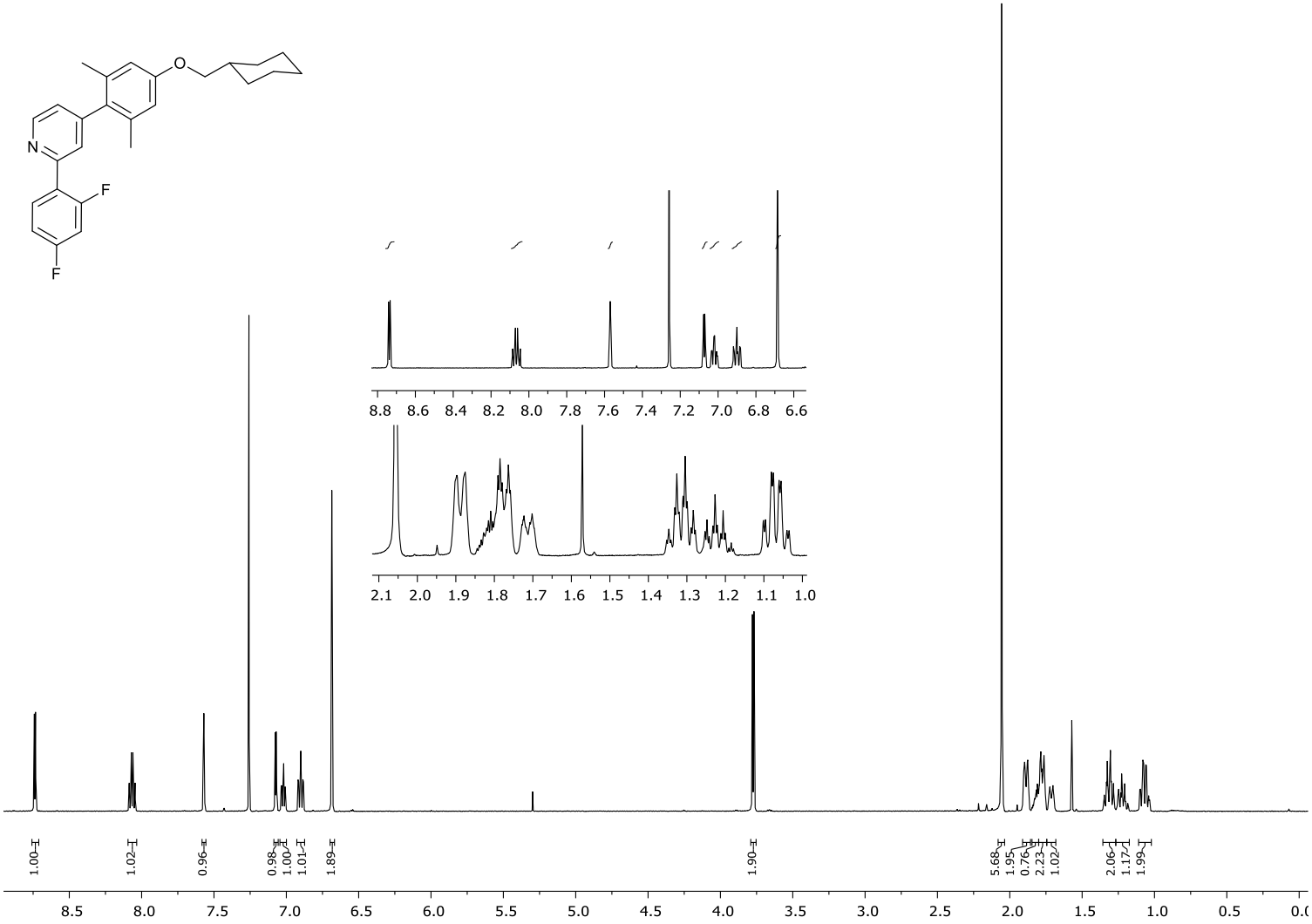

Figure S89. ^{1}H NMR spectrum (600 MHz) of **21** in $CDCl_3$.

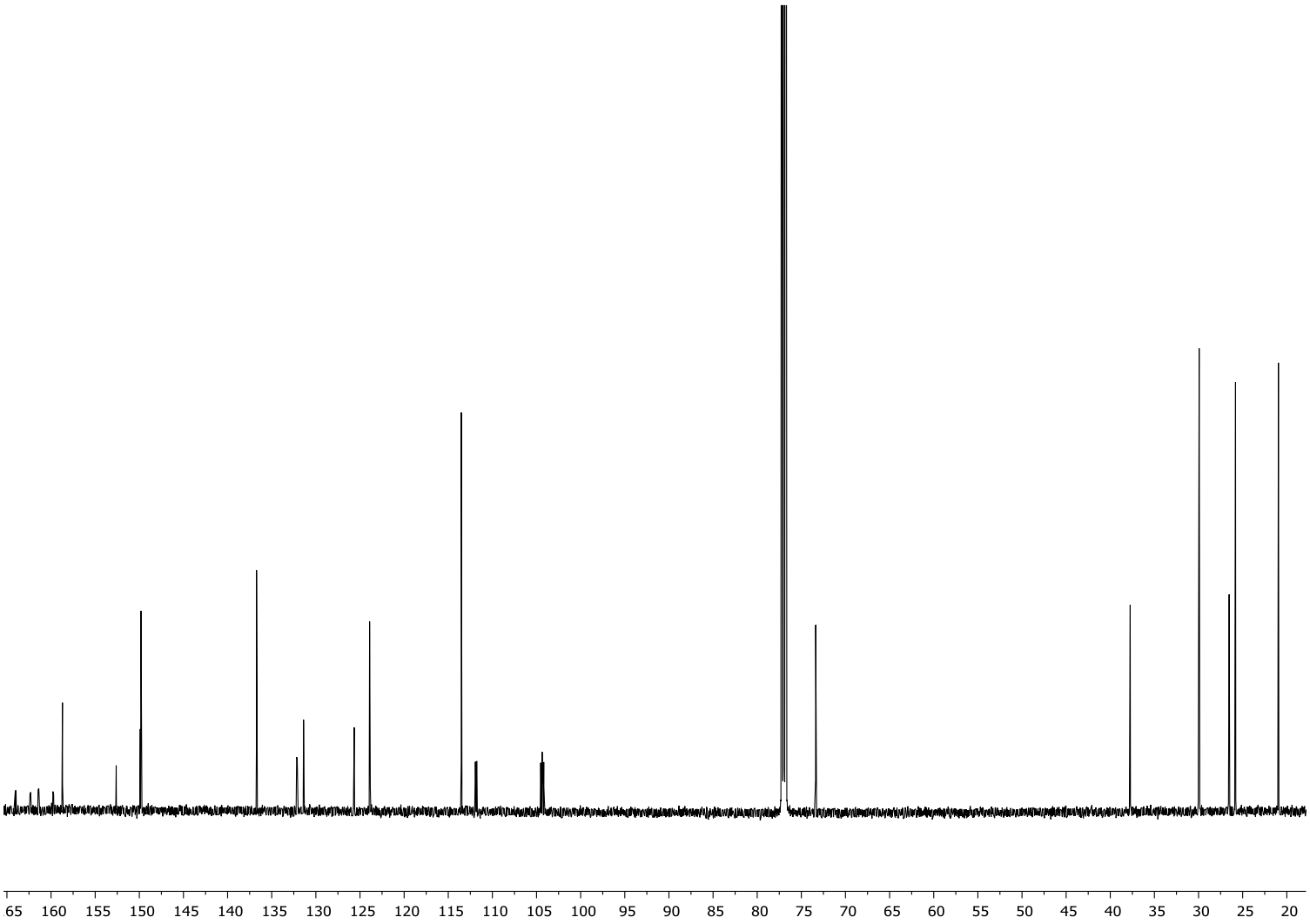

Figure S90. ^{13}C NMR spectrum (151 MHz) of **21** in $CDCl_3$.

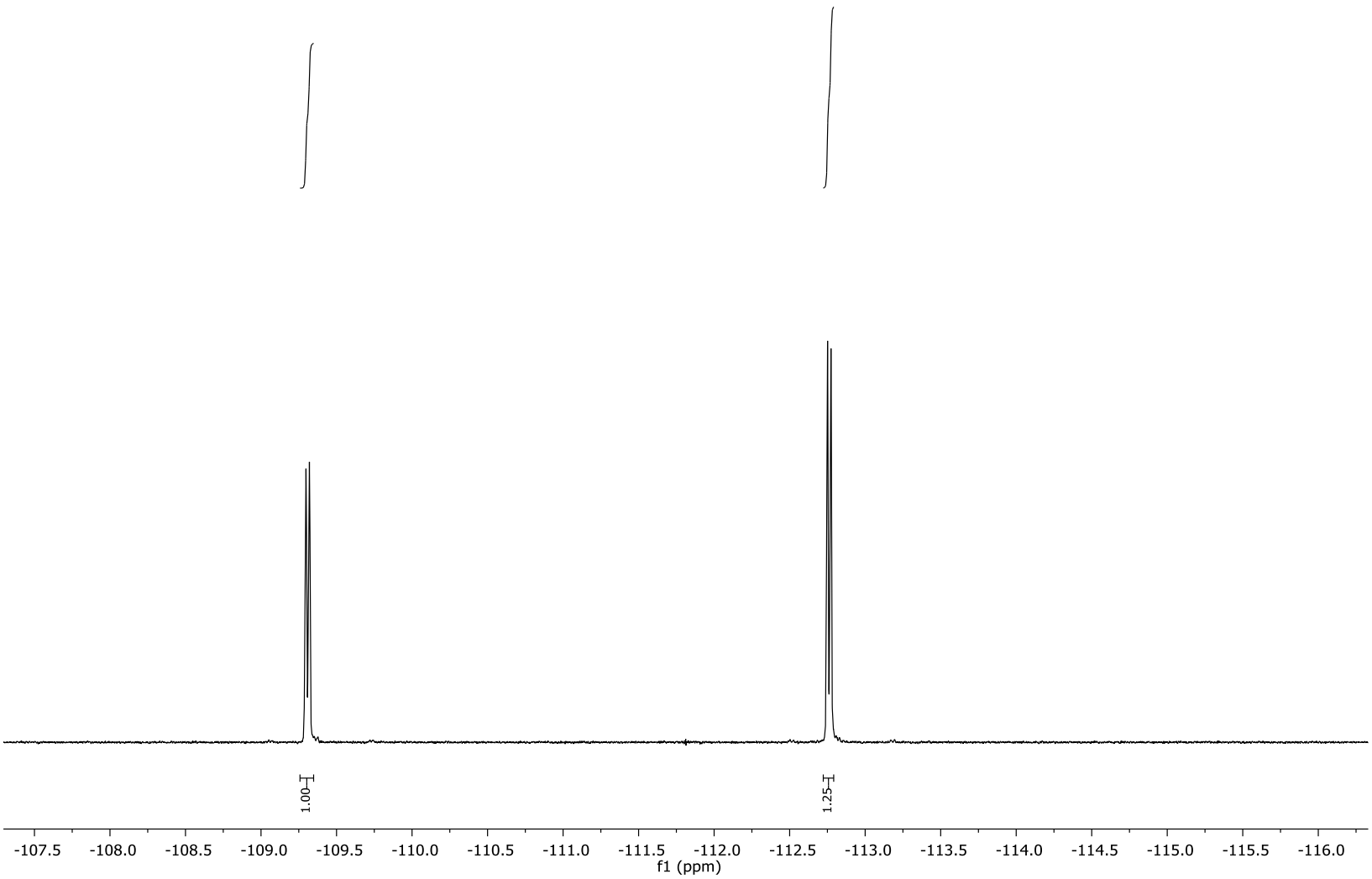

Figure S91. $^{19}F\{^{1}H\}$ NMR spectrum (376 MHz) of **22** in $CDCl_3$.

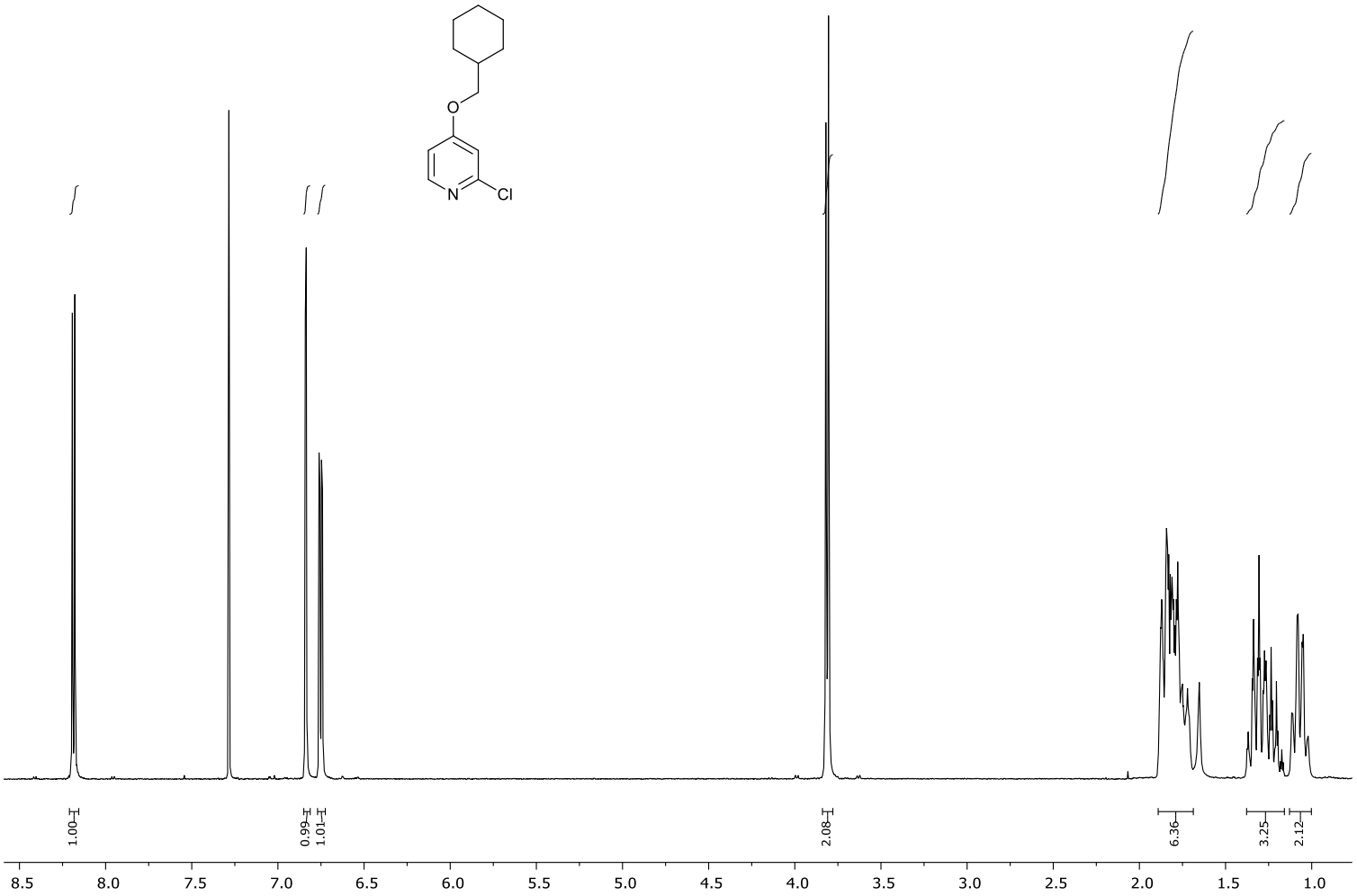

Figure S92. ^{1}H NMR spectrum (400 MHz) of **28** in $CDCl_3$.

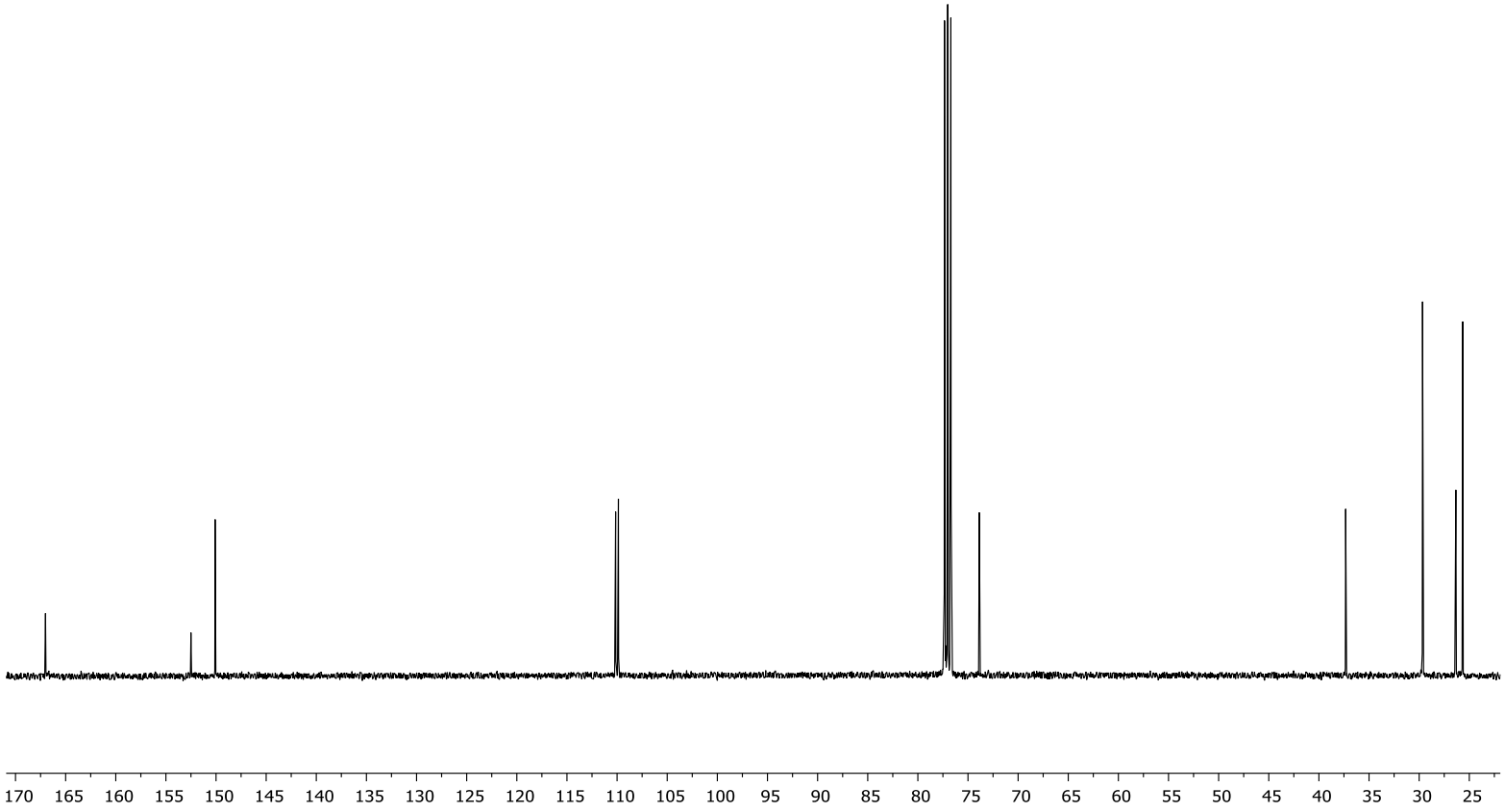

Figure S93. ^{13}C NMR spectrum (101 MHz) of **28** in $CDCl_3$.

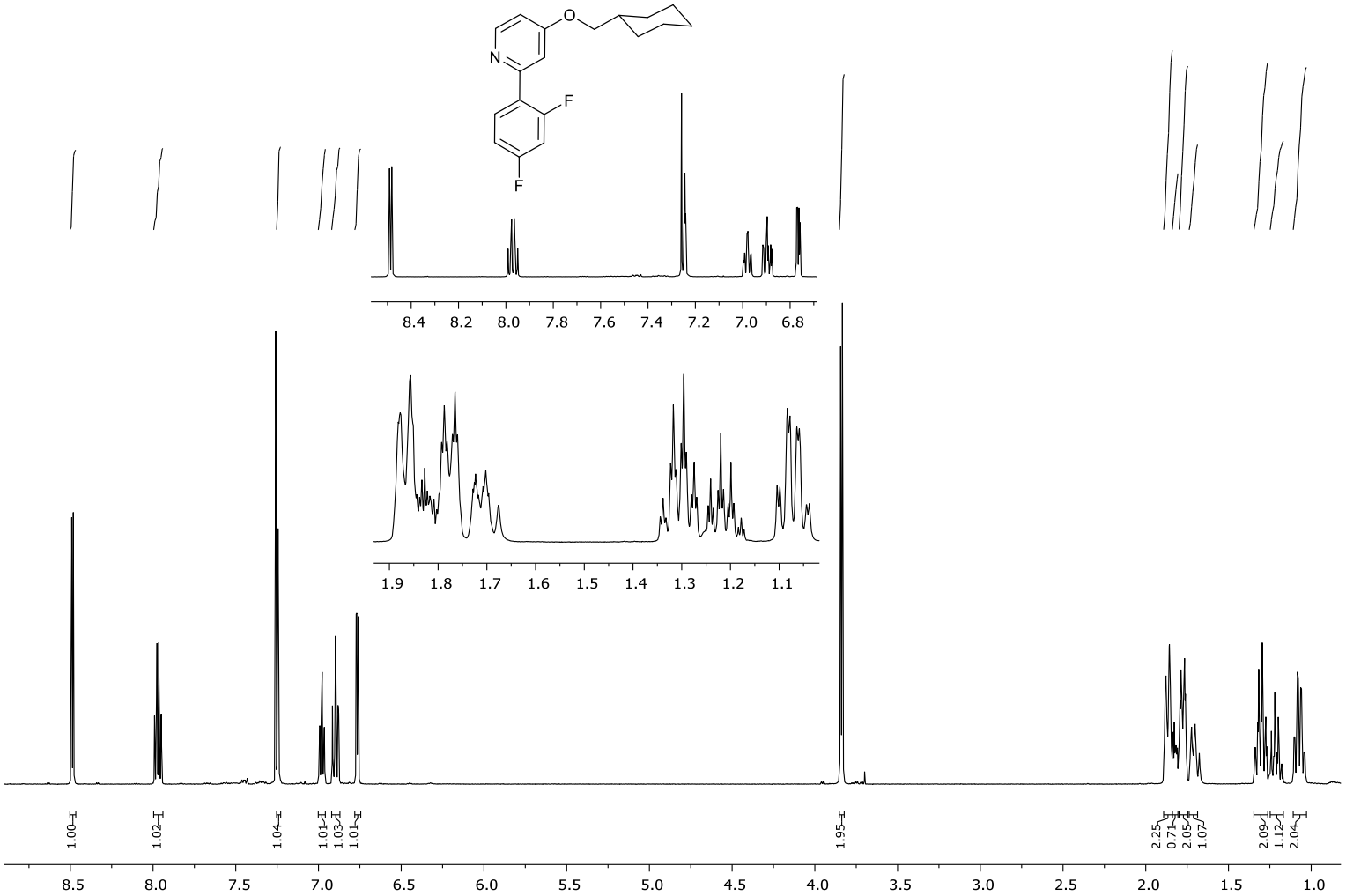

Figure S94. ^{1}H NMR spectrum (600 MHz) of **22** in $CDCl_3$.

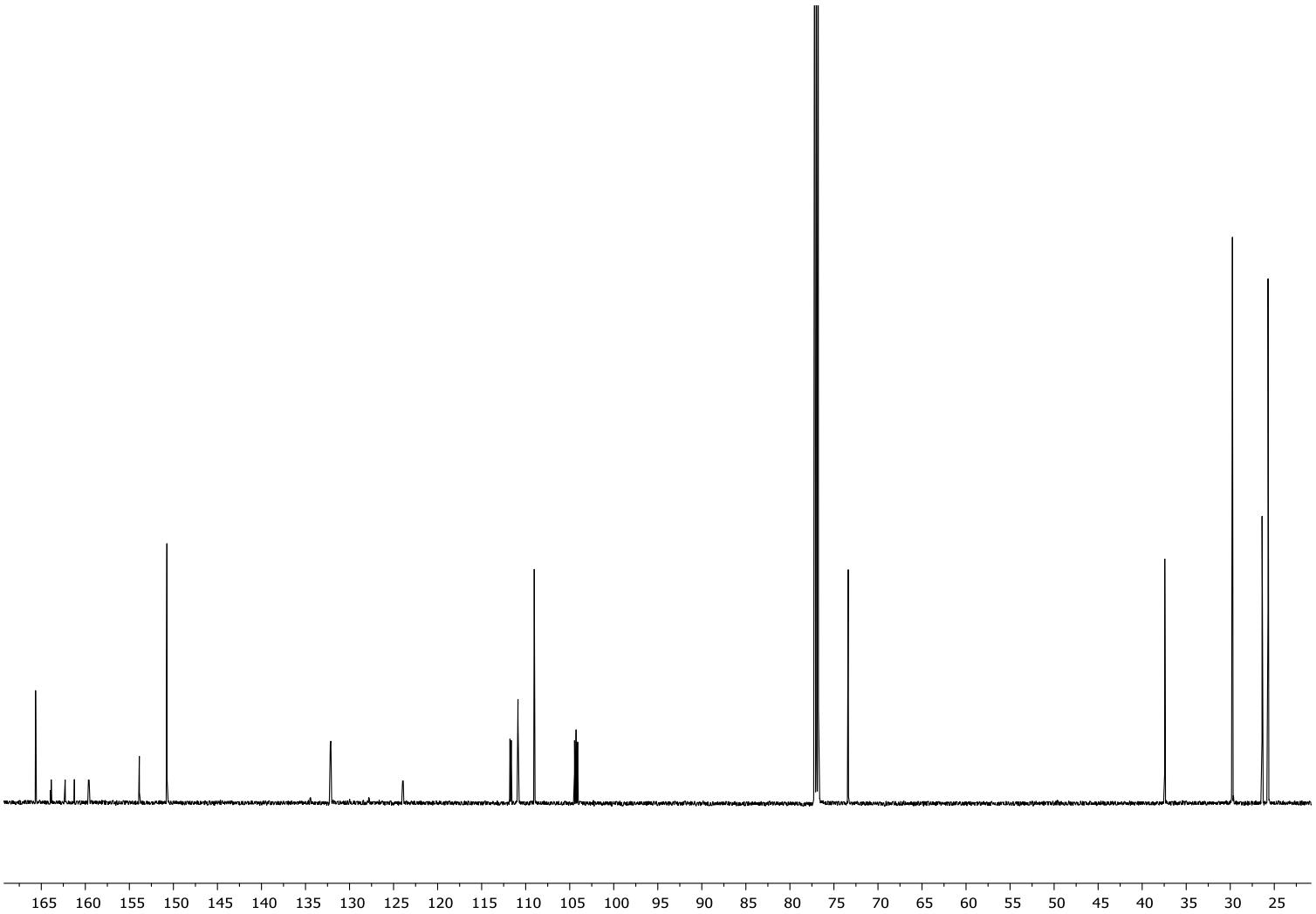

Figure S95. ^{13}C NMR spectrum (151 MHz) of **22** in $CDCl_3$.

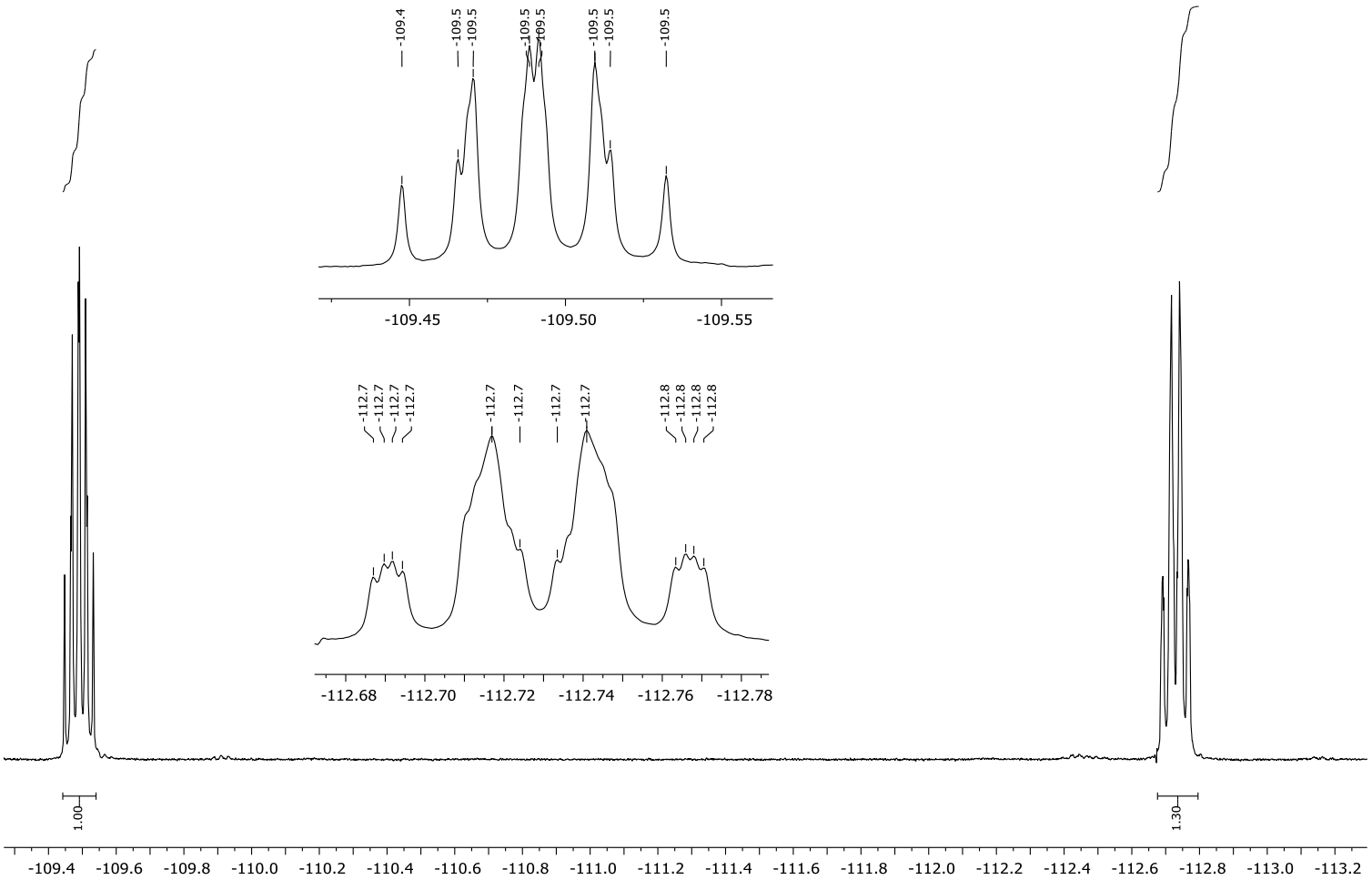

Figure S96. $^{19}F\{^{1}H\}$ NMR spectrum (376 MHz) of **22** in $CDCl_3$

X–ray Crystallography

Table S1. Selected geometrical parameters of diiridium complexes (bond distances averaged, in Å).

CCDC numbers are as follows: **7** $3CH_2Cl_2$ = 1576081, **9 =** 1576082, α-**10** = 1576083, β-**10 =** 1576084, **11** $2CH_2Cl_2$ = 1576093, **12** $5CH_2Cl_2$ = 1576094, **13** $2.25CD_2Cl_2$ = 1576095**.**

	7 $3CH_2Cl_2$	**9**	α-**10**	β-**10**	**11** $2CH_2Cl_2$	**12** $5CH_2Cl_2$[a]	**13** $2.25CD_2Cl_2$
Space group	$P\bar{1}$	$I4_1/a$	$C2/c$	$P2_1/n$	$P\bar{1}$	$P\bar{1}$	$P\bar{1}$
Molec. symm	C_i	C_i	C_2	--	--	C_i	--
Ir centres	ΔΛ	ΔΛ	ΔΔ, ΛΛ	ΔΔ, ΛΛ	ΔΔ, ΛΛ	ΔΛ	ΔΔ, ΛΛ
Ir…Ir, Å	5.091	5.089	5.117	5.062	5.082	5.147, 5.152	5.070
Ir-C (*trans*-O)	1.998(2)	2.006(6)	2.001(2)	1.994(4)	1.992(7)	1.994(3)	1.988(4)
Ir-C (*trans*-N)	2.001(2)	1.994(6)	1.997(2)	2.002(4)	2.000(7)	1.992(3)	1.996(4)
Ir-N, stacked	2.032(2)	2.005(6)	2.040(1)	2.033(3)	2.033(5)	2.029(3)	2.035(3)
Ir-N, non-stacked	2.042(2)	1.973(6)	2.044(1)	2.031(3)	2.037(5)	2.042(3)	2.031(3)
OCNNCO folding, °	planar	planar	6.8	24.3	14.3	planar	17.9
Ir displacement, Å	0.01	0.23	0.06	0.28, 0.39	0.26, 0.20	0.52, 0.00	0.17, 0.24
Ir-O	2.152(2)	2.161(2)	2.156(1)	2.147(3)	2.142(5)	2.144(2)	2.127(3)
Ir-N	2.171(2)	2.170(3)	2.180(1)	2.164(3)	2.169(5)	2.214(2)	2.175(3)
N-N	1.438(3)	1.435(5)	1.439(2)	1.443(4)	1.448(6)	1.445(2)	1.436(4)
N-C	1.312(3)	1.308(4)	1.314(2)	1.307(5)	1.305(8)	1.310(4)	1.301(5)
C-O	1.286(2)	1.279(4)	1.283(2)	1.275(4)	1.279(8)	1.268(4)	1.278(4)
Θ, °[b]	8.5	5.9	13.5	6.9, 8.7	4.6, 6.0	--	6.2, 3.4
D, Å[c]	3.32	3.24	3.42	3.39, 3.35	3.33, 3.30	--	3.27, 3.19

[a] contains two crystallographically non-equivalent centrosymmetric dimers; [b] interplanar angle between ring *A* of the bridging ligand and ring *B* of the cyclometalating ligand (see Figure 4); [c] distance between the plane of ring *B* and the centroid of ring *A*.

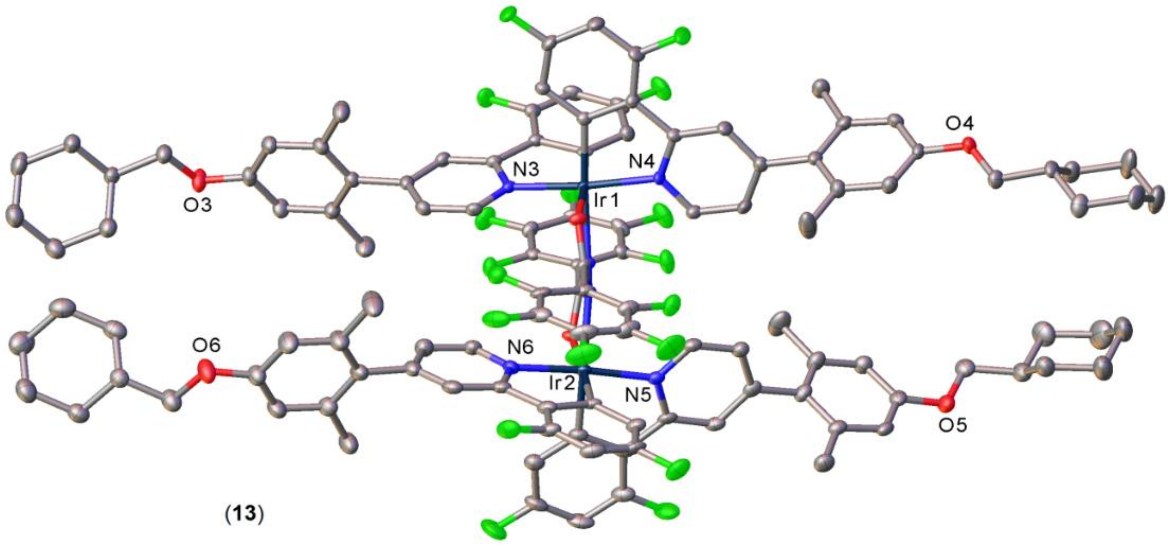

Figure S97. X-ray molecular structure of *rac* **13**. Thermal ellipsoids are drawn at 50% probability level. H atoms are omitted for clarity.

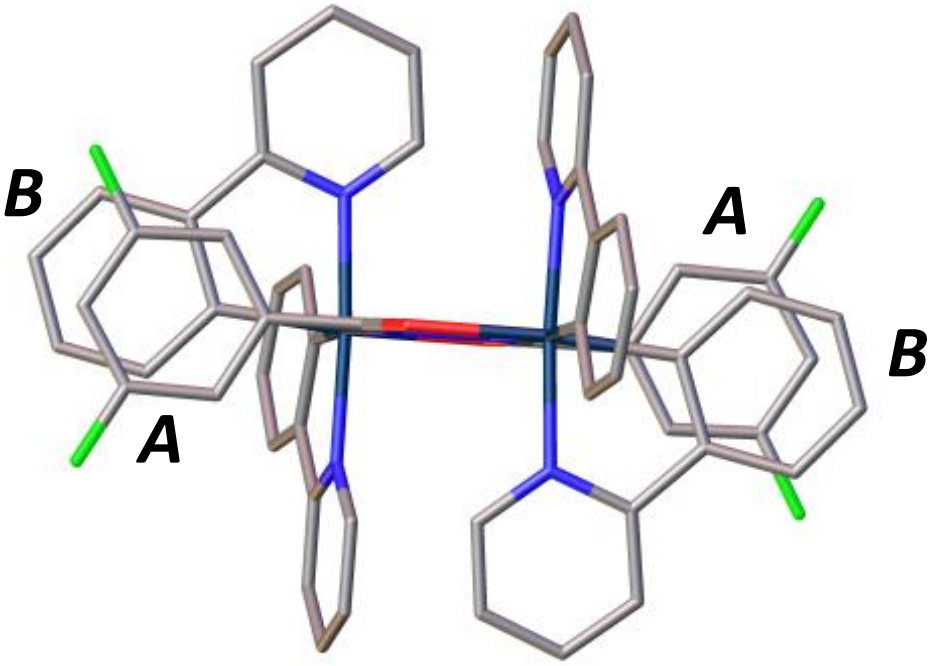

Figure S98. Molecular structure of *meso* **7** viewed perpendicular to the plane of the cyclometalating phenyl moieties to highlight intramolecular π–π interactions. The bridge (*A*) and cyclometalating ligand (*B*) phenyl groups that are engaged in intramolecular π–π stacking are labelled (see Table S1).

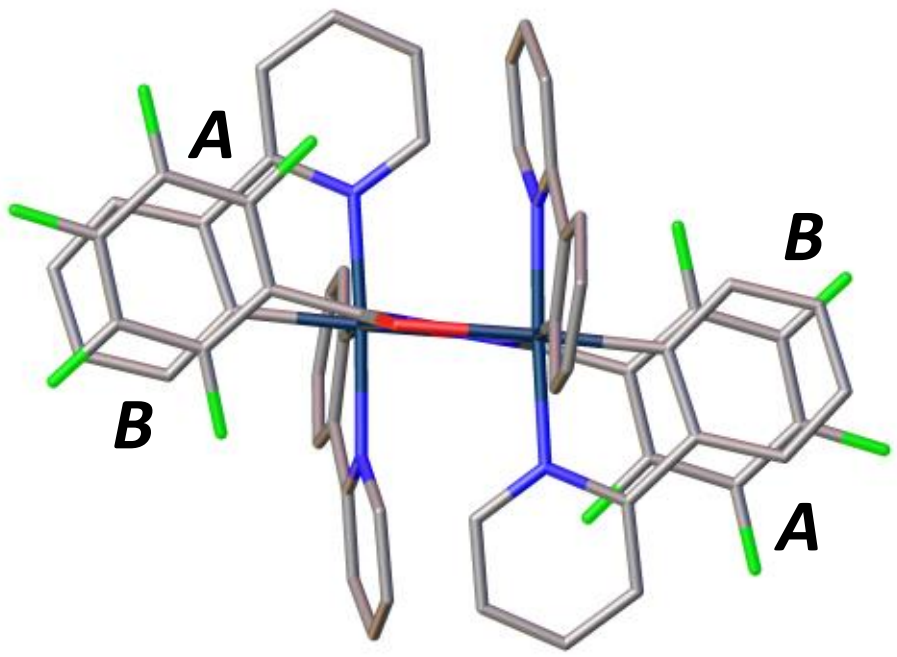

Figure S99. Molecular structure of *meso* **9** viewed perpendicular to the plane of the cyclometalating phenyl moieties to highlight intramolecular π–π interactions. The bridge (*A*) and cyclometalating ligand (*B*) phenyl groups that are engaged in intramolecular π–π stacking are labelled (see Table S1).

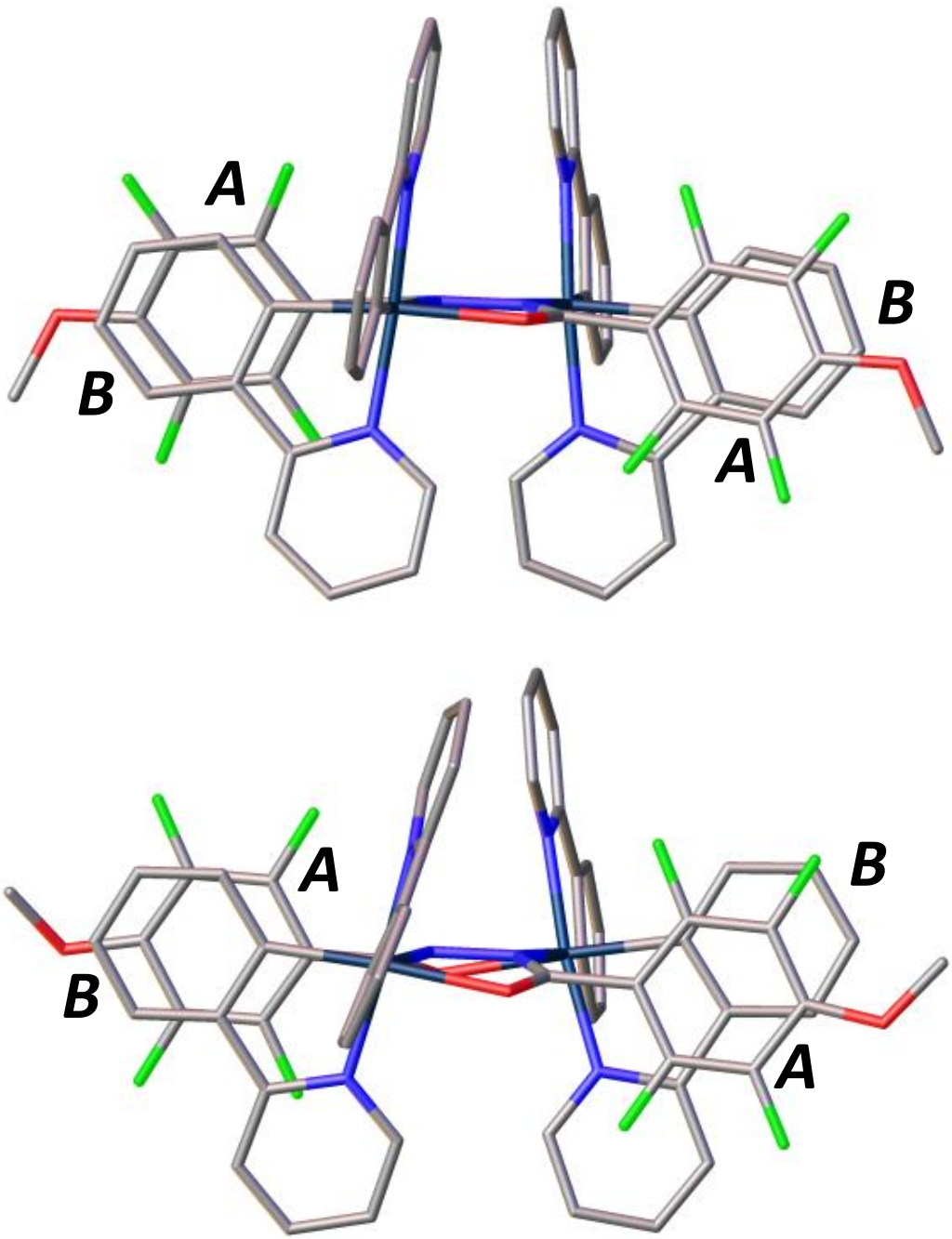

Figure S100. Molecular structures of α-ΔΔ **10** (top) and β-ΔΔ **10** (bottom) viewed perpendicular to the plane of the cyclometalating phenyl moieties to highlight intramolecular π–π interactions. The bridge (*A*) and cyclometalating ligand (*B*) phenyl groups that are engaged in intramolecular π–π stacking are labelled (see Table S1).

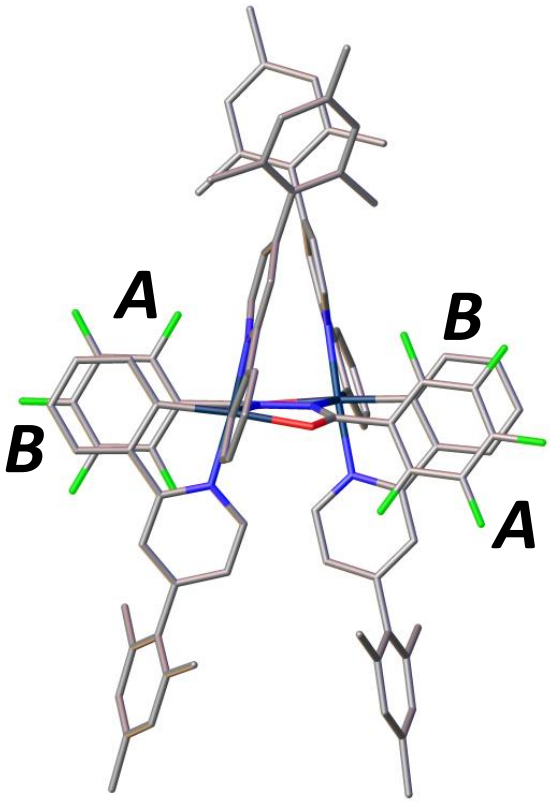

Figure S101. Molecular structure of ΔΔ **11** viewed perpendicular to the plane of the cyclometalating phenyl moieties to highlight intramolecular π–π interactions. The bridge (*A*) and cyclometalating ligand (*B*) phenyl groups that are engaged in intramolecular π–π stacking are labelled (see Table S1).

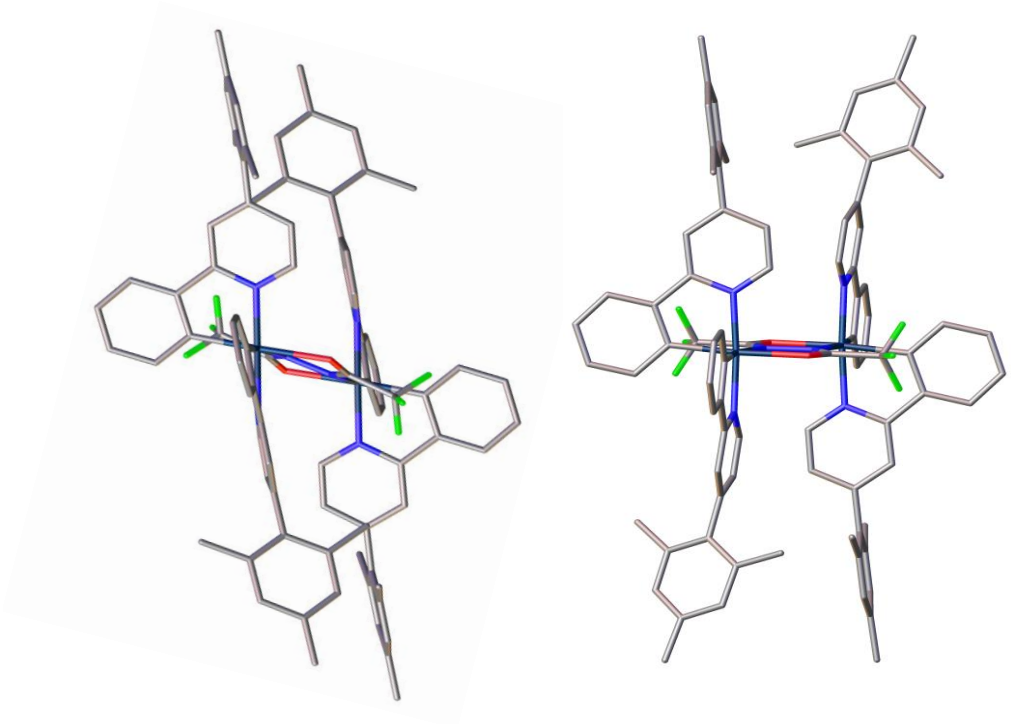

Figure S102. Molecular structures of molecule A (left) and molecule B (right) of *meso* **12** viewed perpendicular to the plane of the cyclometalating phenyl moieties.

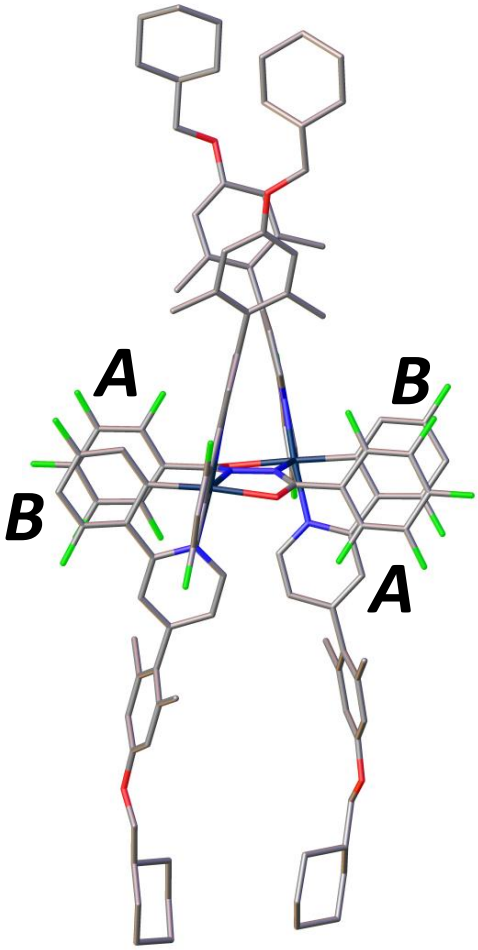

Figure S103. Molecular structure of **ΔΔ 13** viewed perpendicular to the plane of the cyclometalating phenyl moieties to highlight intramolecular π–π interactions. The bridge (*A*) and cyclometalating ligand (*B*) phenyl groups that are engaged in intramolecular π–π stacking are labelled (see Table S1).

Electrochemistry

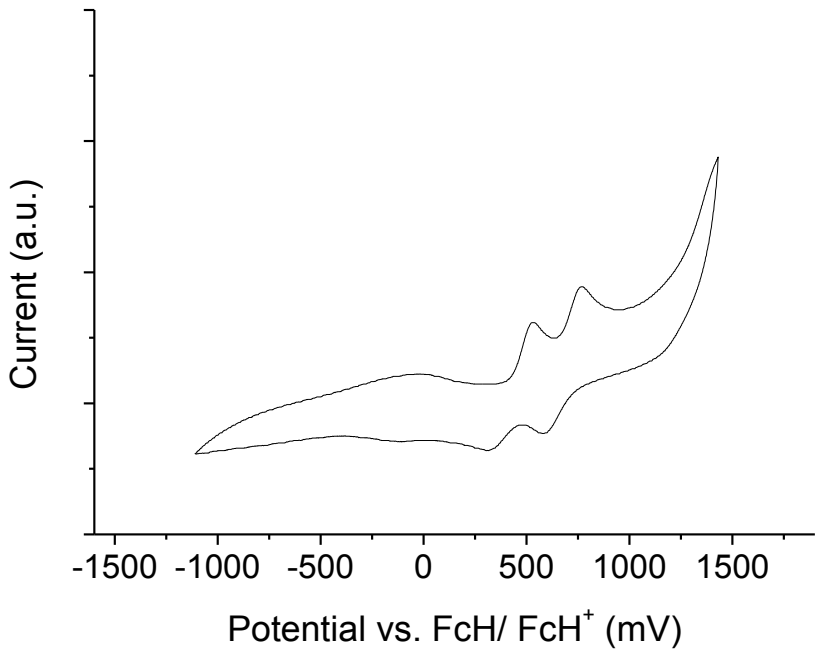

Figure S104. Cyclic voltammogram in 0.1 M *n*-Bu_4PF_6/ DCM showing the oxidation processes for complex **7**.

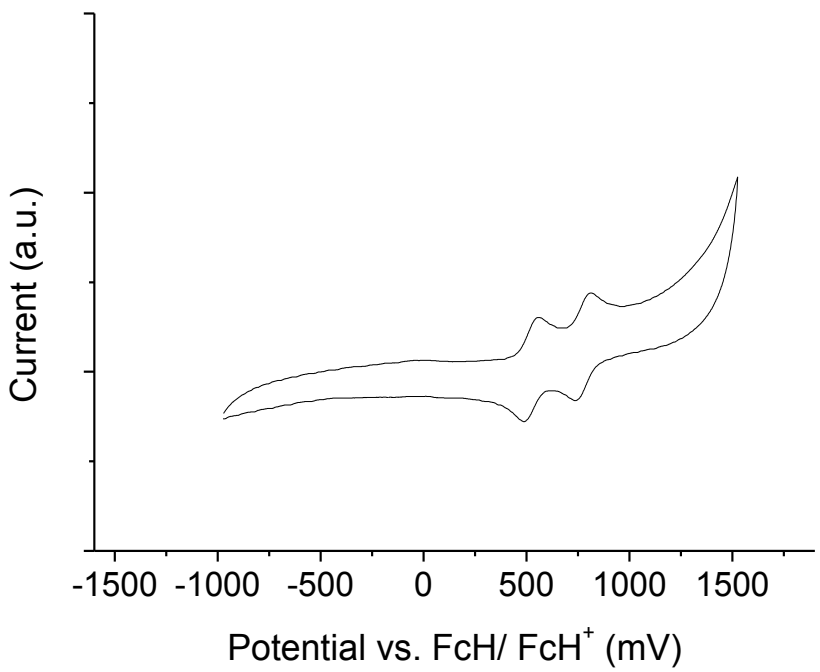

Figure S105. Cyclic voltammogram in 0.1 M *n*-Bu_4PF_6/ DCM showing the oxidation processes for complex **8**.

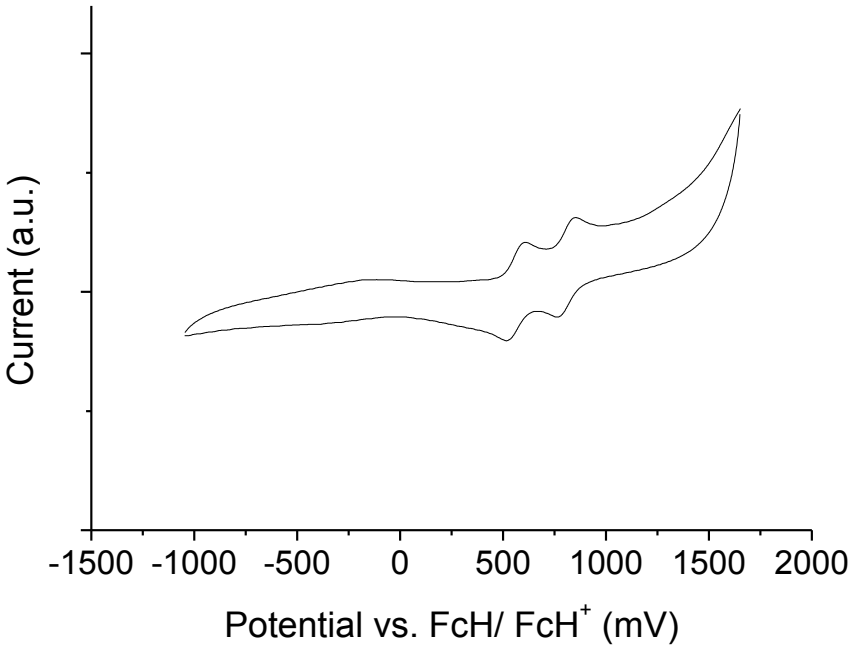

Figure S106. Cyclic voltammogram in 0.1 M *n*-Bu_4PF_6/ DCM showing the oxidation processes for complex **9**.

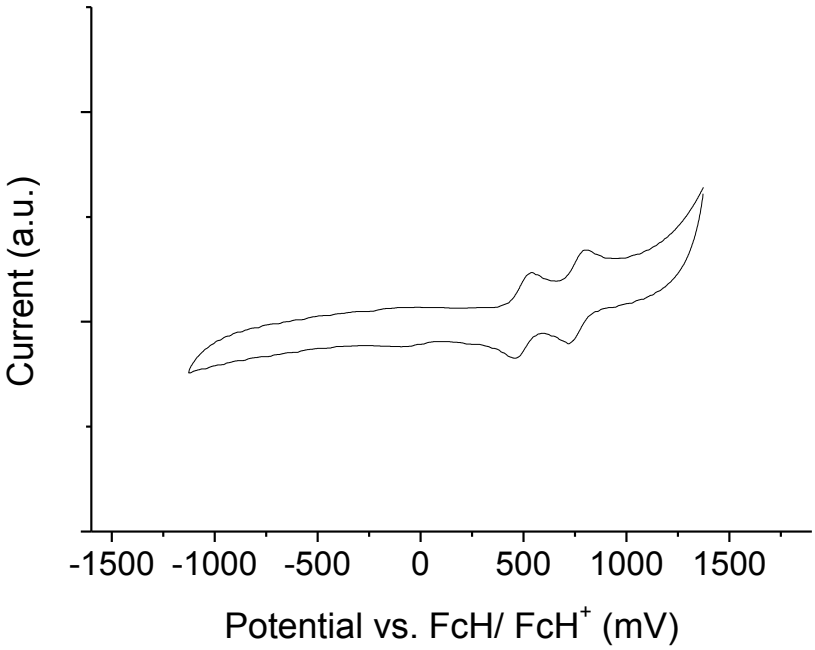

Figure S107. Cyclic voltammogram in 0.1 M *n*-Bu_4PF_6/ DCM showing the oxidation processes for complex **10**.

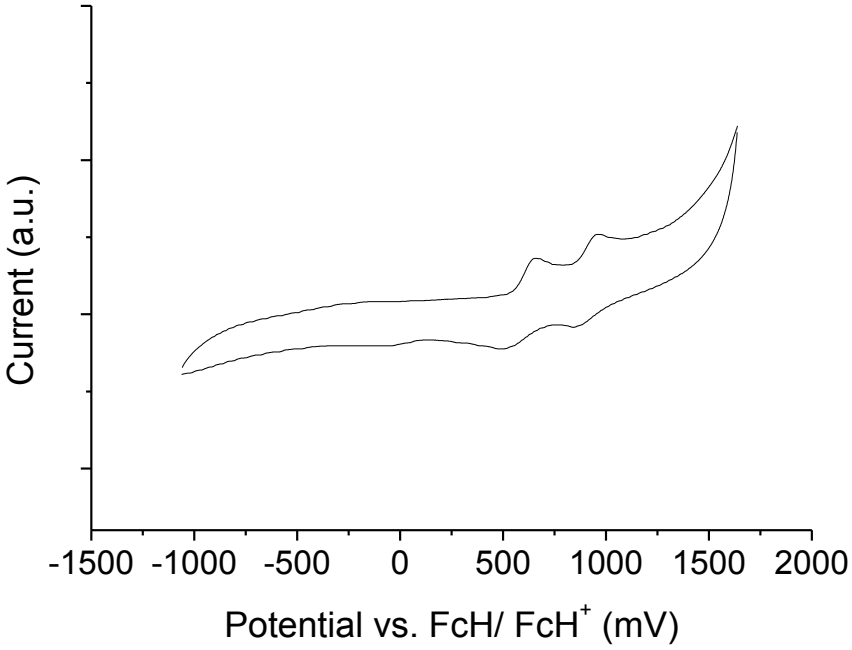

Figure S108. Cyclic voltammogram in 0.1 M *n*-Bu_4PF_6/ DCM showing the oxidation processes for complex **11**.

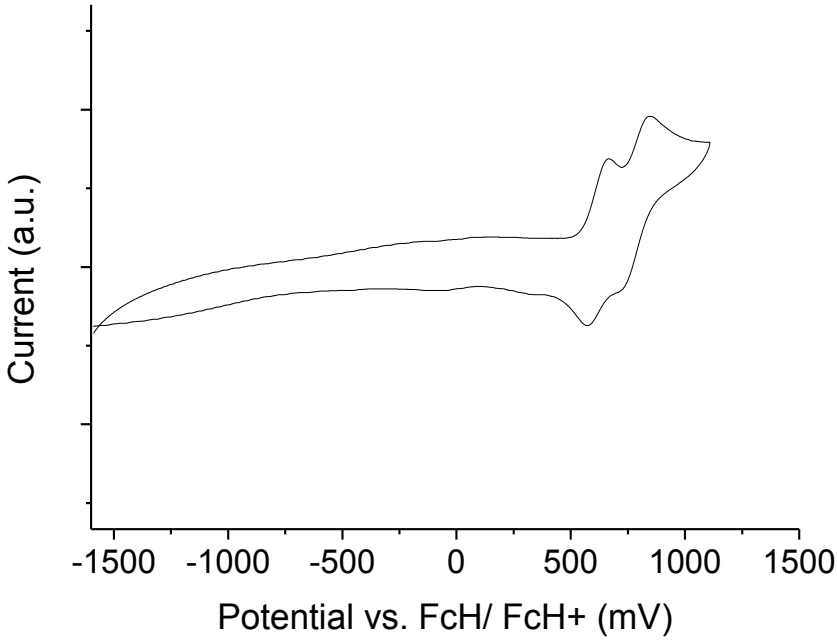

Figure S109. Cyclic voltammogram in 0.1 M *n*-Bu_4PF_6/ DCM showing the oxidation processes for complex **12**.

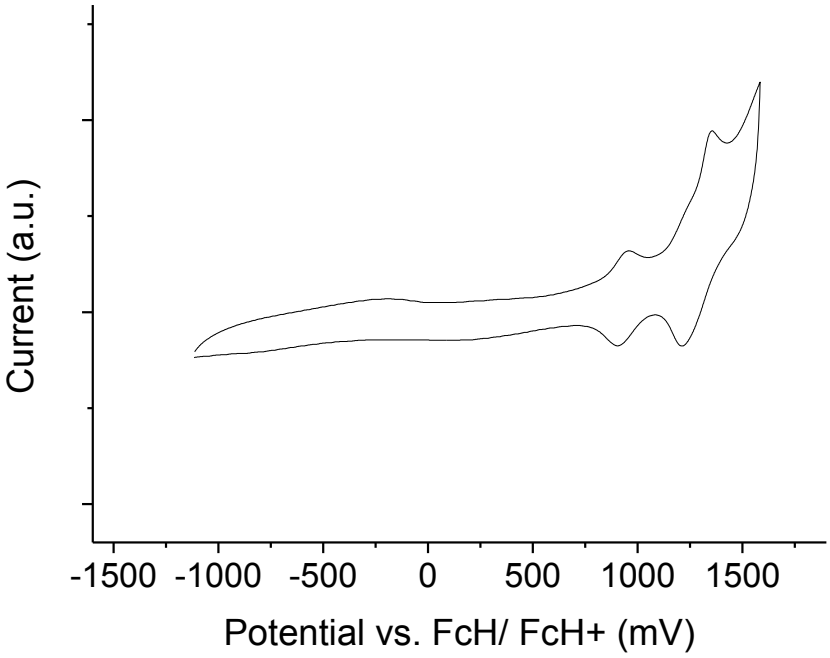

Figure S110. Cyclic voltammogram in 0.1 M *n*-Bu_4PF_6/ DCM showing the oxidation processes for complex *meso* **13**.

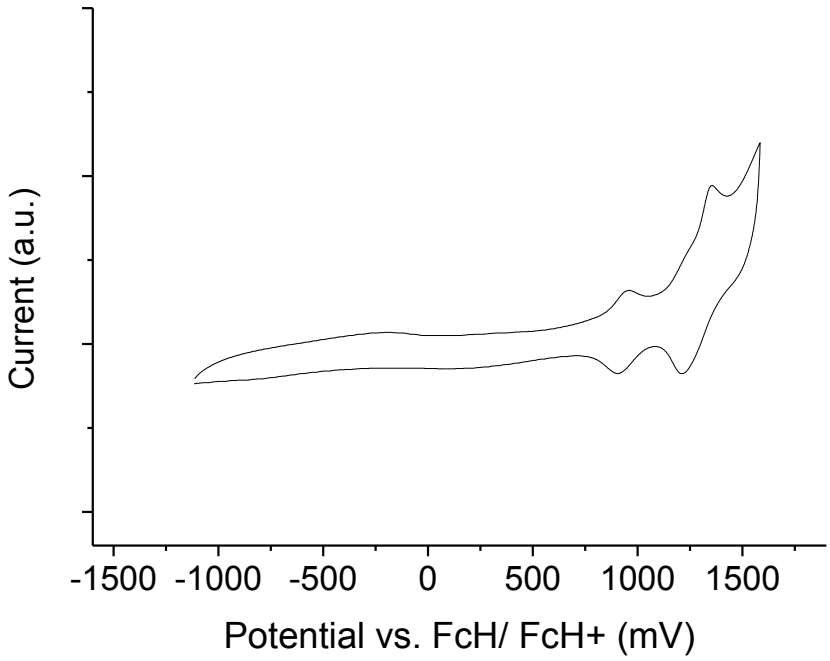

Figure S111. Cyclic voltammogram in 0.1 M *n*-Bu_4PF_6/ DCM showing the oxidation processes for complex *rac* **13**.

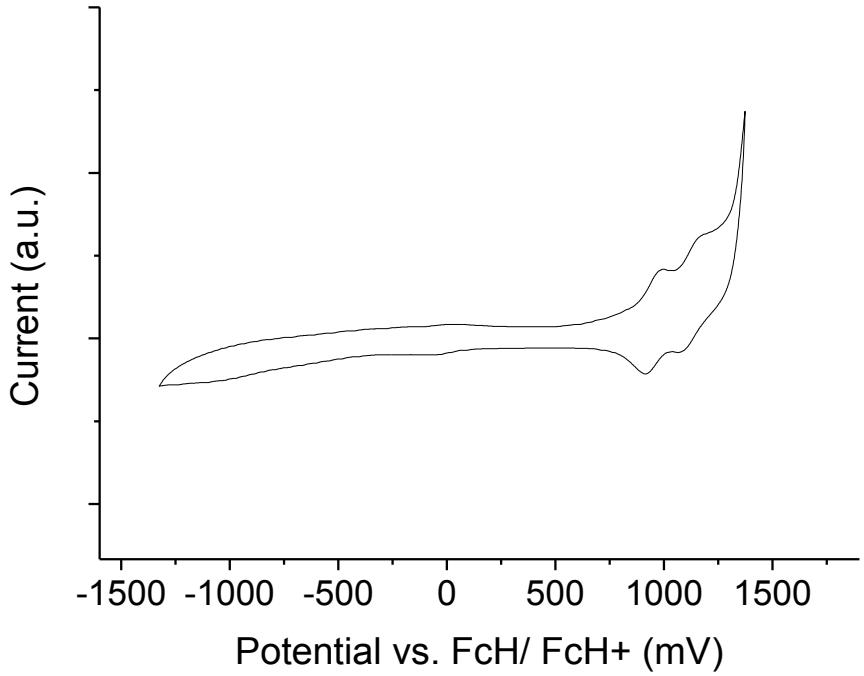

Figure S112. Cyclic voltammogram in 0.1 M *n*-Bu_4PF_6/ DCM showing the oxidation processes for complex **14**.

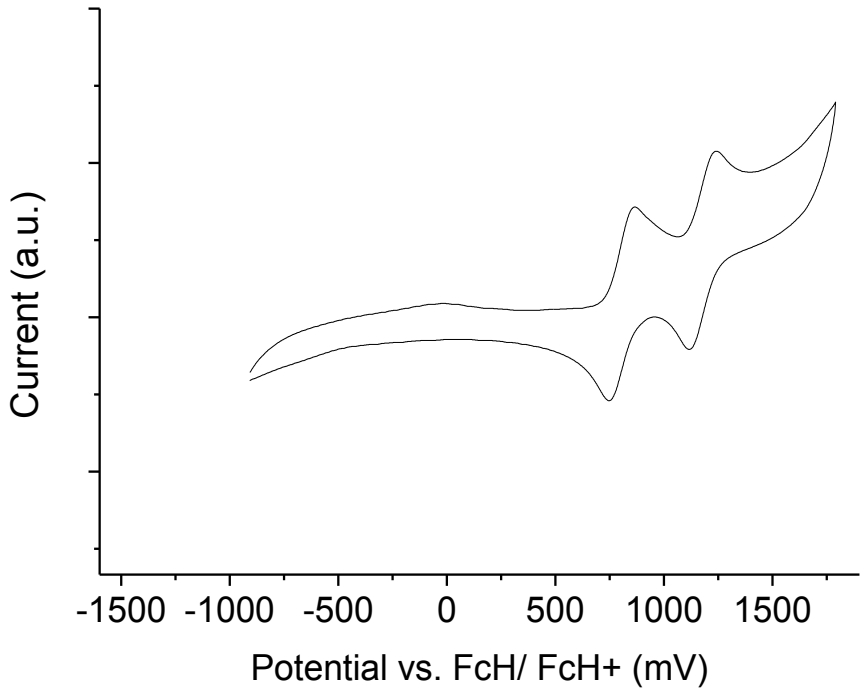

Figure S113. Cyclic voltammogram in 0.1 M *n*-Bu_4PF_6/ DCM showing the oxidation processes for complex **15**.

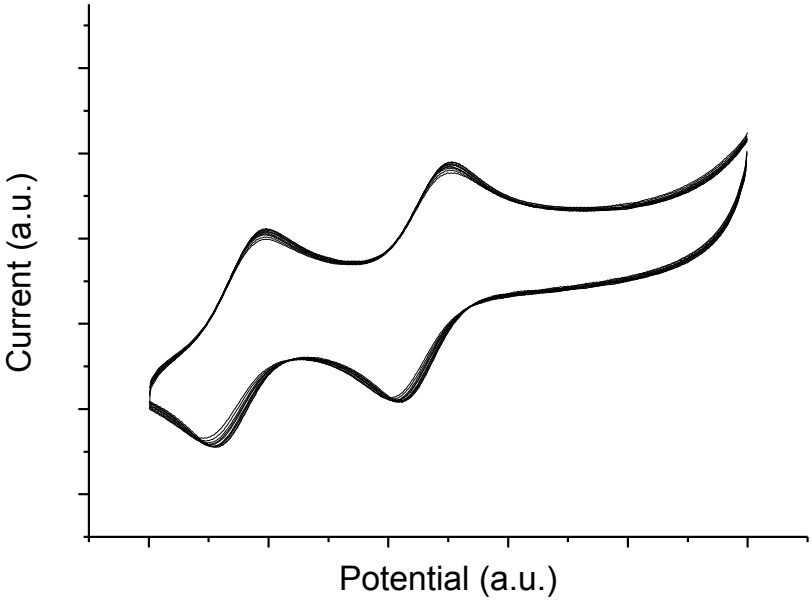

Figure S114. Cyclic voltammograms in 0.1 M *n*-Bu_4PF_6/ DCM showing the oxidation processes for complex **11** over 10 consecutive scans. The potential axis is arbitrary due to the absence of internal ferrocene. The oxidation potentials slightly drift due to the use of a quasireference electrode.

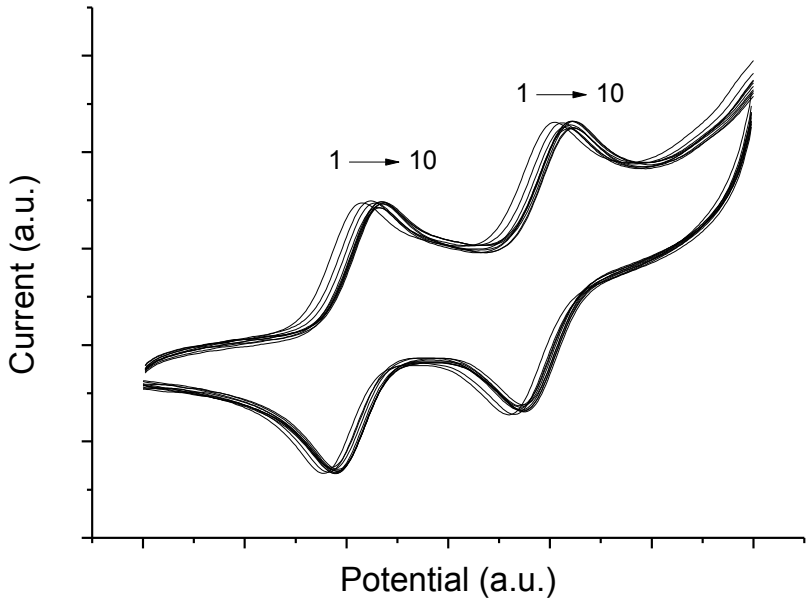

Figure S115. Cyclic voltammograms in 0.1 M *n*-Bu_4PF_6/ DCM showing the oxidation processes for complex **15** over 10 consecutive scans. The potential axis is arbitrary due to the absence of internal ferrocene. The oxidation potentials slightly drift due to the use of a quasireference electrode.

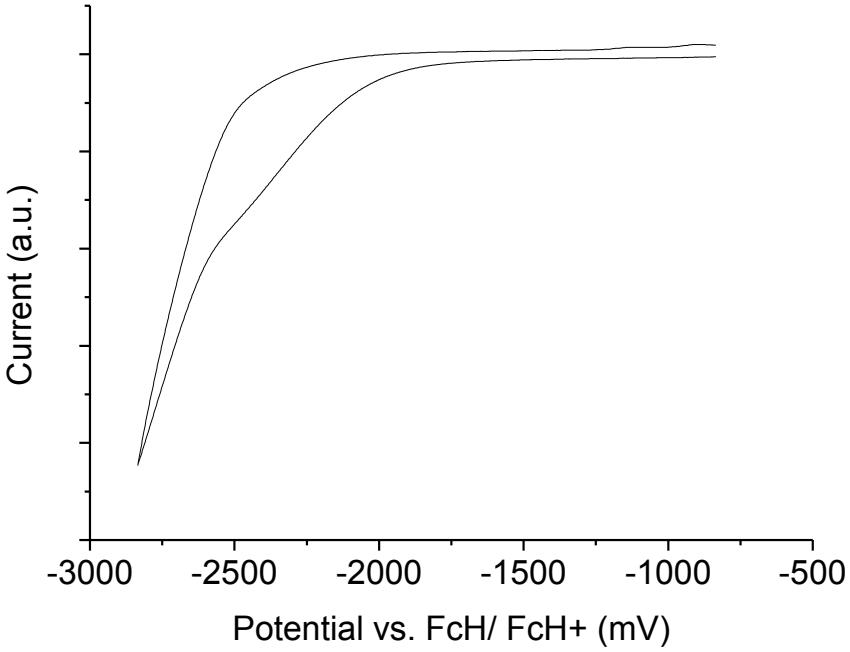

Figure S116. Cyclic voltammogram in 0.1 M *n*-Bu_4PF_6/ THF showing the reduction process for complex **7**.

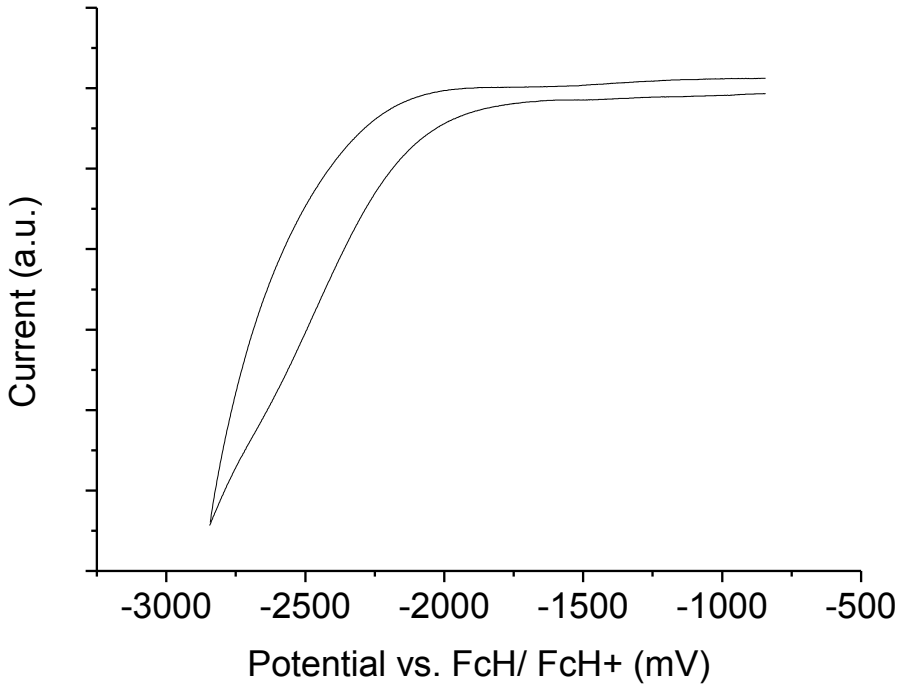

Figure S117. Cyclic voltammogram in 0.1 M *n*-Bu_4PF_6/ THF showing the reduction process for complex **8**.

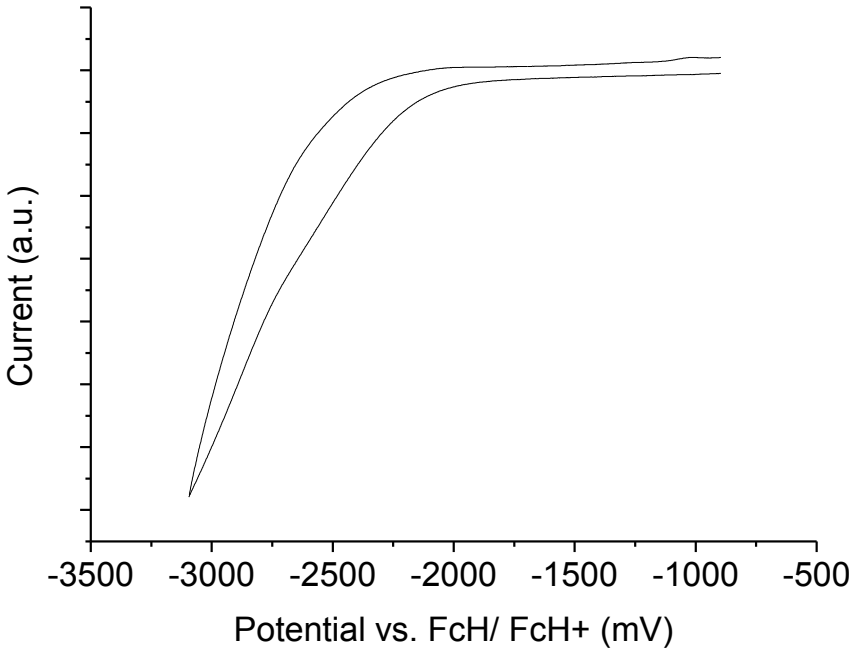

Figure S118. Cyclic voltammogram in 0.1 M *n*-Bu_4PF_6/ THF showing the reduction process for complex **9**.

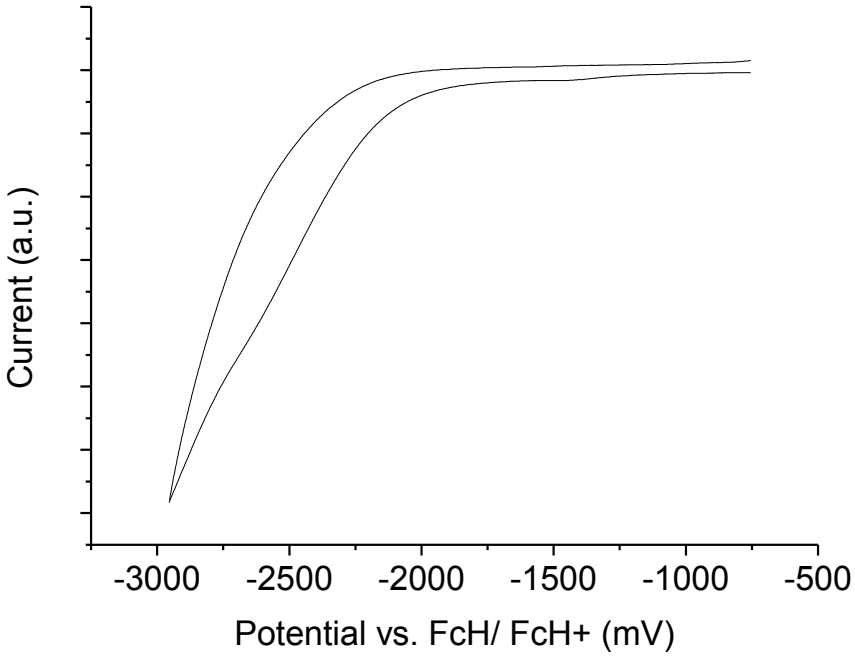

Figure S119. Cyclic voltammogram in 0.1 M *n*-Bu_4PF_6/ THF showing the reduction process for complex **10**.

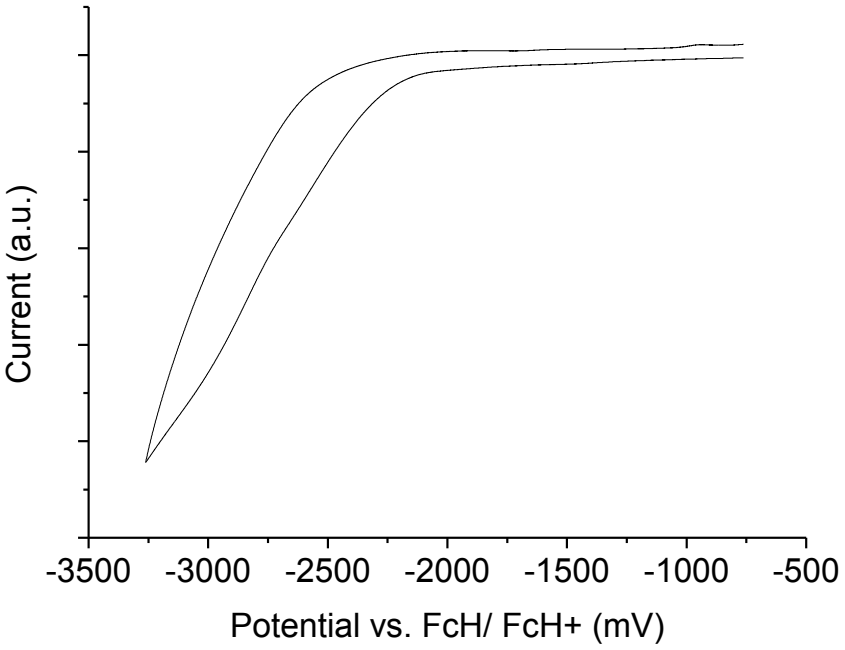

Figure S120. Cyclic voltammogram in 0.1 M *n*-Bu_4PF_6/ THF showing the reduction process for complex *rac* **11**.

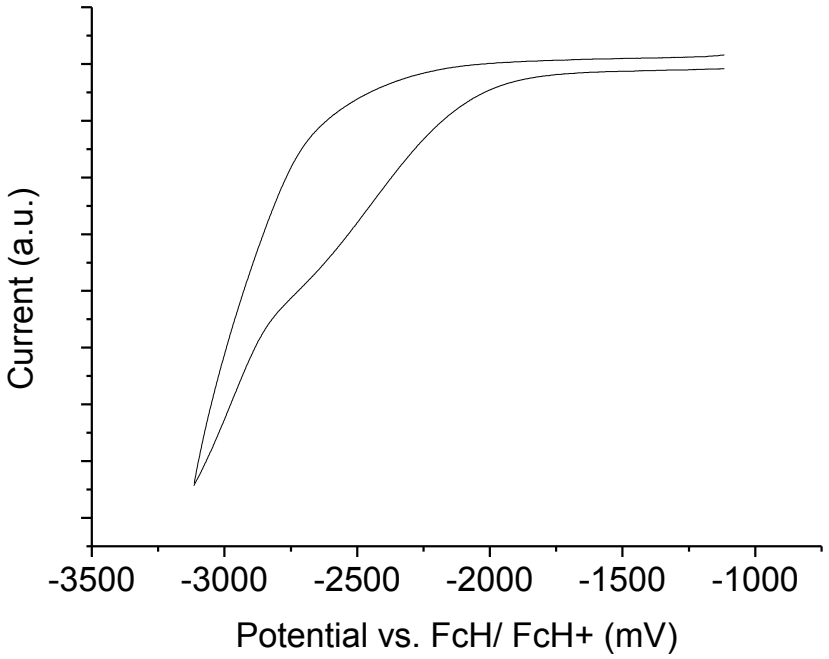

Figure S121. Cyclic voltammogram in 0.1 M *n*-Bu_4PF_6/ THF showing the reduction process for complex *meso* **12**.

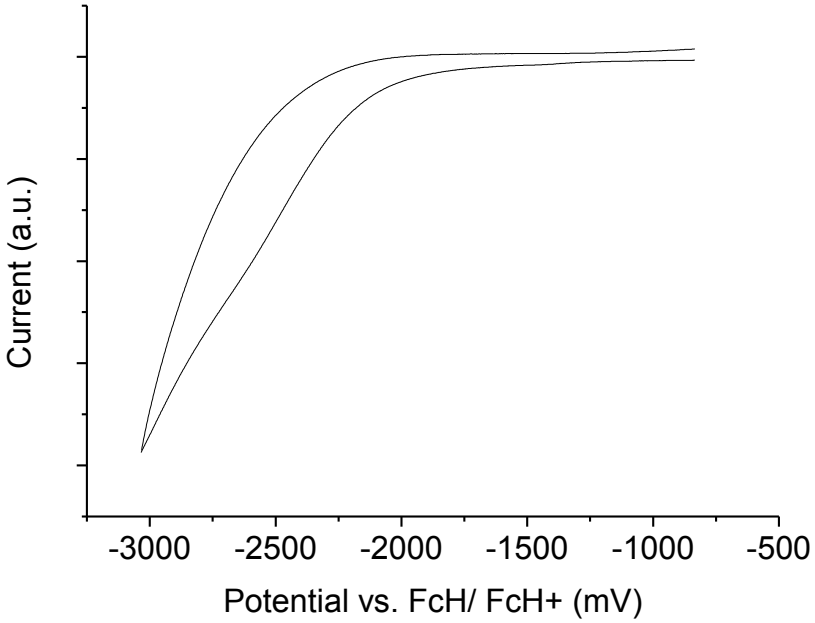

Figure S122. Cyclic voltammogram in 0.1 M *n*-Bu_4PF_6/ THF showing the reduction process for complex *meso* **13**.

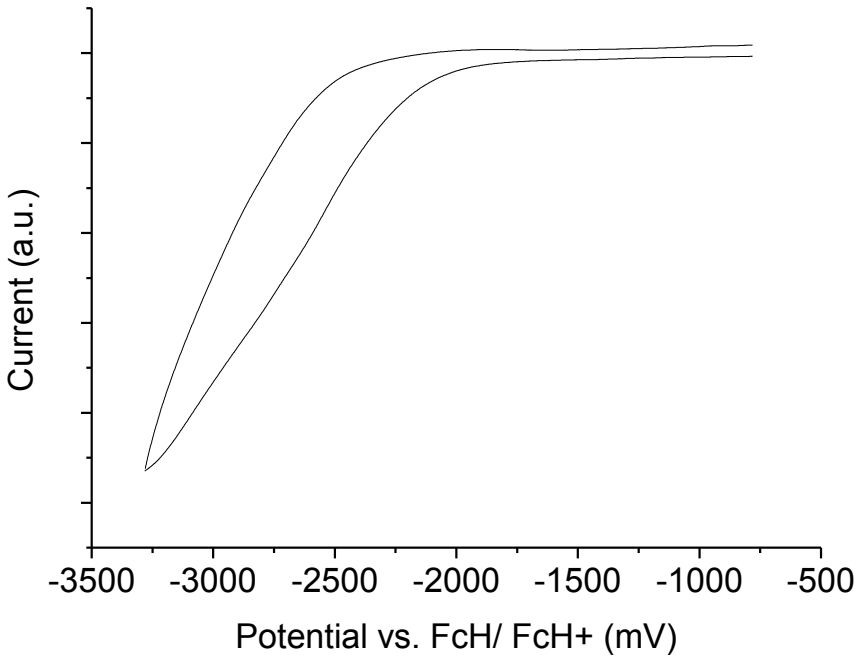

Figure S123. Cyclic voltammogram in 0.1 M *n*-Bu_4PF_6/ THF showing the reduction process for complex *rac* **13**.

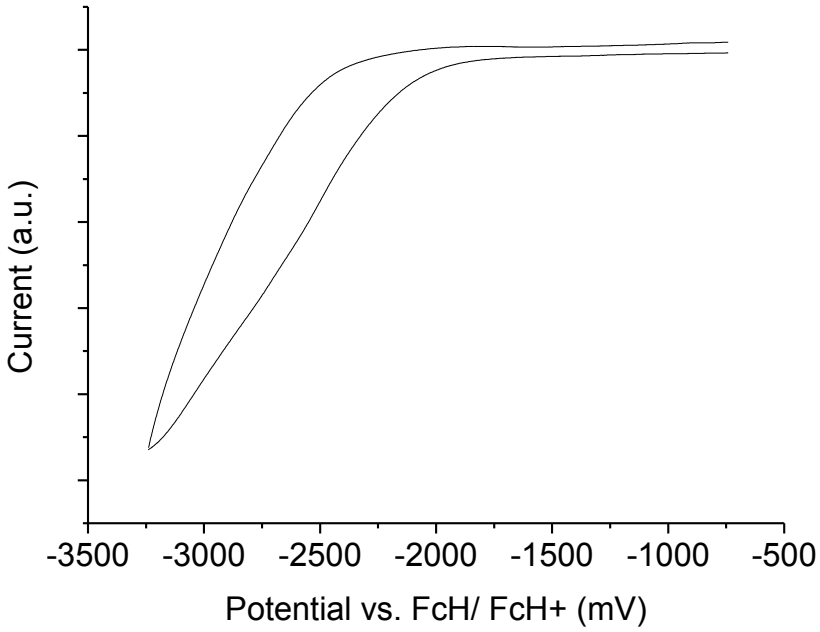

Figure S124. Cyclic voltammogram in 0.1 M *n*-Bu_4PF_6/ THF showing the reduction process for complex **14**.

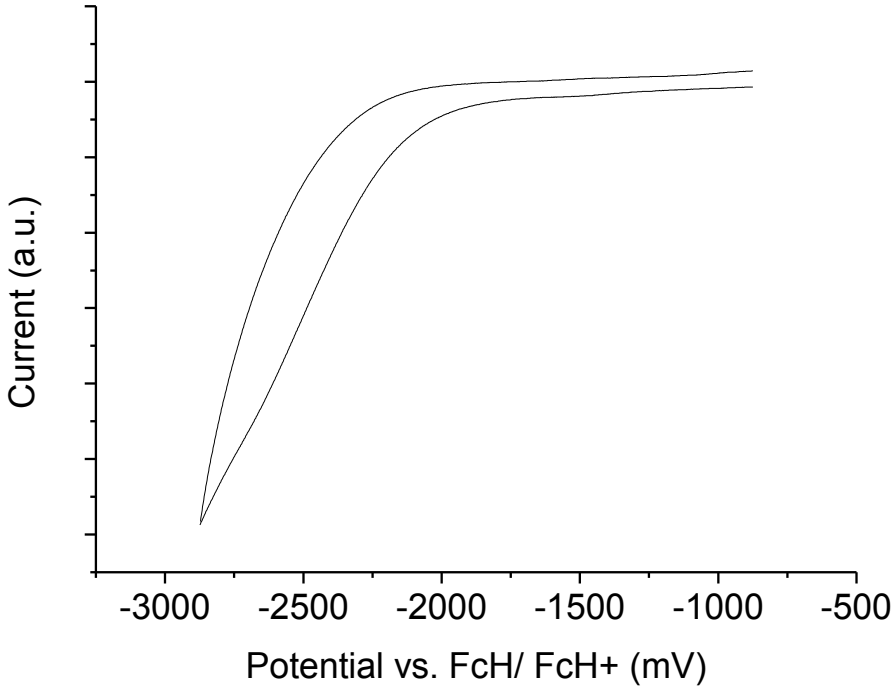

Figure S125. Cyclic voltammogram in 0.1 M *n*-Bu_4PF_6/ THF showing the reduction process for complex **15**.

Computations

Table S2 Summary of the HOMO compositions for the most stable minima of the *rac* and *meso* diastereomers of the complexes.

Complex	Isomer	Ir	Bridge centre	Bridge aryl	Ph[a]	Py[b]
7	*meso*	42	28	1	23	6
	rac	38	41	2	14	5
8	*meso*	45	18	1	31	5
	rac	48	4	0	42	6
9	*meso*	45	16	1	33	5
	rac	48	4	0	42	6
10	*meso*	45	20	1	29	5
	rac	40	44	2	9	5
11	*meso*	44	22	1	28	6
	rac	47	4	0	42	6
12	*meso*	45	4	-	46	6
	rac	45	3	-	46	6
13	*meso*	42	35	1	15	5
	rac	40	44	2	8	6
14	*meso*	45	4	-	44	7
	rac	45	4	-	44	7
15	*meso*	42	42	1	9	6
	rac	42	46	1	4	7

The atom/ group contributions are stated as percentages. [a]Phenyl moieties of the cyclometalating ligands [b]Pyridyl moieties of the cyclometalating ligands.

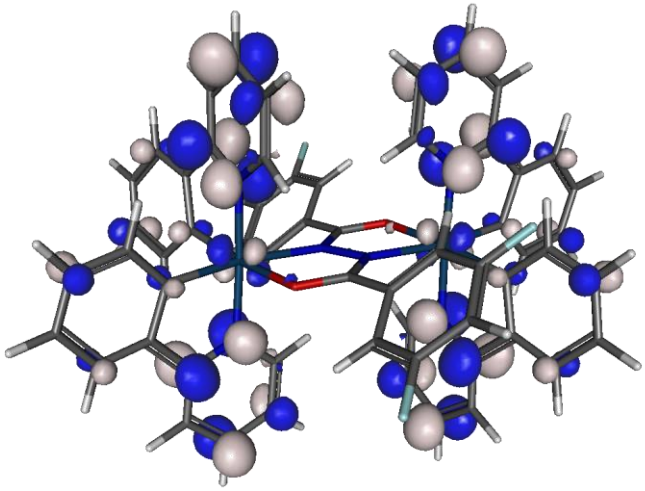

LUMO

–1.50 eV

Ir : Bridge : F_2 : Ph : Py

5 : 2 : 1 : 21 : 72

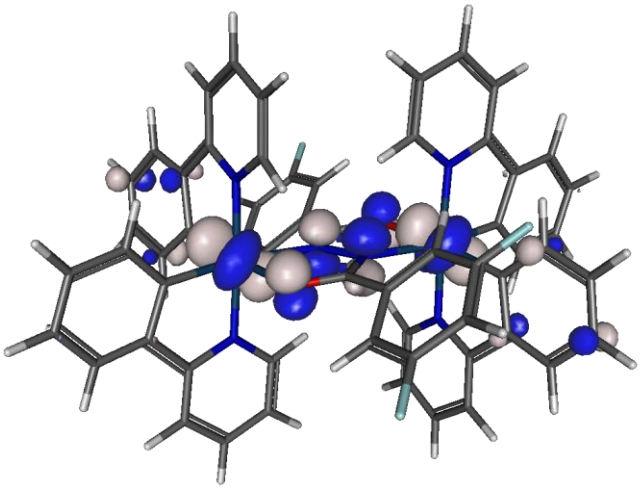

HOMO

–4.95 eV

Ir : Bridge : F_2: Ph : Py

42 : 28 : 1 : 23 : 6

Figure S126. Frontier molecular orbitals for the most stable minimum of *meso* **7**

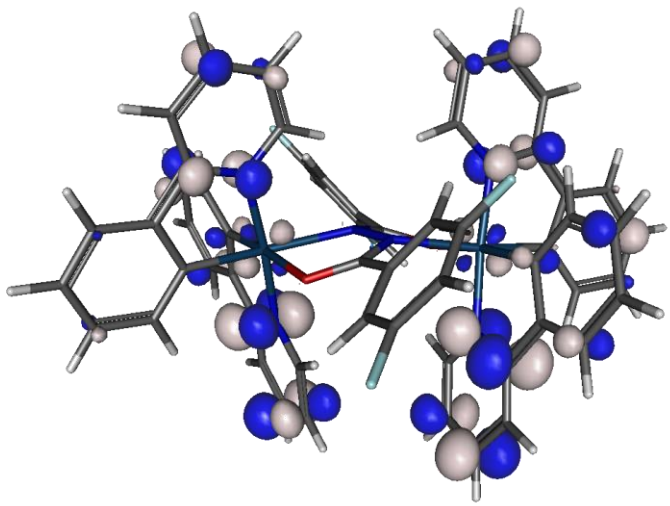

LUMO

–1.47 eV

Ir : Bridge : F_2: Ph : Py

5 : 1 : 1 : 22 : 70

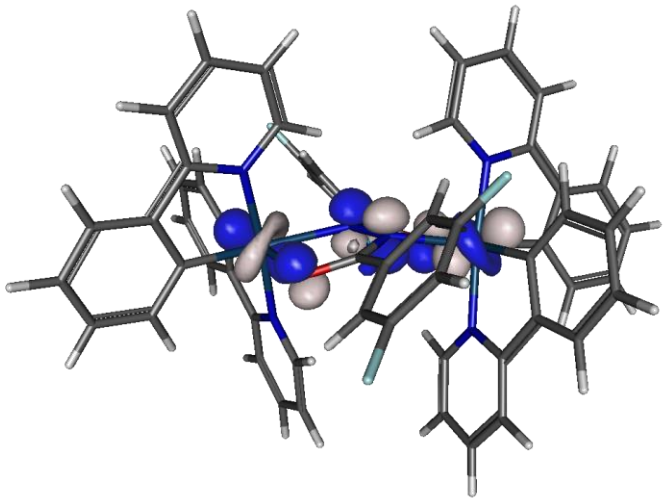

HOMO

–4.92 eV

Ir : Bridge : F_2 : Ph : Py

38 : 41 : 2 : 14 : 5

Figure S127. Frontier molecular orbitals for the most stable minimum of *rac* **7**

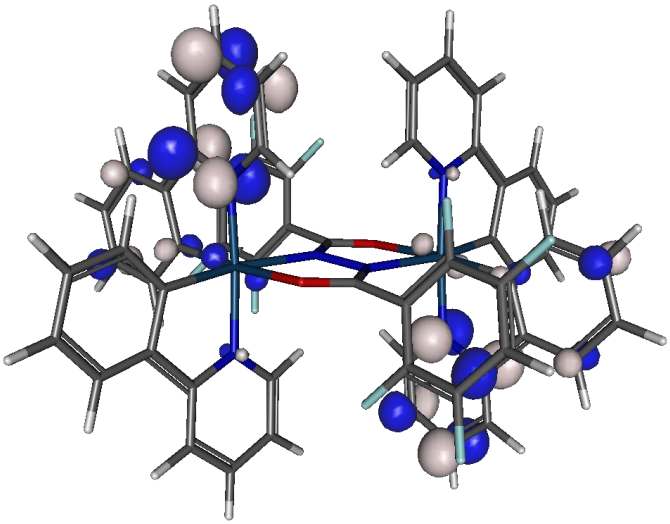

LUMO

–1.46 eV

Ir : Bridge : F_4 : Ph : Py

5 : 1 : 1 : 23 : 71

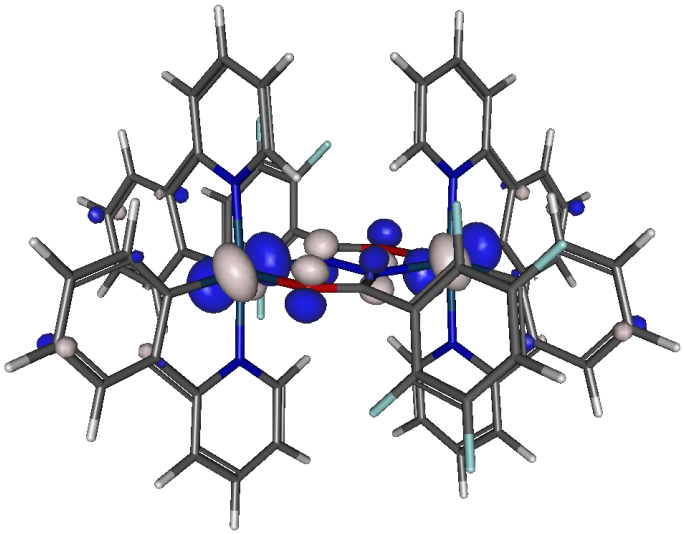

HOMO

–4.95 eV

Ir : Bridge : F_4 : Ph : Py

45 : 18 : 1 : 31 : 5

Figure S128. Frontier molecular orbitals for the most stable minimum of *meso* **8**

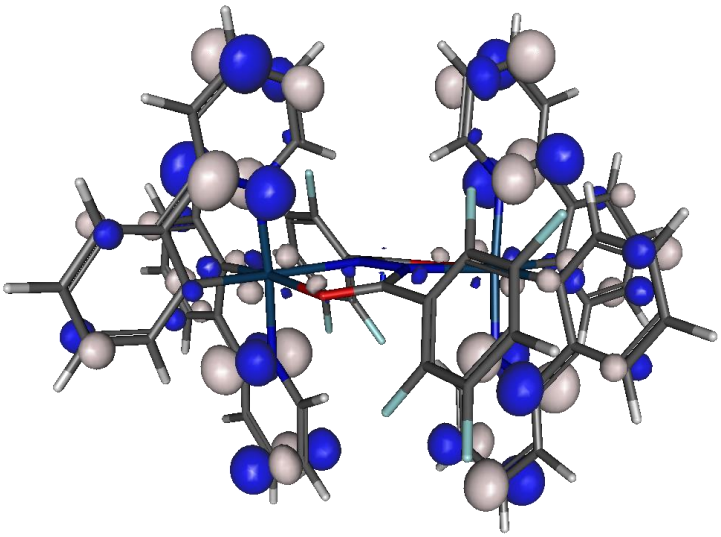

LUMO

–1.43 eV

Ir : Bridge : F_4 : Ph : Py

4 : 2 : 4 : 22 : 68

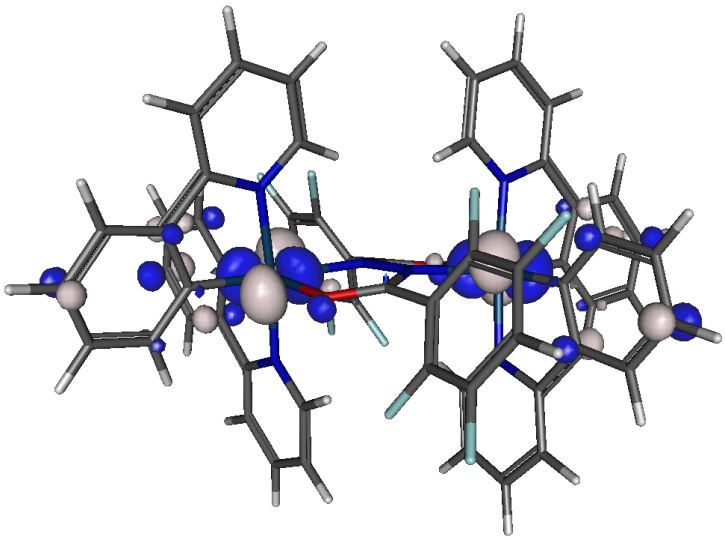

HOMO

–4.97 eV

Ir : Bridge : F_4 : Ph : Py

48 : 4 : 0 : 42 : 6

Figure S129. Frontier molecular orbitals for the most stable minimum of *rac* **8**

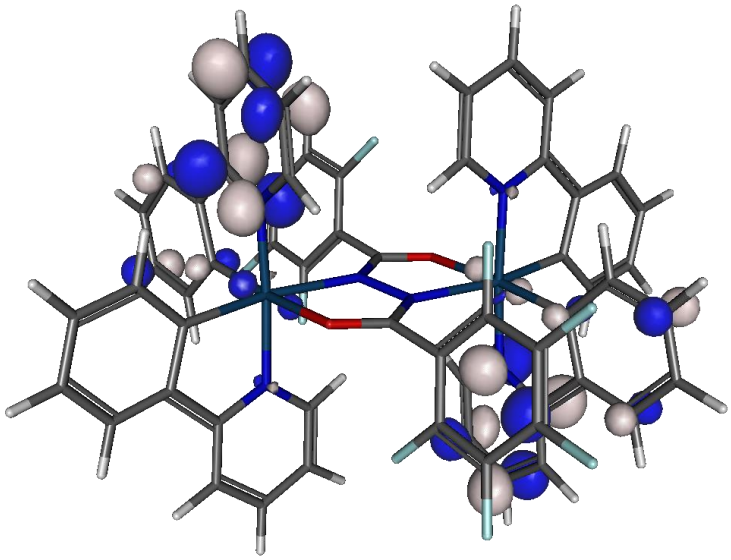

LUMO

–1.56 eV

Ir : Bridge : F_5 : Ph : Py

5 : 1 : 1 : 23 : 70

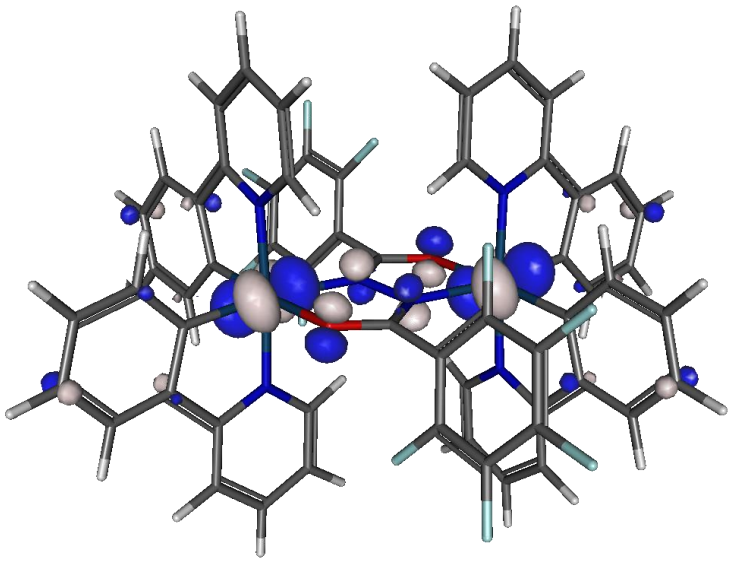

HOMO

–5.06 eV

Ir : Bridge : F_5 : Ph : Py

45 : 16 : 1 : 33 : 5

Figure S130. Frontier molecular orbitals for the most stable minimum of *meso* **9**

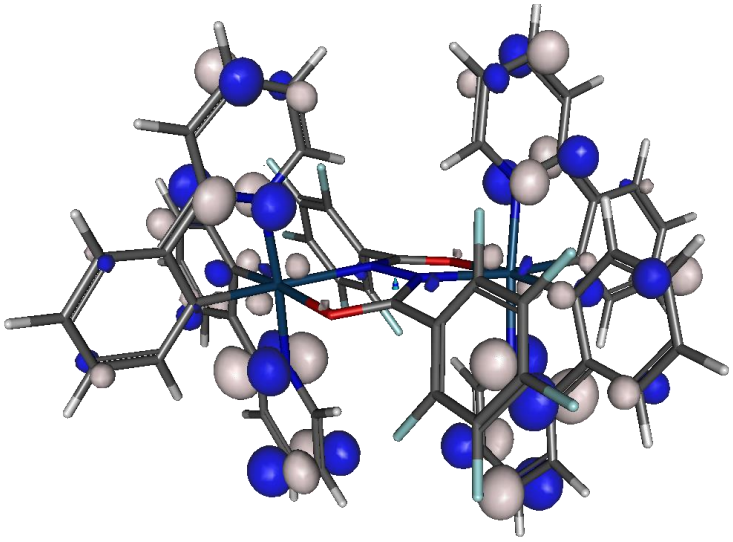

LUMO

–1.53 eV

Ir : Bridge : F_5 : Ph : Py

4 : 2 : 3 : 22 : 68

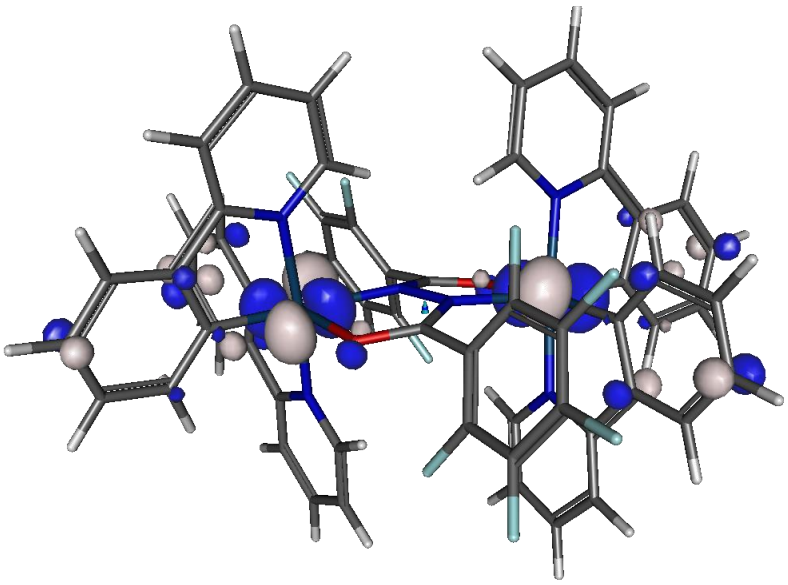

HOMO

–5.07 eV

Ir : Bridge : F_5 : Ph : Py

48 : 4 : 0 : 42 : 6

Figure S131. Frontier molecular orbitals for the most stable minimum of *rac* **9**

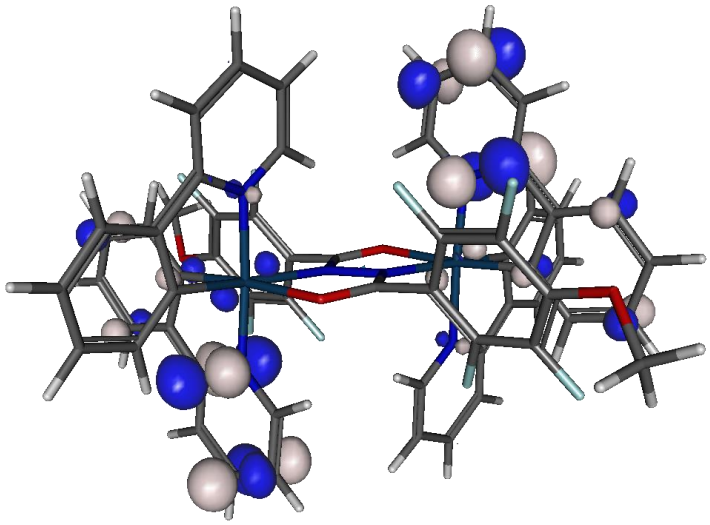

LUMO

–1.39 eV

Ir : Bridge : F_4 : Ph : Py

5 : 1 : 1 : 22 : 71

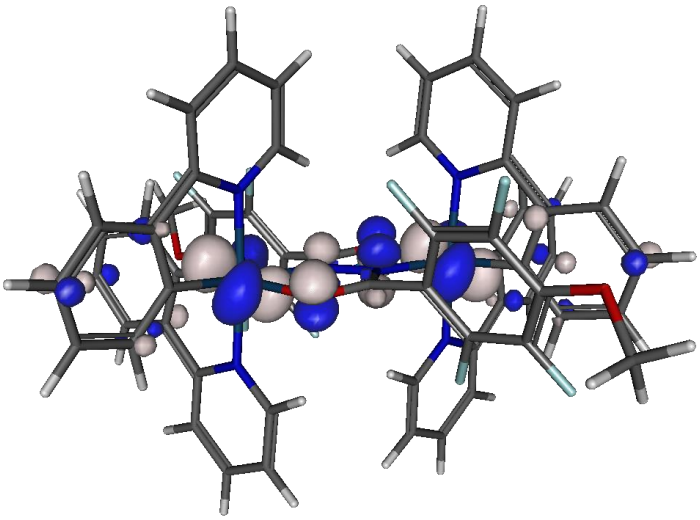

HOMO

–4.88 eV

Ir : Bridge : F_4 : Ph : Py

45 : 20 : 1 : 29 : 5

Figure S132. Frontier molecular orbitals for the most stable minimum of *meso* **10**

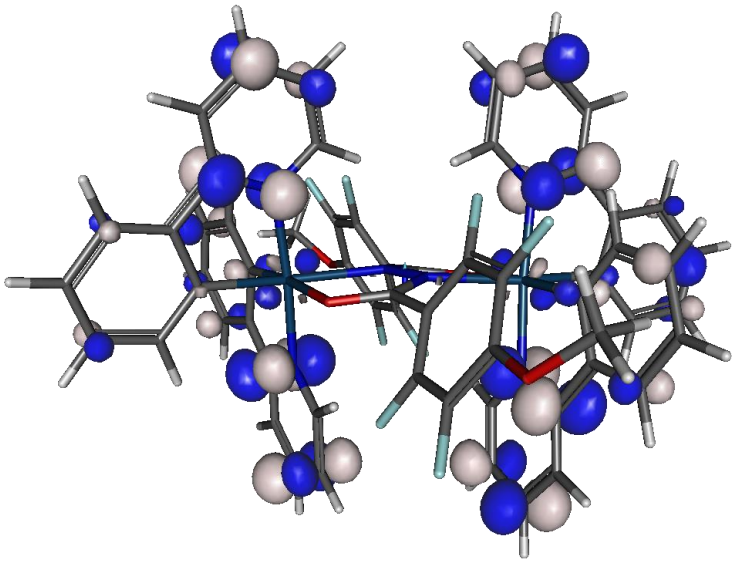

LUMO

–1.38 eV

Ir : Bridge : F_4 : Ph : Py

4 : 1 : 1 : 24 : 70

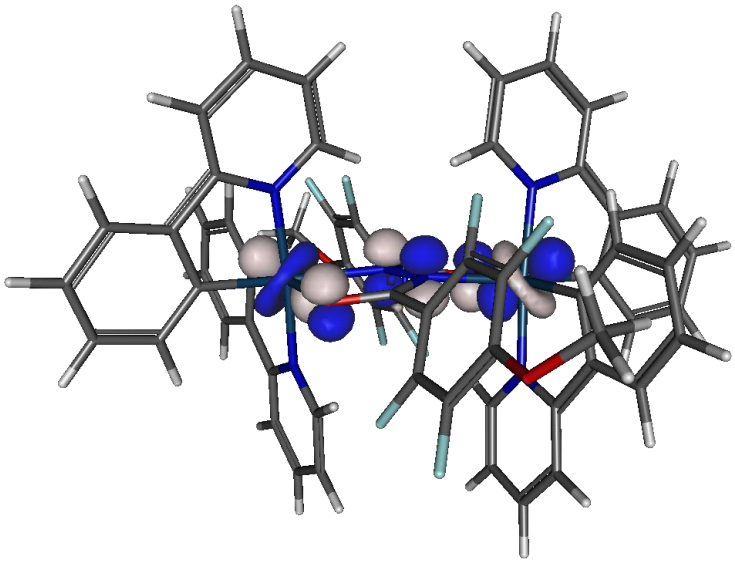

HOMO

–4.91 eV

Ir : Bridge : F_4 : Ph : Py

40 : 44 : 2 : 9 : 5

Figure S133. Frontier molecular orbitals for the most stable minimum of *rac* **10**

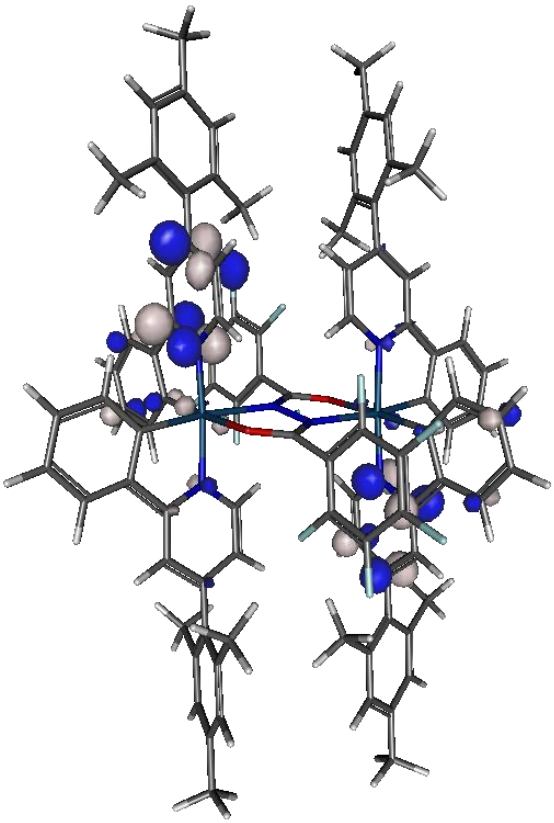

LUMO

–1.48 eV

Ir : Bridge : F_5 : Ph : Py

5 : 1 : 1 : 22 : 67

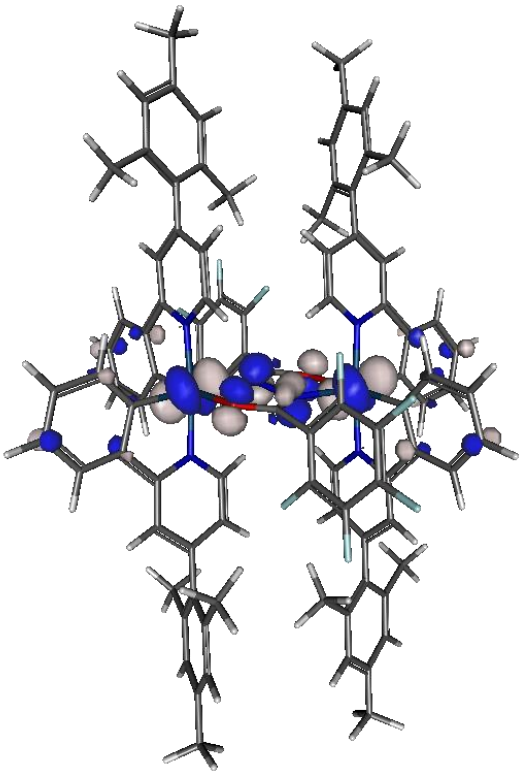

HOMO

–4.96 eV

Ir : Bridge : F_5 : Ph : Py

44 : 22 : 1 : 28 : 6

Figure S134. Frontier molecular orbitals for the most stable minimum of *meso* **11**

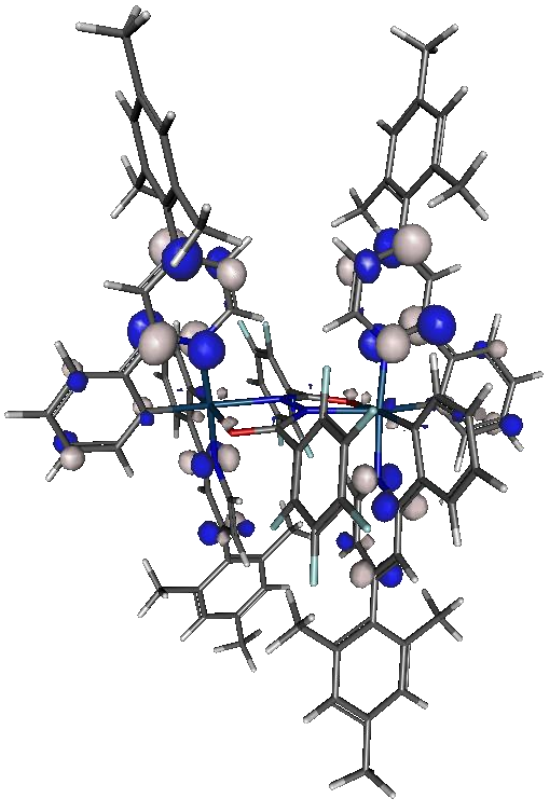

LUMO

–1.46 eV

Ir : Bridge : F_5 : Ph : Py

4 : 3 : 6 : 21 : 64

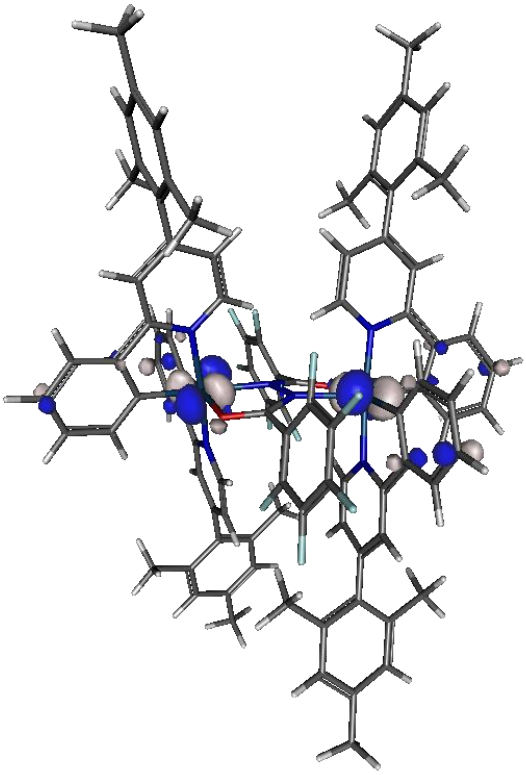

HOMO

–5.02 eV

Ir : Bridge : F_5: Ph : Py

47 : 4 : 0 : 42 : 6

Figure S135. Frontier molecular orbitals for the most stable minimum of *rac* **11**

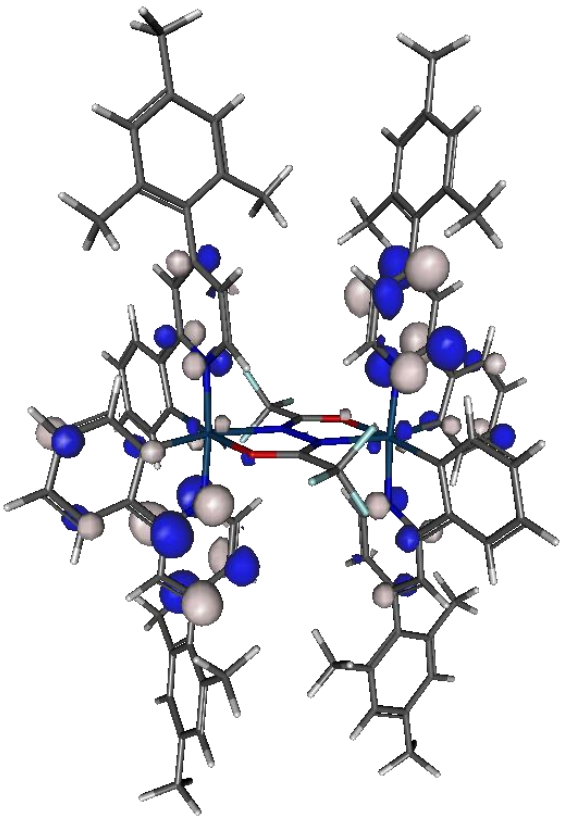

LUMO

–1.42 eV

Ir : Bridge : Ph : Py

4 : 2 : 21 : 69

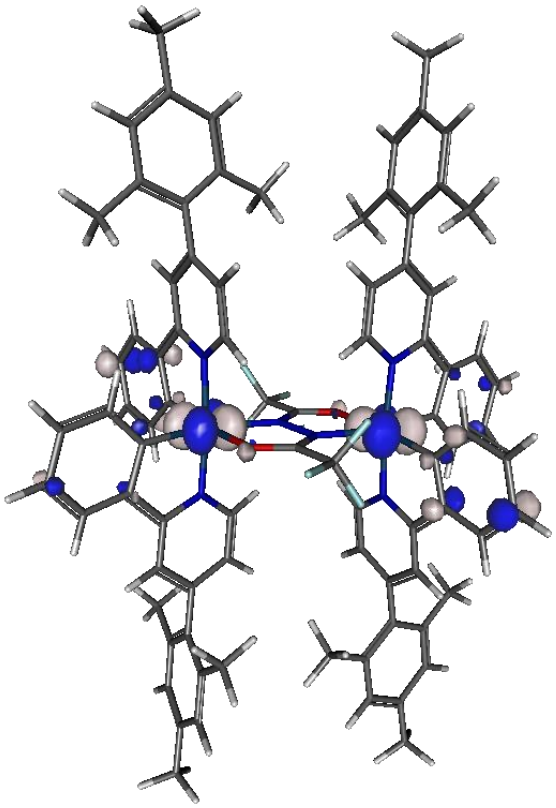

HOMO

–4.98 eV

Ir : Bridge : Ph : Py

45 : 4 : 46 : 6

Figure S136. Frontier molecular orbitals for the most stable minimum of *meso* **12**

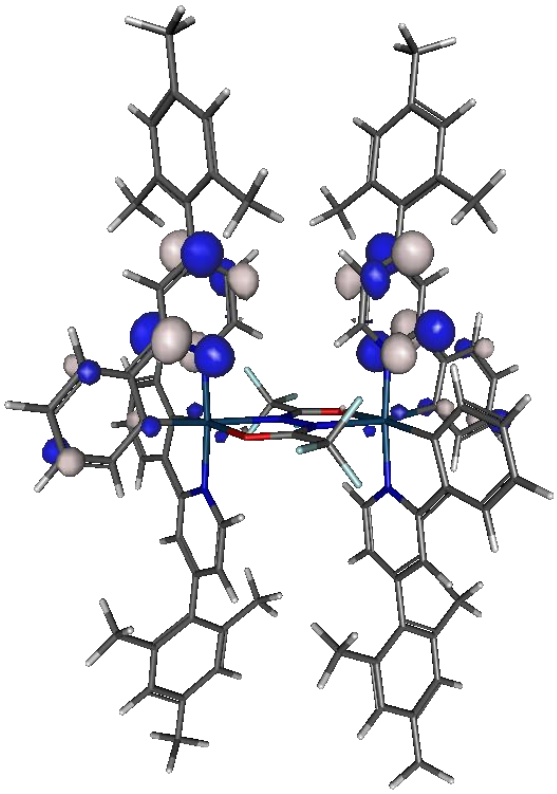

LUMO

–1.44 eV

Ir : Bridge : Ph : Py

4 : 2 : 21 : 71

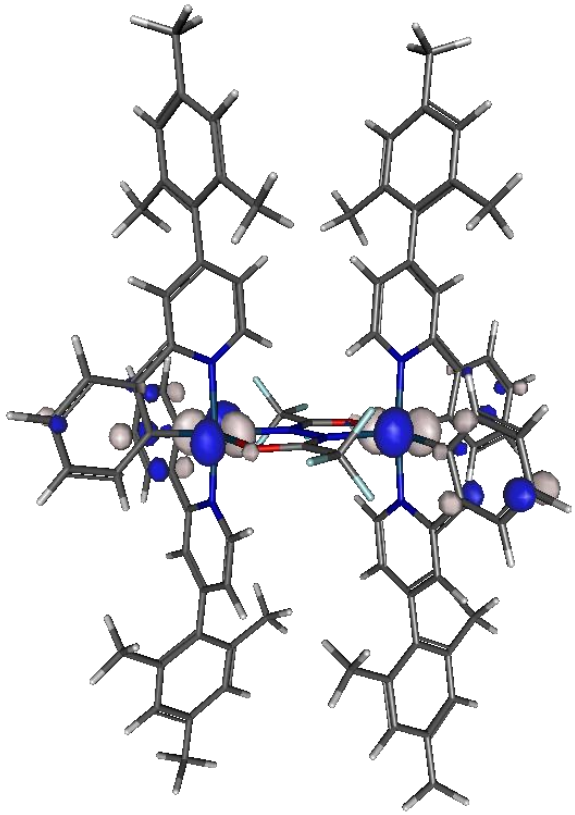

HOMO

–4.97 eV

Ir : Bridge : Ph : Py

45 : 3 : 46 : 6

Figure S137. Frontier molecular orbitals for the most stable minimum of *rac* **12**

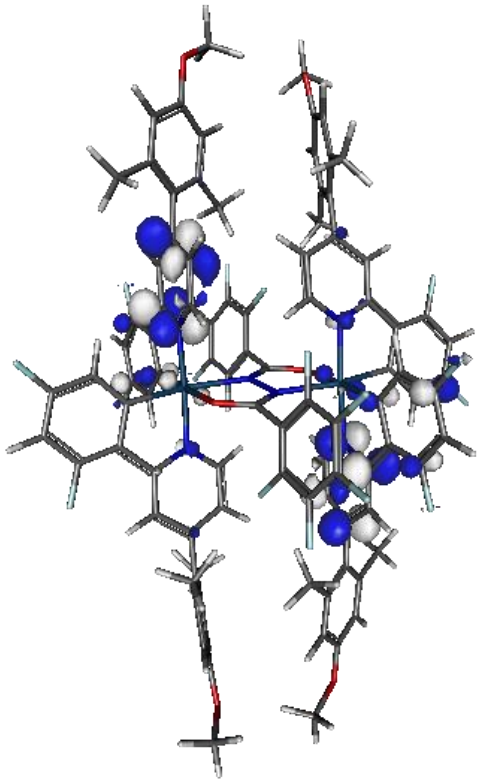

LUMO

–1.73 eV

Ir : Bridge : F_5 : Ph : Py

5 : 1 : 2 : 20 : 66

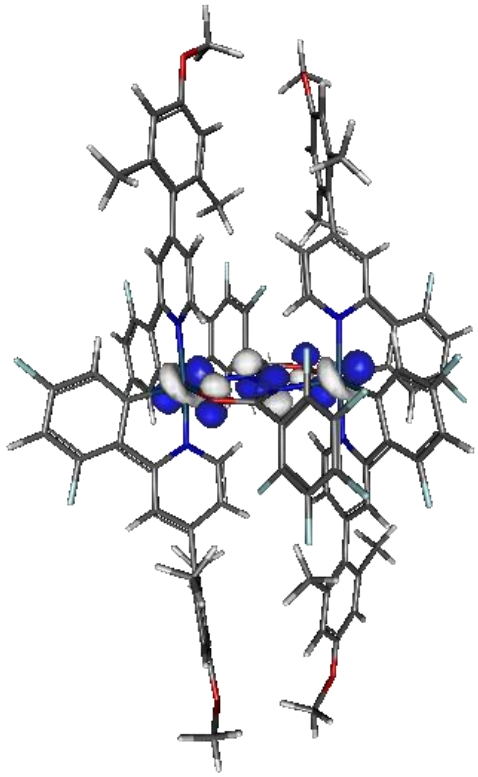

HOMO

–5.44 eV

Ir : Bridge : F_5 : Ph : Py

42 : 35 : 1 : 15 : 5

Figure S138. Frontier molecular orbitals for the most stable minimum of *meso* **13**

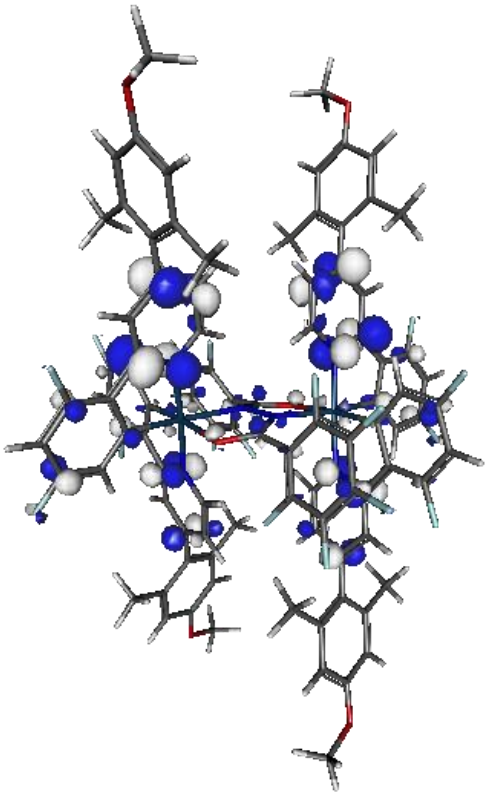

LUMO

–1.73 eV

Ir : Bridge : F_5 : Ph : Py

4 : 4 : 9 : 21 : 61

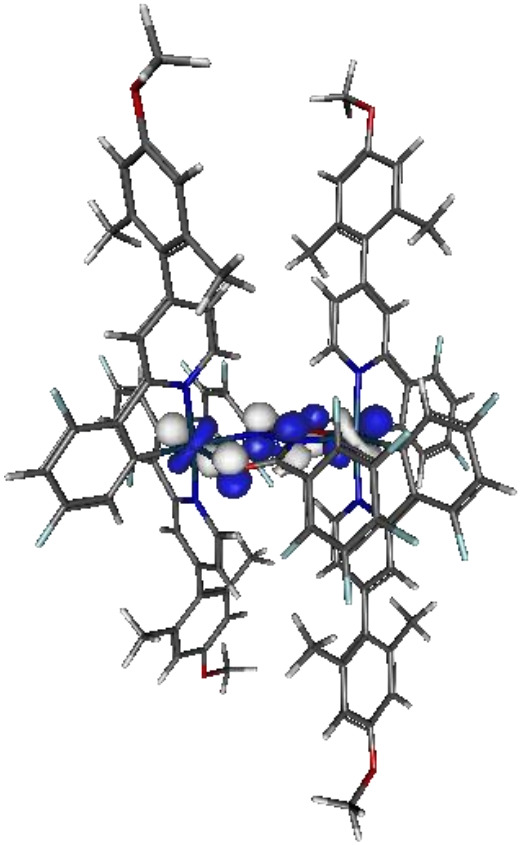

HOMO

–5.47 eV

Ir : Bridge : F_5 : Ph : Py

40 : 44 : 2 : 8 : 6

Figure S139. Frontier molecular orbitals for the most stable minimum of *rac* **13**

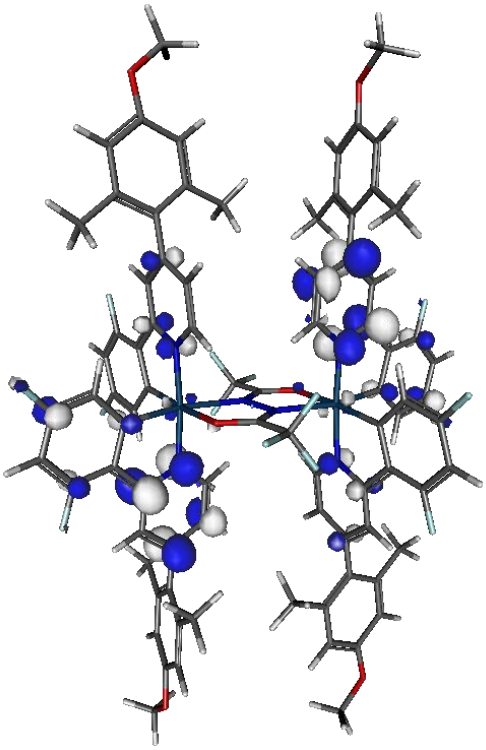

LUMO

–1.71 eV

Ir : Bridge : Ph : Py

4 : 2 : 22 : 68

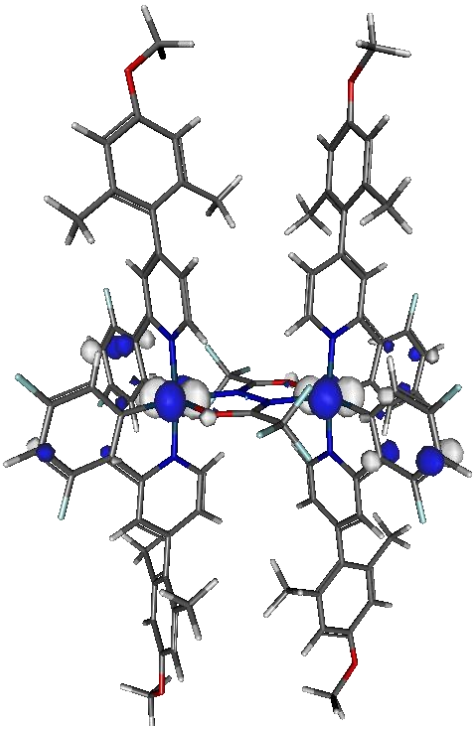

HOMO

–5.53 eV

Ir : Bridge : Ph : Py

45 : 4 : 44 : 7

Figure S140. Frontier molecular orbitals for the most stable minimum of *meso* **14**

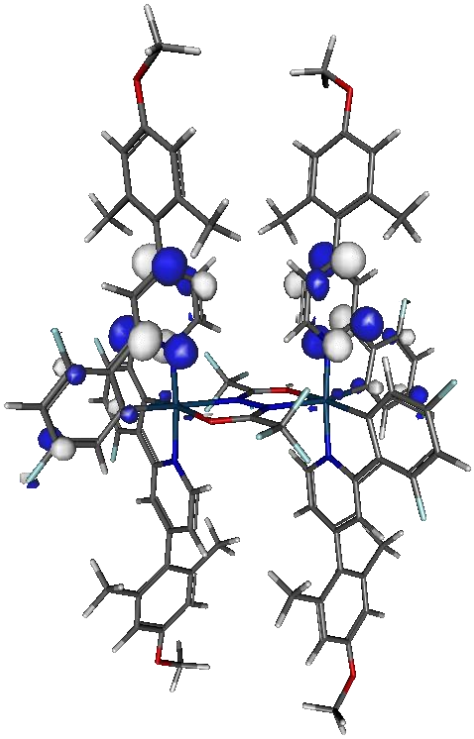

LUMO

–1.72 eV

Ir : Bridge : Ph : Py

4 : 2 : 22 : 70

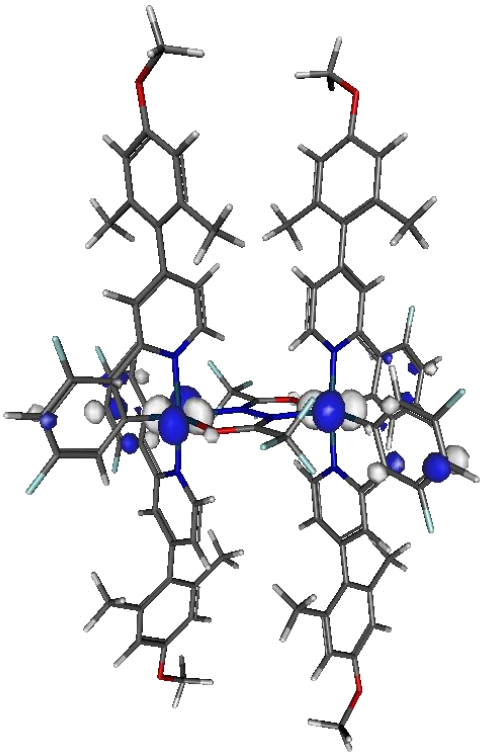

HOMO

–5.53 eV

Ir : Bridge : Ph : Py

45 : 4 : 44 : 7

Figure S141. Frontier molecular orbitals for the most stable minimum of *rac* **14**

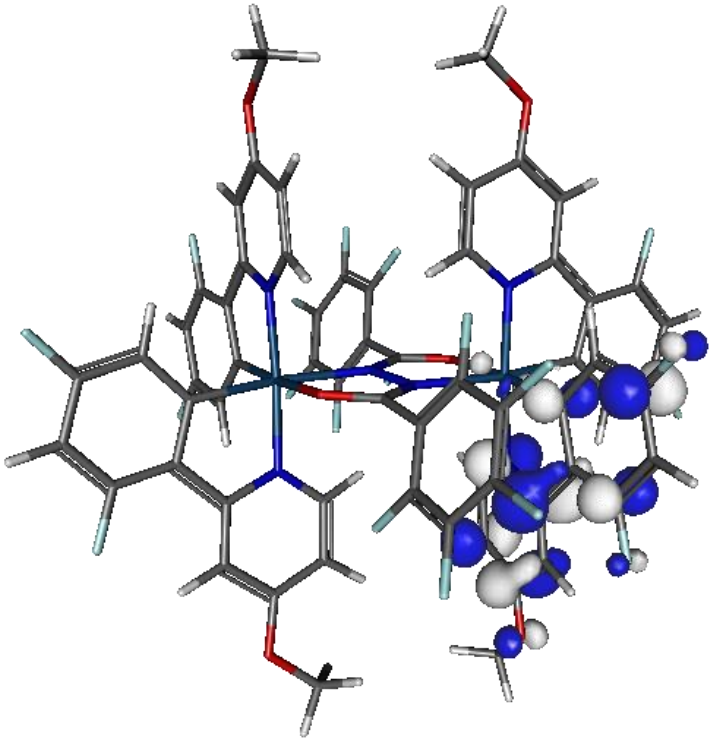

LUMO

–1.55 eV

Ir : Bridge : F_5 : Ph : Py

4 : 1 : 2 : 31 : 63

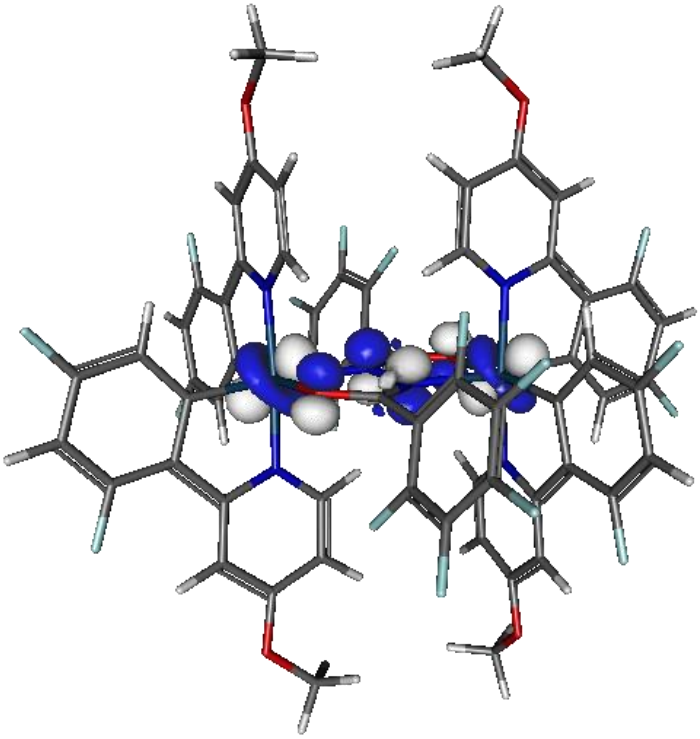

HOMO

–5.36 eV

Ir : Bridge : F_5 : Ph : Py

42 : 42 : 1 : 6 : 6

Figure S142. Frontier molecular orbitals for the most stable minimum of *meso* **15**

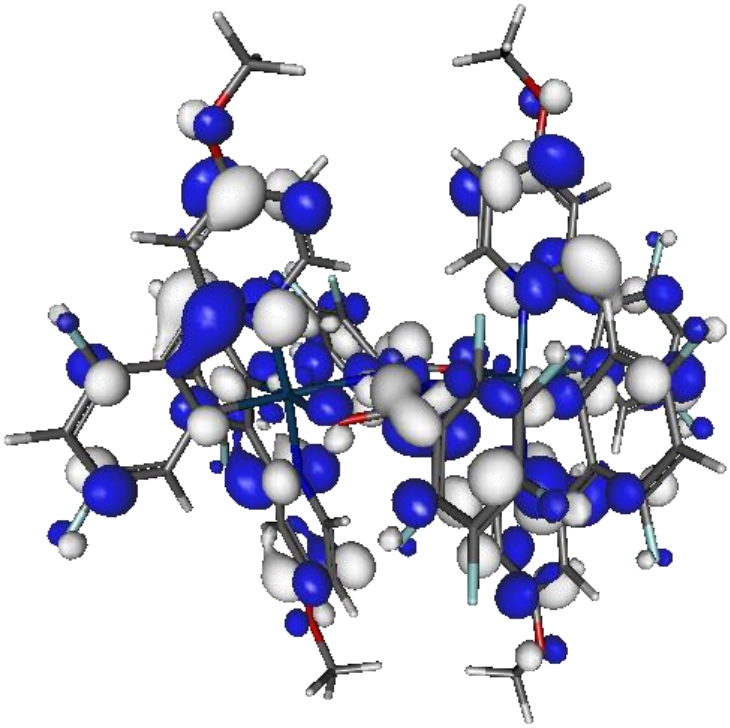

LUMO

–1.50 eV

Ir : Bridge : F_5 : Ph : Py

3 : 8 : 17 : 23 : 48

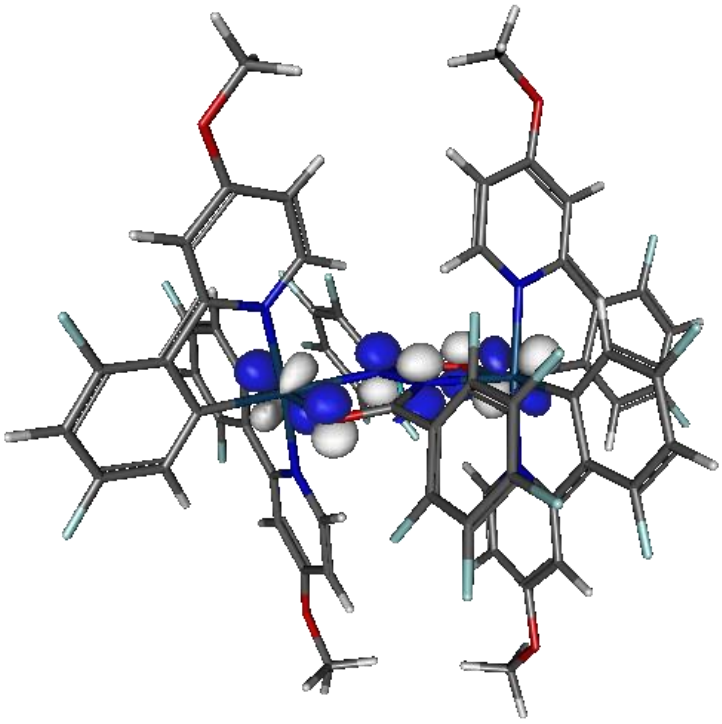

HOMO

–5.34 eV

Ir : Bridge : F_5 : Ph : Py

42 : 46 : 1 : 4 : 7

Figure S143. Frontier molecular orbitals for the most stable minimum of *rac* **15**

Thermal analysis

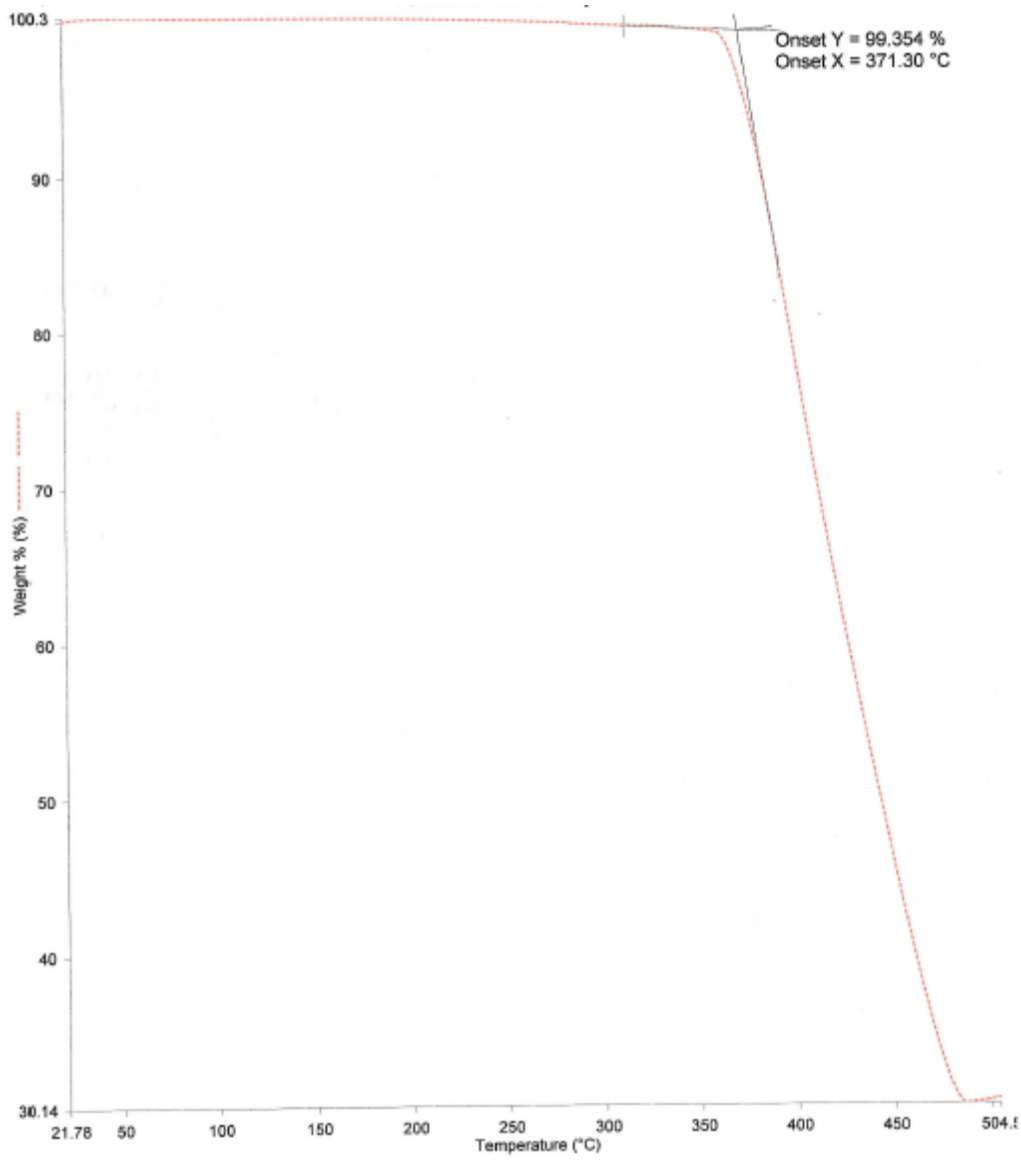

Figure S144. TGA trace of complex **7**. Onset = 371 °C.

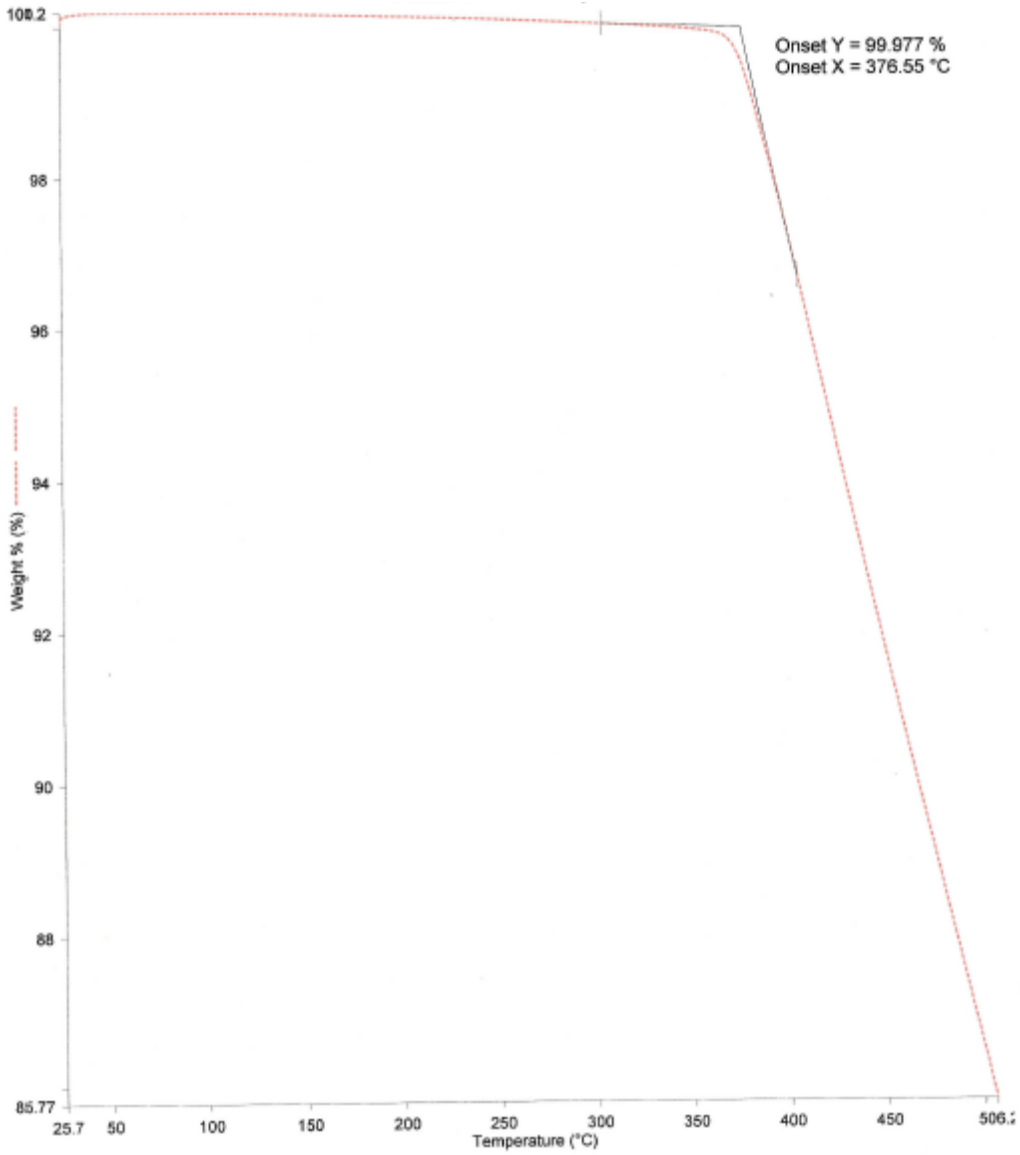

Figure S145. TGA trace of complex **8**. Onset = 377 °C.

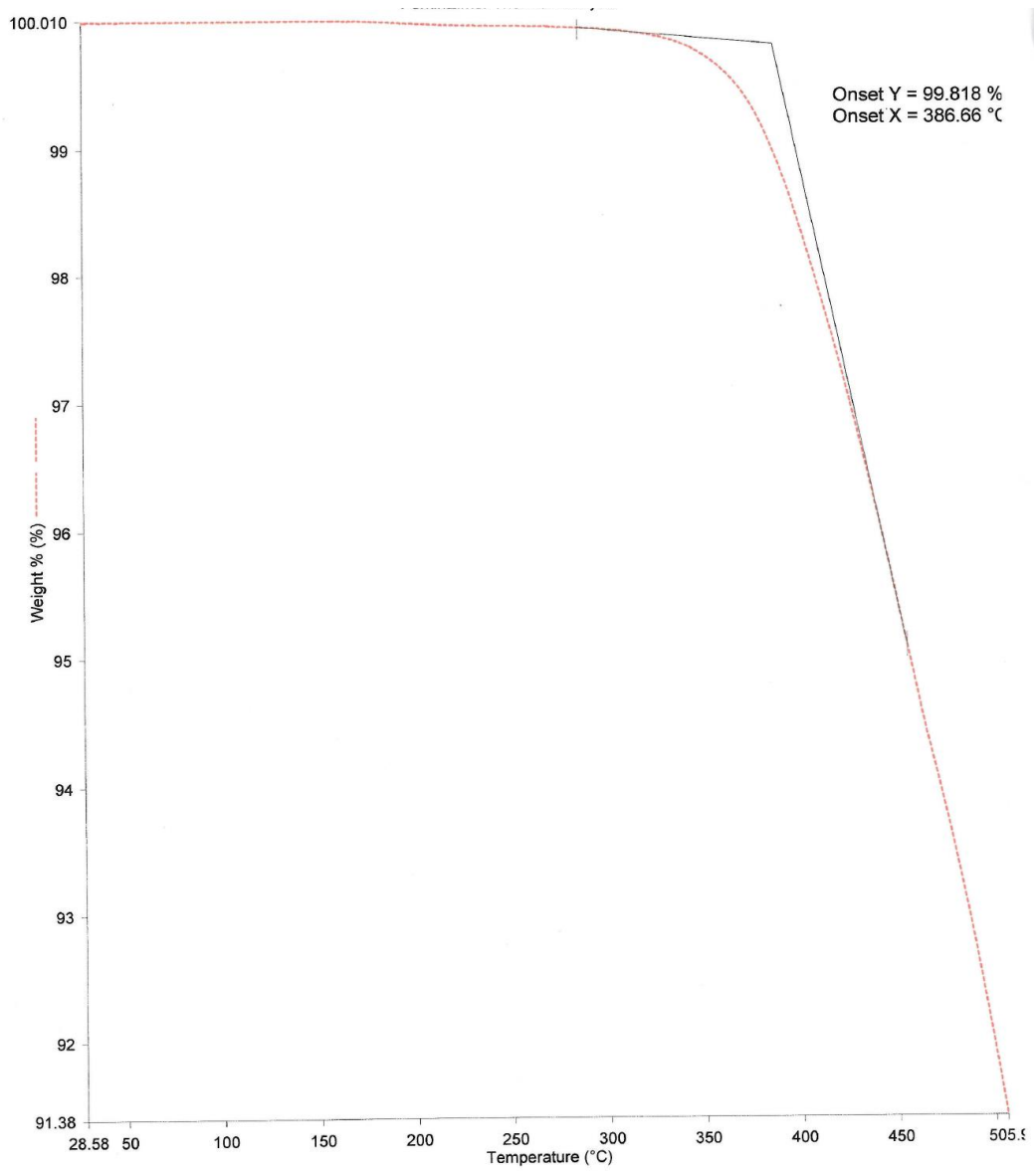

Figure S146. TGA trace of complex **9**. Onset = 387 °C.

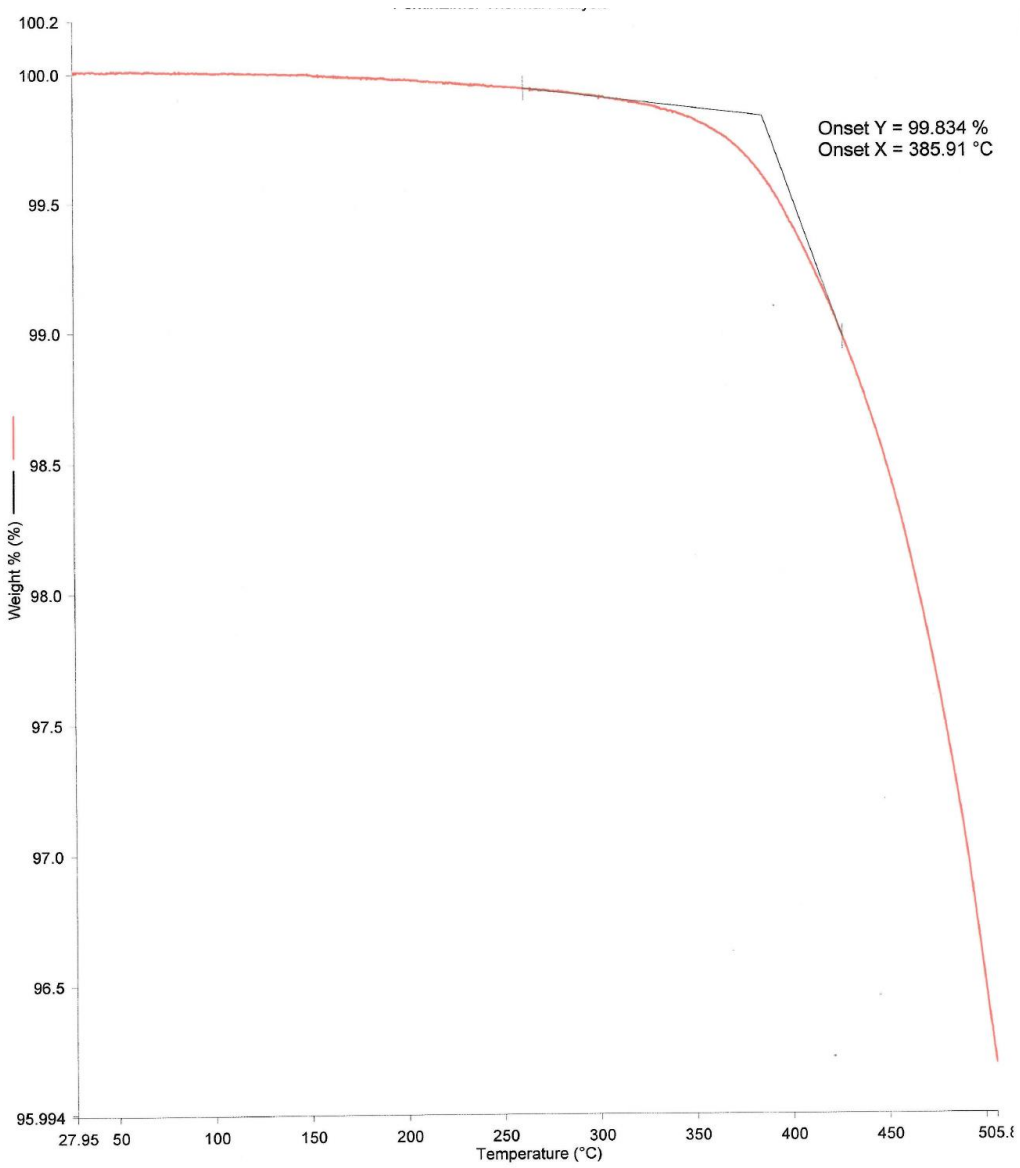

Figure S147. TGA trace of complex **10**. Onset = 386 °C.

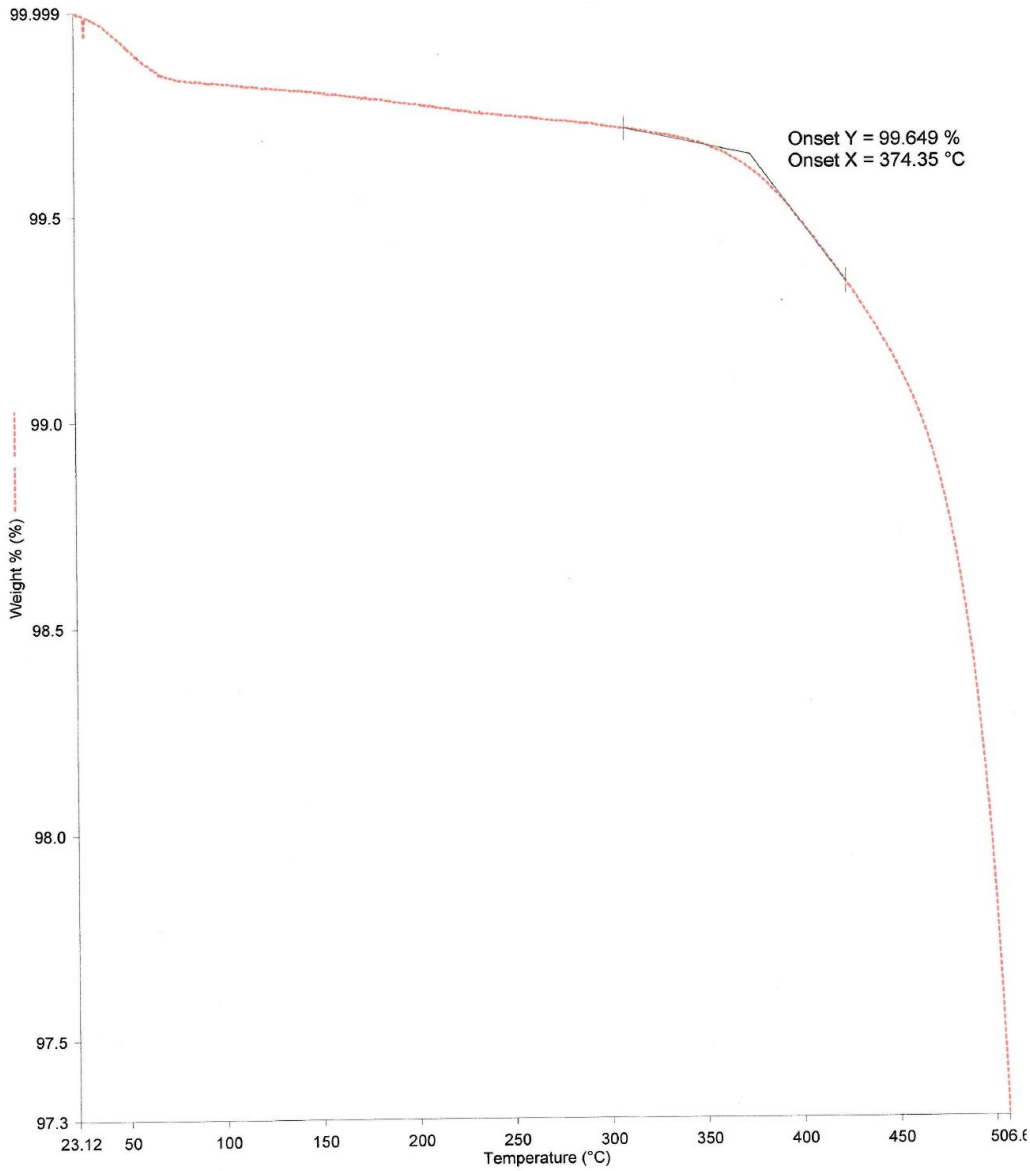

Figure S148. TGA trace of complex **11**. Onset = 374 °C.

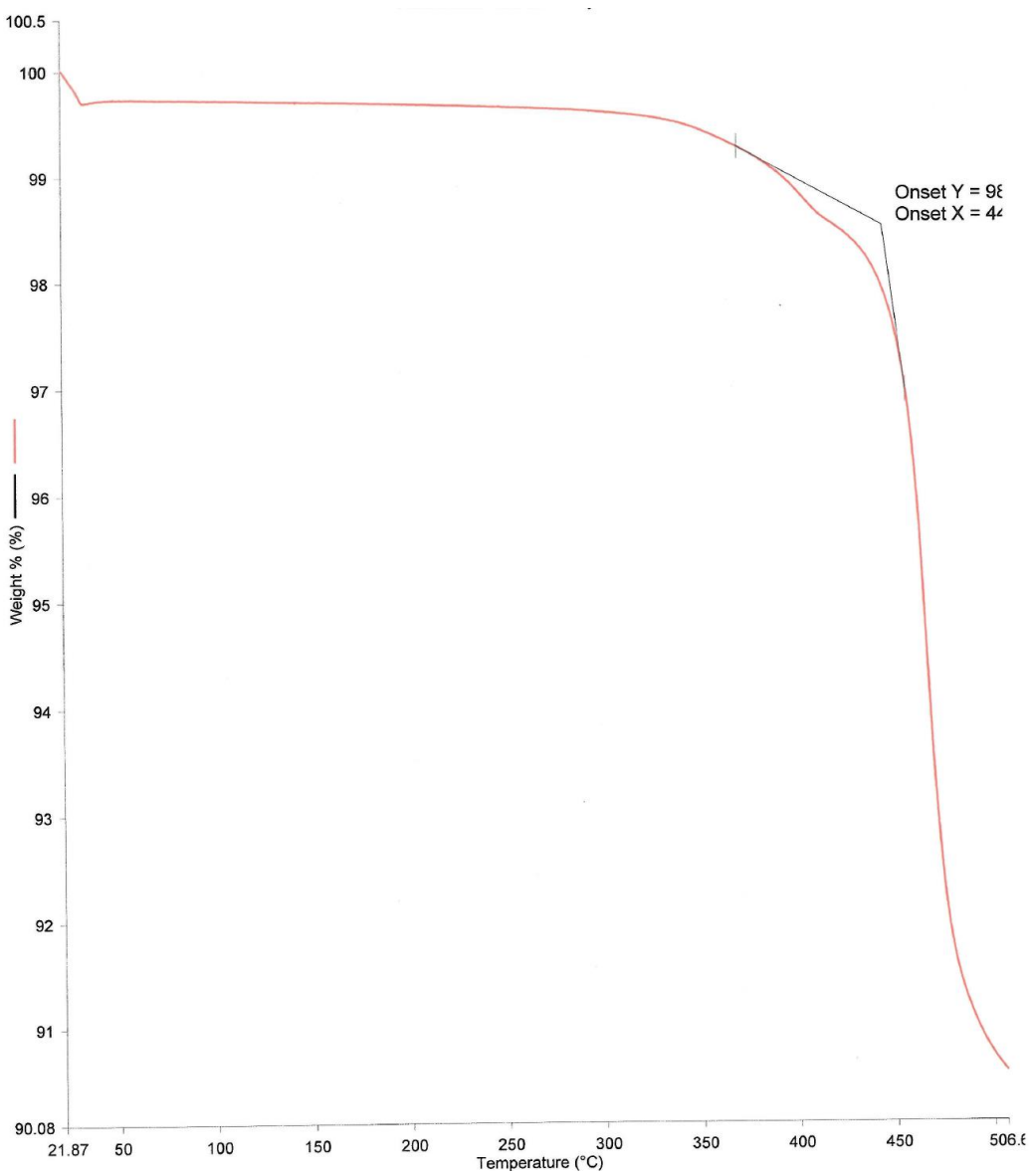

Figure S149. TGA trace of complex **12**. Onset = 440 °C.

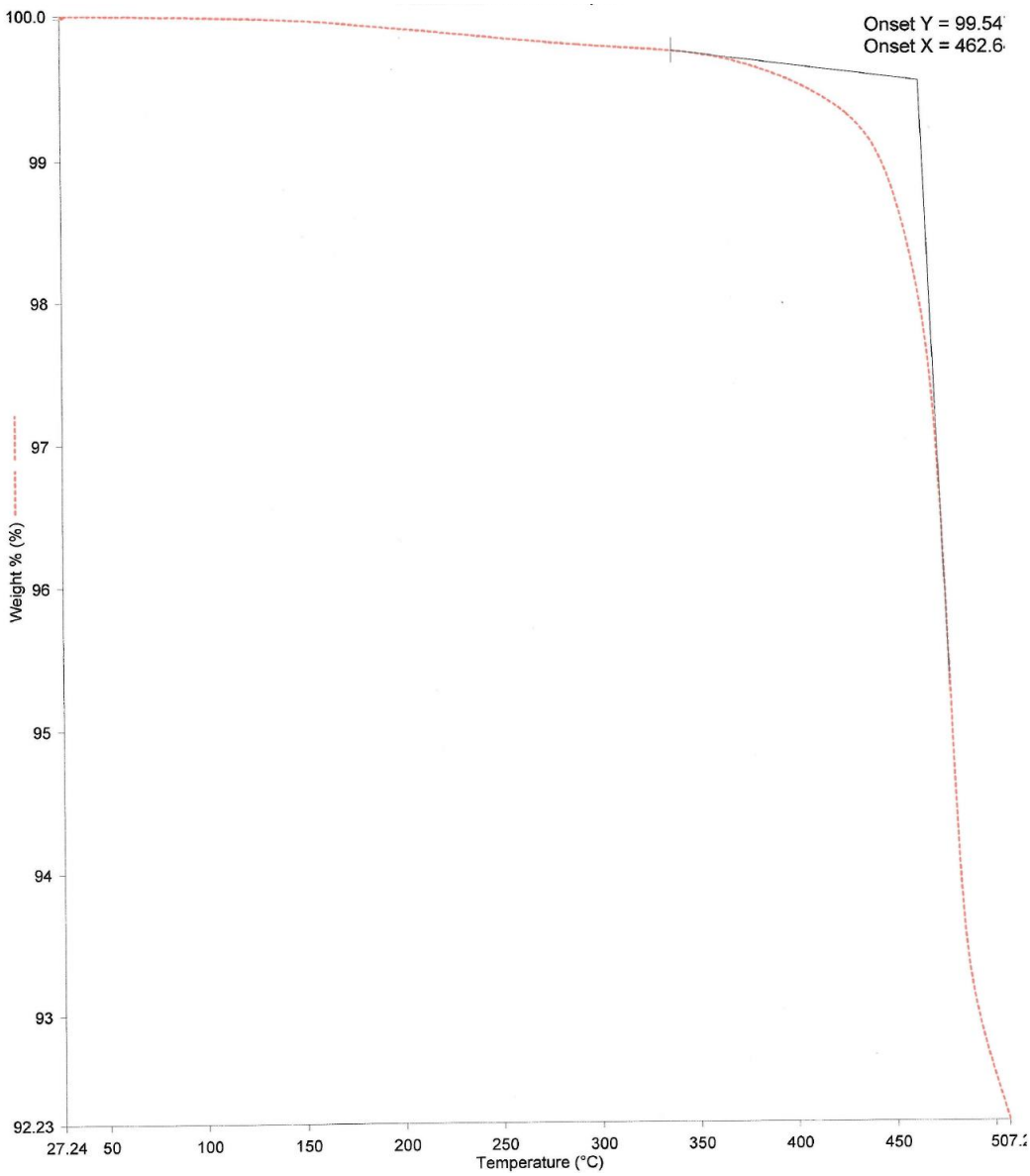

Figure S150. TGA trace of complex *meso* **13**. Onset = 463 °C.

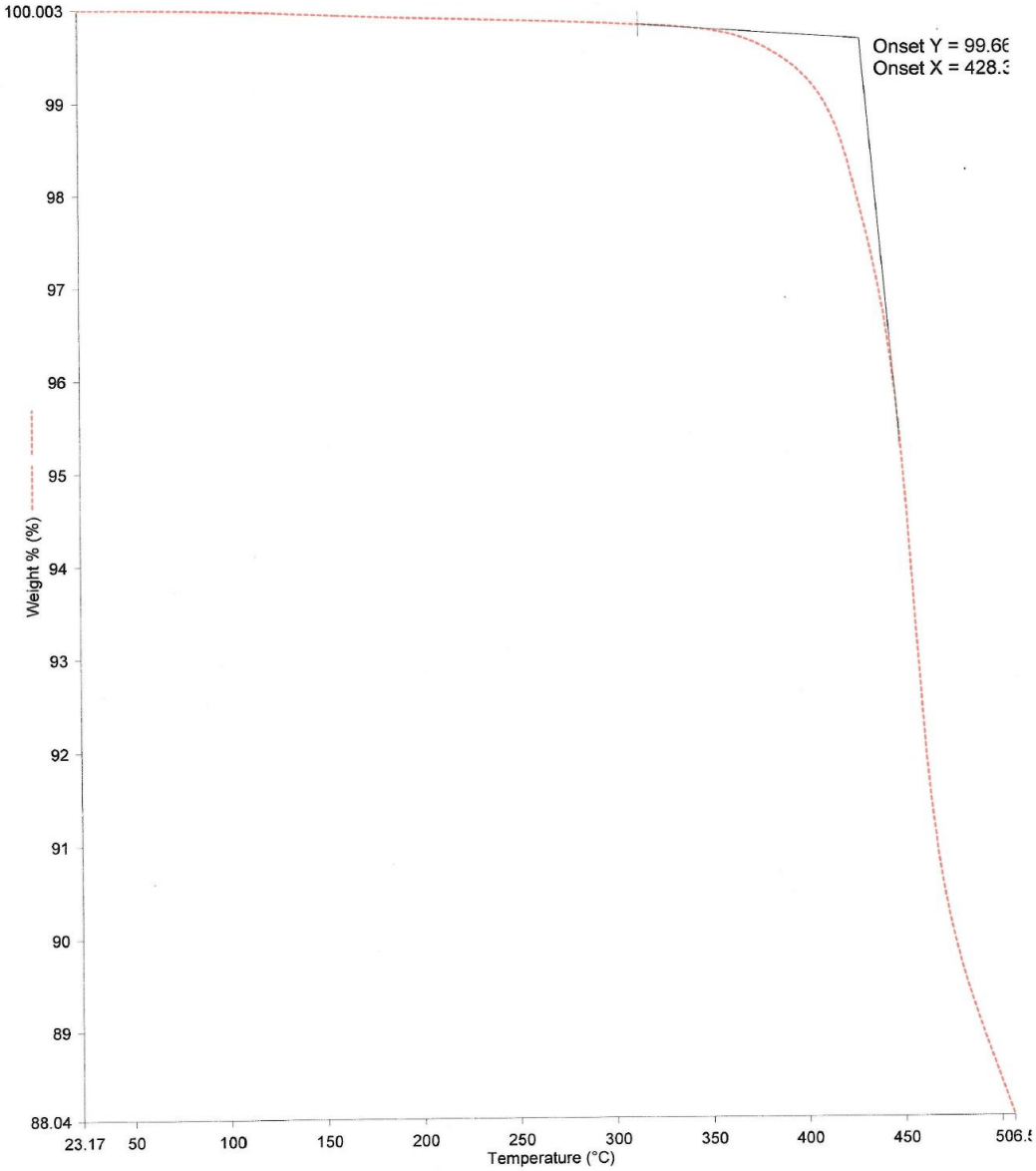

Figure S151. TGA trace of complex *rac* **13**. Onset = 428 °C.

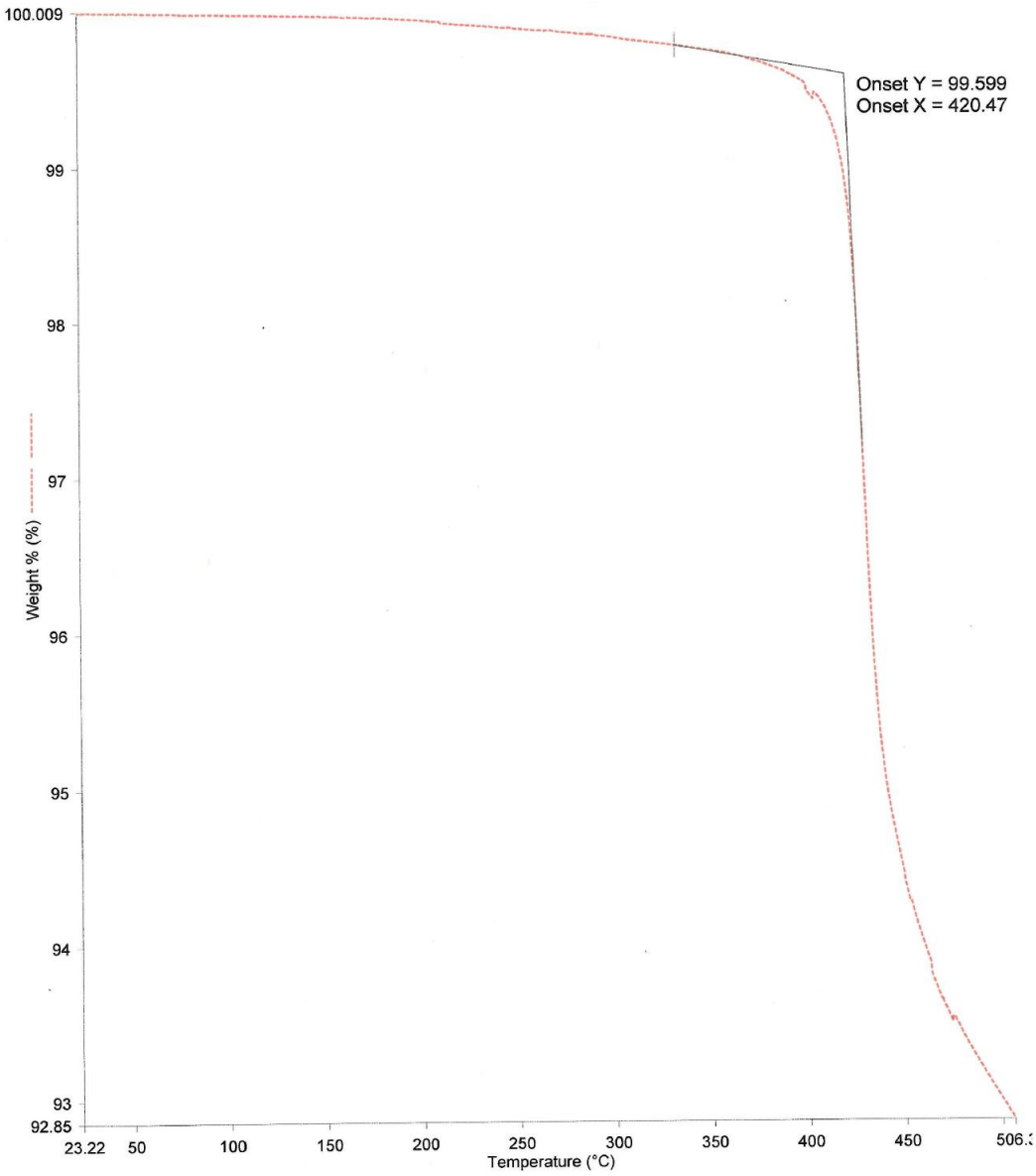

Figure S152. TGA trace of complex **14**. Onset = 420 °C.

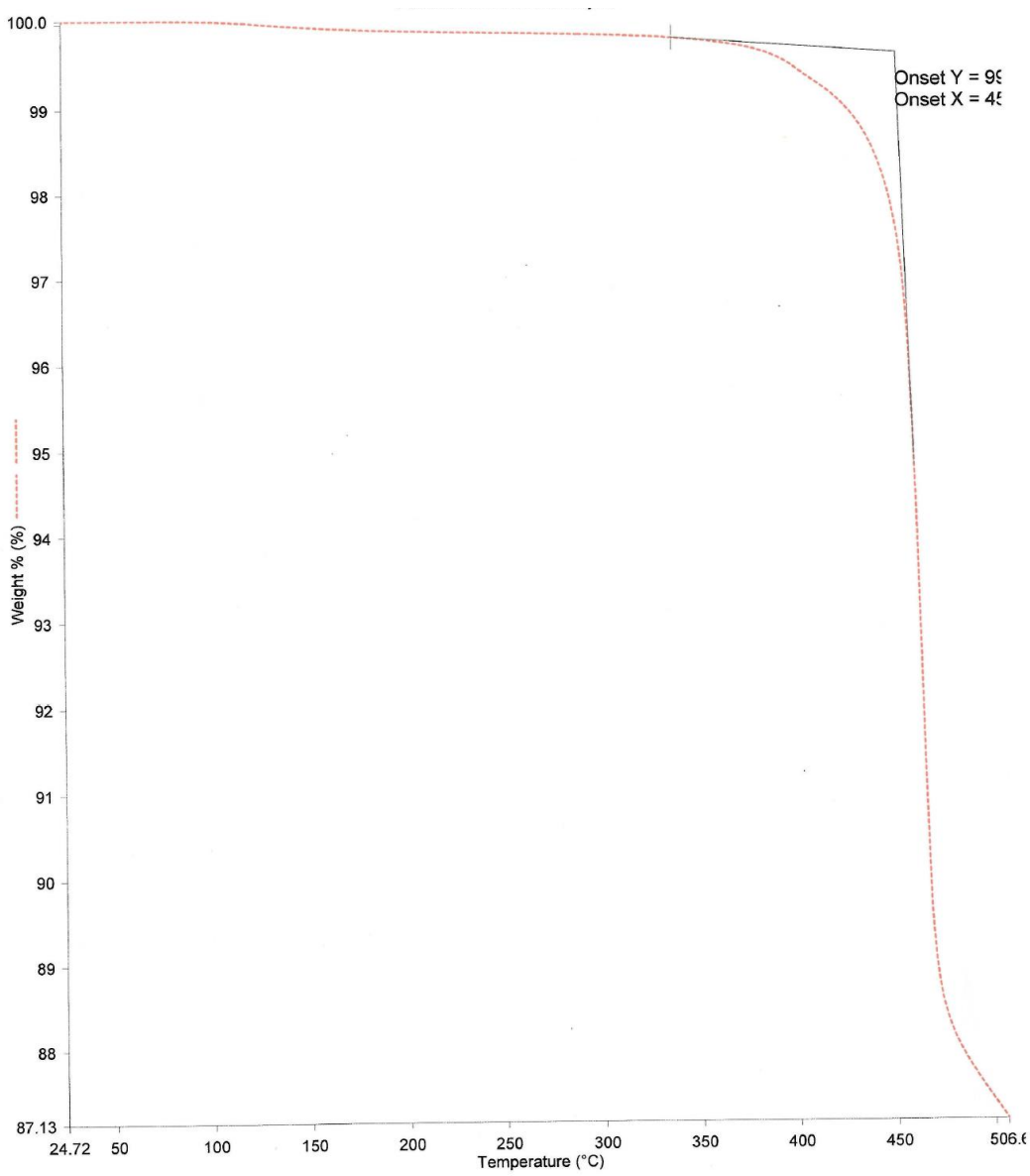

Figure S153. TGA trace of complex **15**. Onset > 450 °C.

Photophysics

Table S3. Tabulated absorption data for complexes **7–15** recorded in room temperature DCM solutions.

Complex	Isomer	λ_{abs} /nm (ε × 10^3 / $M^{-1}cm^{-1}$)
7	*mixture*	263 (77), 285sh (52), 310sh (30), 352 (15), 408 (7.5), 460 (4.3)
8	*mixture*	262 (70), 305sh (32), 345 (14), 380 (8.3), 400 (7.5), 455 (3.9)
9	*mixture*	261 (66), 281sh (50), 303sh (33), 345 (14), 400 (7.2), 453 (3.9)
10	*mixture*	262 (66), 281sh (50), 305sh (30), 347 (13), 377 (7.7), 401 (7.0), 451 (3.7)
11	*rac*	264 (80), 282 (70), 348 (19), 381 (11), 404 (10), 455 (5.5)
12	*meso*	265 (87), 281sh (81), 343 (25), 400 (11), 452 (5.4)
13	*meso*	255 (96), 274sh (79), 305sh (51), 336 (36), 384 (14), 430 (4.2), 460 (1.7)
	rac	255 (94), 276sh (73), 205sh (51), 335 (35), 386 (14), 430 (4.4), 460 (1.7)
14	*	252 (89), 272sh (77), 312sh (46), 331 (38), 382 (12), 429 (2.5), 457 (0.5)
15	*	239 (95), 259 (91), 291sh (44), 328 (21), 360 (13), 374 (11), 416 (3.3)
FIrpic	-	277 (50), 301 (34), 304 (33) 337sh (14), 357sh (8.9), 400 (6.2), 454 (0.8)[a]

[a]Values taken from ref 17. *Single diastereomer of unknown absolute configuration. sh = shoulder

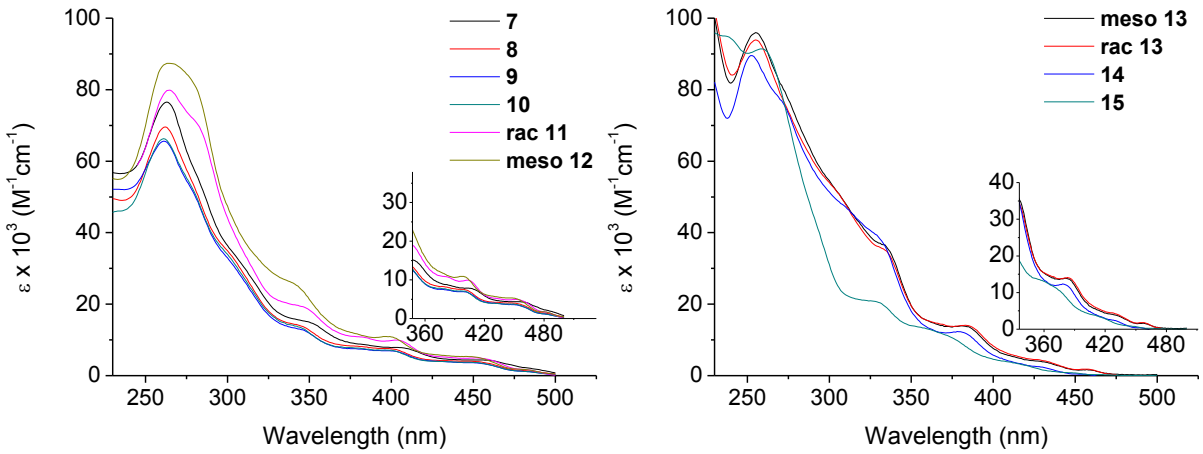

Figure S154. Absorption spectra of complexes **7–15** recorded in room temperature DCM solutions. Insets are expansions of the 350–500 nm regions.

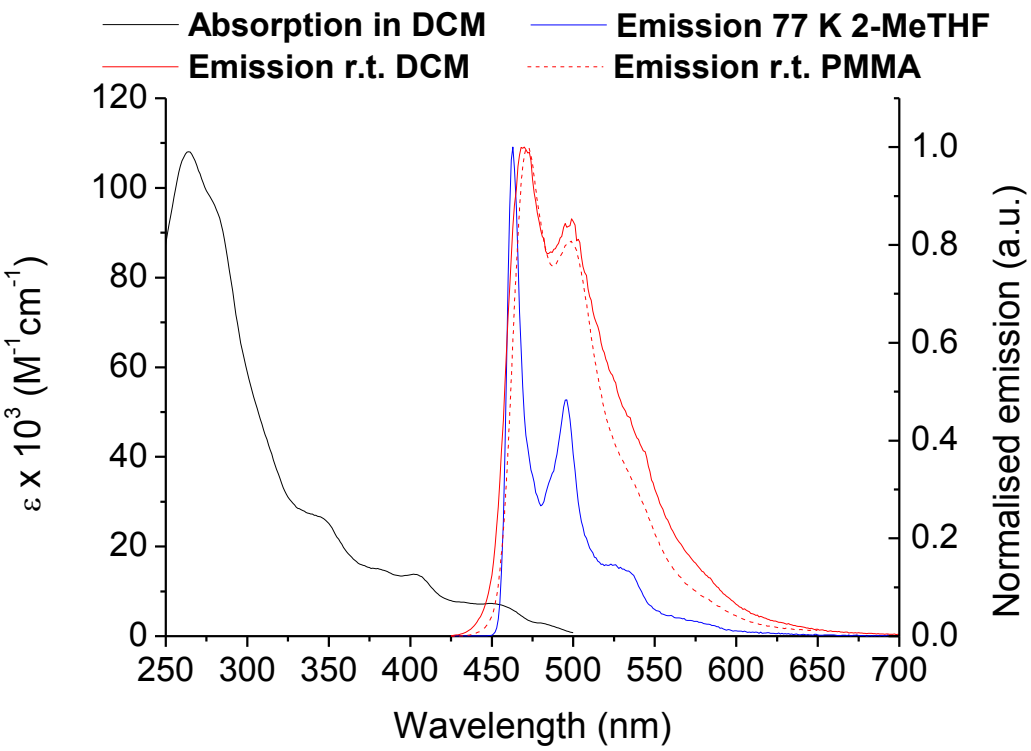

Figure S155. Spectral data for *rac* **13**.

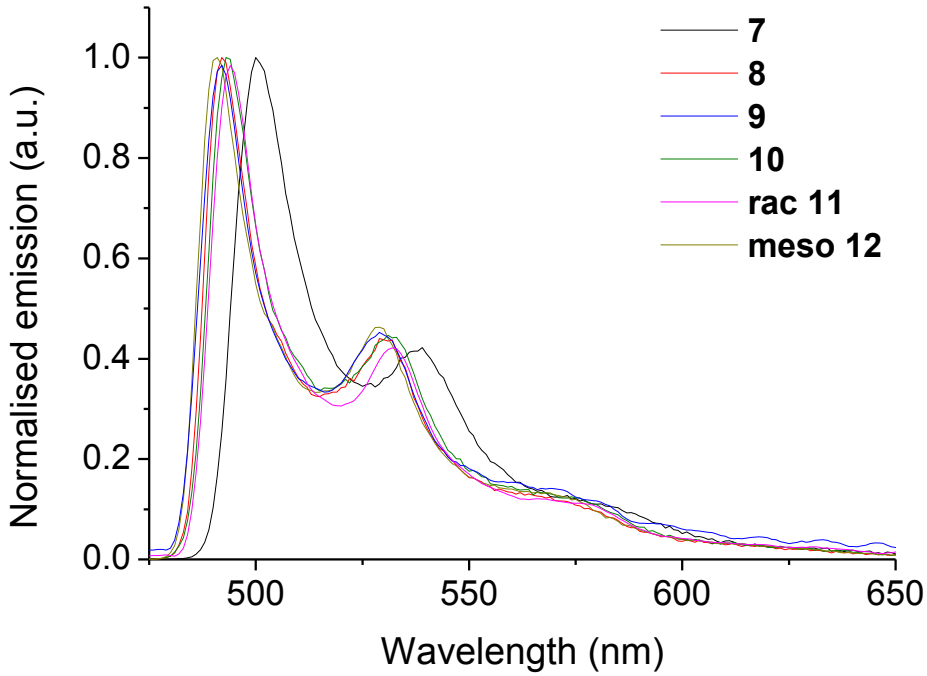

Figure S156. Normalised emission spectra of complexes **7**–**12** in 2-MeTHF glasses at 77 K (λ_{exc} 355 nm).

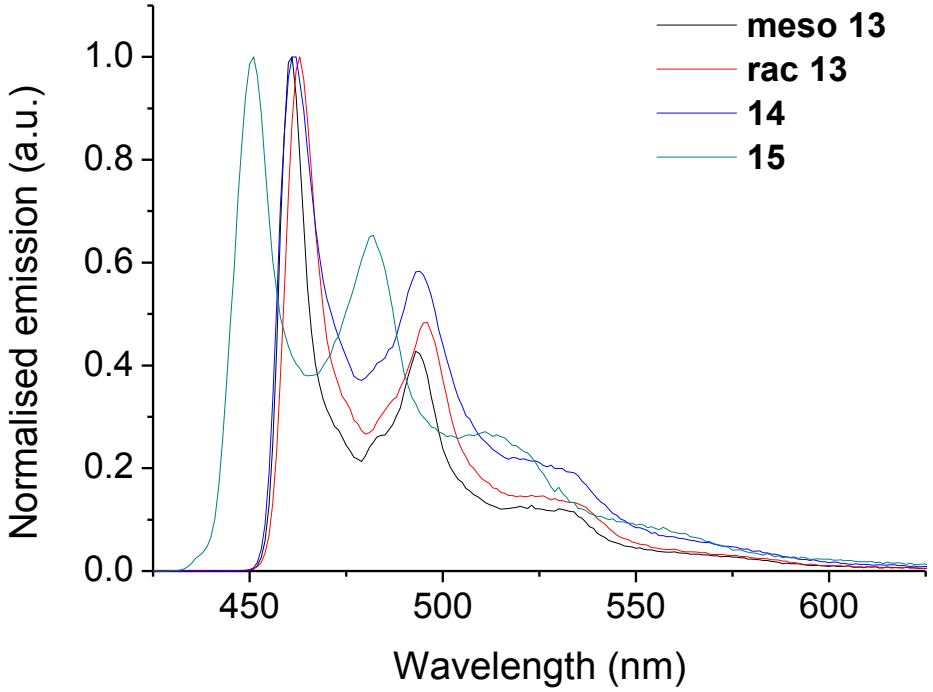

Figure S157. Normalised emission spectra of complexes **13**–**15** in 2-MeTHF glasses at 77 K (λ_{exc} 355 nm).

References

1 S. Sprouse, K. A. King, P. J. Spellane and R. J. Watts, *J. Am. Chem. Soc.*, 1984, 6647–6653.

2 V. N. Kozhevnikov, Y. Zheng, M. Clough, H. A. Al-Attar, G. C. Griffiths, K. Abdullah, S. Raisys, V. Jankus, M. R. Bryce and A. P. Monkman, *Chem. Mater.*, 2013, **25**, 2352–2358.

3 Gaussian 09, Revision A.02, M. J. Frisch, G. W. Trucks, H. B. Schlegel, G. E. Scuseria, M. A. Robb, J. R. Cheeseman, G. Scalmani, V. Barone, B. Mennucci, G. A. Petersson, H. Nakatsuji, M. Caricato, X. Li, H. P. Hratchian, A. F. Izmaylov, J. Bloino, G. Zheng, J. L. Sonnenberg, M. Hada, M. Ehara, K. Toyota, R. Fukuda, J. Hasegawa, M. Ishida, T. Nakajima, Y. Honda, O. Kitao, H. Nakai, T. Vreven, J. A. Montgomery, Jr., J. E. Peralta, F. Ogliaro, M. Bearpark, J. J. Heyd, E. Brothers, K. N. Kudin, V. N. Staroverov, R. Kobayashi, J. Normand, K. Raghavachari, A. Rendell, J. C. Burant, S. S. Iyengar, J. Tomasi, M. Cossi, N. Rega, J. M. Millam, M. Klene, J. E. Knox, J. B. Cross, V. Bakken, C. Adamo, J. Jaramillo, R. Gomperts, R. E. Stratmann, O. Yazyev, A. J. Austin, R. Cammi, C. Pomelli, J. W. Ochterski, R. L. Martin, K. Morokuma, V. G. Zakrzewski, G. A. Voth, P. Salvador, J. J. Dannenberg, S. Dapprich, A. D. Daniels, O. Farkas, J. B. Foresman, J. V. Ortiz, J. Cioslowski, D. J. Fox, Gaussian, Inc., Wallingford CT, 2009.

4 A. D. Becke, *J. Chem. Phys.*, 1993, **98**, 5648.

5 C. Lee, W. Yang and R. G. Parr, *Phys. Rev. B*, 1988, **37**, 785–789.

6 P. J. Hay and W. R. Wadt, *J. Chem. Phys.*, 1985, **82**, 270–283.

7 W. R. Wadt and P. J. Hay, *J. Chem. Phys.*, 1985, **82**, 284–298.

8 P. J. Hay and W. R. Wadt, *J. Chem. Phys.*, 1985, **82**, 293–310.

9 G. A. Petersson, A. Bennett, T. G. Tensfeldt, M. A. Al-Laham, W. A. Shirley and J. Mantzaris, *J. Chem. Phys.*, 1991, **94**, 6081–6090.

10 J. Melorose, R. Perroy and S. Careas, *J. Chem. Phys.*, 1988, **89**, 2193–2218.

11 A.-R. Allouche, *J. Comput. Chem.*, 2011, **32**, 174–182.

12 N. M. O'Boyle, A. L. Tenderholt and K. M. Langner, *J. Comput. Chem.*, 2008, **29**, 839–845.

13 L. Krause, R. Herbst-Irmer, G. M. Sheldrick and D. Stalke, *J. Appl. Crystallogr.*, 2015, **48**, 3–10.

14 G. M. Sheldrick, *Acta Crystallogr. A*, 2008, **A64**, 112–122.

15 O. V. Dolomanov, L. J. Bourhis, R. J. Gildea, J. A. K. Howard and H. Puschmann, *J. Appl.Crystallogr.*, 2009, **42**, 339–341.

16 G. M. Sheldrick, *Acta Crystallogr. C*, 2015, **71**, 3–8.

17 H. Benjamin, Y. Zheng, A. S. Batsanov, M. A. Fox, H. A. Al-Attar, A. P. Monkman and M. R. Bryce, *Inorg. Chem.*, 2016, **55**, 8612–8627.

18 R. Davidson, Y. Hsu, T. Batchelor and A. Beeby, *Dalton Trans.*, 2016, **45**, 11496–11507.

19 L.-O. Pålsson and A. P. Monkman, *Adv. Mater.*, 2002, **14**, 757–758.

20 D. G. Congrave, Y.-t. Hsu, A. S. Batsanov, A. Beeby and M. R. Bryce, *Organometallics*, 2017, **36**, 981–993.

21 N. Ai, A. Yoshinobu, O. Kazushi, S. Shimpei, I. Toshiya, I. Satoshi, US2005265686 (A1), 2005.

22 V. V. Il'in, O. V. Slavinskaya, Y. A. Strelenko, A. V. Ignatenko and V. A. Ponomarenko, *Bull. Acad. Sci. USSR, Div. Chem. Sci. English Transl.*, 1992, **40**, 2177–2180.

23 D. R. Martir, C. Momblona, A. Pertegás, D. B. Cordes, A. M. Z. Slawin, H. J. Bolink and E. Zysman-Colman, *ACS Appl. Mater. Interfaces*, 2016, **8**, 33907–33915.